annual progress report

2008

VEHICLE TECHNOLOGIES PROGRAM

ENERGY STORAGE RESEARCH AND DEVELOPMENT

U.S. Department of Energy
Energy Efficiency and Renewable Energy
Bringing you a prosperous future where energy is clean, abundant, reliable, and affordable

U.S. Department of Energy
Office of Vehicle Technologies
1000 Independence Avenue S.W.
Washington, D.C. 20585-0121

FY 2008

Progress Report for Energy Storage Research and Development

Energy Efficiency and Renewable Energy
Vehicle Technologies

David Howell
Acting Team Lead, Hybrid and Electric Systems

January 2009

TABLE OF CONTENTS

LIST OF FIGURES

LIST OF TABLES

I. INTRODUCTION

In 2008, U.S. consumers experienced historically high and (relatively) low gasoline prices which, for a period, rose in real terms to levels not seen since the early 1980s[1]. Partially as a result of the high gasoline prices (approaching $4/gallon for part of the year), sales of hybrid electric vehicles (HEVs) remained strong in 2008[2] – roughly at the same level as in 2007, and several automakers announced plans to introduce plug-in hybrid electric vehicles (PHEVs)[3] as well as full electric vehicles (EVs). The total HEV sales remained about 2-3 percent of all vehicle sales. An important step for the further market penetration of HEVs, as well as the electrification of the nation's personal transportation, is the development of cost-effective, long lasting, and abuse-tolerant Li-ion batteries.

The United States Department of Energy's (DOE's) continuing research and development (R&D) into advanced batteries for transportation offers the possibility of reducing our dependence on foreign oil and the potential negative impacts of increasing prices for that oil. It also directly supports the Administration's Advanced Energy Initiative, released in February 2006, which calls for the development of PHEVs with a 40 mile all-electric range. In FY2008, this work expanded to include a major new effort on high-energy batteries for PHEVs and underwent a relative deemphasizing of efforts on HEVs.

I.A Vehicle Technologies Program

The DOE's Vehicle Technologies (VT) Program office[4] works with industry to develop advanced transportation technologies that would reduce the nation's use of imported oil (since almost 96% of the US transportation fleet uses oil). Technologies being supported by VT include hybrid drive technologies, advanced energy storage devices (batteries and ultracapacitors), power electronics and motors, advanced structural materials, and advanced combustion engines and fuels, etc.

Collaboration with automakers enhances both the relevance and the potential for success of these programs. DOE works in partnership with the U.S. automakers through the United States Council for Automotive Research (USCAR)—an umbrella organization for collaborative research among Chrysler LLC, Ford Motor Company, and General Motors Corporation[5]. This partnership is focused on funding high-reward/high-risk research that promises improvements in critical components needed for more fuel efficient and cleaner vehicles.

I.B Energy Storage Research & Development Overview

Energy storage technologies, including batteries and ultracapacitors, have been identified as critical enabling technologies for advanced, fuel-efficient, vehicles. The Energy Storage Research and Development effort within the VT Program is responsible for researching and improving advanced batteries and ultracapacitors for a wide range of vehicle applications, including HEVs, PHEVs, and EVs. The office is working in close partnership with the automotive industry,

[1] http://www.eia.doe.gov/emeu/steo/pub/fsheets/real_prices.html
[2] http://www.hybridcars.com/market-dashboard.html
[3] http://www.greencarcongress.com/2007/07/toyota-to-obtai.html, http://www.gm-volt.com/
[4] See http://www.eere.energy.gov/vehiclesandfuels/.
[5] For more information, please see http://www.uscar.org/guest/view_partnership.php?partnership_id=1.

represented by the United States Advanced Battery Consortium (USABC). The effort consists of three major activities: battery development, applied battery research for transportation, and focused fundamental battery research.

Battery Development is further organized into benchmark testing and full system development.

- *Benchmark Testing* – The benchmark testing of emerging technologies is needed to remain abreast of the latest industry developments. Working with the national laboratories, VT purchases and independently tests hardware against manufacturers' specifications and the most applicable technical targets.

- *Full System Development* – In cooperation with industry, efforts are focused on developing (and evaluating) lithium batteries and ultracapacitor technologies for vehicles. Specifically, this work is focused on developing batteries for HEV and PHEV applications and ultracapacitor technologies for the 42 Volt start/stop application.

Applied Battery Research is focused on addressing the cross-cutting barriers that face Li-ion systems which are closest to meeting all energy and power requirements for use in vehicles. Several national laboratories participate in this activity, each bringing its own expertise to address the barriers: life, abuse tolerance, low-temperature performance, and cost.

Focused Fundamental Battery Research addresses fundamental problems of chemical instabilities that impede the development of advanced batteries, investigates new and promising materials, provides a better understanding of why systems fail, and develops models to predict system failure and enable system optimization. National laboratories, universities, and some commercial entities participate in this activity.

Contributors to the work described in this document are identified in Appendix A, highlights from 2008 (for the applied and exploratory research programs) are provided in Appendix B, and a list of acronyms is provided in Appendix C. A color version of this report (since several figures have color content) can be accessed at http://www1.eere.energy.gov/vehiclesandfuels/resources/fcvt_reports.html.

We are pleased with the progress made during the year and look forward to continued work with our industrial, government, and scientific partners to overcome the challenges that remain to developing advanced energy storage systems for vehicle applications.

David Howell
Acting Team Lead, Hybrid and Electric Systems
Vehicle Technologies Program

II. BATTERY TECHNOLOGY DEVELOPMENT

One of the primary objectives of the Energy Storage effort is the development of durable and affordable advanced batteries (and ultracapacitors) for use in a full range of vehicle applications, from start/stop to full-power HEVs, EVs, and PHEVs. The battery technology development activity spans three areas: *system development* of full battery systems; *benchmark testing* of emerging technologies in order to remain abreast of the latest industry developments; and *Small Business Innovative Research (SBIR)* to fund early-stage R&D for small businesses/entrepreneurs.

II.A System Development

System Development is focused on the small-scale manufacture of cells, batteries, and ultracapacitors for both high-power applications such as HEVs and 42 Volt start/stop systems and high-energy applications such as PHEVs. All system development for light duty vehicles is conducted in collaboration with industry through the USABC. All of the USABC subcontracts are awarded competitively and are cost-shared by the developer at a minimum of 50 percent.

Work on new battery technologies is organized into High-Energy Storage and High-Power Energy Storage. The following sections highlight the requirements and battery development activities within each of these areas.

High-Energy Battery R&D

The PHEV research and development activity is now underway. Requirements for PHEV batteries were developed in close coordination with industry (through the USABC) and a summary of those is shown in Table II- 1. (For more details and for other goals, see http://www.uscar.org/guest/view_team.php?teams_id=11.)

Table II- 1. Summary Requirements for PHEV Batteries

Characteristics at the End of Life		High Power/Energy Ratio Battery	High Energy/Power Ratio Battery
Reference Equivalent Electric Range	miles	**10**	**40**
Peak Pulse Discharge Power (2 sec/10 sec)	kW	**50/45**	**46/38**
Peak Regen Pulse Power (10 sec)	kW	**30**	**25**
Available Energy for CD (Charge Depleting) Mode, 10 kW Rate	kWh	**3.4**	**11.6**
Available Energy in Charge Sustaining (CS) Mode	kWh	**0.5**	**0.3**
CD Life	Cycles	**5,000**	**5,000**
CS HEV Cycle Life, 50 Wh Profile	Cycles	**300,000**	**300,000**
Calendar Life, 35°C	year	**15**	**15**
Maximum System Weight	kg	**60**	**120**
Maximum System Volume	Liter	**40**	**80**
System Recharge Rate at 30°C	kW	**1.4 (120V/15A)**	**1.4 (120V/15A)**
Unassisted Operating & Charging Temperature	°C	**-30 to +52**	**-30 to +52**
Maximum System Price @ 100k units/yr	$	**$1,700**	**$3,400**

The high-energy efforts are focused on overcoming the technical barriers associated with commercialization of PHEV batteries, namely:

- **Cost –** The current cost of Li-based batteries (the most promising chemistry) is approximately a factor of three-five too high on a kWh basis. The main cost drivers being addressed are the high cost of raw materials and materials processing, the cost of cell and module packaging, and manufacturing costs.
- **Performance –** The performance barriers include the need for much higher energy densities to meet the volume/weight requirements, especially for the 40 mile system, and to reduce the number of cells in the battery (thus reducing system cost).
- **Abuse Tolerance –** Many Li batteries are not intrinsically tolerant to abusive conditions such as a short circuit (including an internal short circuit), overcharge, over-discharge, crush, or exposure to fire and/or other high temperature environments. The use of Li chemistry in these larger (energy) batteries increases the urgency to address these issues.
- **Life –** The ability to attain a 15-year life, or 300,000 HEV cycles, or 5,000 EV cycles are unproven and are anticipated to be difficult. Specifically, the impact of combined EV/HEV cycling on battery life is unknown and extended time at high state of charge (SOC) is predicted to limit battery life.

In April 2007, USABC issued a solicitation for PHEV development contracts. Four projects were selected for award. The following paragraphs summarize those ongoing efforts.

Li-ion Battery Development (10 and 40 mile PHEVs)

Johnson Controls – Saft (JCS), a joint venture created by Johnson Controls Inc. and Saft Batteries to complement the two companies' strengths in high-volume manufacturing (specifically for the auto industry) and Li-ion electrochemistry, has been awarded a 24-month contract to develop 10 and 40 mile PHEV Li-ion batteries with significantly reduced cost and improved energy density. The approach is focused on the following key technical challenges:

- Improving the energy/power densities and specific power/energy at cell and pack levels.
- Understanding typical failure modes during PHEV cycling and designing countermeasures to ensure compliance with the life goals
- Understanding, and improving, the abuse tolerance behavior of the PHEV battery system
- Achieving the projected price targets based upon manufacturing and supply chain efficiencies based on market projections for raw materials price

Li-ion Polymer Battery Development (10 mile PHEV)

Compact Power Inc. (CPI) was awarded a 27-month $12.9M contract to develop cells and batteries for a 10 mile PHEV using a blend of layered and $LiMn_2O_4$ spinel-based cathode. The focus of this research will be to develop and optimize the new cell through:

- Calendar and cycle life testing and validation
- Available energy improvement
- Studies on low temperature performance
- Abuse tolerance studies

Nano-Phase Iron Phosphate Battery Development (10 and 40 mile PHEVs)

A123Systems was awarded a 36-month, $12.5M contract to develop battery technology for 10 and 40 mile PHEVs using their Nanophosphate™ ($LiFePO_4$) cathode material.

The development of the 10 and 40-mile PHEV battery systems technology will focus on cost reduction, cycle life, system weight and volume, and available energy. The work will also determine the impact of long-term deep cycling and calendar life testing. The PHEV-10 mile system will utilize a cylindrical cell design, based on the HEV cell design, while the PHEV-40 will use a pouch cell for weight and volume reduction. A123 will investigate and develop higher voltage, higher energy phosphate materials for the cathode, including $LiMnPO_4$, for the 40 mile system. The support work will focus on the development of an improved separator for the higher energy cells for both systems.

High Rate Low Cost Li-ion Battery Development (10 mile PHEV)

EnerDel was awarded an 18-month contract to develop a 10 mile PHEV cell using their nano-phase lithium titanate (LTO) coupled with a high voltage positive material, with an average cell voltage of approximately 3.2V. The nano-phase LTO is characterized by extremely small primary particles (10 to 20nm) agglomerated into 1 to 2 μm secondary particles that can be more easily processed into electrodes and can provide higher electrode density. The combination of these chemistries will enable EnerDel to achieve a battery that has the safety characteristics from the $Li_4Ti_5O_{12}$ material and the energy density necessary for the PHEV from the $LiMn_{1.5}Ni_{0.5}O_4$ material. The $LiNi_{1/3}Co_{1/3}Mn_{1/3}O_2$ (NMC) material will be used as a secondary cathode in the event that a high-voltage electrolyte cannot be developed in the appropriate time frame.

High-Power Energy Storage

High-power energy storage devices are among the critical technologies essential for the development and commercialization of HEVs. This effort is focused on overcoming the technical barriers associated with commercialization of high-power batteries, namely:

- **Cost –** The current cost of Li-based batteries is approximately a factor of two too high on a kW basis. The main cost drivers being addressed are the high cost of raw materials and materials processing, the cost of cell and module packaging, and manufacturing costs.
- **Performance –** The barriers related to battery performance include a loss in discharge power at low temperatures and power fade over time and/or when cycled.
- **Abuse Tolerance –** Many high-power batteries are not intrinsically tolerant to abusive conditions such as short circuits (including internal short circuits), overcharge, over-discharge, crush, or exposure to fire and/or other high-temperature environment.
- **Life –** The calendar life target for hybrid systems (with conventional engines) is 15 years. Battery life goals were set to meet those targets. A cycle life goal of 300,000 cycles has been attained in laboratory tests. The 15-year calendar life is yet to be demonstrated. Although several mature electrochemistries have exhibited a 10-15 year life through accelerated aging, more accurate life prediction methods need to be developed.

Battery requirements for HEVs were developed in coordination with industry (through the USABC) and are shown in Table II- 2.

Table II- 2. Summary Energy Storage Targets for Power Assist Hybrid Electric Vehicles

Characteristics	Minimum value	Maximum value
Pulse discharge power (kW)	**25 (for 10 seconds)**	**40 (for 10 seconds)**
Maximum regenerating pulse (10 s; kW)	**20 (50 Wh pulse)**	**35 (97 Wh pulse)**
Total available energy (kWh)	**0.3**	**0.5**
Cycle life (cycles)	**300k 25-Wh cycle (7.5 MWh)**	**300k 50-Wh cycle (15 MWh)**
Cold-cranking power at −30ºC (three 2-sec pulses, 10-s rests between; kW)	**5**	**7**
Calendar life (years)	**15**	**15**
Maximum weight (kg)	**40**	**60**
Maximum volume (liters)	**32**	**45**
Production price @ 100k units/year ($)	**$500**	**$800**
Operating temperature (ºC)	**−30 to +52**	**−30 to +52**

Specific objectives of this activity include:

- By 2010, develop an electric drive train energy storage device with a 15-year life at 300 Wh with a discharge power of 25 kW for 18 seconds and a cost of $20/kW.
- Develop hardware for specific applications that can be tested against respective performance targets and used for subsystem benchmarking.

The USABC is continuing to support the development of Li-ion technology through contracts with JCS (Li-ion), CPI/LG Chem (Li-ion polymer), EnerDel (Mn spinel/Lithium titanate), and A123Systems (iron phosphate). Details on these contracts and on development work on ultracapacitors follows.

Li-ion Battery Development (40kW HEV)

In May 2006, the USABC awarded a contract to the joint venture Johnson Controls-Saft for development of a 40 kW Li-ion battery with significantly reduced cost and improved abuse tolerance.

The contract was 24 months in duration, and concentrated on establishing state of the art cell-making capability at the Milwaukee location, and on leveraging Johnson Controls, Incorporated (JCI) high-volume manufacturing expertise to enable the best possible system cost. Development in Milwaukee has yielded electrodes that are nearly identical to those produced at Saft's facility in Bordeaux, France and recent projections of the high-volume production price look promising. The program was completed in September 2008.

Li-ion Polymer Battery Development (25kW HEV)

In September 2006, CPI was awarded an 18-month, $6.2M contract to continue development of Li-ion polymer cell technology for HEV applications using a $LiMn_2O_4$ spinel-based cathode. $LiMn_2O_4$ spinel is an attractive cathode for HEV batteries due to the fact that Mn is abundant, environmentally benign, potentially abuse-tolerant, and capable of high-rates of discharge.

CPI has recently achieved significant gains in calendar life estimates, which are currently being validated through testing at national laboratories. The CPI contract ended in early 2008 with final deliverables now undergoing testing at the national laboratories.

Nano-Phase Iron Phosphate Battery Development (25kW HEV)

In December 2006, A123Systems was awarded a 36-month, $15M contract to modify their doped, iron Nanophosphate™ ($LiFePO_4$) based power tool cell for HEV vehicle use. This cathode material is particularly attractive for automotive use due to its intrinsic abuse tolerance (although the anode reactivity remains to be mitigated), high-power capabilities, and stable cycling.

In 2008, A123Systems focused on developing new and more efficient nanophosphate manufacturing techniques, optimizing a low-temperature electrolyte, perfecting their thinner and higher power electrode design, and investigating the cost advantages of a prismatic cell design.

High Rate Low Cost Li-ion Battery Development (25kW HEV)

In August 2007, Enerdel was awarded an 18 month, $6.5M development contract to further develop and scale up their LTO/Mn spinel high-power cell materials and demonstrate their performance, life, and cost, in full sized (4-6 Ahr) cells, as well as in modules. The goals of this project are to demonstrate with test data that the LTO/ Mn-spinel system can meet the performance, life and cost goals of the USABC program, to identify failure modes of the cell, and design packaging approaches to address them. Testing on recent cells has achieved 240,000 cycles and appears able to reach the goal of 300,000 cycles.

Ultracapacitor Research and Development

Ultracapacitors' very high-power capability makes them a candidate technology for the 42V start-stop applications (requirements are shown in Table II- 3). To this end, the USABC contracted with NESSCAP to develop ultracapacitors for that application. The primary barriers addressed were the low energy density and high cost of the systems. The tasks included materials and electrode formulation, production verification, and module design.

NESSCAP ultracapacitors have been extensively tested by the Idaho National Laboratory (INL). By the end of the two-year contract that ended in August 2007, cells based on the USABC-5 electrode formulation were delivered to INL. After one million cycles, the USABC-5 cell is still meeting power and energy goals for the 42V application. A no-cost extension was initiated in November 2007 to complete and deliver modules and additional cells to three national labs – Sandia National Laboratories (SNL), National Renewable Energy Laboratory (NREL), and INL. This task was completed in September 2008. During this period, the USABC-5 formulation was further improved. A new formulation, called USABC-5.2, was developed. After 200,000 cycles, a USABC-5.2 cell outputs power and energy that scale to 9.6kW and 33.5Wh at the module level. It is expected that a 42V module with USABC 5.2 cells will weigh 13kg and occupy 14.9l.

II.B Thermal Management and Simulation

NREL performs battery thermal analysis and characterization, simulation and requirements analysis. This activity addresses issues related to battery thermal control and improving the thermal performance of energy storage devices through thermal characterization and testing, measuring thermal properties, modeling, analysis, and control strategies. It also conducts simulation and requirements analysis for DOE and the FreedomCAR Energy Storage Technical Team.

Table II- 3. Summary Ultracapacitor Requirements

Energy Storage Goals		Ultracapacitors[4]		
Characteristics	**Unit**	**12V Start-Stop**	**42V Start-Stop**	**42V Transient Power Assist**
Discharge Pulse Power	kW	4.2 for 2 sec	6 for 2 sec	13 for 2 sec
Regen Pulse Power	kW			8 for 2 sec
Cold cranking power @ -30°C (3 pulses)	kW	4.2 @ ≥7V for 2 sec	8 @ ≥21V for 2 sec	
Available Energy	Wh	15@ 1 kW	30 @ 1 kW	60 @ 1 kW
Calendar Life	year	15		
Cycle Life	cycle	750k cycles or 150k miles		
Maximum Self-discharge	var.	4% (72 hours from V_{max})		
Maximum Operating Voltage	Vdc	17	48	
Minimum Operating Voltage	Vdc	9	27	
Maximum System Weight	kg	5	10	20
Maximum System Volume	liter	4	8	16
Operating Temperature Range	°C	-30 to +52		
Selling Price @100,000 units/year	$	40	80	130

II.B.1 Battery Thermal Analysis and Characterization Activities

Thermal Characterization of A123Systems 26650 M1 Iron Phosphate Li-ion Cells (Smith) – The team performed a baseline thermal characterization of A123Systems' 26650-size, 2.2 Ah cell, commercially available on the consumer market. The 26650 cell, with a carbon anode and iron phosphate cathode, was originally developed for portable power tool applications. The team measured the heat generation rate and efficiency of the cells at temperatures of 30˚C, 0˚C, -15˚C and -30˚C. Thermal efficiency of the cell during constant current *discharge* at the C/1 rate (where C is rated capacity) was 97.8%, 90.1%, 79.9% and 47.6% at those respective temperatures. The average heat generation rate for various discharge profiles at 30˚C is shown in Figure II-1. Interestingly, thermal efficiency during C/1 constant current *charge* remained high, >92%, even at the very low temperature of -30˚C. Efficiency was also measured for scaled power profiles meant to represent normal (25 Wh) and aggressive (US06) driving of a midsize hybrid car. For a battery sized with 192 cells, the round-trip energy efficiency was 94.5% for the normal profile and 90.1% for the aggressive profile, with both tests run at 30˚C and 50% SOC. Partial discharge tests within various SOC windows showed the 75% to 50% window to be most efficient, and the 25% to 0% window to be least efficient.

The team also measured heat capacity and took infrared thermal images of those cells. Thermal imaging during a high-rate 70 Amp continuous discharge caused the positive end of the can wall to become 3.5˚C hotter than the other sides; thermal imaging during sustained 24.6 Amp root mean square (RMS) cycling also showed sides neighboring other cells to become 2˚C hotter than the front of the cell exposed to natural convective cooling. In the latter test, terminal ends were about 5˚C hotter than the outer can wall which is surrounded by cardboard insulation not efficient at removing heat. Despite the cardboard insulation, the cell performed reasonably well, showing no significant areas of thermal concern.

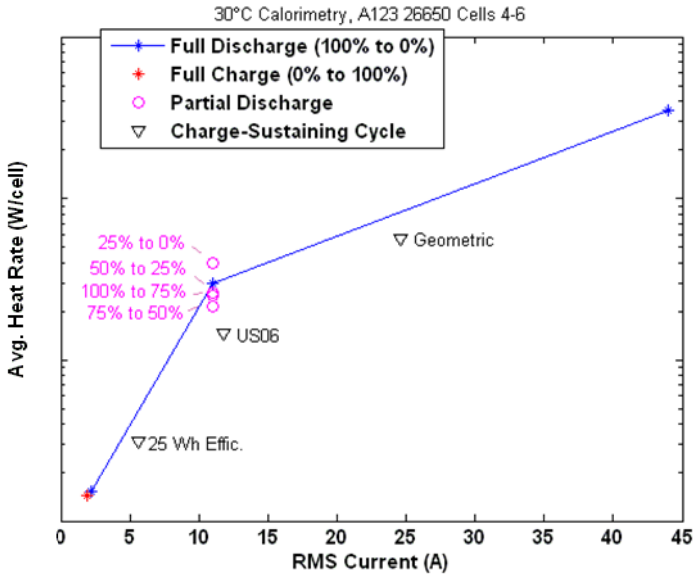

Figure II-1. Average heat generation rates for various discharge profiles at 30˚C for the A123Systems' 26650 cells.

Thermal Characterization of A123Systems' 32113 Ultra Cells to Aid Thermal Design of Packs (Smith) – The team performed thermal characterization testing of A123systems' 32113 cells designed for HEV applications. The cell uses a carbon anode and iron phosphate cathode. Thermal efficiency of the cell during constant current *discharge* from 80% to 20% SOC at the C/1 rate ranged from ~100% to 75.5% over the test temperature range of 45˚C to -30˚C. Efficiency was also measured for scaled power profiles for normal (25Wh) and aggressive (US06) driving of a midsize hybrid car.

A high-rate 150 Amp continuous discharge caused the middle of the can wall to become 4-5˚C warmer than the ends; sustained 40.4 Amp RMS cycling (comparable to aggressive US06 driving) resulted in a uniform temperature profile with < 1˚C variation along the can wall. There were no areas of thermal concern. Compared to the 26650 cell, the 32113 cell showed a higher efficiency, lower heat generation and better thermal uniformity.

The equivalent heat generation resistances for the various charge/discharge profiles and temperatures are shown in Figure II-2. Figure II-3 shows infrared thermal images of three A123Systems 32113 cells connected in series at the end of a 150 Amp continuous discharge and 40.4 Amp RMS pulse cycling.

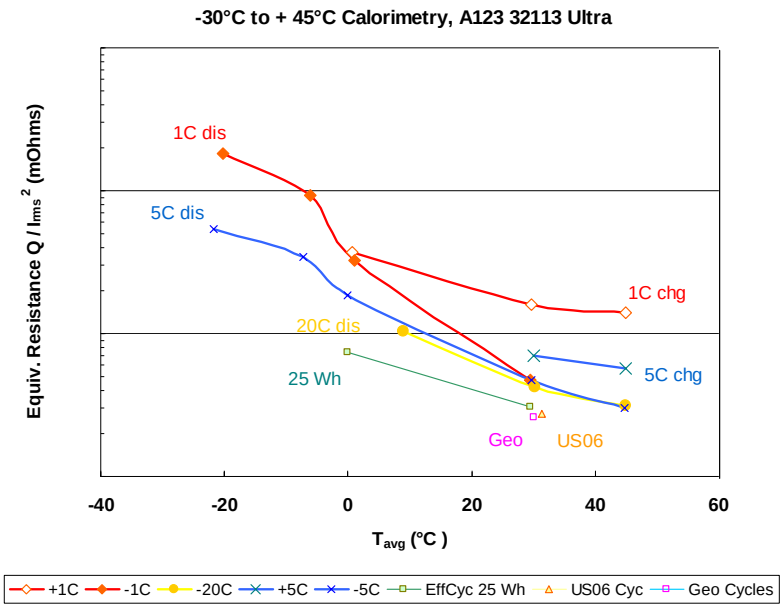

Figure II-2. Equivalent heat generation resistance for various charge/discharge profiles and temperatures for the A123Systems 32113 cells.

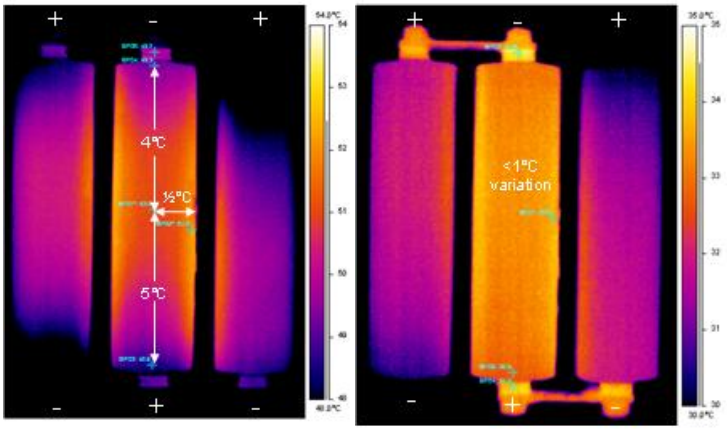

Figure II-3. Infrared thermal images of three A123Systems 32113 cells connected in series at the end of a 150 Amp continuous discharge (left) and 40.4 Amp RMS pulse cycling (right). The thermal performance of the center cell is representative of most cells in a module and they performed well thermally.

Thermal Characterization of the CPI/LG Chem Cells (Smith) – The team completed thermal characterization of CPI/LG Chem prototype Gen 4.2 Li-polymer cells, with a carbon anode and manganese spinel cathode, developed for HEV applications. Thermal efficiency of the cell during 5C constant current discharge ranged from 96.3% to 55.6% over the test temperature range of 45˚C to -30˚C. Efficiency was also measured for scaled power profiles for normal (25Wh) and aggressive (US06) driving of a midsize hybrid car. The round-trip energy efficiency was 97.5% for the normal profile and 94.9% for the aggressive profile, with both tests run at 30˚C and 50% SOC. At 0˚C, the round-trip efficiency for the aggressive profile decreased to 86.7%. Figure II-4

shows average heat generation rate, expressed in terms of an equivalent resistance by dividing it with the square of the RMS current, for various constant current discharge and cycling profiles. The charge-sustaining cycling profiles generate approximately half the heat compared to constant current discharge tests due to reduced polarization.

Aggressive cycling of Gen 4.2 cells showed a maximum spatial temperature difference on the exterior of the cell at end of discharge of ~5˚C. The exterior portion of the cell over the electrochemically active region of the cells' exterior was generally within 2˚C. There were no hot spots or areas of thermal concern. These results were shared with CPI/LG Chem to enable the design of modules with improved thermal performance.

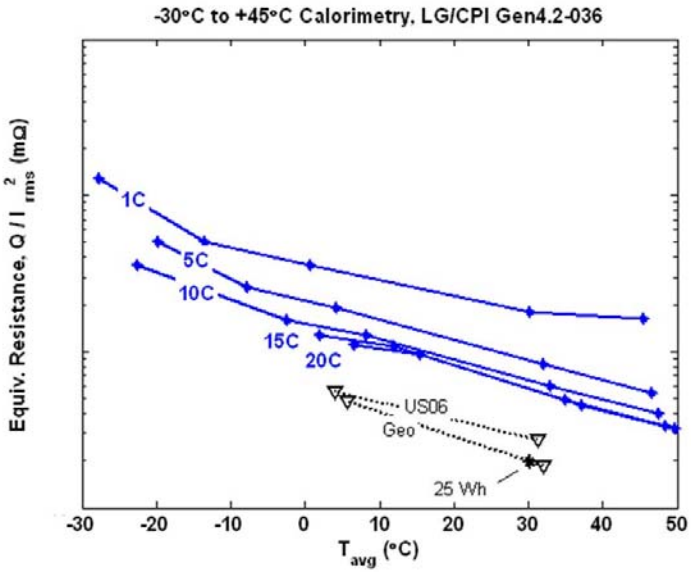

Figure II-4. Equivalent heat generation resistance for various constant current discharge and cycling profiles from -30˚C to 45˚C.

Thermal Performance of CPI HEV Module with LG Chem Cells (Keyser) – The team measured the thermal characteristics of CPI's HEV air-cooled module with LG Chem cells. The module consisted of eight HEV Li-ion cells in series and was subjected to 12 consecutive (2 hours) US06 cycles at an initial depth of discharge (DOD) of 50%. Figure II-5 shows the end cell temperatures after 12 consecutive US06 cycles with an initial starting temperature of 30˚C.

Thermal Characteristics of JCS' $LiNi_{0.8}Co_{0.15}Al_{0.05}O_2$ (NCA) Li- Ion Cells (Keyser) – The third generation of VL6P (approximately 6Ah) cells are designed to provide satisfactory low temperature performance. The Gen 3 cell was slightly less efficient than the first two generations of cells at higher test temperature. The efficiency and heat generation differences between the cells were exacerbated at higher discharge currents – higher test currents resulted in lower efficiencies. However, this cell had a higher discharge capacity than the first two generations of cells at lower test temperatures.

Figure II-6 shows the heat generation of the Gen3 cell as a function of temperature and discharge current. As expected, the heat generation increases as the temperature of the cell decreases.

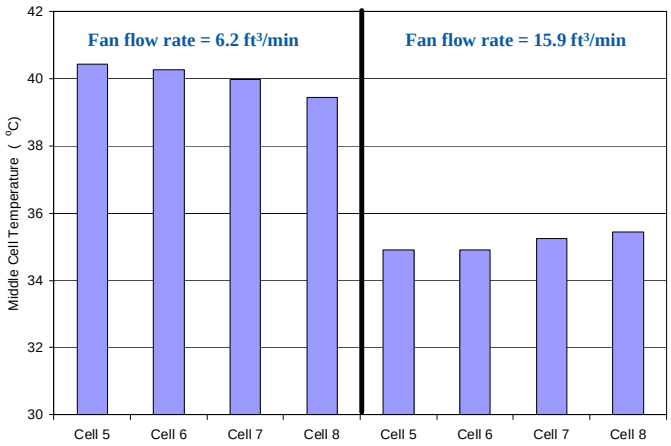

Figure II-5. End cell temperatures of the CPI HEV module after 12 US06 cycles, at two different air-flow rates. The initial temperature is 30˚C

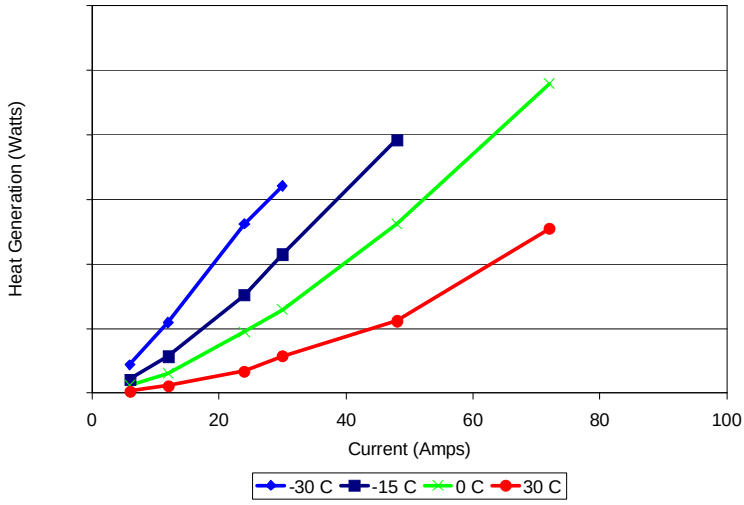

Figure II-6. Heat Generation Rate of JCS VL6P Gen 3 $LiNi_{0.8}Co_{0.15}Al_{0.05}O_2$ (NCA) Li-ion Cell.

Thermal Images of High Energy JCS VL22M and VL41M Cells (Keyser) – The VL41M cell (41Ah) was infrared-imaged under successive charge-depleting and charge-sustaining cycles as well as under a 100 Amp geometric cycle. The VL22M cell was also imaged under the 100 Amp geometric cycle. For both cells, the negative terminals have higher impedance associated with them than the positive terminals (connected to the case and having more surface area to dissipate heat) and the surface temperatures across the cell are relatively uniform (within 2˚C). The VL41M cell under charge-depleting cycles attains a maximum cell surface temperature of 37˚C in still air. The VL22M cell under the 100 Amp geometric cycling achieves a surface temperature of 55 ˚C, which cools to 37.5 ˚C after an hour of cycling with cooling air. No areas of thermal concern were identified. Figure II-7 (left and right) show infrared images of three VL41M and VL22M cells, respectively.

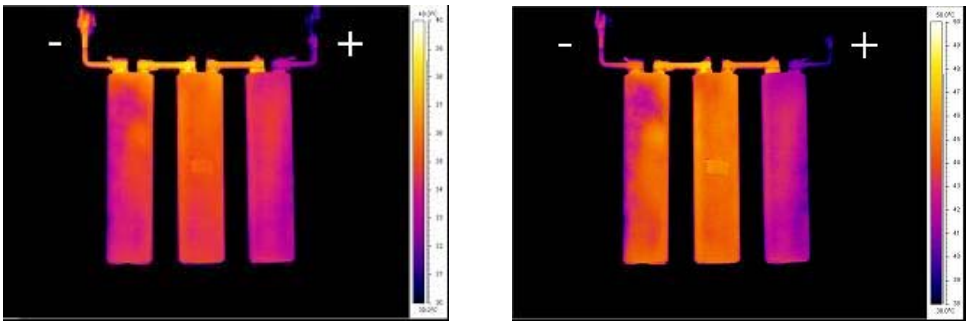

Figure II-7. Infrared thermal image of VL41M cells after 5 charge depleting cycles (left), Infrared thermal image of VL22M cells after 3 hours of geometric cycling (right).

Fabrication and Calibration of Large Calorimeter for Thermal Testing of PHEV Modules (Keyser, Powell) – Currently, the NREL calorimeter measures heat generation from small HEV modules and cells. In 2006, the team identified the need for a larger calorimeter to test larger modules for PHEV applications. After consulting with members of the USABC Technical Advisory Committee and FreedomCAR Energy Storage Technical Team, the team developed detailed technical specifications for the new calorimeter. During FY08, component fabrication of the calorimeter was completed and it was vetted at 30°C. It has gone through readiness verification, calibrated and sensitivity-verified to less than 5% by sending small energy pulses, as low as 100 Joules. Figure II-8 shows the calorimeter response to a 200 Joule energy pulse.

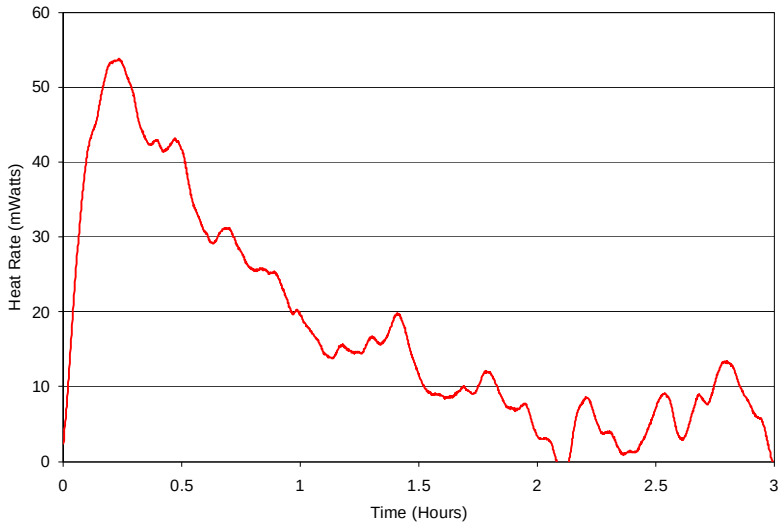

Figure II-8. Large calorimeter response to 200 Joule energy pulse.

II.B.2 Simulation and Requirements Analysis Activities

PHEV Battery Performance, Life, and Cost Tradeoff Analysis (Markel) – Battery models linked with vehicle simulation typically include empirical equivalent circuit models based on test data – suitable for fast simulation but limited in connection to physical battery design parameters such as electrode geometry and electrode materials and to the internal electrochemical characteristics of the module and cell. The goal of this project is to interconnect battery performance, cost, and life

models. The interconnected models would be used to parametrically explore the impact of battery design parameters for a PHEV application.

A battery performance model based on work by Prof. Newman at UC Berkeley was developed and correlated to performance data on the Saft VL41M cell. The composite battery life model includes both mechanical (capturing the stresses of cycling) and thermal (capturing effects of time for temperature and SOC) components. Data from industry and the DOE applied research program was used for the model. Finally, a parameterized cost model used in previous NREL analyses was updated and used. The model was applied to investigate if battery design parameters could be optimized to provide a low cost, long-life solution. A spectrum of battery designs satisfying the USABC PHEV (10 mile) requirements was produced, with an associated range of costs from $4,130 to $3,890. The lowest cost battery was the one with the highest power-to-energy ratio. A high power capability implies that energy stored at a low SOC is still accessible to the vehicle. A large power-to-energy ratio thus enhances the battery's usable energy.

Development of a Simple, Fast, Accurate, Multi-node Thermal Model for Li-ion Cells (Kim) – Increasing the numbers and sizes of cells in a battery pack complicates thermal control of the system. In addition to keeping a battery pack in the optimal temperature range, maintaining temperature uniformity among all cells in a pack is important to prolong life and enhance safety. A battery thermal model that can be coupled with a battery performance model and/or a safety model is required for safe and durable design of Li-ion batteries. Therefore, a multi-node thermal model for Li-ion cells was developed. With National Aeronautics and Space Administration (NASA) funding and test data, NREL has studied designs for safe operation of multi-string 18650 cells for spacesuit applications. The 5-node thermal model was developed to properly resolve temperatures of cell components –for predicting the behavior of the cell under abuse condition (Figure II-9).

As shown in Figure II-9 and Figure II-10, the 5-node thermal model evaluated thermal conductances between the cell nodes and ambient. The model successfully reproduced results from the rigorous finite-volume-method (FVM) model with 41,250 computational grids. The comparison between the rigorous FVM model and the 5-node model is plotted in Figure II-11.

Enhancement and Validation of a Multi-Dimensional Electrochemical/Thermal-Based Battery Models for PHEV Cell and Thermal System Design (Kim, Smith) – In FY07, the team developed a lumped thermal, 1-D electrochemical model solving transport equations based on UC Berkeley/Newman theory. The model was subsequently expanded into a multi-dimensional thermal model including the effect of cell-internal temperature gradients on non-uniform usage of cylindrical cells. In FY08, it was further expanded to include the effects of both temperature and potential field gradients for both cylindrical and flat cells. Shown in Figure II-12, a validation effort was initiated by comparing surface temperatures for a 41 Ah cell undergoing 5 charge depletion and 60 charge sustaining PHEV profiles to the jelly roll (JR) model predictions. The team also performed a modeling trade-off study (Figure II-13) on electrical and thermal performance of various cylindrical cell designs. At normal operating temperatures with a typical cell design, the potential field-effect dominates the temperature field-effect for dictating distribution of material usage (cold temperatures remain to be investigated). As a design rule, opposing terminal designs are favored over same-side terminal designs. The former design has greater uniformity between the positive and negative foil potentials along the jellyroll length,

promoting more uniform active material usage. Also, reducing electronic path length reduces heat generation, shown in Figure III- 13(d), and increases power. Among cylindrical cells, this indicates that flat pancake-like cells would be preferable to very tall, skinny cells.

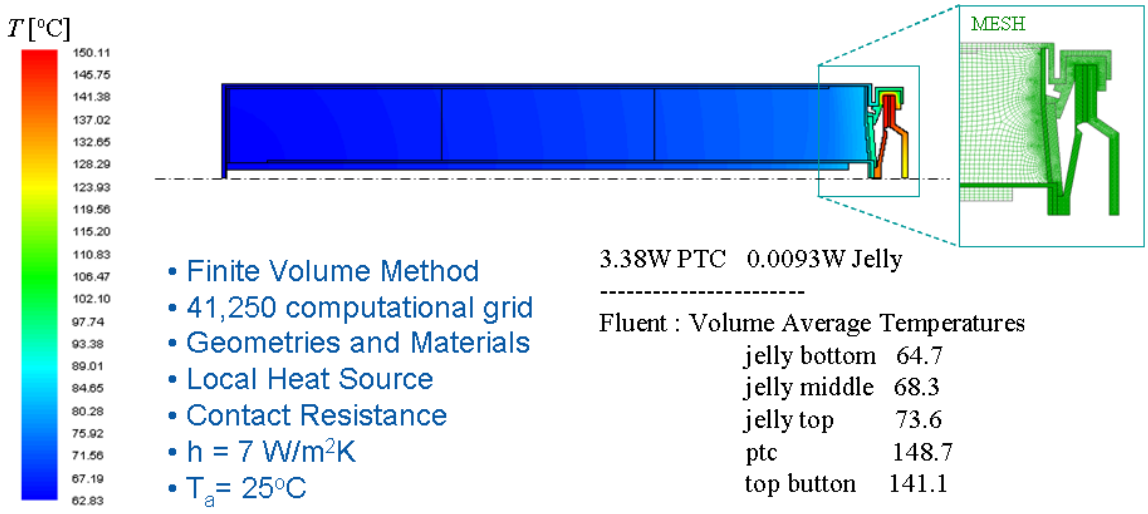

Figure II-9. High resolution FVM model developed based on test data

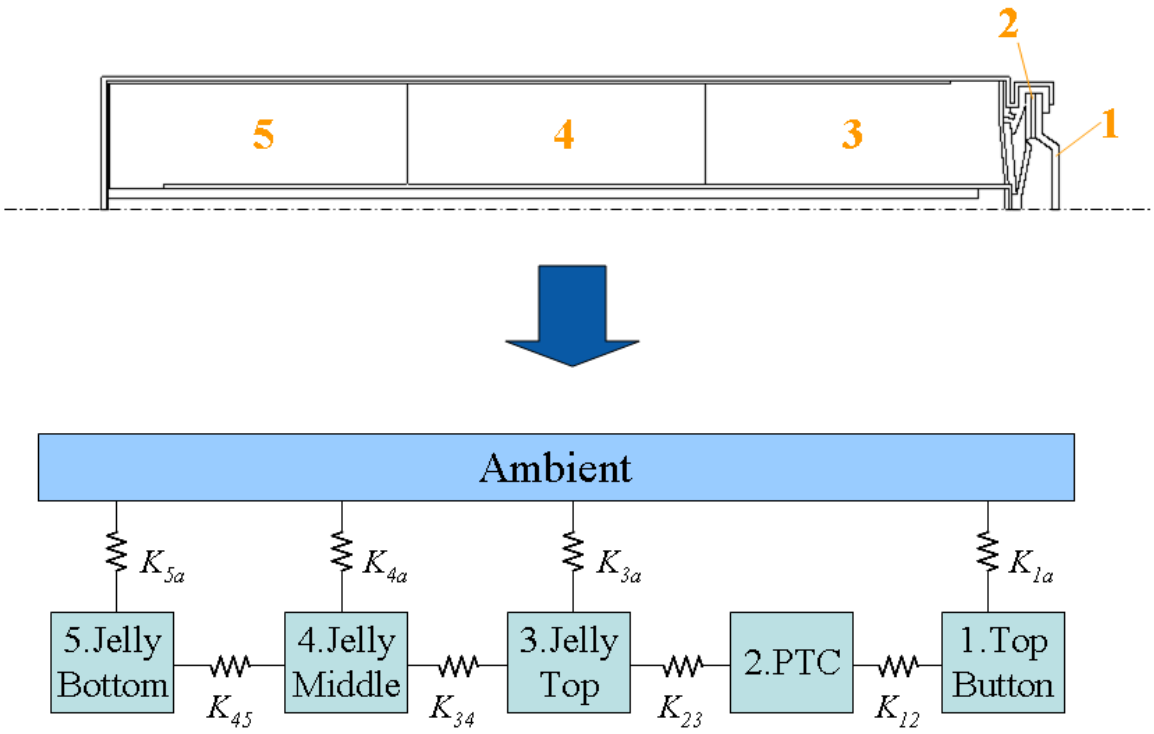

Figure II-10. Schematics for 5-node thermal model

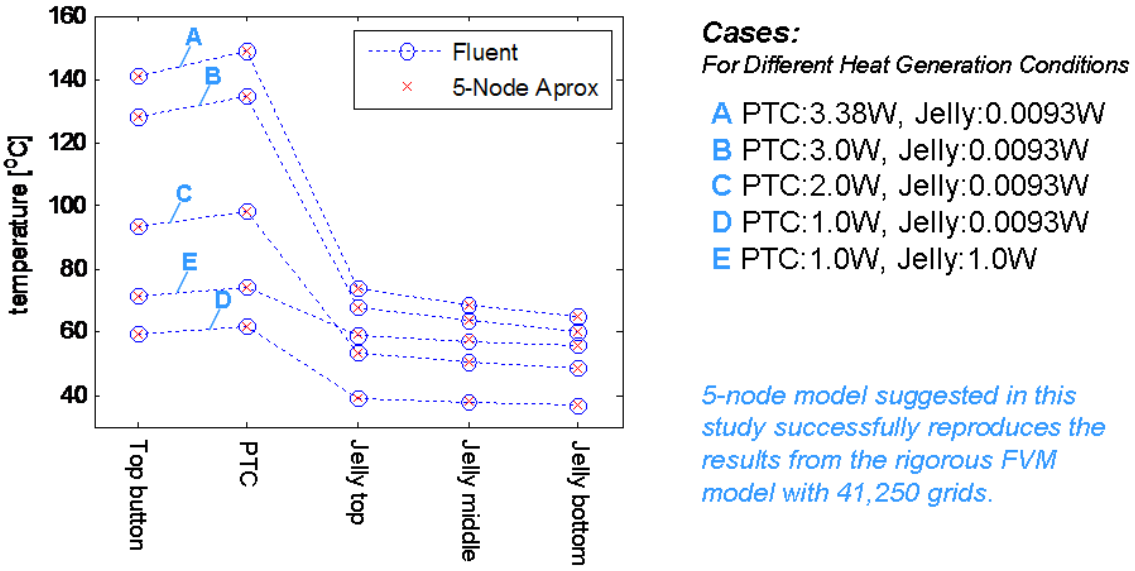

Figure II-11. Comparison between rigorous FVM model and 5-node model

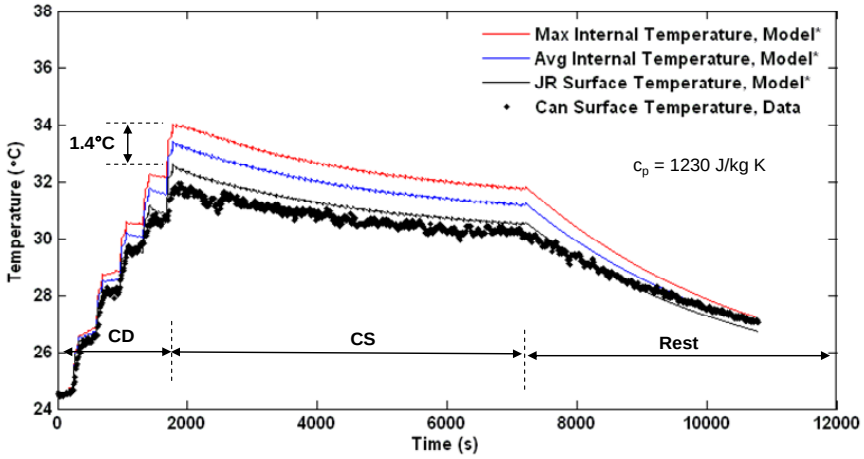

Figure II-12. Comparison of the Multi-Scale, Multi-Dimensional (MSMD) model of the jelly roll (JR) surface to can surface temperature from a JCS VL41M cell. Cycling profile is 5 charge depletion (CD) and 60 charge sustaining (CS) cycles per the USABC PHEV battery test manual.

II.B.3 Industry and International Support Activities

Evaluation of an Asymmetric Li-ion Capacitor from JM Energy (Keyser) – The team is testing JSR Micro's Li-ion capacitor. The cell consists of an activated carbon positive electrode and a Li doped carbon negative electrode with a proprietary electrolyte developed by JSR Corporation. Figure II-14 shows the discharge and regen impedance from the low current hybrid pulse power characterization (HPPC). The impedance of the cell is slightly higher than comparable Li-ion and ultracap cells. It should be noted that the low current HPPC impedance of the cell is approximately the same as the high current HPPC impedance. Typically, ultracapacitors and Li-ion cells display a higher discharge power than regen. However, the LiC cell has the opposite characteristic.

Further tests will include infra-red (IR) imaging and calorimeter testing to assess its thermal performance.

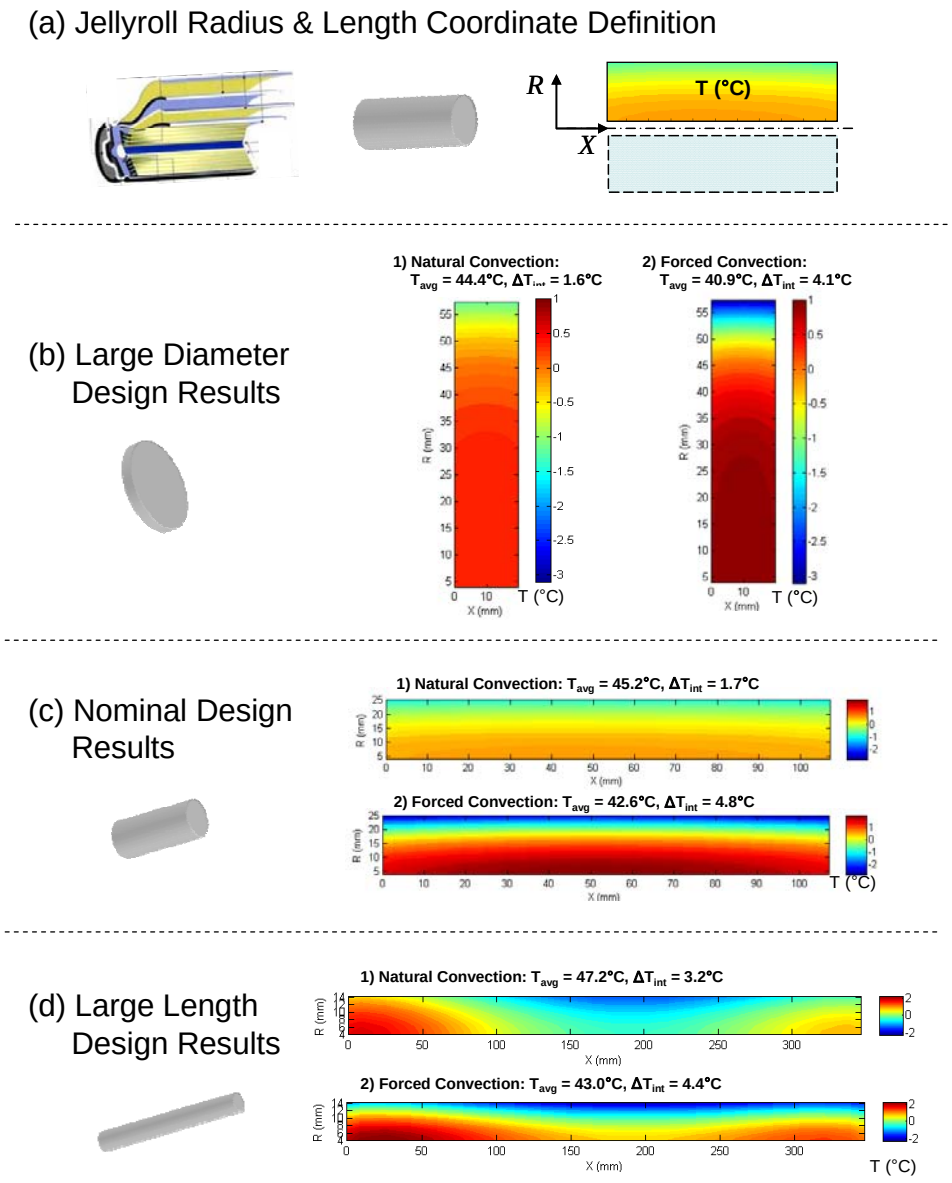

Figure II-13. Internal temperature for three different 20 Ah cell designs at the end of US06/PHEV10 charge depletion cycling. (a) Coordinate definition, (b-d) Temperature distributions for the three cell designs. The large diameter and large height designs both have large surface area for cooling, generally effective at lowering average temperature. The large length design however generates excessive heat due to the long electronic path-length.

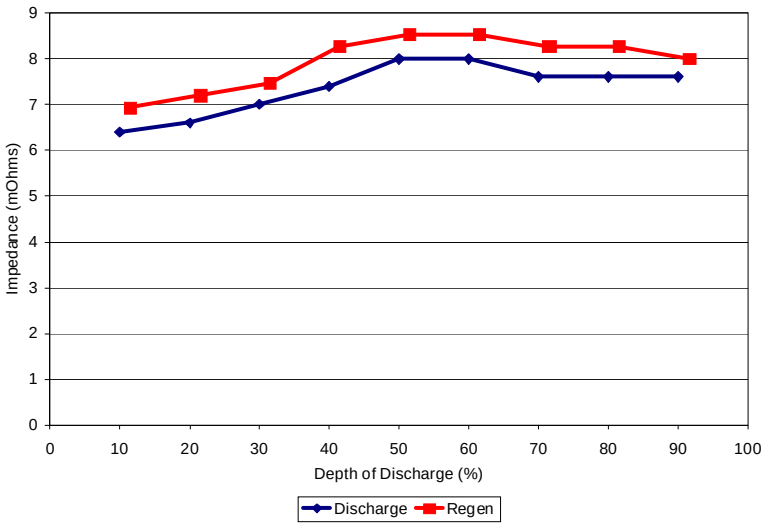

Figure II-14. Discharge and Regen low current HPPC impedance of LIC cell at 30˚C.

II.C Benchmark Testing

Benchmark testing of emerging technologies is important for remaining abreast of the latest industry developments. VT, working through Argonne National Laboratory (ANL) and INL, regularly purchases advanced battery hardware (cells and modules) and independently tests these battery systems against the most applicable USABC technical targets.

II.D Small Business Innovative Research (SBIR)

The SBIR program was created by the Small Business Innovation Development Act of 1982 (P.L. 97-219) and was designed to stimulate technological innovation, strengthen the technological competitiveness of small businesses, and use small businesses to meet Federal research and development needs. Phase I awards of up to $100,000 each for ~9 months are used to explore the feasibility of innovative concepts. Phase II is the principal research or R&D effort, with awards up to $750,000 over a two-year period.

Over the past several years, SBIR/ Small Business Technology Transfer Program (STTR) contracts have provided valuable support to EV and HEV battery development efforts. Phase I contracts awarded in FY 2008 are listed below:

- ***MaxPower, Inc., Harleysville, PA,*** Development of Separators for Li-ion Cells with High Temperature Melt Integrity
- ***Physical Sciences Inc., Andover, MA,*** Stabilized and Protected Lithium Cobalt Phosphate Cathode
- ***Policell Technologies, Inc., Metuchen, NJ,*** Development of Separators for Li-ion Cells with High Temperature Melt Integrity
- ***TIAX, LLC, Cambridge, MA,*** High Voltage Electrolyte for Li-ion Cells
- ***Yardney Technical Products, Inc., Pawcatuck, CT,*** Manganese Oxides-Based 5V Composite Cathode Materials for Li-ion Batteries in HEV and PHEV Applications

Technology Development Publications and Presentations

1. A. Pesaran, "Battery Pack Integration for Plug-In Hybrid Vehicles," Plug-In 2008, San Jose, CA, July 22-24, 2008.
2. A. Pesaran, "Battery Technology for Hybrid and Electric Vehicles - Opportunities and Challenges," AltCar Conference and Expo, Austin, TX, October 17, 2008.
3. G. Kim and K. Smith, "Multi-Scale Multi-Dimensional Model for Better Design and Management of Li-ion Batteries," 214th Electrochemical Society Meeting, Honolulu, HI, October 12-17, 2008.
4. G. Kim, and K. Smith, "Multi-Scale Multi-Dimensional Model for Better Cell Design," 1st International Conference on Advanced Lithium Batteries for Automotive Applications, Chicago, IL, September 15-17, 2008.
5. G. Kim, and K. Smith, "Three-Dimensional Lithium-Ion Battery Model," 4th International Symposium on Large Li- Ion Battery Technology and Application in conjunction with 8th AABC, Tampa, FL, May 2008.
6. G. Kim, J. Gonder, and J. Lustbader, "Evaluation of HEV Battery Thermal Management with Phase-Change Materials," the 23rd Electric Vehicle Symposium, Anaheim, CA, December 2007.
7. J. Lustbader, M. Keyser, J. Gonder, and A. Pesaran, "Thermal Evaluation of a High Voltage Ultracapacitor Module," Advanced Capacitor Word Summit, San Diego, CA, July 2008.
8. K. Smith, G. Kim, and A. Pesaran, "Multi-Dimensional Electrochemical-Thermal Coupled Model of Large Format Cylindrical Lithium Ion Cells," 212th Electrochem. Soc. Mtg., Washington, DC, October 7-12, 2007.
9. T. Markel, K. Smith, and A. Pesaran, "PHEV Battery Trade off Analysis," 8th Advanced Automotive Battery Conference, Tampa, FL, May 2008.

Milestone Reports

1. A. Pesaran, et al., "Thermal Evaluation of Advanced Batteries," NREL Deliverable Report in fulfillment of DOE Milestone, August 2008.
2. G. Kim, and K. Smith, "Electro-Chemical-Thermal Models for Designing Improved Batteries," NREL Deliverable Report in fulfillment of DOE Milestone, September 2008.
3. T. Markel, K. Smith, A. Pesaran, "PHEV Energy Storage Performance/Life/Cost Tradeoff Analysis," NREL Deliverable Report in fulfillment of DOE Milestone, May 2008.

III. APPLIED BATTERY RESEARCH

III.A Introduction

The Applied Battery Research (ABR) program, alternately called Advanced Technology Development (ATD), is being conducted in support of the FreedomCAR and Fuel Partnership which is targeting more fuel-efficient light duty vehicles that can reduce U.S. dependence on petroleum, without sacrificing performance. There is an emphasis on developing and improving critical component technologies; and energy storage technologies are one of these critical components. Energy storage devices enhance the efficiency of the prime power source in HEVs by leveling the load, and they capture braking energy to produce more fuel efficient and cleaner vehicles. In addition, in PHEVs they provide the primary power source for a number of "all-electric" miles, after which the vehicles again operate in HEV mode. Better energy storage systems are needed to help expand the commercial markets for HEVs and to help make PHEVs commercially viable. The energy storage requirements for various vehicular applications were presented in Section II.

The ATD program has been focused on assisting developers of high-power Li-ion batteries to overcome key barriers to the commercialization of this promising technology for use in light-duty HEV applications (and beginning in 2009, high-energy Li-ion batteries for use in PHEVs). The key barriers associated with HEV batteries are:

- High cost,
- Limited life,
- Tolerance to abusive conditions, and
- Operation between -30ºC and +52ºC.

The ATD program was initiated to understand the factors that limit calendar life, abuse tolerance, and performance over the desired temperature range, so that improvements can be made in these areas. Also, it addresses the cost barrier at the cell level through the identification and development of lower-cost and more-stable cell materials and components.

The program has sought to advance the development of more optimal cell chemistries through the identification and development of cell materials that are more chemically, structurally, electrochemically, and thermally stable in the cell environment; as well as possessing a cost advantage over current materials. Conventional high-energy Li-ion batteries, of the type used in consumer electronics, employ sophisticated and relatively expensive electronic controls that limit their exposure to abusive conditions. The program has focused on both understanding and enhancing the inherent abuse tolerance of the cell chemistry, which will help reduce the level of sophistication of the electronic control system and thereby realize cost savings.

Six DOE national laboratories have been collaborating in the program. Argonne National Laboratory (ANL) provides coordination of the program activities for DOE. The other five participating DOE laboratories are Brookhaven National Laboratory (BNL), Idaho National Laboratory (INL), Lawrence Berkeley National Laboratory (LBNL), the National Renewable Energy Laboratory (NREL), and Sandia National Laboratories (SNL). As part of this program, ANL researchers maintain close communications and (in some cases) collaborations with a large

number of international material supply companies, through which they gain access to the latest advanced electrode and electrolyte materials for evaluation.

During fiscal year (FY) 2008, the program focused on the four cell-level areas listed below, each addressing one of the key barriers:

- Understand life-limiting mechanisms and enhance life,
- Understand and enhance low-temperature performance,
- Understand and enhance inherent abuse tolerance, and
- Realize lower cell-level costs via lower cost materials, components, and technologies.

The program is currently shifting its focus from Li-ion battery technologies for HEVs to PHEVs. The new program focus – initiated on October 1, 2008 and now denoted the Applied Battery Research for Transportation (ABR) Program – is discussed in more detail at the end of this section.

The remainder of this section provides technical highlights and progress on the Applied Battery Research program for FY 2008. The information provided is representative only and detailed information is available from publications cited at the end of this section.

III.B Understand Life-Limiting Mechanisms and Enhance Life

Objectives

- Develop and apply novel diagnostics techniques to help elucidate causes of capacity and power fade and to evaluate and screen new materials and components.
- Investigate degradation processes and their relationship to fundamental and engineering-based material properties.
- Understand the impact of various formation protocols on cell life, and their performance.
  - Gain an understanding of the underlying mechanisms that govern the formation, impact on performance of passivation films on the positive and negative electrodes.
  - Quantify conditions that promote favorable solid electrolyte interphase (SEI) formation, as well as conditions that lead to poor SEIs.
- Provide guidance to battery developers and other researchers regarding aging protocols and new tests, analyses, and modeling methodologies related to calendar and cycle life.

Approach

- Use standard test protocols to characterize the aging characteristics of the Gen3 cells.
- Conduct electrochemical studies on Gen3 chemistry cells to examine the role of each electrode in the aging process.
- Apply microscopy, spectroscopy, and diffraction techniques, such as scanning electron microscopy (SEM), X-ray photoelectron spectroscopy (XPS), and X-ray diffraction (XRD), to understand the impact of electrode microstructure on cell life and performance.
- Apply statistical design of experiments (DOEx) approach to investigate the most significant formation cycle parameters (and their interactions).

Accomplishments/Findings

- Evaluated various electrolyte salts, finding that the cell impedance varied with salt according to the following trend: Lithium bis(oxolato)borate (LiBOB) > $LiBF_4$ > LiF_2OB > $LiPF_6$.
- SEIs on graphite electrodes in the presence of various salts were examined. Sample highlights are:
  - LiF and phosphate compounds (Li alkyl phosphates and Li oxyfluorophosphates) are components of the graphite SEI formed in $LiPF_6$ electrolyte.
  - LiF, alkyl borates, such as $B(OMe)_3$, Li borates Li_xBO_y and Li fluoroborates $Li_xBO_yF_z$ are prominent in the graphite SEI formed in $LiBF_4$ electrolyte.
  - A significant quantity of LiF, $Li_xBO_yF_z$ and Li oxalate is present in the SEI of graphite formed in $LiF_2BC_2O_4$ electrolyte.
  - Li oxalate (or alkyl esters of oxalic acid), Li_xBO_y, tri-coordinated borates and various oligomeric compounds are present in the graphite SEI formed in LiBOB.
- Formation conditions were identified for good Gen3 battery performance: higher temperature, higher upper cutoff voltage (UCV), lower cycling rates, non-zero time at rest between cycles, and more instead of fewer total cycles.
- Conclusions from cycling and aging data on cells with Gen3 electrodes:
  - Both positive and negative electrodes contribute to impedance rise when the cell contains the baseline electrolyte.
  - The $LiF_2BC_2O_4$ electrolyte-additive reduces capacity-fade and impedance-rise during 55°C aging.
  - The negative electrode is the main contributor to cell impedance rise in cells containing the additive. The negative electrode impedance rise is mainly in the mid-frequency arc, which is associated with electrode-electrolyte interfacial processes.
  - The positive electrode impedance increase is mainly in the high-frequency arc regime, associated with electronic processes in the electrode.
- Experiments on Massive activated graphite-10 (Mag-10) anodes demonstrated that the local structural damage at their surface occurs because of non-uniform current density distribution within the electrode. Differences in ionic and electronic resistance within the electrode and the SEI contribute to this effect. This causes some particles on the surface of the anode to operate at a higher charge/discharge rate, which may produce large Li concentration gradients within the crystalline structure of graphite, and eventually surpass the tensile strength of graphene planes.
- Ar sputtering was used to investigate graphite damage during cycling. It is postulated that Ar-ion sputtering re-creates the type and extent of surface structural disorder observed in anodes from tested Li-ion cells. The gradual disordering of the anode during cycling leads to a continuous SEI reformation and loss of cyclable Li.
- The Technology Life Validation Technology (TLVT) team completed development of a software tool that helps to implement this validation technology.

Future Studies

- Please see Section III.F for a description of the planned activities in the ABR program.

III.B.1 Introduction

This subsection highlights the progress to understand the life-limiting mechanisms in high-power Li-ion cell chemistries and to relate that information to developing more stable and lower cost cell chemistries. New diagnostics on the Gen3 electrodes (see Table III- 1) have continued using binder and carbon free electrodes and laboratory made pouch cells (~100mAh). The investigation into the impact of formation on cell performance and life has concluded.

Table III- 2 summarizes how the five DOE laboratories contribute to the work.

Table III- 1. General specifications for Gen3 cells.

Positive Electrode	8 wt % PVDF binder 8 wt % carbon black 84 wt % $Li_{1.05}(Ni_{1/3}Co_{1/3}Mn_{1/3})_{0.95}O_2$
Negative Electrode	8 wt % PVDF binder 92 wt % mesocarbon microbeads (MCMB) 10-28
Electrolyte	1.2 M $LiPF_6$ in ethylene carbonate (EC): ethylmethyl carbonate (EMC) (3:7) as baseline, or with 2% $LiBF_2C_2O_4$ as an electrolyte additive.
Separator	25μm PE

Table III- 2. Summary of how DOE laboratories contribute to the "Life Enhancement" focus area.

	ANL	BNL	INL	LBNL	NREL	SNL
SEI/Formation Study, DOEx, Diagnostics	X		X	X		
Gen3 Cell Build Status	X					
TLVT Validation Testing and Data Analysis	X		X	X		X
Structural Changes in Cathodes during Aging & Thermal Excursions		X				
Cell Transport and Electrochemical Modeling	X					

III.B.2 SEI/Formation Study, DOEx, and Diagnostics

Effect of Electrolyte Composition on Cell Impedance (Abraham, Gering, McLarnon) – Li-ion batteries require stable, low impedance passivation layers to protect the electrodes, while allowing rapid Li-ion transport under high current charge/discharge pulses. The team examined the initial cycling and impedance behavior of Li-ion cells containing $LiNi_{0.8}Co_{0.15}Al_{0.05}O_2$ -based positive electrodes, graphite-based negative electrodes, and electrolytes with 3EC:7EMC (by wt.) solvent and 1.2M $LiPF_6$, 1M $LiBF_4$, 1M $LiF_2BC_2O_4$ (LiF_2OB) or 0.7M $LiB(C_2O_4)_2$ (LiBOB) salts. The impedance data were collected in cells containing a Li-Sn reference electrode to isolate the individual electrode impedances. The conclusions from the studies are as follows:

- The "full cell" impedance data varied with electrolyte salt composition according to the following trend: LiBOB > $LiBF_4$ > LiF_2OB > $LiPF_6$.
- The negative electrode impedance showed a trend similar to that of the full cell (Figure III-1, left); this electrode was the main contributor to impedance in the LiBOB and $LiBF_4$ cells. Furthermore, the main differences were observed in the mid-frequency arc of the electrochemical impedance spectroscopy (EIS) data, which indicated differences in the graphite-electrolyte interface.

- The positive electrode impedance values (see Figure III- 1, right) for the $LiBF_4$, LiF_2OB, and $LiPF_6$ cells were comparable; the values were somewhat higher for the LiBOB cell.
- In general, increasing the test temperature from 30 to 55°C reduced impedance of all cells. The improvement in electrode kinetics with test temperature was significant for the negative electrodes, especially for the ones (LiBOB, $LiBF_4$) that showed relatively higher impedances at 30°C. Significant improvements in positive electrode kinetics were observed for the LiBOB cell; smaller improvements were seen for cells with the other salts.

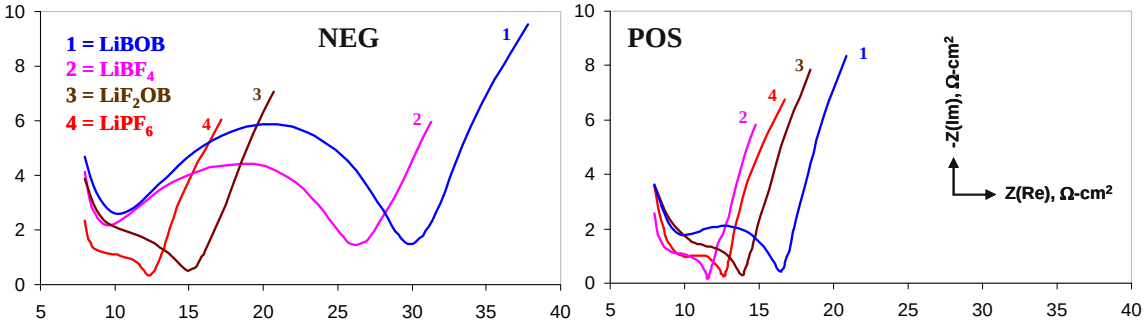

Figure III- 1. Representative positive and negative electrode EIS data (30°C, 25 kHz-0.01 Hz) after formation cycling for cells containing various electrolytes. The data were acquired at a cell voltage of 3.72V.

Cycling and impedance data were also obtained for cells containing additions of $LiBF_4$, LiBOB, LiF_2OB, and vinylene carbonate (VC) to the 3EC:7EMC (by wt.) + 1.2M $LiPF_6$ electrolyte. Cells containing LiBOB, $LiBF_4$ and VC additives displayed impedances that were larger than that of the $LiPF_6$ electrolyte cell, mainly because of higher impedances at the graphite negative electrode. The impedance data show a distinct dependence on additive content, which is consistent with data reported by other investigators.

Examining the SEI Using Binder-free (BF) Graphite Electrodes (Abraham, Gering, McLarnon) – Binder-free (BF) electrodes simplify interpretation of SEI data from studies of graphite surfaces. To date, several SEI studies have been conducted on highly oriented pyrolytic graphite (HOPG) electrodes. However, HOPG electrodes are better suited to studying the SEI on basal planes than on graphite edge planes because of the large basal-to-edge-plane surface-area ratio. Because the SEI formed on graphite edge planes (the sites of Li intercalation) is important from a practical perspective, the studies on HOPG electrodes are of limited value. In this work, the team characterized the SEIs formed on BF graphite electrodes fabricated on Cu foil by electrophoretic deposition (EPD). Initial data from these electrodes, including materials characterization and electrochemical performance, have been reported earlier. The team recently examined the SEIs formed on BF graphite electrodes cycled in cells containing four electrolytes: 1.2M $LiPF_6$, 1M $LiF_2BC_2O_4$, 1M $LiBF_4$, and 0.7M LiBOB in EC: EMC solvent (3:7 by wt.). Electrode samples were examined by the Fourier transform infrared (FTIR) method with attenuated total reflection (ATR), XPS and thermogravimetric analysis (TGA). The highlights from these experiments are as follows:

- LiF and phosphate compounds, such as lithium alkyl phosphates $Li_xPO_yR_z$ (R=CH_3, etc), and lithium oxyfluorophosphates $Li_xPO_yF_z$ are important components of the graphite SEI formed in the $LiPF_6$ electrolyte.

- LiF, alkyl borates, such as $B(OMe)_3$, lithium borates Li_xBO_y and lithium fluoroborates $Li_xBO_yF_z$ are prominent in the graphite SEI formed in the $LiBF_4$ electrolyte. The reduction products of the $LiBF_4$ salt are less soluble in EMC than the related reduction products of $LiPF_6$. The insoluble B containing species may include inorganic/polymer compounds, with or without crosslinking.
- A significant quantity of LiF, $Li_xBO_yF_z$ and lithium oxalate (or alkyl esters of oxalic acid) is present in the SEI of graphite formed in $LiF_2BC_2O_4$ electrolyte. The data also support the presence of organic species/oligomeric compounds that decompose at elevated temperatures.
- Lithium oxalate (or alkyl esters of oxalic acid), Li_xBO_y, tri-coordinated borates and various oligomeric compounds are present in the graphite SEI formed in LiBOB. These compounds appear to be insoluble in EMC, and decompose at temperatures above 200°C. The graphite SEI may be fairly thick because graphite peaks are not observed in the XPS data and abundant organic decomposition products are suggested by the TGA data (see Figure III- 2).
- Lithium alkoxides, such as CH_3OLi, and possibly small amounts of lithium alkyl carbonates, such as lithium diethylene carbonate, may also be present in the graphite SEI but these species are washed off during electrode rinsing. The data does not support the presence of Li_2CO_3 in any of the graphite SEI.

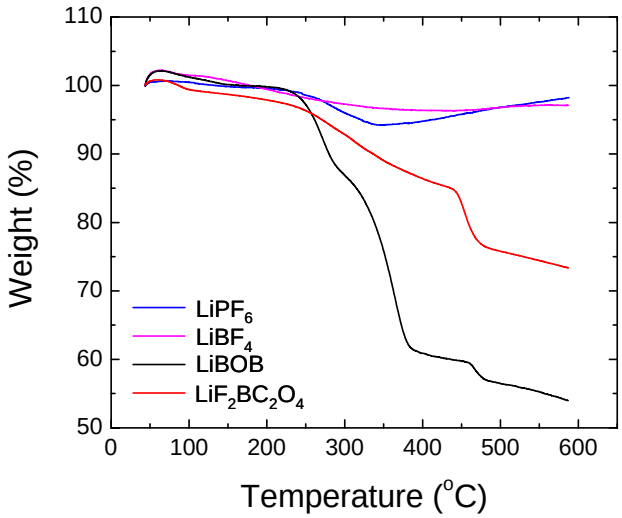

Figure III- 2. TGA weight change data from graphite samples removed from EMC-rinsed electrodes that were cycled in various electrolytes. The differences between the plots reflect differences in the composition of the graphite SEI.

Design of Experiments (DOEx) for SEI Formation of Gen3 Cell Materials (Gering) – A DOEx was devised to explore the relationship between formation parameters and cell performance for the Gen3 Enerland chemistry. The goal was to further understand the formation process for Gen3 cells, and to provide insights into how to improve battery performance and life. The complete study involved six formation parameters, using 31 test conditions split between three stages. A total of 186 button cells (type 2032) were built, formed, and tested. The team found the following formation conditions are preferred for good Gen3 battery performance: higher temperature, higher

UCV, lower cycling rates, non-zero time at rest between cycles, and more instead of fewer total cycles. In particular, through statistical analyses it was seen that both cell capacity and conductance showed the best performance for the conditions of {T=50°C, UCV=4.2V, $C_{ch}=C_1/10$, $C_{dis}=C_1/24$, $t_{ocv}=4$, $n_{cyc}=3$}, where the listed parameters correspond to temperature (T), upper cutoff voltage (UCV), charge and discharge cycling rates (C_{ch}, C_{dis}), open circuit rest periods (t_{ocv}), and the net number of complete formation cycles per cell (n_{cyc}).

During battery production, increased formation time decreases throughput and increases cost. Therefore, a specific formation optimization *(at 40°C and upper cutoff voltage of 4.2V)* was performed: by minimizing all of the time-related processes (cycling rates, t_{ocv}, n_{cyc}, and their interactions). The response variable expressions (RVEs) were used as predictors for investigating numerous combinations of variables (covering 81 conditions, many of them off-matrix) that would yield predicted cell capacity and conductance for the conditions relevant to minimization of formation time.

The results were that the shortest formation time to meet the above requirements had the following specifications (Case 1): {$C_{ch} = C_1/10$, $C_{dis} = C_1/10$, t_{ocv}, = 4, n_{cyc}, = 3}, which gives a total formation time of 72 hours, yielding a ratio of final-to-initial capacity of 0.505. Another option (Case 2) emerged that totaled 44 hours {$C_{ch} = C_1/3$, $C_{dis} = C_1/3$, t_{ocv}, = 5, n_{cyc}, = 4} and yielding a ratio of final-to-initial capacity of 0.610; however, it appears the overall RVE for capacity is overly sensitive to t_{ocv}, yielding overpredicted values for capacity as t_{ocv} is raised well past the experimental matrix value of 3 hours. Nonetheless, overall results indicate that total formation times between two to three days are feasible if the cycling rates are increased while increasing both t_{ocv} and the total number of formation cycles. Reasonable interpolations between the above two cases (say, {$C_{ch} = C_1/5$, $C_{dis} = C_1/5$, t_{ocv}, = 4, n_{cyc}, = 4} for 56 hours) should also yield reasonable optimization of formation time.

Lastly, it should be noted that the ratio of final-to-initial cell conductance does not necessarily track with cell capacity under time optimization. For example, for the Case 1 conditions listed above, the predicted final-to-initial cell conductance ratio has a value of 0.327, while the value for Case 2 conditions is 0.321. Thus, the statistical model predicts that for the above conditions Gen3 cells would undergo a greater relative reduction in conductance over time than in capacity.

III.B.3 Gen3 Cell Build Status, Testing, & Diagnostics

Gen3 Cell Aging, Diagnostics, & Modeling (Bloom, Abraham, Dees, Henriksen, McLarnon) – Pouch cells (400 mAh) and 18650-sized cells (700 mAh) containing the Gen3 chemistry were tested using the same test conditions as the Gen2 baseline cells.[6] There were two types of cells, baseline and additive ($LiF_2BC_2O_4$). The test matrix and cell distribution are given in Table III- 3.

[6] I. Boom, S. Jones, V. Battaglia, G. Henriksen, J. Christophersen, R. Wright, C. Ho, J. Belt, and C. Motloch, J. Power Sources, 124 (2003) 538.

Table III- 3. Test matrix and cell distribution for the Gen3 cells.

	25°C	45°C	55°C
Calendar		5 pouch (A)* 2 pouch (B) 4 18650 (A) 1 18650 (B)	5 pouch (A) 2 pouch (B) 4 18650 (A) 1 18650 (B)
Cycle	5 pouch (A)	4 pouch (A) 3 18650 (A)	

*(A)=additive; (B)=baseline

Before testing started, the cells were characterized in terms of C/1 and C/25 capacities, hybrid pulse-power response at the low current level (HPPC-L), i.e. 5C, and EIS. The characterization tests are carried out at 25ºC. The tests are stopped every 28 days and the cells are re-characterized to gauge performance changes in the cells.

The cell testing status is given in Table III- 4. For the pouch cells, both cycle-life variant groups have completed 48 weeks and are continuing to cycle. The 45°C calendar-life pouch cells are also continuing to test, but the 55°C cells have already been removed due to rapid degradation. For the 18650-size cells, the cycle-life group was removed from test after 8 weeks due to leaking. The initial values of the area specific impedance (ASI) are given in Table III- 5. From Table III- 5, it can be seen that the initial ASI values from the pouch cells are higher than the corresponding 18650 cells, and lower than those from the Gen2 baseline cells.

Table III- 4. Cell testing status.

	25ºC	45ºC	55ºC
Calendar		pouch (A) – 40 weeks pouch (B) – 24 weeks 18650 (A) – 28 weeks 18650 (B) – 20 weeks	pouch (A) – 32 weeks pouch (B) – 12 weeks 18650 (A) – 28 weeks 18650 (B) – 12 weeks
Cycle	pouch (A) – 40 weeks	pouch (A) – 48 weeks 18650 (A) – 40 weeks	

Table III- 5. Initial ASI values at 25ºC and 60%SOC.

Deliverable	ASI, ohm-cm^2
Pouch	24.4 (A) 26.5 (B)
18650	39.7 (A) 34.2 (B)
Gen2	28.1

The average ASI values from the pouch cells are plotted versus time in Figure III- 3, and those from the 18650-size cells, in Figure III- 4. The best-fit curves for the Gen2 baseline cells are also shown. As the cells age at temperature, the ASI values increase. For the pouch cells with the additive, the ASI values from the Gen3 cycle life tests at 25ºC are below the corresponding values

from the Gen2 cells. However, the values from the calendar life tests and the cycle life test are higher than those from Gen2.

Comparing the time-dependent behavior of the Gen3 18650-size cells at 45ºC with that from the Gen2 cells shows different behavior from that seen in either the Gen2 or the Gen3 pouch cells. At first the average ASI increases and then decreases, until, after ~20 weeks, is on par with that from the Gen2 cells. The ASI values from the baseline cells in both cases increases markedly and more rapidly than that seen in Gen2 baseline cells. Therefore, the additive helps slow down the ASI increase.

Diagnostics (Bloom, Abraham, Dees, Henriksen, McLarnon) – Electrochemical cycling and aging data on cells with Gen3 electrodes were obtained from 2032-type coin cells (1.6 cm^2 electrodes), pouch cells (25 cm^2 electrodes) and from larger cells (32 cm^2 electrodes) that incorporated a Li-Sn reference electrode (RE). The positive active material was $Li_{1.05}(Ni_{1/3}Co_{1/3}Mn_{1/3})_{0.95}O_2$, the negative active material was MCMB-10 graphite. The baseline electrolyte was 1.2 M $LiPF_6$ in 3EC:7EMC (by wt.); most cells also contained 2-3 wt% $LiF_2BC_2O_4$ as an electrolyte additive. Performance degradation studies were conducted with electrodes obtained from various sources (Enerland, Toyota, and Nippon Chemical). The chemistry-related aging trends were, in general, similar for cells containing those various electrodes. The conclusions from the studies are as follows:

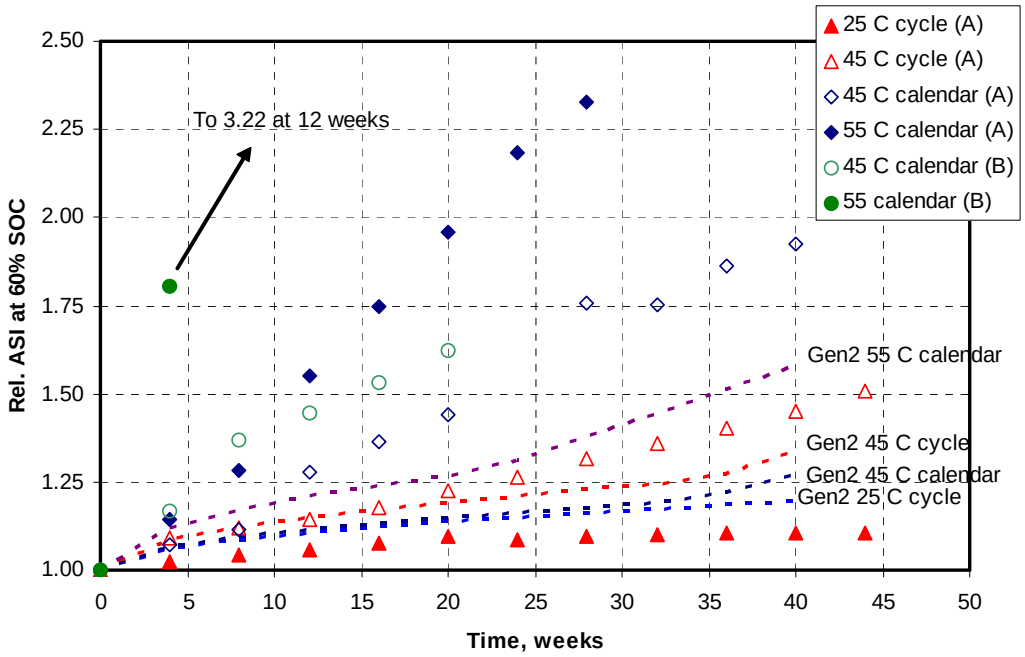

Figure III- 3. Average ASI vs. time comparing the values obtained from the Gen3 pouch cells with those from Gen2 baseline cells. The curves represent the best-fit to Gen2 data and the points are the Gen3 data under the same conditions.

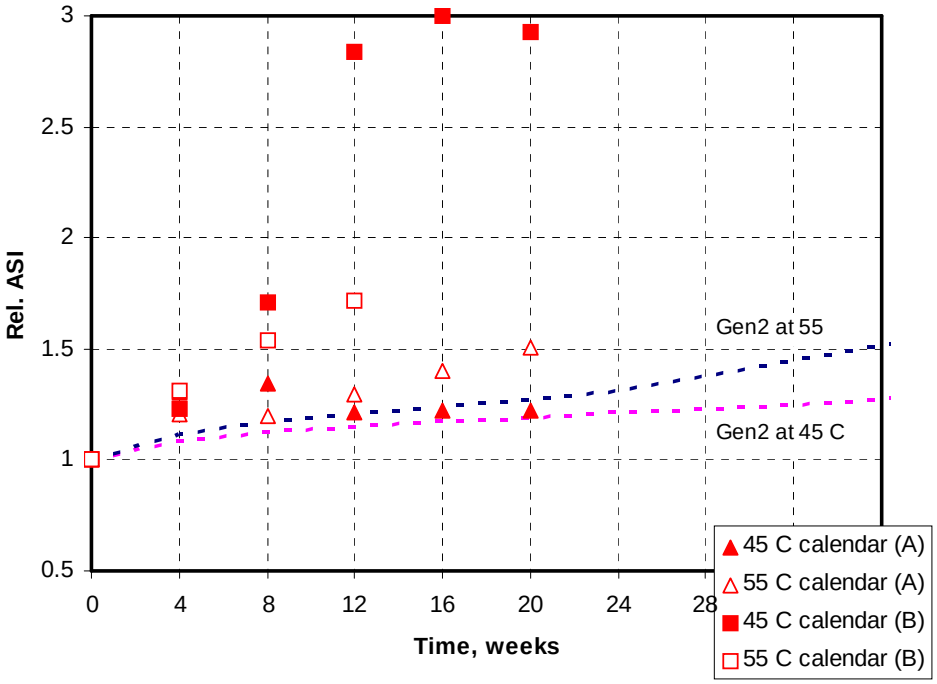

Figure III- 4. Average ASI vs. time comparing the values obtained from the 18650-size Gen3 cells with those from Gen2 baseline cells. The curves represent the best-fit to Gen2 data and the points are the Gen3 data under the same conditions.

- Both positive and negative electrodes contribute to impedance rise, when the cell contains the baseline electrolyte.
- The $LiF_2BC_2O_4$ electrolyte-additive has a beneficial effect on cell performance during 55°C aging: both capacity-fade and impedance-rise are lower for cells containing the additive compared to cells containing only the baseline electrolyte.
- The negative electrode is the main contributor to cell impedance rise in cells containing the $LiF_2BC_2O_4$ electrolyte-additive; a representative dataset is shown in Figure III- 5. The negative electrode impedance rise is mainly in the mid-frequency arc regime, which is associated with electrode-electrolyte interfacial processes.
- Figure III- 5 shows that the positive electrode impedance increase occurs mainly in the high-frequency arc regime, which is associated with electronic processes in the electrode. Other data suggest that these increases in the high-frequency arc are probably associated with degradation of contact between oxide particles and the electron-conducting carbons. The mid-frequency arc width increase is minimal, which indicates that the $LiF_2BC_2O_4$ electrolyte-additive inhibits interfacial impedance rise in the positive electrode.

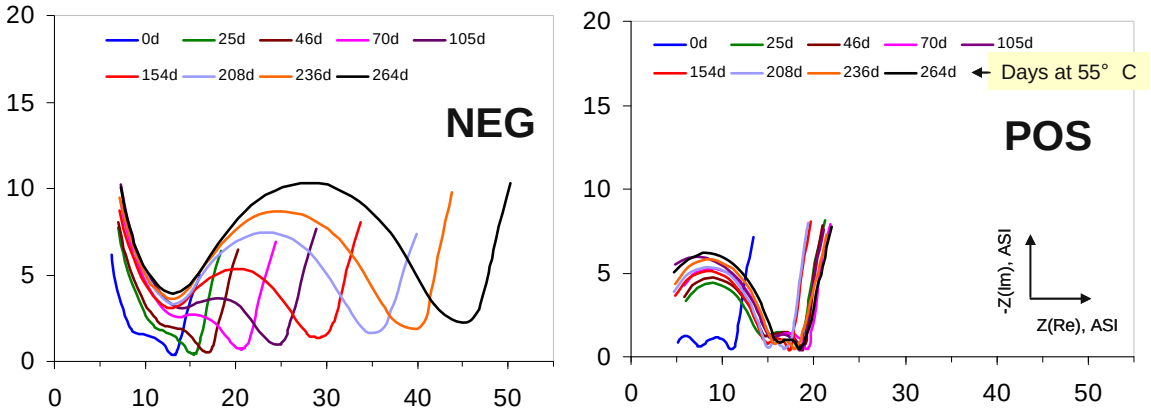

Figure III- 5. Representative positive and negative electrode impedance data full from a Gen3 cell that contained Gen2 + 3 wt% $LiF_2BC_2O_4$ electrolyte. The cell was aged at 4V and 55°C. The EIS data were acquired at 3.72V, 30°C, and in the 100 kHz-10 MHz frequency range.

Gen3 electrodes harvested from fresh and aged reference electrode cells were examined using various electrochemical and physiochemical diagnostic techniques. The conclusions from these studies are:

- Positive electrode capacity loss, determined by (<C/25 rate) cycling of the aged electrodes against a Li counter electrodes, is very small. The increased impedance on aging and the dissolution of transition metals into the electrolyte have little effect on electrode capacity.
- XRD data show no changes to the Gen3 oxide structure after aging. However, XPS studies indicate that the $LiF_2BC_2O_4$ electrolyte-additive modifies the composition of positive electrode surface films. B-containing oligomers, arising from $LiF_2BC_2O_4$, appear to inhibit electrode impedance rise by forming a protective layer at the oxide-electrolyte interface.
- The negative electrodes show a distinct capacity loss, even after the aged electrodes are rinsed to remove surface films. This capacity loss may result from isolation of graphite particles resulting from cell aging because XRD data show no changes to the bulk graphite structure. Data obtained by dynamic secondary ion mass spectrometry (SIMS) and chemical analysis measurements show that transition metals accumulate at the graphite electrode on aging (~100 ppm); a representative SIMS dataset is shown in Figure III- 6. The higher impedance of the aged graphite anodes may be the result of SEI modification induced by this accumulation of transition metals.

Graphite Disordering in Li-ion Cells (Bloom, Abraham, Dees, Henriksen, McLarnon) – The mechanism of graphite disordering remains poorly understood, with few relevant studies in the literature. Modeling studies of spherical graphitic carbon demonstrated that charge/discharge rates above 4C can produce stress in a 5 µm particle that is sufficiently large to surpass the tensile strength for some types of graphitic carbons. It was also shown that the tensile strength is exceeded at rates above 16C for all types of graphitic carbons. Interestingly, SEM images of cycled Mag-10 anodes do not show any evidence of structural breakdown or particle fracture when compared to fresh un-altered electrodes. However, taking into account the increased I_D/I_G ratios observed in the Raman spectra of graphitic anodes from tested Li-ion cells, it is concluded that the crystalline disorder in graphite anodes is limited to the surface of the particle and does not affect the bulk of the material.

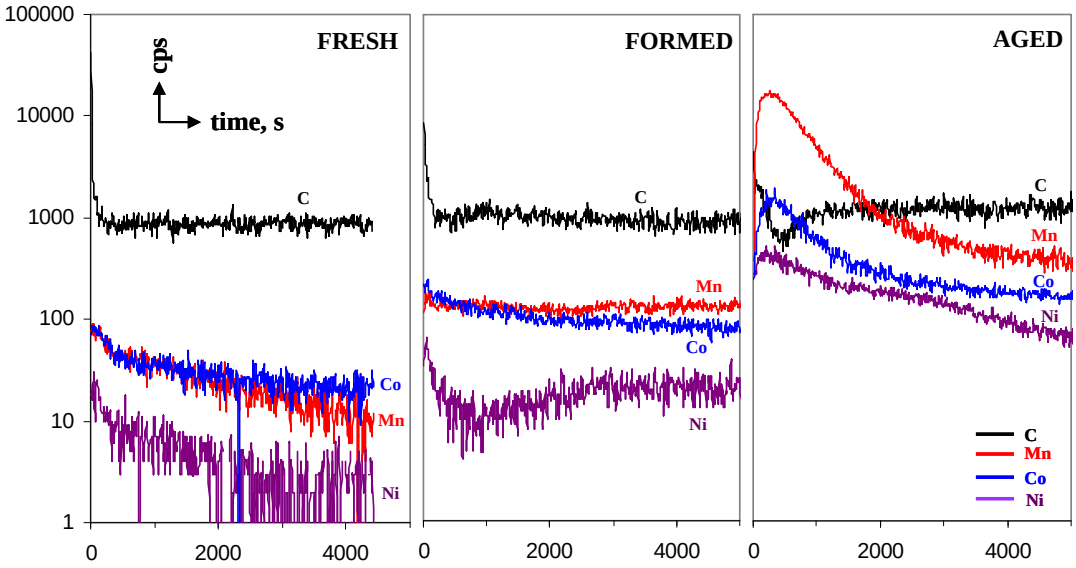

Figure III- 6. SIMS data showing C, Mn, Co and Ni contents as a function of sputter depth in fresh (no electrolyte exposure), formed (no aging) and aged (38 wks, 4V, 55°C) Gen3 graphite anodes. The X-axis shows sputtering time in seconds, and the Y-axis shows counts per second (cps).

Experiments carried out with Mag-10 anodes demonstrated that the local structural damage at the surface of the electrodes occurs because of non-uniform current density distribution within the electrode. Differences in ionic and electronic resistance within the electrode and the SEI contribute to this effect. This causes some particles on the surface of the anode to operate at a higher charge/discharge rate, which may produce large Li concentration gradients within the crystalline graphite, and eventually surpass the tensile strength of the graphene planes.

Origin of Irreversible Capacity Loss (ICL) in Graphite Anodes (Abraham, Gering, McLarnon) – It has been previously shown that the graphite anodes suffer severe surface structural damage upon prolonged cycling in rechargeable Li-ion batteries. This is evidenced in the Raman spectra of graphite anodes from tested Li-ion cells by the increased prominence of the D-band (~1330 cm^{-1}) with respect to the G-band (1580 cm^{-1}). This effect has been reported for Mag-10 and KS-15 graphite anodes and appears to occur generally in all graphitic carbons.

The team has investigated the effect of the surface structural damage in graphite on the electrochemical performance of the anodes. Surface structural disorder in graphite Mag-10 anodes was artificially recreated using argon-ion sputtering. Raman measurements reveal a striking similarity of the surface structure disorder of Ar-ion sputtered Mag-10 electrodes and Mag-10 anodes from tested Li-ion cells. A full diagnostic evaluation of these surface-modified anodes was carried out and possible implications for Li-ion cell degradation mechanism discussed.

The structure and morphology of the sputtered Mag-10 anodes were studied and compared with the un-altered electrode. SEM images of a fresh and sputtered Mag-10 anodes display much higher surface density of small graphene zones with irregularly shaped edges in the sputtered samples. The Ar-ion bombardment expelled carbon atoms from the hexagonal lattice of the surface graphene sheets and created local shallow structural disorder. No evidence of deep etching or exfoliation of the graphene layers was found, as it is often observed during exposure of graphitic carbons to short high-intensity pulse ion beams. Brunauer Emmett Teller (BET) measurements of

the un-altered and sputtered Mag-10 graphite powders revealed that Ar-ion bombardment induces no significant variation in surface area, even after sputtering for 1800 s.

The Raman spectra of graphite typically exhibit two intense peaks assigned to the G- and D-bands at 1580 and 1330 cm^{-1} that correspond to the E_{2g2} and A_{1g} carbon vibration modes, respectively. The D-band to G-band integrated area ratio (I_D/I_G) is often used as a parameter for evaluating carbon structural properties. The increased intensity of the D-band relative to the G-band is typically associated with (a) a higher content of disordered carbon and/or (b) a decrease of the graphite crystallite size in the a direction (L_a).

The Raman spectra of the un-altered and sputtered Mag-10 electrodes, shown in Figure III- 7(a), clearly show that the intensity of the "disorder" band at 1330 enlarges significantly with respect to the G-band (1580 cm^{-1}) with increased sputtering time.

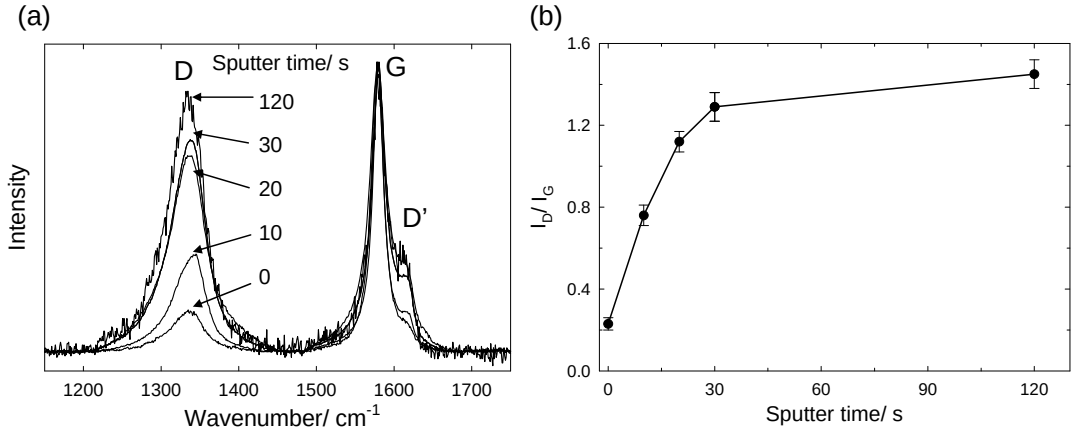

Figure III- 7. (a) Average Raman spectra of un-altered and sputtered (10s, 20s, 30s and 120s) Mag-10 anodes. Intensity is normalised to the G-band at 1580 cm^{-1} (b) I_D/I_G average ratio with respect to sputtering time.

A rapid increase of the I_D/I_G ratio from 0.23 for the un-altered electrode to 1.28 after sputtering for 30s followed by a moderate increase to 1.4 for Mag-10 anodes sputtered for 120 s, as shown in Figure III- 7(b), indicates that most of surface disorder is induced into graphite during the first 30 seconds, and then layers of graphite are slowly etched away.

Representative Raman maps (Figure III- 8) of, (a) un-altered, and (b) 120s sputtered Mag-10 graphitic anodes, show the surface distribution of the integrated area ratio of the Raman D-band with respect to the G-band (I_D/I_G). Light areas on the map signify ordered graphitic areas, whereas dark areas represent disordered areas. The map of a 120s sputtered graphite electrode contains a heterogeneous distribution of disordered graphite (dark areas) compared to the map of the fresh electrode.

The average surface disorder of the Mag-10 electrode sputtered for 120 s corresponds exactly to the structural damage observed in Mag-10 anodes removed from tested Li-ion cells developed and tested within the ATD Program. Moreover, Raman maps of the I_D/I_G ratio of the Mag-10 graphite anodes from tested Li-ion cells show a non-uniform surface structural degradation pattern, which is nearly identical to the Ar-ion sputtered electrodes. Thus, it is postulated that by using argon-ion

sputtering the team was able to re-create the type and extent of surface structural disorder observed in anodes from tested Li-ion cells.

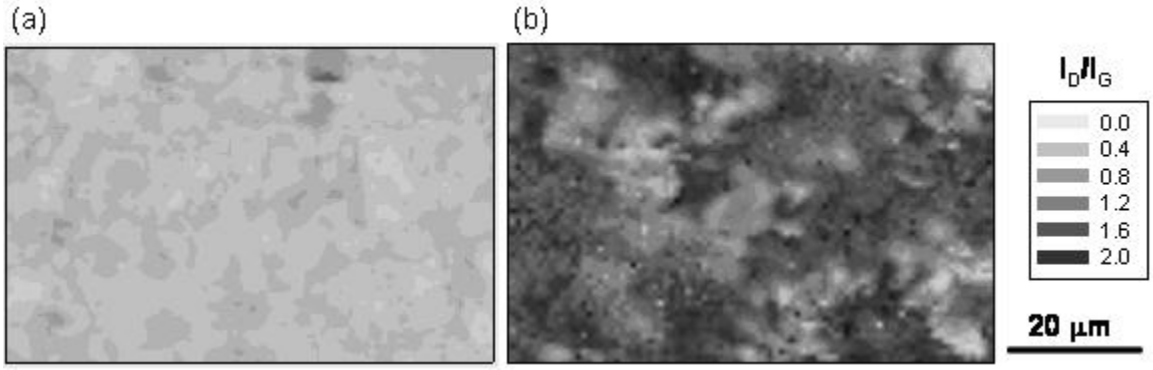

Figure III- 8. Raman I_D/I_G ratio images of (a) unaltered and (a) 120s sputtered Mag-10 graphite electrode.

The first galvanostatic charge and discharge scans of the un-altered and sputtered anodes are shown in Figure III- 9. The first lithiation for un-altered and sputtered Mag-10 anodes consumed *ca*. 400 and 530mAh/g, respectively. The sputtering process did not reduce the reversible charge capacity of the electrode (350mAh/g), which is close to the theoretical maximum for graphite of 372mAh/g for the formation of LiC_6 (q'_{rev}). However, the ICL almost doubled from 18 ± 1 to 34 ± 10 % for the un-altered and 120s sputtered electrode.

The induced surface structural disorder did not affect the bulk of the graphite, but significantly altered its surface reactivity and was responsible for approximately double the amount of irreversible charge consumed in the formation of the SEI. The results imply that similar irreversible processes may occur during cycling of graphite anodes, which gradually develop a similar degree of surface disorder.

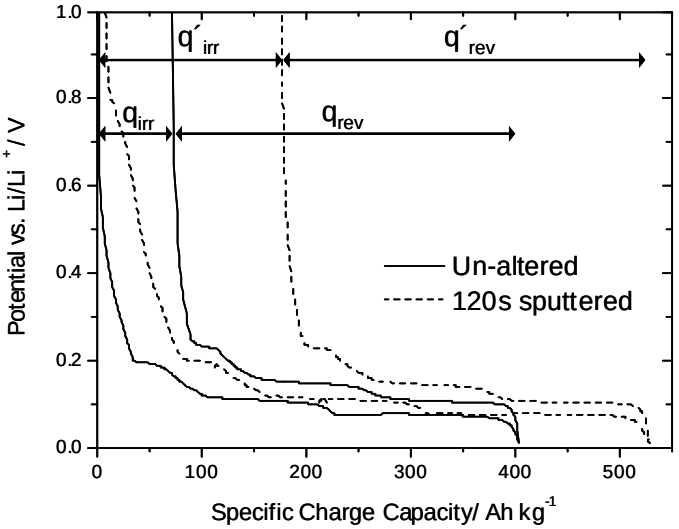

Figure III- 9. First galvanostatic charge-discharge curves of un-altered and 120s sputtered Mag-10 graphite in 1.0 M $LiPF_6$, EC: Dimethyl carbonate (DMC), 1:1 w/w at *C*/25.

Impedance spectra of un-altered and 120s sputtered Mag-10 anodes after the three formation cycles show very similar impedance behaviour. FTIR spectra of the SEI layer on electrochemically cycled un-altered and 120s sputtered Gen-2 anodes show comparable bands for both electrodes, nevertheless the band intensities for the sputtered anode are somewhat more intense, suggesting a thicker SEI film.

The team postulates that the gradual disordering of the graphite anode during prolonged cycling leads to a continuous SEI reformation. Fragmentation of surface graphene planes exposes fresh carbon edge sites to the electrolyte, which react immediately to continuously reform the SEI. The charge consumed in this long-term irreversible process diminishes the amount of cycleable lithium in the cell and shifts the cathode to a higher state of charge, thereby reducing the overall reversible capacity of the cell.

Modeling (Dees) – Early in this fiscal year, the emphasis of the electrochemical modeling effort in the Gen3 cell diagnostic area was focused on examining the impact on performance of the high frequency arc in the EIS studies on the Enerland Gen3 positive electrodes. During the previous year, the likely source of the relatively large high frequency impedance arc was identified as the electronic contact resistance associated with the contact between the oxide active material and the conductive carbon additive. As an example of the studies conducted, the current and concentration distributions in the positive electrode, as well as overall and individual components of electrode impedance, were examined as a function of the electrode electronic resistive effects.

The methodology for the electrochemical model is described in detail in the literature[7]. Two versions of the model are utilized in this effort. One version is used to simulate the cell response from EIS studies, and the other is used to examine DC studies, such as HPPC tests. The underlying basis for both models is the same, and so is the parameter set. After completing the contact resistance studies, the emphasis of the modeling activities shifted towards methods to more efficiently estimate the interfacial and active material diffusion model parameters. These parameters are generally estimated by fitting the EIS electrochemical model to electrode EIS diagnostic studies. Streamlining the parameter estimation process would greatly shorten the analysis time for new electrodes.

The general methodology for the electrochemical model follows the work of Professor Newman at Berkeley. Continuum based transport equations using concentrated solution theory describe the movement of salt in the electrolyte. Volume-averaging of the transport equations accounts for the composite electrode geometry. Electrode kinetics, thermodynamics, and diffusion of lithium in the active material particles are also included. The detailed theoretical description of the active material/electrolyte interface, the SEI, is based on post-test analytical diagnostic studies. The SEI region is assumed to be a film on the active material and layer at the surface of the active material. The film is taken to be an ill-defined mixture of organic and inorganic material through which lithium ions from the electrolyte must diffuse and/or migrate across to react electrochemically at the surface of the active material. The lithium is then assumed to diffuse through the surface layer

[7] D. Dees, E. Gunen, D. Abraham, A. Jansen, and J. Prakash, *J. Electrochem. Soc.*, 152 (7) (2005) A1409, D. Abraham, S. Kawauchi, and D. Dees, Electrochim. *Acta*, 53 (2008) 2121, D. Dees, E. Gunen, D. Abraham, A. Jansen, and J. Prakash, *J. Electrochem. Soc.*, 155 (8) (2008) A603.

and into the bulk active material. Capacitive effects are incorporated into the model at the electrochemical interfaces and a localized electronic resistance between the current carrying carbon and the oxide interface can also be included. The model can also accept multiple particle fractions with unique characteristics.

Using equivalent circuit model curve fitting software readily available for EIS data, an equivalent circuit model was developed for the SEI that corresponds to the electrochemical SEI model described above. While a perfect match between the two SEI models was not possible, an acceptable representation of the electrochemical SEI model using the equivalent circuit SEI model was obtained. The assumed use of a single set of SEI parameters and because the current distribution in Li-ion electrodes is relatively uniform (i.e. ~ ±10%) there is only a minor distortion of the EIS data because of the composite electrode structure. This allows the equivalent circuit SEI model to be used to fit the interfacial parameters to a relatively good approximation. However, a similar conclusion cannot be drawn from trying to fit the low frequency Warburg impedance data. Nevertheless, being able to use the equivalent circuit model to estimate the SEI parameters has proven to save considerable analysis time.

III.B.4 TLVT Validation and Testing

Technology Life Validation Test (Battaglia, Bloom, Christophersen, Thomas) – A goal of the ATD program is to develop methods to accurately predict the life of Li-ion batteries in an HEV environment with a high level of confidence given only 1 or 2 years of accelerated testing. To aid in the method development, thirty 7-Ah Li-ion cells were tested for calendar life at 30, 40, 47.5 and 55°C. The bulk of the testing protocols and data were presented in the FY 2007 annual progress report and only a brief overview is presented here. The test matrix appears in Table III- 6.

Every 31.5 days, the calendar-life test was stopped and the cells were cooled to 30ºC. Changes in cell resistance were gauged by using the minimum pulse power characterization (MPPC) test.[8]

A statistically-robust modeling strategy was developed and tested using the aging data. The results from the model were used in Monte Carlo simulations to predict battery life with a high degree of confidence. The relative resistance data were initially fit to the model equation (Eq. 1),

Table III- 6. Test matrix for the calendar life test. SOC_{Max}=62% SOC

Temp., ºC	SOC	Number of cells
30	SOC_{Max}	3
40	SOC_{Max} – 10%	3
	SOC_{Max}	3
	SOC_{Max} + 10%	3
47.5	SOC_{Max} – 10%	3
	SOC_{Max}	3
	SOC_{Max} + 10%	3
55	SOC_{Max} – 10%	3
	SOC_{Max}	3
	SOC_{Max} + 10%	3

[8] Battery Technology Life Validation Test Manual, INEEL/EXT-04-01986, February, 2005.

$$\hat{Y}_i(T;t) = 1+ \exp(b_0 + b_1/T)t^z, \quad \text{(Eq. 1)}$$

where $\hat{Y}_i(T;t)$ is relative resistance of a cell aging for time *t* and at absolute temperature *T*, and b_0, b_1 and *z* are fitting parameters. During the work, the relative resistance model equation was generalized to include the effects of stress factors other than temperature. The general form of the model equation is (Eq. 2),

$$\hat{Y}i(X_1;X_2;\ldots;X_n;t) = 1+ \exp(b_0 + b_1X_1 + b_2X_2 + \ldots + b_nX_n)t^z, \quad \text{(Eq. 2)}$$

where $X_1, X_2,\ldots,X_n$ represent the stress factors and $b_1, b_2,\ldots,b_n$ are their coefficients which are calculated from the fitting process. [It should be recognized that this linearizable equation is of limited utility to those stress factors that lead to an exponential dependence with additive functionality.] Additionally, an error model was developed to gauge the lack-of-fit in the fitting process, as given in Eqs. 3 and 4.

$$\gamma(T;t)=\delta_i(\hat{Y}_i(T;t)-1) + \pi_i(t), \quad \text{(Eq. 3)}$$

where δ_i represents the cell-specific, proportional error and $\pi_i(t)$ represents the effects of measurement error; and, by definition leads to the following expression for the variance of the data

$$Var(\gamma(T;t))=Var(\hat{Y}_i(T;t))=\sigma_\delta^2(\hat{Y}_i(T;t)-1)^2 + \sigma_\pi^2, \quad \text{(Eq. 4)}$$

where $\sigma_\delta^2 = Var(\delta_i)$ and $\sigma_\pi^2 = Var(\pi_i(t))$.

The statistical/mathematical methodology described here has been implemented in a computer program featuring a user-friendly interface that takes the user through the steps needed to perform the data analysis and modeling. It requires that the user has a life equation available; that time is an explicit variable in it; and that it has been linearized. The program also performs a series of Monte Carlo simulations to estimate life and the upper and lower confidence intervals of the estimate.

The software development is now complete. Examples, shown in Figure III- 10, Figure III- 11, and Figure III- 12, display its data input screens and results viewed from its desktop. Figure III- 13 shows some of the results from a typical data analysis. The software provides the user with a simple method to describe the data to be analyzed and displayed. The outputs include:

- The estimated values of the fitted parameters to the life and variance data.
- Line fits through the data.
- An estimate of the life of the cells at a given SOC and temperature.
- The distribution of life estimates from the Monte Carlo simulation.
- The 95% upper and lower confidence limits of the life estimate.

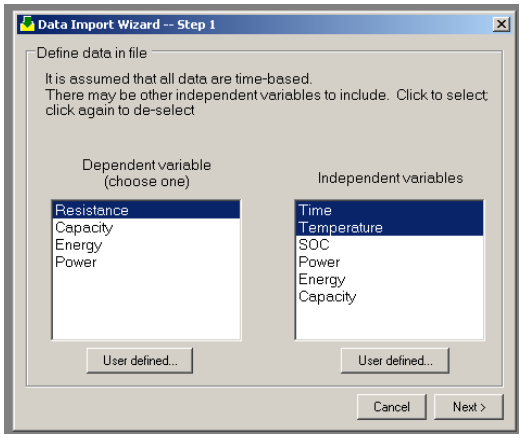

Figure III- 10. Start of data analysis: define the data to be used.

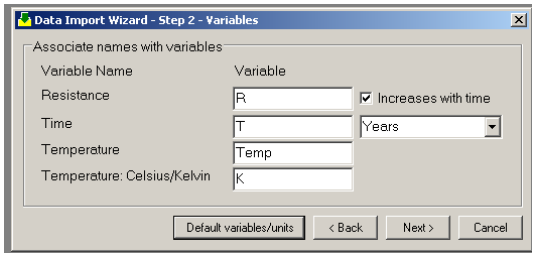

Figure III- 11. Associate variables and their names

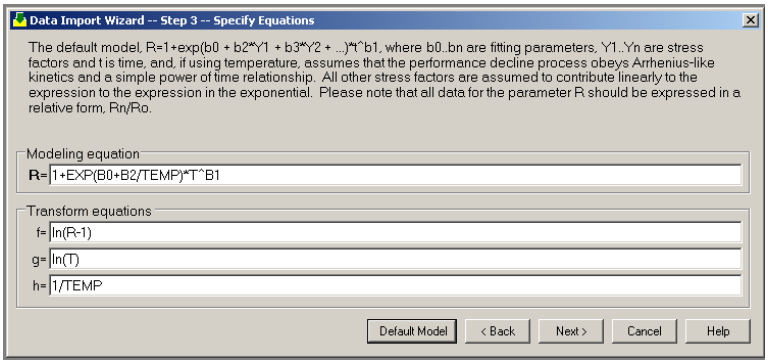

Figure III- 12. Define the model equation and associated variable transform equations. The transform equation linearizes the input data.

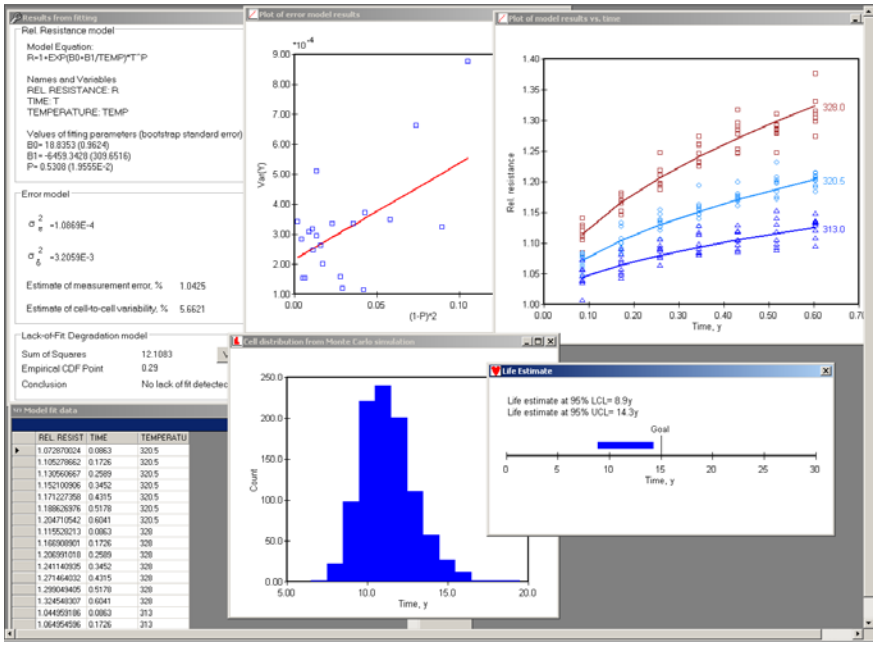

Figure III- 13. Desktop image showing some of the results from a typical data analysis.

III.B.5 Structural Changes in Cathodes during Aging & Thermal Excursions

Doped $LiFePO_4$ (Yang, Yoon) – Due to the higher voltage plateaus relating to Mn, Co, and Ni doping of $LiFePO_4$, these materials are good candidates as cathode materials for Li-ion batteries for PHEVs. Through collaborative studies with Dr. Zaghib at Hydro-Québec in Canada and Prof. H. Huang's group at the Chinese Academy of Sciences, transition metal element doped $LiFePO_4$ materials have been studied by *in situ* XRD and X-Ray absorption spectroscopy (XAS) techniques. It was reported that the electrochemical activity of Mn or Co can be improved significantly in the solid solution of phosphates such as $LiFe_xMn_{1-x}PO_4$ and $LiFe_xCo_{1-x}PO_4$. Therefore, it is important to investigate the effects of the state of solid solution on the kinetics of each phase transition reaction from M^{2+} to M^{3+}, as well as the electronic and crystal changes during Li intercalation and de-intercalation.

Figure III- 14 shows the first charge curve of carbon coated $LiFe_{1/4}Mn_{1/4}Co_{1/4}Ni_{1/4}PO_4$ (**C**-$LiFe_{1/4}Mn_{1/4}Co_{1/4}Ni_{1/4}PO_4$) at a C/7 charging rate. *In situ* XAS shows clear edge shifts in the Fe, Mn, and Co K-edge regions during the 1st charge, indicating that the plateaus I, II, and III are attributed to the redox reactions of Fe^{2+}/Fe^{3+}, Mn^{2+}/Mn^{3+} and Co^{2+}/Co^{3+}, respectively. However, no significant changes of either edge position or shape in the Ni K-edge region were observed during 1st charge up to 5.3 V. This indicates that the apparent voltage plateau above 5 V (higher than III, and not marked) does not originate from the Ni^{2+} to Ni^{3+} reaction, but is likely from electrolyte decomposition at high voltage. In order to study the Ni^{2+} to Ni^{3+} reaction, electrolyte with electrochemical stability above 5V is needed.

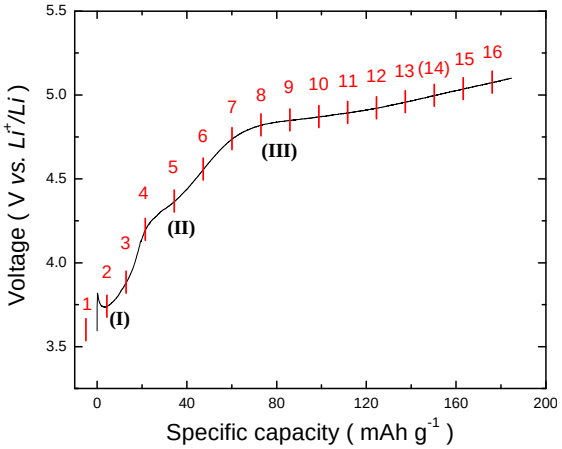

Figure III- 14. 1st charge curve of C-$LiFe_{1/4}Mn_{1/4}Co_{1/4}Ni_{1/4}PO_4$ during *in situ* XRD measurement.

In situ synchrotron XRD patterns of C- $LiFe_{1/4}Mn_{1/4}Co_{1/4}Ni_{1/4}PO_4$ are shown in Figure III- 15. The numbers marked beside the patterns correspond to the scan numbers marked on the charge curve in Figure III- 14.

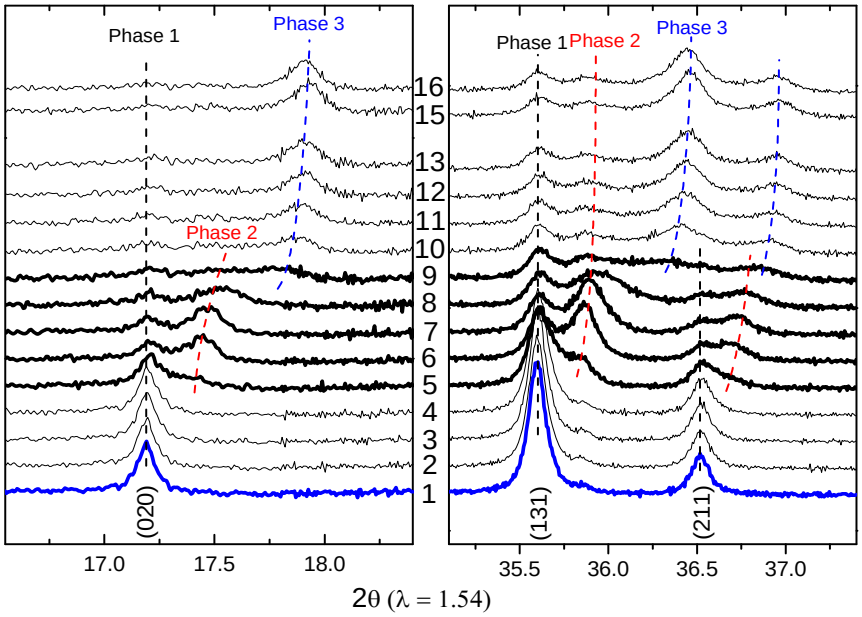

Figure III- 15. *In situ* XRD patterns of C-$LiFe_{1/4}Mn_{1/4}Co_{1/4}Ni_{1/4}PO_4$ during 1st charge

The structure marked as phase 1 is for C-$LiFe_{1/4}Mn_{1/4}Co_{1/4}Ni_{1/4}PO_4$ before charging. Upon charging (i.e., Li deintercalation), the reflections of the new intermediate phase 2 appeared at slightly higher 2θ values with growing intensities, and then the structure transforms to the final phase 3 of the fully delithiated compound (i.e., $Fe_{1/4}Mn_{1/4}Co_{1/4}Ni_{1/4}PO_4$). While the position of reflections from phase 1 does not change noticeably, the reflections from phase 2 and 3 are clearly moving toward higher angles, indicating a solid solution region. These results will be used to design and improve the Mn-, Co-, and Ni-doped lithium iron phosphate materials.

Spinel $LiMn_2O_4$ and NMC Composite Cathode (Yang, Yoon) – In collaboration with LG Chemical through a cooperative research and development agreement (CRADA), the structural changes of the composite cathode ($LiMn_2O_4$ and layered $LiNi_{1/3}Co_{1/3}Mn_{1/3}O_2$ in 1:1 wt%) in both Li-half and Li-full cells during charge/discharge were studied by *in situ* XRD. This cathode has the potential to reduce cost and capacity fading, and offers increased capacity. Figure III- 16(a) shows the first charge curve of the cathode with a cut-off voltage of 5.2V using a constant current charge at a C/7 rate.

In situ XRD patterns of the composite cathode collected at certain potential ranges are plotted in Figure III- 16(b). The *in situ* XRD spectra for the composite cathode in the Li-half cell tracked the structural changes of each component. At the early SOC, the lithium de-intercalation takes place in the NMC component only. When the cell voltage reaches approximately 4.0 V vs. Li/Li^+, lithium deintercalation from the spinel $LiMn_2O_4$ component starts and becomes the major contributor to the cell capacity. When the voltage passed 4.3 V, the major structural changes are from the NMC component, while the $LiMn_2O_4$ component is almost unchanged.

In order to examine the structural changes of the composite cathode in a full cell, a 10mAh pouch cell (2.5-4.2V) using $LiMn_2O_4$-$LiNi_{1/3}Co_{1/3}Mn_{1/3}O_2$ composite as cathode with an MCMB anode was fabricated by LG Chem. The pre-charged cell was discharged and then charged at C/2 rate. The *in situ* XRD patterns are plotted in Figure III- 17. The XRD patterns marked as #1 and #2 correspond to the beginning and ending of the discharge process, respectively; while the #3 and #4 correspond to where the charge current was supplied and cut off, respectively. When cycled between 2.5 V and 4.2V, the structural changes are dominated by the spinel $LiMn_2O_4$ component, with much less changes in the NMC component, comparing with the Li-half cell. These results show the structural changes relating to the contributions of each component to the cell capacity at certain charge/discharge state, which is helpful in designing and optimizing the composite cathode.

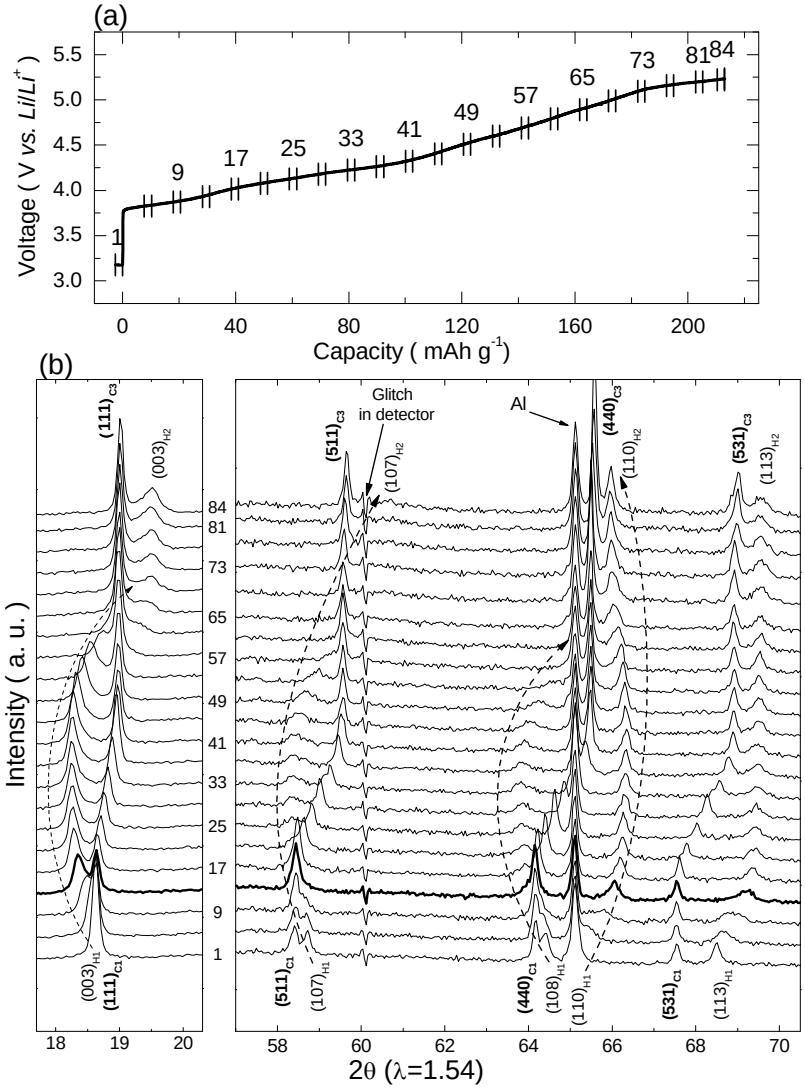

Figure III- 16. (a) First charge curve of $LiMn_2O_4$-$LiNi_{1/3}Co_{1/3}Mn_{1/3}O_2$ composite cathode in the Li-half cell at C/7 rate, and (b) corresponding *in situ* XRD patterns.

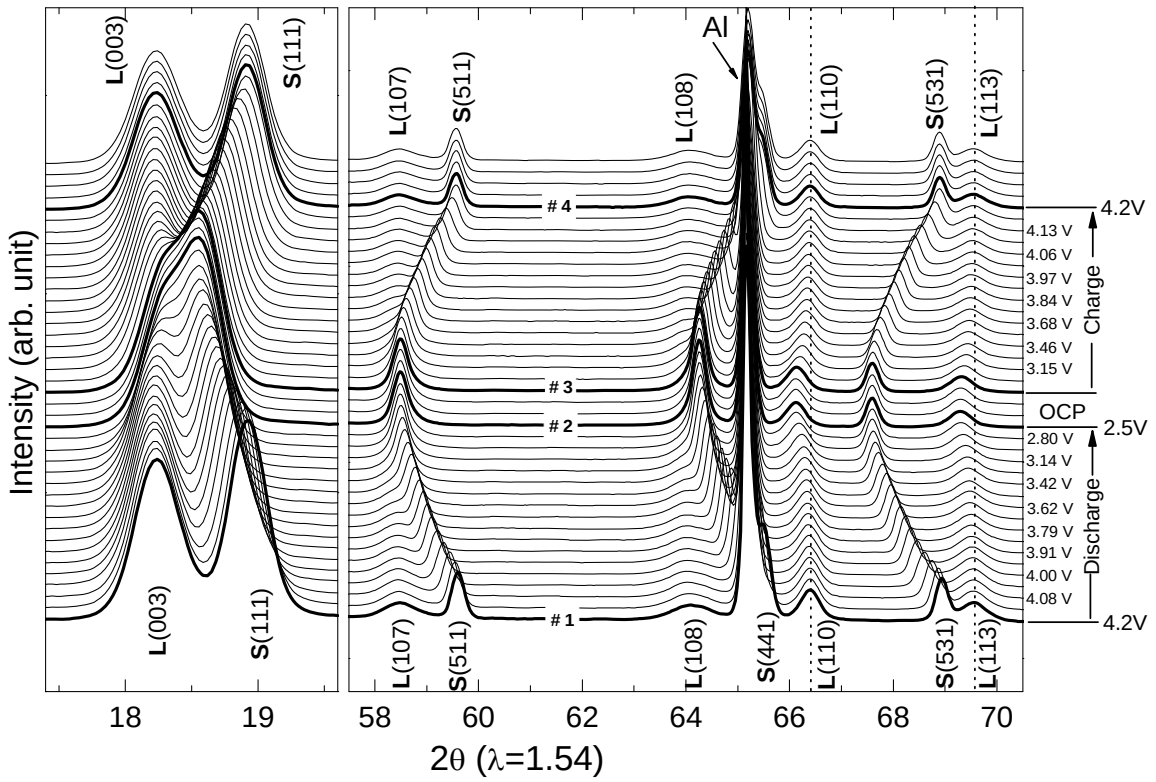

Figure III- 17. *In situ* XRD patterns of the pouch-type Li-full cell during discharge/charge. Pattern #1: before discharge; Pattern #2: after discharge; Pattern #3: before charge; Pattern #4: after charge.

Diagnostics Studies of Gen2 ($LiNi_{0.8}Co_{0.15}Al_{0.05}O_2$) and Gen3 Cathodes (Yang, Yoon, Nam, and Lee) – A new *in situ* soft XAS technique has been developed at BNL which allows monitoring of the oxidation states of cathode materials at both surface and bulk simultaneously during heating. This technique has been applied to study the oxidation state changes of each transition metal at the surface and in the bulk for both cathodes. This technique was used on the Gen2 cathode at 100% SOC. The oxidation state for nickel at the surface probed by the partial electron yield (PEY) are quite different than in the bulk probed by the fluorescence yield modes during heating. As shown in Figure III- 18 for the Ni L-edge spectra, the reduction of Ni^{4+} ions to Ni^{2+} at the surface was clearly observed indicating that the surface of the electrode is decomposed at much lower temperature than the bulk.

Figure III- 19 shows the comparison of surface structural changes between the Gen2 and Gen3 cathode at 100% SOC during heating. While the majority of Ni ions at the surface of the Gen2 cathode reduce to Ni^{2+} at 300°C, most of the Ni ions at the surface of the Gen3 material still remain at Ni^{3+}, showing a better thermal stability. These results are in good agreement with the early studies concluding that the higher Ni content usually results in poor thermal stability.

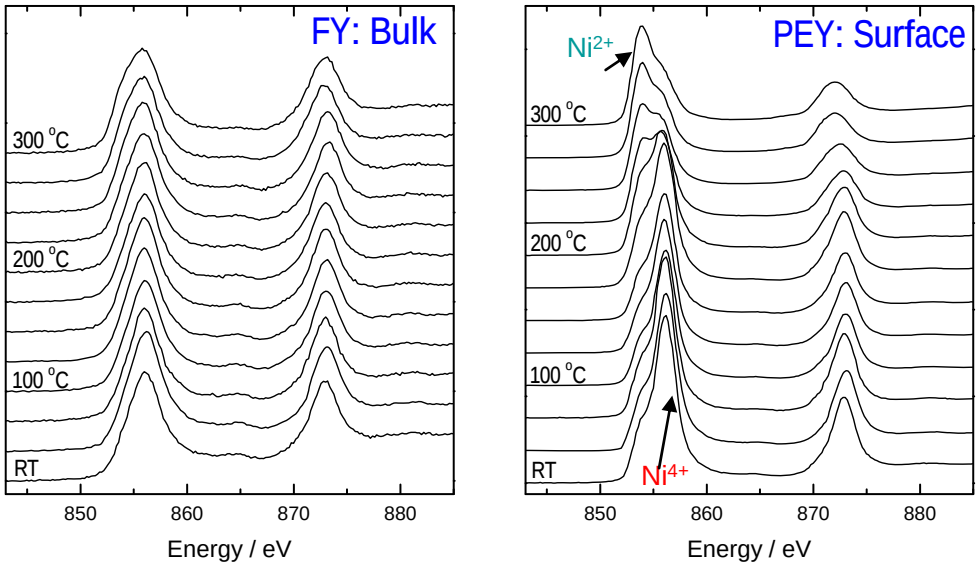

Figure III- 18. Ni L-edge XAS $LiNi_{0.8}Co_{0.15}Al_{0.05}O_2$ cathode at 100% SOC in bulk and at surface**.**

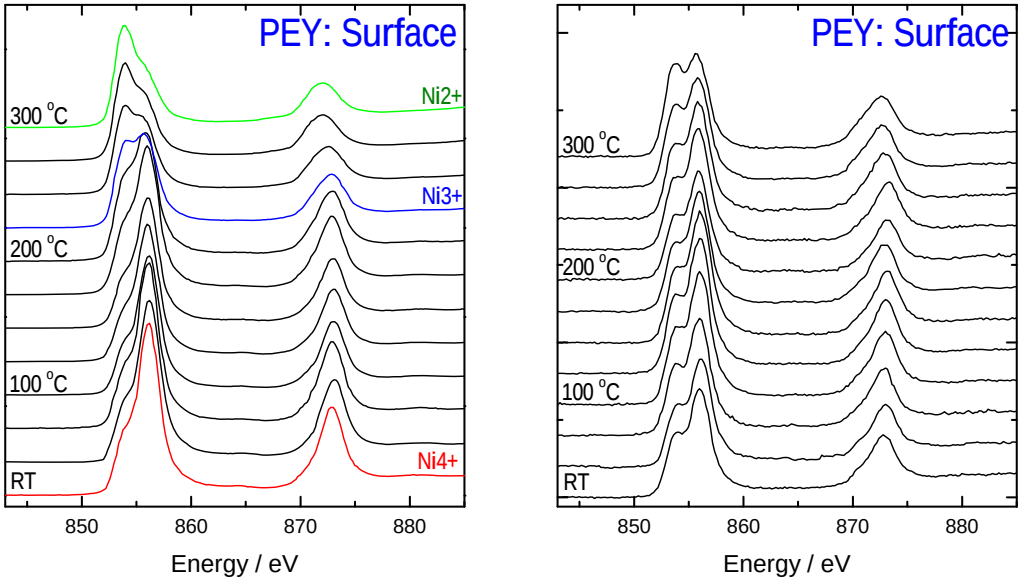

Figure III- 19. Comparison of surface Ni L-edge XAS between $LiNi_{0.8}Co_{0.15}Al_{0.05}O_2$ (left) and $LiCo_{1/3}Ni_{1/3}Mn_{1/3}O_2$ (right) cathodes at 100% SOC during heating from room temperature to 300°C.

III.C Understand and Enhance Low-Temperature Performance

Objectives

- Thoroughly characterize the Gen3 cell chemistry at low temperatures, including the power loss during high-current pulse discharge.
- Understand factors that limit low-temperature performance and identify approaches to enhance that performance.

Approach

- Investigate new electrolytes and salts, and anodes with varying surface areas, and understand their role in modifying low temperature performance.
- Use electrochemical microcalorimetry to quantify any lithium deposition on the graphite in Li-ion cells at low temperatures
- Develop models of low-temperature electrolyte and cell behavior.

Accomplishments/Findings

- Based on observations, it appears that Li-ion power loss at low temperature is inherent to Li-ion kinetics with no fundamental solution identified as of yet. Engineering approaches will most likely be necessary in the design of HEV battery systems to mitigate the effects of low temperature. Specific observations include:
  - EIS studies indicated that the main rise in impedance occurs in the mid frequency range. Processes that occur in this frequency range are generally interfacial in nature.
  - *In situ* micro reference electrode data indicate that the impedance rise at low temperature is shared nearly equally between the positive and negative electrodes and is not significantly influenced by the direction of current flow.
  - The choice of active material (carbon, graphite, metal-oxide, inter-metallic alloys, etc.) does not have a significant effect on the low temperature performance.
  - Alternative electrolytes (acetonitrile (ACN), γ–Butyrolactone (γBL), non-EC carbonates, ketones, sulfolanes, esters, ionic liquids, etc.) show similar low temperature behavior as typical carbonate-based electrolytes.
- Microcalorimetry studies of Li plating show that very little of the deposited lithium actually reacted with the electrolyte, making it extremely difficult to use the microcalorimetry studies as a quantitative tool to measure the lithium deposition rate.
- Electrolyte modeling indicates that local ion and solvent concentration gradients may produce limiting conditions during cycling at low temperature that contribute to a lower rate of charge transfer at the cathode, while ion enrichment at the anode side can result in a local worsening of transport properties.

Future Studies

- Please see Section III.F for a description of the planned activities in the ABR program.

III.C.1 Introduction

This subsection provides highlights and progress on understanding the factors that limit low-temperature performance of high-power Li-ion cells and identifying methods to enhance that performance via cell material and component changes. The limitations include possible Li plating on the negative electrode during charging and a major loss of discharge power ≤-10ºC. The latter

cannot be explained by the conductivity of the electrolyte. Efforts this year involved further studies to thoroughly characterize these limitations in the Gen3 chemistry, evaluating alternative electrolyte salts and solvents, and developing low-temperature electrolyte and cell transport models. Table III- 7 provides a summary of how the participating DOE laboratories contribute to this focus area.

Table III- 7. Summary of how DOE laboratories contribute to the "Low-Temperature Performance" focus area.

	ANL	BNL	INL	LBNL	NREL	SNL
Low-Temperature Performance Characterization	X					
Low-Temperature Electrolyte Modeling			X			
Low-Temperature Cell Performance Modeling	X					

III.C.2 Low-Temperature Performance Characterization

Based on the many observations made, it appears that Li-ion power loss at low temperature is inherent to Li-ion kinetics with no fundamental solution identified as of yet. Engineering approaches will most likely be necessary in the design of HEV battery systems to mitigate the effects of low temperature. Specific observations include:

- EIS studies indicate that the main rise in impedance occurs in the mid frequency range. Processes that occur in this frequency range are generally interfacial in nature.
- *In situ* micro reference electrode data indicate that the impedance rise at low temperature is shared nearly equally between the positive and negative electrodes and is not significantly influenced by the direction of current flow.
- The choice of active material (carbon, graphite, metal-oxide, inter-metallic alloys, etc.) does not have a significant effect on the low temperature performance.
- Salt molarity and temperature are found to have a significant influence on electrolyte viscosity, but the influence of electrolyte viscosity on impedance was minimal.
- From Binder and Carbon Free (BCF) thin film electrodes, it is found that the binder and carbon may play a significant role at room temperatures, but only a minor role at low temperature.
- Higher surface area does improve the low temperature performance by providing more surface area for the electrochemical reactions to take place, but the power robbing mechanism still dominates – just over a larger surface.
- Alternative electrolytes (acetonitrile (ACN), γ-Butyrolactone (γBL), non-EC carbonates, ketones, sulfolanes, esters, ionic liquids, etc.) show similar low temperature behavior as typical carbonate-based electrolytes.
- Surface modification of graphite and soft carbon does not affect the low temperature performance.
- Pulse current level has a dramatic influence on impedance at temperatures below 0°C, especially at -30°C. A decreasing resistance with increasing current is fully explained by Butler-Volmer kinetics. Impedance response at low temperature is clearly dominated by Butler-Volmer kinetics at the electrode-electrolyte interface and not diffusion.

Alternative Solvents (Jansen) – A major effort was initiated last year to explore novel carbonate-free solvent systems in 2032-sized coin cells. The lithium titanate ($Li_4Ti_5O_{12}$) was used as the negative electrode because it cycles at 1.55 V above lithium potential, which helps to alleviate the concern over solvent reduction at the negative electrode. A variety of cyclic and linear

solvents were evaluated. A few of these solvent systems were selected for further study in larger cell formats to shed light on the electrolyte-electrode interface.

Planar cells with 32 cm² electrode areas were made with the following solvents: Diethyl Carbonate (DEC), γBL, ACN, and Methyl Ethyl Ketone (MEK). Diethyl carbonate was selected to assess the influence of EC. γBL was selected to test the effect of having a non-carbonyl ether linkage in a cyclic molecule. ACN was selected because it is a simple molecule that is free of oxygen, and is used widely in ultra-capacitors which do not suffer power losses at low temperature anywhere near the extent that Li-ion batteries do. MEK was selected to test the influence of having a carbonyl group without ether linkage. In last year's work, it was observed that most ketone solvents failed on addition of $LiPF_6$ because ketones are susceptible to attack by Lewis acids. Hence, a non-Lewis acid salt, LiBOB, was used for this study.

Capacity utilization and HPPC ASI were determined for these electrolyte systems at 30, 0, and -30°C. The ASI results are presented in Figure III- 20 with a comparison to the baseline EC/EMC electrolyte. Non-carbonate based electrolytes also suffer from low temperature power loss. They all experience an order of magnitude increase in impedance upon reaching -30°C with similar activation energies (the higher slope for the ACN electrolyte could be due to impedance effects from ACN oxidation). Numerous other solvent systems were tested in 2032 coin cells with similar results. These other solvents included: substituted furans, oxazolines, esters, sulfolanes, and thiazolines. No solvent (or additive) system has been found yet that has significantly lower activation energy.

Ionic Liquid (IL) (Jansen) – An ionic liquid (IL), was investigated to see if it provided enhanced performance at low temperature. An electrolyte was made from 1M $LiPF_6$ in 1-ethyl-3-methylimidazolium-BF_4 (EtMeIm-BF_4) This IL has a melting point of 15°C, but it does not re-solidify until -63°C and can thus be used as a "liquid" electrolyte at -30°C. It has been explored in literature for use in Li-ion electrolytes, but generally was found to have poorer coulombic efficiency compared to typical liquid electrolytes.

Preliminary data from a $Li_4Ti_5O_{12}$ / NMC cell using 1 M $LiPF_6$ in (EtMeIm-BF_4) is presented in Figure III- 21. While this cell system did not perform as well as hoped, it did provide an indication that ionic liquids will most likely not help Li-ion's poor low temperature performance. The ASI of the ionic liquid was an order of magnitude higher that the EC/EMC electrolyte at all temperatures, and the cycle life was only a few cycles. Electrolyte additives could most likely improve the life, efficiency, and impedance of the EtMeIm-BF_4 electrolyte, but the initial data suggest that it would probably not be worthwhile. Other ILs could be investigated in the future if they become readily available.

Surface Modifications (Jansen) – One approach to investigating the electrode-electrolyte interface was to modify the surface morphology of the active material particles. Several carbon materials were made available from Hitachi Chemical Company that were produced with and without surface modifications. The starting materials were natural graphite with a nominal 20μm particle size and soft carbon with a nominal 10μm particle size. Planar cells were made with 32 cm² electrode areas using Gen3 positive electrodes and 1 M $LiPF_6$ in EC:EMC electrolyte. The results of these cell tests are summarized in Figure III- 22. It is apparent that surface modifications

do not have a significant effect on low temperature performance. Soft carbon's better performance in this study is most likely due to its smaller jagged particles (exposed surface area and morphology).

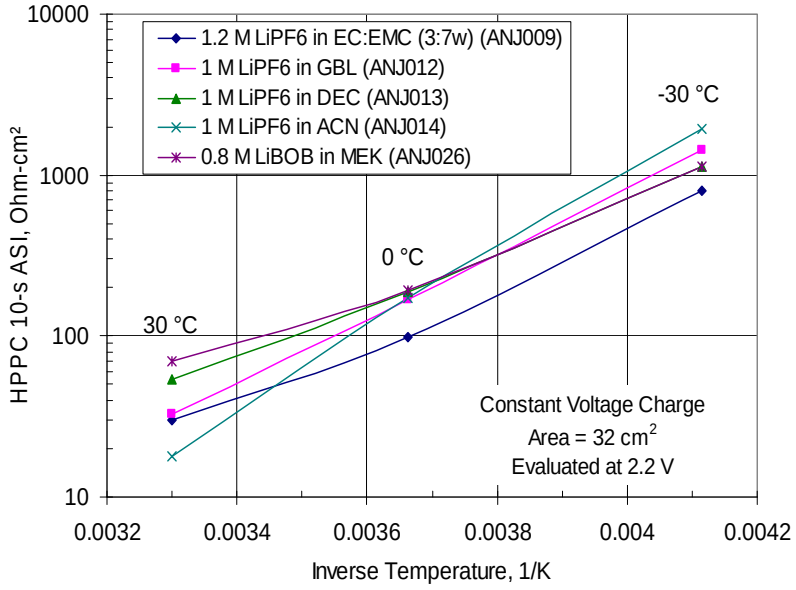

Figure III- 20. Comparison of HPPC ASI results for several alternative solvent-based electrolytes in cells with $Li_4Ti_5O_{12}$ vs. Gen3 positive electrodes.

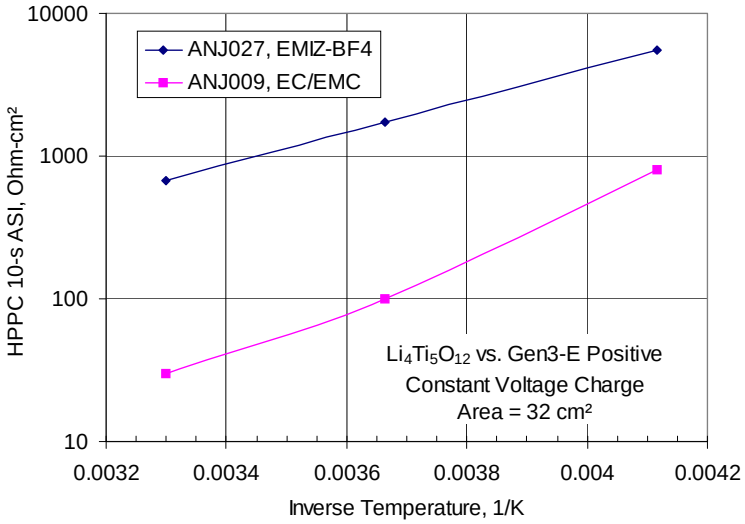

Figure III- 21. Comparison of HPPC ASI comparison of 1M $LiPF_6$ in ionic liquid 1-ethyl-3-methylimidazolium-BF_4 versus 1.2 M $LiPF_6$ in EC:EMC (3:7 w/w).

III.C.3 Low Temperature Electrolyte Modeling

(Gering) **–** Exploratory transport calculations were done using improved predictions and accounting of electrolyte properties over spatial and time domains. In addition, ion solvation/desolvation was explicitly considered. The results underscore the necessity of such an

approach to track the various species over pulse duration, and demonstrate how electrolyte speciation affects local transport properties. In some cases, at low temperatures, the resultant solvent speciation may produce limiting conditions that contribute to a lower rate of charge transfer at the cathode, while ion enrichment at the anode side can result in a local worsening of transport properties. Another issue is whether the reallocation of electrolyte species during a pulse can promote local emergence of thermodynamic phase transitions that would also be more prone to occur at low temperatures.

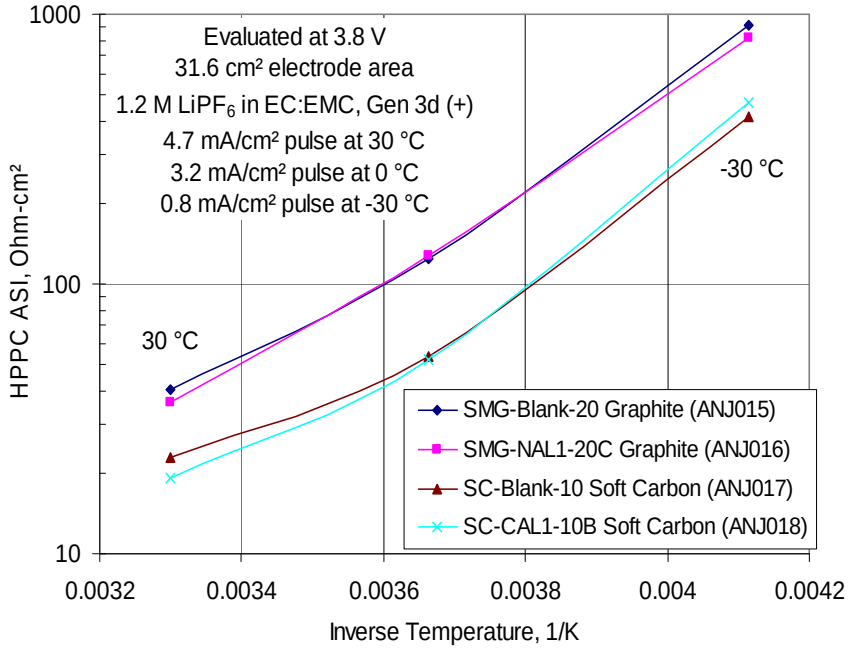

Figure III- 22. HPPC ASI for surface modified and unmodified (blank) graphite and soft carbon from Hitachi Chemical Co.

Efforts in FY 2008 centered around achieving accurate transport modeling of electrolytes in simulated Gen2 cells, focusing on low temperature performance. Of interest are interfacial regions (e.g., double-layers) where speciation of ions and solvent is more manifest. To facilitate accurate interpretation of solvent-ion and ion-ion effects, an advanced chemical physics model, denoted advanced electrolyte model (AEM) based in part on ion solvation has been integrated with a transport module to investigate how electrolyte components speciate during pulse conditions. The target electrolyte for this work is the Gen2 system which is comprised of EC-EMC (3:7 by mass) with 1.2 M $LiPF_6$. Due to the nature of electrolyte composition in double layer regions, it was necessary to model properties for local concentrations approaching or exceeding 5M (each ion) under conditions of enriched or depleted solvent, while allowing for local non-electroneutrality. As such, the AEM provided an accurate rendering of electrolyte properties, spanning between the electrodes, without the need for oversimplifying assumptions such as property averaging and local electroneutrality. Such oversimplifications can mask the causes of performance limitations. The model is of value because it provides a realistic and accurate molecular-based simulation of electrolyte performance in an operating Li-ion cell.

Transport of ions under the influence of a potential gradient (field) can alter ion-specific and bulk electrolyte properties since ion migration could disrupt ion solvation. Higher ionic velocities will

produce a more profound effect on these properties, akin to the Wien Effect[9]. The AEM model predicts the shift in ion solvation due to the potential gradient for all charged species, and has determined that the reduction of solvation numbers is very small for pulse conditions considered herein. Such stability of the solvated lithium complex will yield greater Faradaic co-transport of solvent, becoming more problematic for cell performance at low temperatures due to more stable Li^+-solvent interactions, slower Li^+ desolvation kinetics, and lowered solvent diffusivity.

Traditional methods are employed in executing electrolyte transport calculations. This involves an accurate rendering of species fluxes under pulse conditions and time, considering one-dimensional transport. Selected features of the transport module are:

- Continuity expressions for all mobile species in a given electrolyte (single cations and anions, solvent, ion pairs, and triple ions (ABA, BAB) over (x,t) for 'A' = cation, 'B' = anion,
- Diffusion of all electrolyte species,
- Diffusion potential,
- The effects of ion solvation on solvent co-transport, and how this changes with species velocities,
- Explicit consideration of lithium desolvation kinetics,
- Electrolyte properties for conditions of non-electroneutrality,
- Limiting packing fractions of electrolyte species,
- Considers a fine matrix of spatial dimension in x versus pulse time to accommodate investigation of double-layer regions (e.g., Δx=2.5 nm, and Δt=25 ms),
- Calculates current, resistance, net charge delivered, etc. over (x,t), and
- Pulse type (constant potential or constant current; charge or discharge; duration and magnitude.)

Figure III- 23(a-d) shows the results for modeling Gen2 electrolyte transport behavior for a constant current discharge pulse of 0.2 mA/cm^2, comparing -30°C and 30°C conditions over a pulse duration of 1.25 s (50 time steps). Impedance parameters related to Gen2 electrode materials were utilized to support the calculations. Note that the C_j, values are dimensionless concentration profiles of electrolyte species, that is, molar concentrations normalized with respect to time zero values. Also, the ordinates in Figure III- 23 have a log basis, but their magnitudes differ between the anode and cathode sides. The results emphasize the complexity of considering all electrolyte species simultaneously. Departure from time-zero values is seen for all species, generally within 20-30 nm of the electrode SEI surfaces, wherein the speciation complexity increases at the lower temperatures. For the given conditions, the voltage potential is insufficient to cause a noteworthy diminution of solvators around lithium ions as they are transported across the cell. Hence, solvent depletion is seen at the anode side, Figure III- 23(a,c), as lithium ions emerge from the carbon host and become solvated, and solvent accumulation is seen at the cathode side, Figure III- 23(b,d), due to desolvation of lithium ions just prior to them entering the SEI and undergoing the charge transfer step. The small amount of solvent depletion seen on the cathode side (where $C'_{solvent} < 1$), e.g. Figure III- 23(b), is due to a relatively smaller amount of solvent carried by anions as they are transported toward the anode. The predicted segregation of solvent is more manifest at the lower temperature since solvent diffusivity is significantly lower at -30°C in comparison to 30°C.

[9] The Wien Effect is defined as n increase in the conductance of an electrolyte at very high potential gradients.

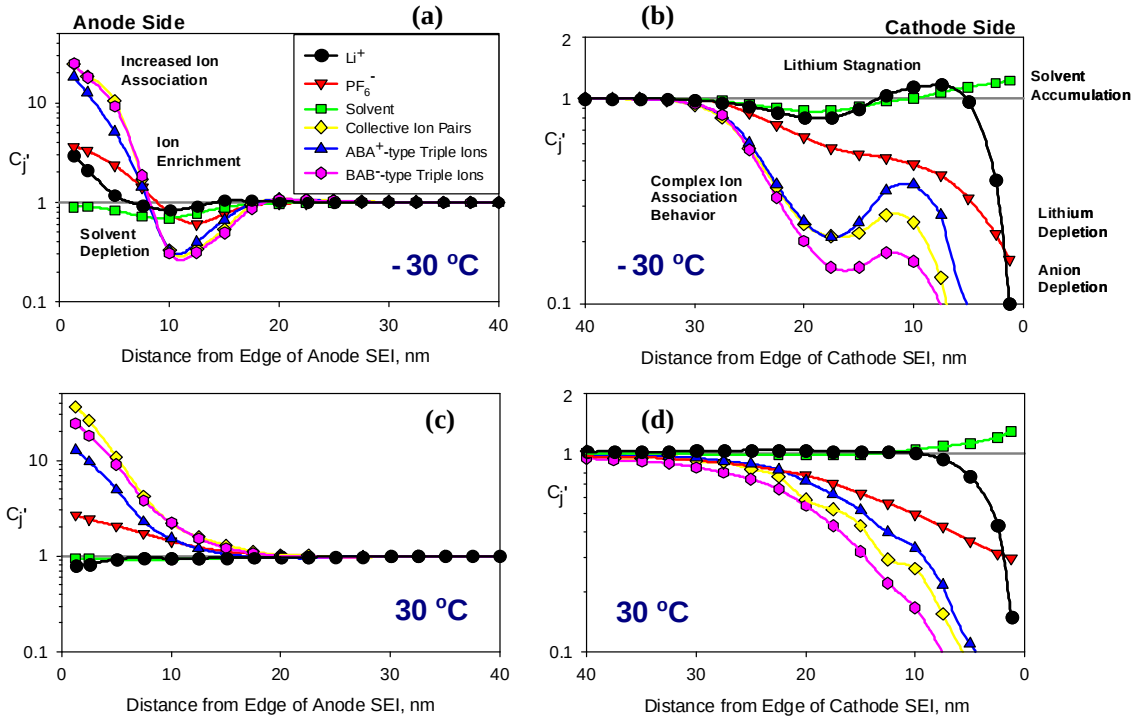

Figure III- 23. Speciation of electrolyte components (dimensionless conc.) for pulse conditions given above.

Ion and solvent depletion or enrichment would generally contribute to a local reduction or increase in viscosity, respectively, with a possible shift up or down in electrolyte conductivity. However, all species must be simultaneously considered in determining the local proportions of single ions to their associated forms, and how they influence the macroscopic transport properties. Thus, although solvent depletion may cause a drop in viscosity, the reduced solvent permittivity would promote greater ion association that could actually result in a net drop in conductivity. Lastly, Figure III- 23(b, d) show the tendency for Li^+ to stagnate behind the region of solvent accumulation. The effect is worse at -30 °C due to lower lithium diffusivity, and contributes to higher viscosity and lower conductivity in the affected region. Also contributing to this stagnation is the rate of lithium desolvation, which is slower at lower temperatures due to higher lithium solvation numbers and higher solvent-lithium binding energies. If such rates become limiting, they would impact the effective rate of charge transfer at the cathode.

Generation of solvent and ion gradients has a direct impact on local electrolyte properties, such as viscosity, effective conductivity, and ion diffusivity, as seen in Figure III- 24(a-d). Note that a log scale is used for all y axes in Figure III- 24. Effective conductivity is derived from both ionic conductance and diffusivity. Noteworthy observations include a significant increase in viscosity and commensurate decrease in conductivity and Li^+ diffusivity near the anode side SEI at -30 °C, spatial variation among the transport properties at the cathode side at -30°C, and how such spatial variations are greatly diminished at 30 °C for both sides. Thus, under discharge pulse conditions at low temperatures, transport limitations in the electrolyte are more severe near the anode side

SEI-electrolyte region, while one would expect kinetic limitations involving the electrolyte to govern performance at regions in proximity to the cathode side SEI.

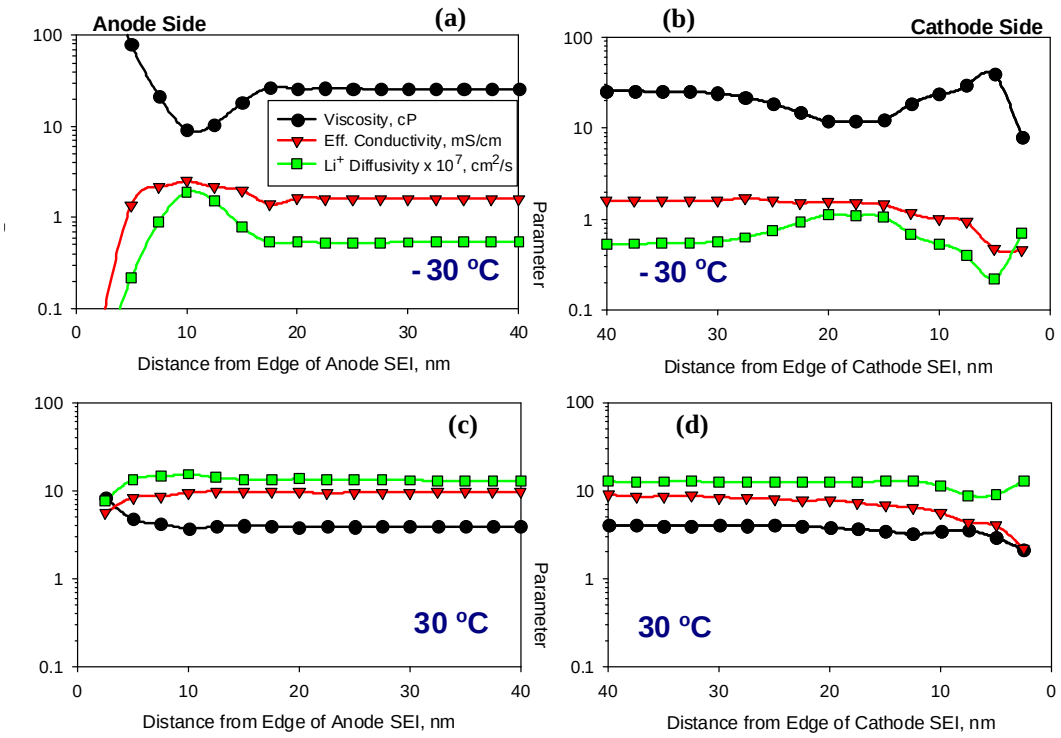

Figure III- 24. Spatial variance of transport properties (Gen2 electrolyte) under pulse conditions given above.

III.C.4 Low Temperature Cell Performance Modeling

(Dees) **–** The electrochemical cell modeling effort this year in the area of low temperature performance continued to examine the issue of lithium plating on graphitic anode materials during charging. A short description and references for the electrochemical model can be found in Section III.B.3. Last fiscal year, a combined modeling and experimental effort was conducted to fully quantify the lithium transport in the graphitic active material as a function of temperature. Galvanostatic Intermittent Titration Technique (GITT) studies were conducted on the Gen3 negative electrode from room temperature down to -30°C. This year the modeling studies have focused on integrating the active material lithium diffusion and SEI phenomena for the graphitic negative electrode. Accurately accounting for all the impedance effects is critical before introducing the lithium plating as a side reaction in the model. Also, since quantitatively measuring the lithium plating rate on graphite at low temperatures would greatly enhance confidence in the model simulations, electrochemical microcalorimetry was explored as an experimental tool to determine the lithium deposition rate.

Li deposited on the graphitic active material should be relatively reactive to the electrolyte solvents, even at low temperatures. Also, oxidation of even small amounts of metallic lithium on the surface of the graphite during regen current pulses should be easily detected from the cell's

heat signature. Thus, electrochemical microcalorimetry should be an effective method to quantify the lithium deposition rate on the graphite in Li-ion cells at low temperatures. Studies initiated last year with Gen3 cells showed no detectable lithium plating at temperatures down to 0°C, which agreed with low-temperature cycling studies conducted at Argonne. This year a series of graphitic negative electrodes of varying thicknesses and loading were fabricated so that electrochemical microcalorimetry studies could be conducted on cells where lithium deposition could be controlled. The graphitic negative electrodes were paired in cells with both lithium electrodes (half cells) and standard positive electrodes (full cells) for study in the microcalorimeter. Both the half cells and full cells exhibited similar heat signatures from the deposition of lithium. While the heat signature was very clear, it was also obvious that the lithium was much more stable on the surface of the graphite than originally anticipated. The studies indicated that very little of the deposited lithium actually reacted with the electrolyte, making it extremely difficult to use microcalorimetry studies as a quantitative tool to measure the lithium deposition rate.

The electrochemical modeling of the graphitic negative electrode proved to be more fruitful than the microcalorimetry studies. Early work with modeling the Gen2 graphitic negative electrode showed that a model similar to the positive electrode did not accurately describe the electrode impedance over a wide range of electrochemical studies. Modeling of the Gen3 negative electrode GITT studies indicated that the difference between the positive and negative electrodes resulted from the multi-phase behavior of the graphite active material during lithium intercalation and de-intercalation. Including the multi-phase behavior into the model did solve the problem, but greatly added to the complexity of the model, even for simple cases such as constant current discharge. Methods to simplify the model were also examined. A simplified model was developed that adequately accounted for the impedance effects, but did not sufficiently capture the multi-phase reactions.

III.D Understand and Enhance Abuse Tolerance

Objectives

- Understand cell component roles in the abuse characteristics of high-power Li-ion cells.
- Identify and develop more stable cell components that enhance the inherent abuse tolerance of Li-ion cells.
- Validate inherent abuse tolerance enhancements at the cell level and quantify them.
- Assess the role of alternative separators on the abuse tolerance characteristics of cells with a given cell chemistry.

Approach

- Use accelerated rate calorimetry (ARC) and differential scanning calorimetry (DSC) to identify the role of each cell component on the thermal characteristics of the Gen3 and other cell chemistries.
- Fabricate 18650 cells with the most promising cell components and additives to validate and quantify respective enhancements using ARC and thermal block tests.

Accomplishments/Findings

- A thin film coating of AlF_3 increased the temperature for onset of self heating of the charged $LiNi_{0.8}Co_{0.15}Al_{0.05}O_2$ from 170ºC to 240ºC, and the overall heat was slightly reduced compared to non-coated material.
- Research into the role of carbon on thermal runaway showed that a secondary SEI is formed after the breakdown of the initial SEI, then continuously is broken down and reformed leading to heat generation. The amount of accumulated heat generated at the anode at temperatures lower than 200ºC may be enough to trigger a thermal runaway regardless of the nature of the cathode, especially in large batteries.
- Carbon with a small particle size and the highest surface area shows the largest heat when compared to carbon with larger particle size.
- Amorphous or soft coatings on graphite were investigated. The accumulated heat from a coated material is significantly lower than that from non-coated material.
- A new redox shuttle, designated pentafluorophenyl)-tetrafluoro-1,3,2-benzodioxaborole (PFPTFBB), showed stable overcharge shuttle ability at 4.2V at C/10 for over 100 cycles and 100% overcharge. The shuttle was shown to be stable from room temperature up to 55ºC at least through 100 cycles.
- Tests have been conducted to stimulate internal short circuits using nickel particles placed on the separator in button cells. Ultrasonic vibration resulted in almost immediate shorting of the cell.
- New Tonen separators were measured at both the material and cell level and indeed showed significant improvement in shutdown properties.

Future Studies

- Please see Section III.F for a description of the planned activities in the ABR program.

III.D.1 Introduction

This subsection highlights the progress on understanding the inherent abuse tolerance of high-power Li-ion cell chemistries and using this knowledge to identify alternative materials and cell components that enhance their abuse tolerance. The cell chemistries used in conventional Li-ion cells are thermodynamically unstable. During the initial charge/discharge cycle, passivation films are formed on the active surfaces of the electrodes which stabilize the system. Detailed studies are reported here on the individual components of the Gen3 cell and the cell chemistry has been thoroughly studied in terms of its thermal and overcharge abuse characteristics. Table III- 8 provides a summary of how the DOE laboratories contribute to this focus area.

Table III- 8. Summary of how the DOE laboratories contribute to the "Abuse Tolerance" focus area.

	ANL	BNL	INL	LBNL	NREL	SNL
Thermal Abuse Studies	X					X
Overcharge Tests with Advanced Materials	X					X
Thermal Abuse Modeling					X	

III.D.2 Thermal Abuse

Component-Level Studies (Amine) – In past reports, the team identified that cathodes which generate a significant amount of oxygen when charged at an elevated temperature usually generate a large amount of heat. This heat generation is caused by the oxidation of solvent from oxygen released from the oxide. This reaction starts at the cathode surface, because of the high oxygen activity at the surface of the particles, and then propagates into the bulk, creating a thermal event. For improved safety, it is important to select cathodes that generate less oxygen when charged, and/or to protect the surface of the cathode particles with a thin film barrier. The surface coating used here is a very thin film of stable AlF_3. The aluminum in AlF_3 does not change oxidation state during cycling, and AlF_3 cannot be attacked by trace HF in the electrolyte that can cause a film to detach from the surface of the cathode particle. As a result, the AlF_3 film should remain intact during cycling and aging.

Figure III- 25 shows the DSC curves of a fully charged (4.3V) $LiNi_{0.8}Co_{0.15}Al_{0.05}O_2$ based cell with and without the AlF_3 film. The effect of the AlF_3 coating is pronounced because of the high reactivity of $LiNi_{0.8}Co_{0.15}Al_{0.05}O_2$ when fully charged. The AlF_3 coating increases the onset temperature from 170ºC to 240ºC, and the overall heat is slightly reduced compared to non-coated material. These results show that the breakdown of the stable AlF_3 film at the surface of these oxide cathodes requires very high-energy and a high temperature, which translates into the increased onset temperature.

However, most of the thermal events in oxide cathode materials usually take place above 200ºC, which is higher than the temperature for the cell thermal event, which takes place at 130ºC. Therefore, it is suspected that the carbon anode may play an initial role. One of the main objectives is to investigate the role of carbon in cell safety and, more specifically, the heat associated with the decomposition of the SEI.

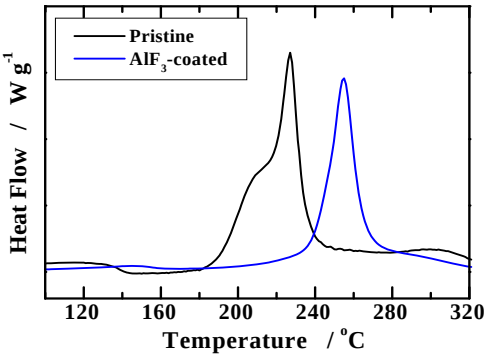

Figure III- 25. 1 DSC curves of fully charged cell to 4.3 V of $LiNi_{0.8}Co_{0.15}Al_{0.05}O_2$ particles with and without AlF_3 film.

Figure III- 26 shows the DSC curve for mesocarbon microbead (MCMB) graphite that a) has been charged and then discharged to form a passivation film and b) has been fully lithiated. The DSC curves were recorded between room temperature and 400ºC. The onset temperature for the breakdown of the SEI is lower than 100ºC and the amount of heat generated is 73 J/g. However, fully charging the cell releases a significant amount of heat because of the continuous breakdown and formation of the secondary SEI at the graphite surface up to 200ºC. To prove that a secondary SEI is formed after the breakdown of the initial SEI, the team first cycled a half cell based on Li/MCMB three times to form the initial SEI. The gas generated during the formation was analyzed by gas chromatography (GC)- mass spectroscopy (MS), and the cell was degassed and sealed, then heated to 100ºC to break down the initial SEI layer. Immediately after exposing the cell at 100ºC, the gas composition was similar to that during the formation of the initial SEI. This result indicates that after the breakdown of the initial SEI film, a similar secondary SEI was formed, generating further heat as indicated by the continuous heat observed between 70ºC and 200ºC. The amount of accumulated heat generated at temperatures lower than 200ºC may be enough to trigger a thermal runaway in a cell regardless of the nature of the cathode, especially in large batteries with a large number of cells. This result demonstrates that, unlike what is speculated in the literature, the thermal abuse issue for Li-ion cells should be addressed at both the oxide and anode.

To study this matter further, the team selected SMG carbon made by Hitachi Chemicals from the same sources (and by the same process) but having a different surface area (Table III- 9). By doing so, the team eliminated the effect of carbon morphology and focused only on the effect of surface area, which has a direct relationship with the SEI. Figure III- 27(a) shows the accumulated heat from a DSC curve between 70°C and 210°C for fully-charged SMG carbon with different particle sizes. Carbon with the small particle size and thus the highest surface area shows the largest heat when compared to carbon with larger particle size (20μm). Figure III- 27(b) shows the normalized heat flow of fully charged SMG carbon with different particle sizes calculated from the DSC curve. As expected, the heat flow increases with a decrease in particle size and an increase in surface area. Therefore, lower surface area carbon could result in much lower heat caused by the continuous breakdown and formation of the passivation film and could result in a more abuse tolerant battery.

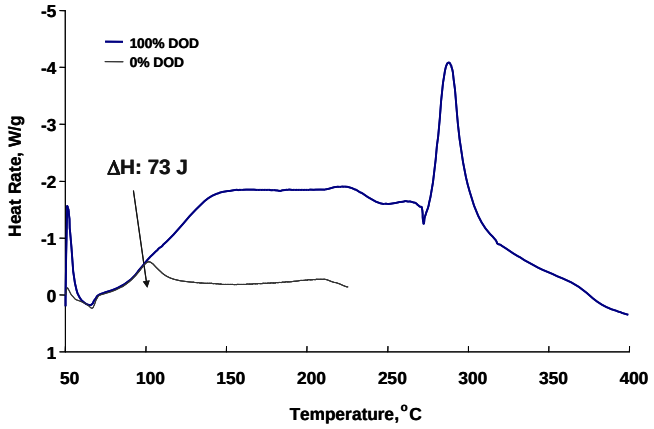

Figure III- 26. DSC curves of MCMB graphite (lower) charged and then discharged to form a passivation film, and (upper) fully charged.

Table III- 9. Physical characteristics of SMG carbon.

Material	Unit	MCMB	SMG-NA L1-20C	SMG-NA L1-15C	SMG-NA L1-10C	SMG-NA L1-7C	SMG-(blank) L1-20C
Average Particle Size	μm	25	23.4	17.4	11.9	7.8	19.8
S.S.A.	$x10^3$ m^2/kg	1.3	2.0	2.9	4.2	6.3	5.0

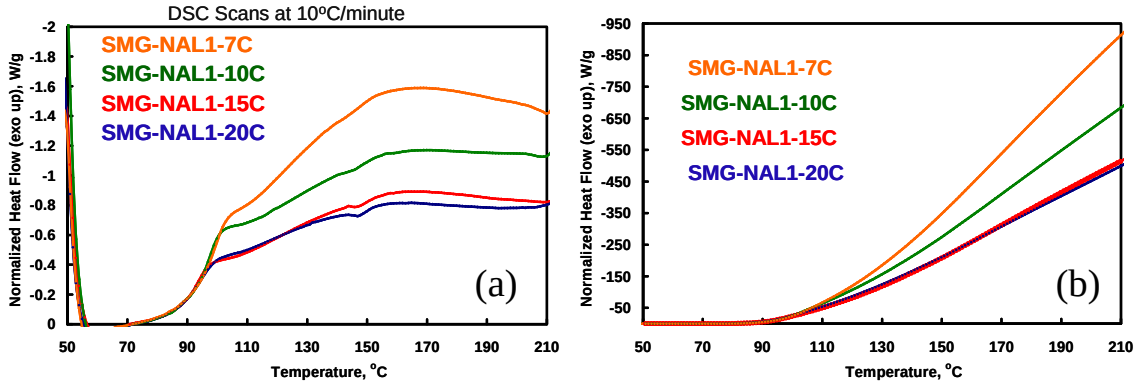

Figure III- 27. (a) Accumulated heat from a DSC curve between 70ºC and 210ºC for fully charged SMG carbon with different particle sizes, and (b) Normalized heat flow of fully charged SMG carbon with different particle sizes.

To address carbon safety, several firms are investigating an amorphous or soft coating on graphite to reduce the surface area of carbon. Figure III- 28 shows the DSC curve of SMG carbon with 5-m^2/g surface area and 20μm average particle size and a similar carbon coated with soft carbon having similar particle size but a significantly lower surface area of 2 m^2/g. The DSC curve shows that the accumulated heat from the coated material is significantly lower than that from non-coated material. This technique, combined with the use of electrolyte additives that form stable SEIs and

can push the onset temperature of SEI breakdown higher, could provide the ultimate solution to reducing the effect of the carbon anode on cell thermal runaway.

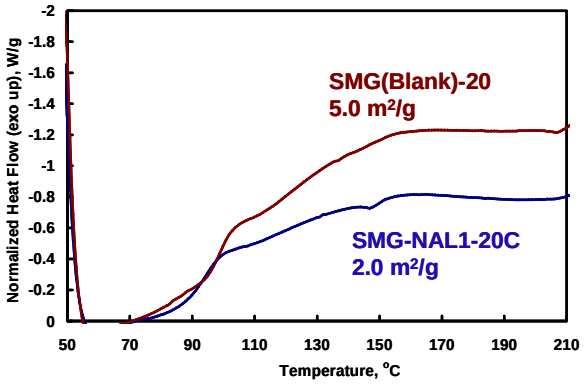

Figure III- 28. DSC curves of SMG carbon with 5-m^2/g surface area and 20μm average particle size and a similar carbon coated with soft carbon having similar particle size but significantly lower surface area of only 2 m^2/g.

Creation and Testing of Internal Short Circuits (Roth) – Internal short circuits, presumably caused by very small metallic particles which penetrate the separator, have resulted in a number of well publicized safety events and massive cell recalls. Tests have been performed at SNL to stimulate internal short circuits using nickel particles placed on the separator in button cells. Ultrasonic vibration resulted in almost immediate shorting of the cell (Figure III- 29). This technique promises to be a useful method for studying the response to internal short circuits with different cell materials and designs. Full cell (18650) tests are currently being conducted.

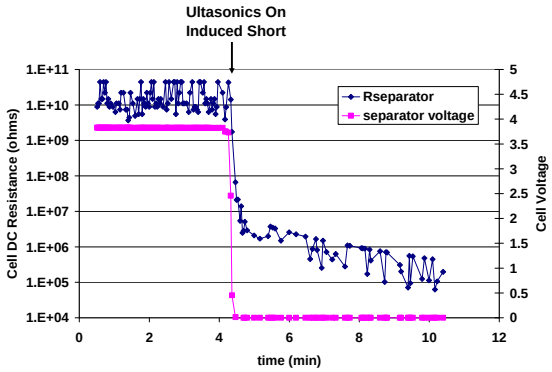

Figure III- 29. Internal short in a coin cell induced by Ni particles and ultrasonic vibration.

Component-Level Separator Response (Roth) – Separator integrity is critical to the safety and abuse tolerance of Li-ion cells. A loss of separator integrity can lead to internal shorts which can result in immediate and rapid disassembly of the cell with gas release and fire. Separator shutdown of one cell in a series connected string can result in high voltages across that cell leading to failure of that cell separator. The shutdown properties of separators soaked in electrolyte were measured using AC impedance methods as well as measurement of DC voltage breakdown as a function of temperature. Several commercial separators were measured and their properties compared with

their performance in full cells under abuse conditions (Figure III- 30). New Tonen separators, reported to have better high-temperature integrity, were measured at both the material and cell levels and showed significant improvement. Different lots with increasing mechanical strength showed stable and reproducible shutdown properties.

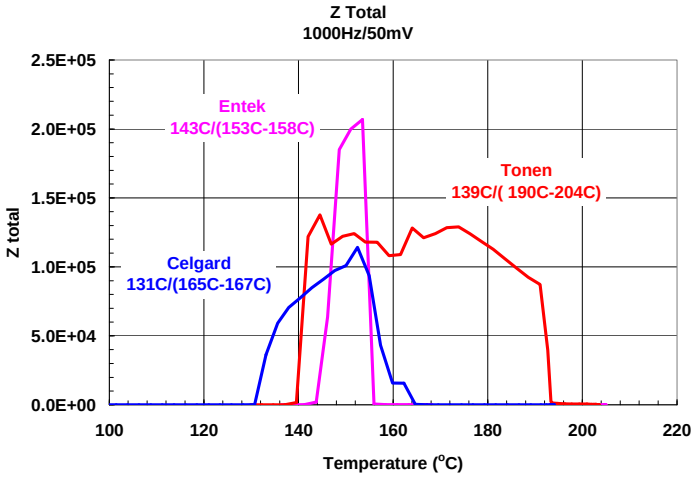

Figure III- 30. Comparison of separator impedances for some commercial separators at high temperatures.

The cell integrity was also measured as a function of electrode surface roughness which showed that the separator impedance is less using actual coated electrode material compared to smooth nickel electrodes. This indicates the importance of maintaining smooth and contamination free surfaces in the full cells.

The integrity of the separator above shutdown was measured with applied potentials similar to that occurring in cell strings. Material level tests of the Tonen separator showed it maintained integrity for 27 minutes at 140°C, shown in Figure III- 31(a), while a full cell tested during overcharge and using Tonen separator did not show loss of integrity during a one hour hold above shutdown, shown in Figure III- 31(b).

Cell Level Abuse Tests (Roth) – One goal of the thermal abuse program is to demonstrate improved abuse tolerance in Li-ion cells based on new stable electrode materials and additives. Much of the studies have concentrated on the most stable cathodes using the $LiMn_2O_4$ spinel and $LiFePO_4$. The thermal properties of these materials have been characterized and used to determine the effect on full cell abuse response including heat generation, gas generation, and flammability. Such methods as ARC and thermal ramp tests have been used to determine the material properties and associated cell thermal response.

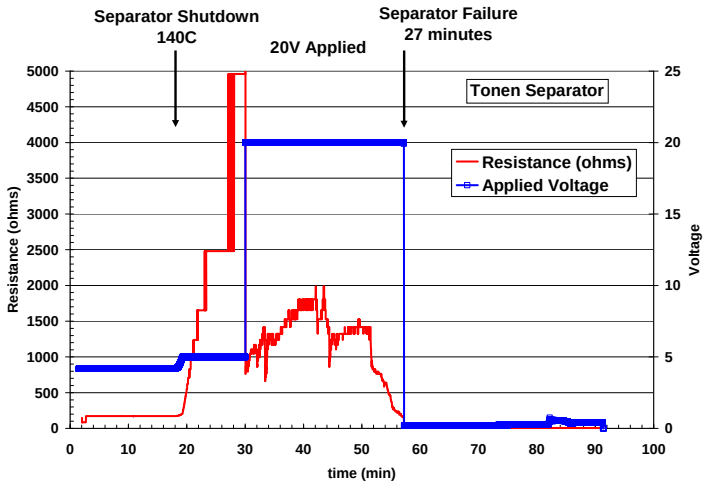

(a)

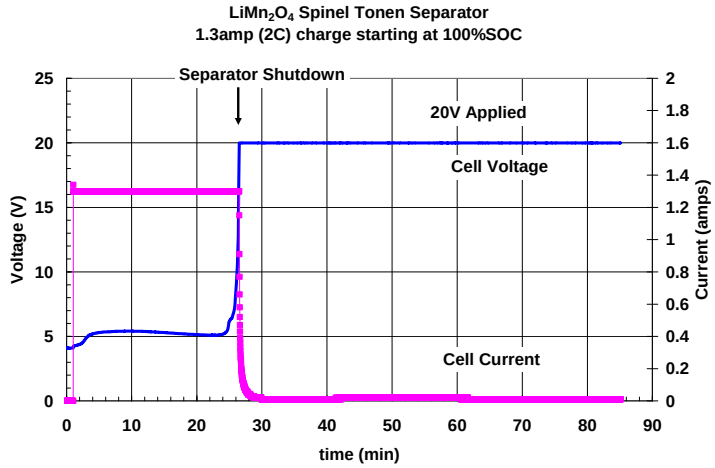

(b)

Figure III- 31. (a) Integrity of separator above shutdown with applied 20V overpotential that was maintained for 27 minutes before failure. (b) Integrity of separator in a full 18650 cell above shutdown with applied 20V overpotential.

ARC Study (Roth) – ARC measurements allow comparison of the heat generation enthalpies and reaction kinetics as well as the gas evolution profiles. Measurements were performed on 18650 cells and also on complete cell electrodes removed from fully charged cells and resealed in 18650 cans. These measurements allowed determination of the relative contributions of the anode and cathode to the full cell heat and gas generation. The team has extended the measurement database of cathode chemistries by evaluating $LiMn_2O_4$ spinel and $LiFePO_4$. Figure III- 32(a) shows the improvement in ARC thermal runaway response for cathodes with reduced oxygen generation while Figure III- 32(b) shows an expanded view comparing $LiMn_2O_4$ and $LiFePO_4$ cells. $LiFePO_4$ shows lower enthalpy due to reduced oxygen generation during high-temperature decomposition but also shows that the anode is still an important source of energy.

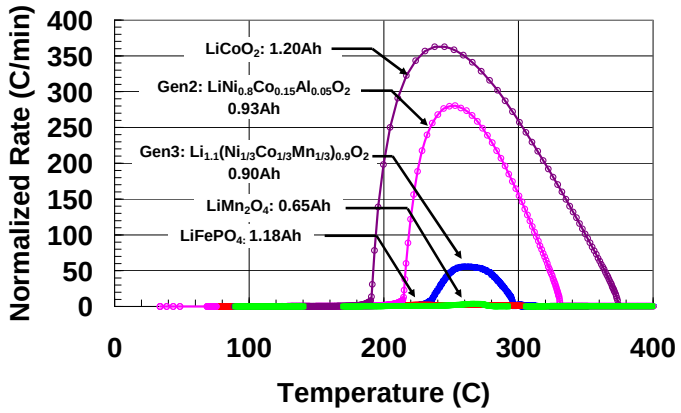

(a)

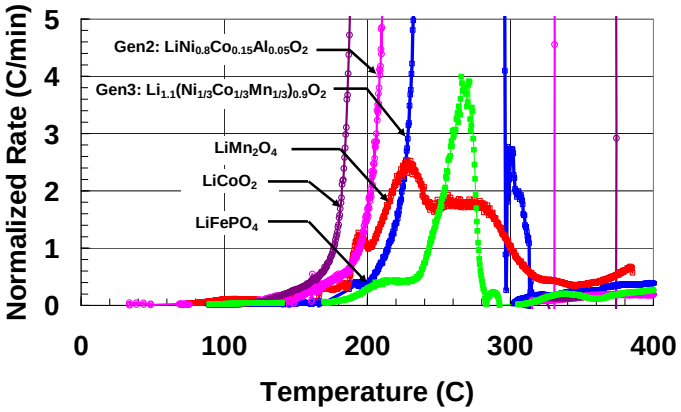

(b)

Figure III- 32. (a) Comparison of ARC profiles for different cathode chemistries showing improved abuse response, b) Expanded views of ARC profiles showing the low energy and kinetics for $LiMn_2O_4$ and $LiFePO_4$ cells.

Cell thermal runaway with highly reactive cathodes are dominated by the cathode runaway profile. Figure III- 33(a) and (b) show ARC profiles for a $LiCoO_2$ cell compared with the individual cell electrodes which had removed from a fully charge cell and resealed in 18650 cans. The $LiCoO_2$ cathode clearly dominates while the anode contributes to the kinetics of the reaction at a much lower rate. The results for several commercial $LiFePO_4$ cells were measured and compared to cells built in the laboratory using coated electrodes supplied by Hydro-Québec. Figure III- 34 shows the ARC profile of two commercial cells, one designed as a power cell and the other as an energy cell. The onset of thermal runaway is almost identical while the energy cell shows greater enthalpy of reaction as expected. Only a 0.2 Ah difference in capacity resulted in a significant increase in response. Finally, ARC profiles were taken for three commercial cells with diffeent capacities which all showed similar onset temperatures. Some variance in total reaction energy and rate was observed that may result from differences in anodes and electrolytes in the cells.

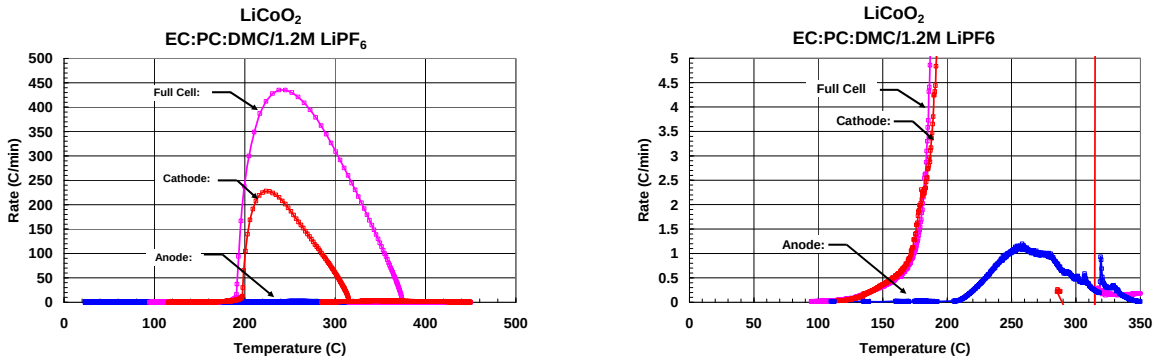

(a) (b)

Figure III- 33. (a) ARC profiles for full $LiCoO_2$ 18650 cell and the individual electrodes showing primary cathode response, (b) Expanded view of $LiCoO_2$ 18650 cell showing relatively small contribution of anode.

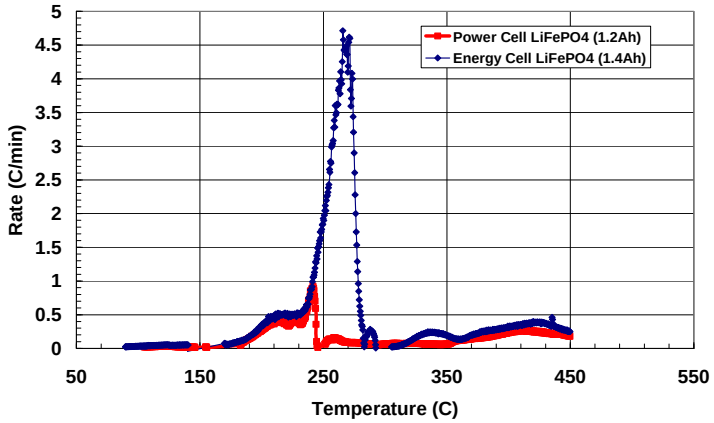

Figure III- 34. ARC profiles of commercial $LiFePO_4$ cells showing higher rate for energy cell vs. power cell.

Thermal Ramp Response/Flammability (Roth) – The thermal abuse response of these cells and the flammability of the vented gases were measured using a thermal block apparatus developed at SNL that allows determination of the onset of cell heat generation and also records the flammability of the vented gases/electrolyte in the presence of an external ignition source. Cells were ramped in open air at 6˚C/min until thermal runaway occurred. $LiFePO_4$ cells showed the onset of heat generation around 220°C followed by a low-rate thermal runaway at 240°C as is shown in Figure III- 35 (a) for two commercial cells with different capacities. As a comparison, a cell with $LiMn_2O_4$ is also shown with similar runaway temperature but much higher heating rate. The runaway that was observed in the $LiFePO_4$ cells resulted from the anode reaction with the electrolyte after the protective SEI was fully decomposed. Figure III-35 (b) shows that the capacity normalized response for the two $LiFePO_4$ cells are quite similar indicating that chemistry primarily determines cell response even for different size cells. All of the cells undergoing thermal ramp also showed flammability of the vent gases. Internal gas generation from electrolyte decomposition aerosolizes the flammable electrolyte and results in

flame. Flame retardants have not yet resulted in a non-flammable electrolyte under these conditions.

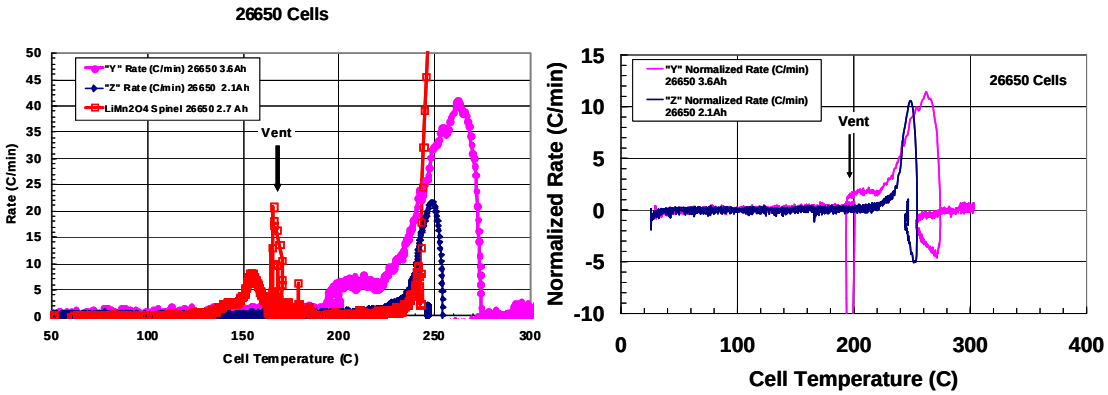

(a) (b)

Figure III- 35. (a) Thermal ramp profiles of two commercial $LiFePO_4$ cells and a $LiMn_2O_4$ spinel cell showing similar runaway temperatures. Higher heating rates were seen with increasing capacity for the $LiFePO_4$ cells, (b) Thermal ramp profiles of two commercial $LiFePO_4$ cells normalized by capacity showing similar normalized response rates independent of cell capacity.

III.D.3 Overcharge Abuse

Redox Shuttle Overcharge Protection (Amine) – Battery overcharge represents an important issue for Li-ion batteries. Overcharge generally occurs when current is forced through the battery and the charge delivered exceeds its charge-storing capability. Overcharge of Li-ion batteries can lead to chemical and electrochemical reactions for battery components, a rapid temperature elevation, and thermal runaway and catastrophic failures. The overcharge issues become more significant for larger batteries because of the increased amount of active material. Therefore, for large batteries designed for transportation, satellite or storage applications the overcharge issue needs to be addressed. ANL has been developing new redox shuttle additives that can be incorporated into the electrolyte to protect Li-ion batteries against overcharge. A successful redox shuttle can be electrochemically oxidized and reduced reversibly at a potential value slightly higher than the working potential of the cathode. With incorporation of the redox shuttle in the electrolyte, the Li-ion batteries could normally operate in voltage ranges below the redox potential of the redox shuttle. When the battery is overcharged, its voltage would first reach this redox potential and activate the redox mechanism, which becomes the only active component, to transfer the excessive charge through the battery without any battery damage. Under such a mechanism, the battery voltage would remain constant and no overcharge would take place. In most cases, the amount of redox shuttle is less than 3 percent (by weight) in the electrolyte. Such a small amount should not affect cell performance but could significantly enhance its safety characteristics. In addition, having an effective overcharge redox shuttle system can eliminate the need for expensive electronic cell balancing systems used in current batteries having multiple cells either in parallel or in series. ANL has developed a new redox shuttle (shown in Figure III- 36) and referred to as pentafluorophenyl)-tetrafluoro-1,3,2-benzodioxaborole (PFPTFBB).

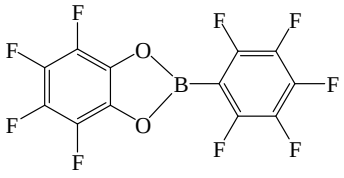

Figure III- 36. Redox Shuttle PFPTFBB

Figure III- 37 shows cyclic voltammograms of 0.05 M PFPTFBB and 1.2 M $LiPF_6$ in EC/ EMC (3:7, by weight). Both the counter and reference electrodes were lithium foils, and the working electrode was a platinum disk (Φ = 1 mm). The onset potential of PFPTFBB is ~4.3 V vs. Li^+/Li, which is high enough to provide overcharge protection for most state-of-the-art positive electrode materials. This low redox potential is very convenient because it can allow for better stability of the electrolyte compared to shuttles that operate at 4.6V at which value the electrolyte starts to decompose. Figure III- 38 shows the voltage profile of two identical graphite/$LiNi_{0.8}Co_{0.15}Al_{0.05}O_2$ cells during the initial overcharge testing cycle. The electrolyte used was 1.2 M $LiPF_6$ in EC/ Propylene carbonate (PC)/DMC (1:1:3, by weight) with 5 wt% PFPTFBB. At the beginning, the cells were normally charged with a constant current of C/10. Both cells were fully charged in about 10 hours, and the voltage of both cells continued to increase until the positive potential met the redox potential of PFPTFBB, at which point the cell voltage was ~4.2 V. Figure III- 38 also shows a flat voltage of 4.2 V for the 10-hour overcharge, because the redox reaction of PFPTFBB gets activated at this point.

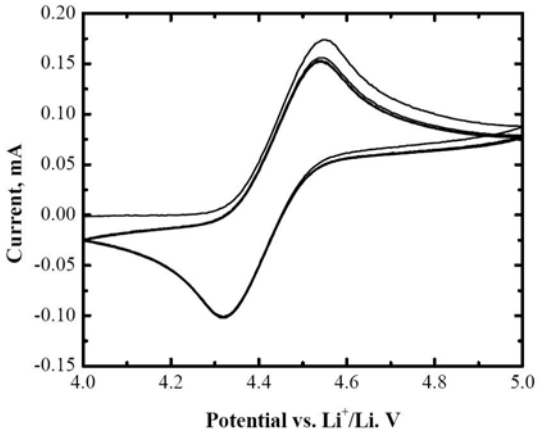

Figure III- 37. Cyclic voltamogram of 1.2 M $LiPF_6$ in EC/PC/DMC (1:1:3) w/ 3wt% (tetrafluorobenzo-1, 2-dioxyl)-pentafluorophenyl-borane.

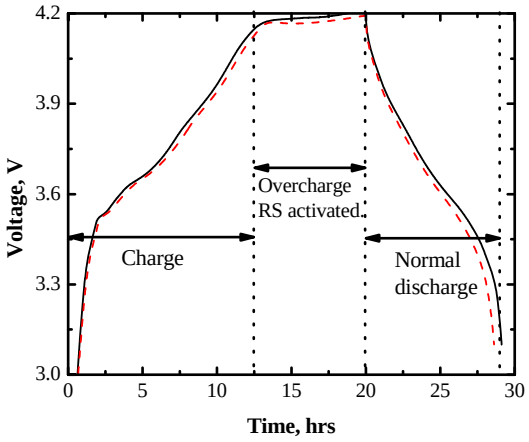

Figure III- 38. Voltage profiles of two graphite/$LiNi_{0.8}Co_{0.15}Al_{0.05}O_2$ Li-ion cells during the overcharge test.

Figure III- 39 shows the charge/discharge capacity of a graphite/$LiNi_{0.8}Co_{0.15}Al_{0.05}O_2$ cell containing 5 wt% PFPTFBB in the electrolyte, which was 1.2 M $LiPF_6$ in EC/PC/DMC (1:1:3, by weight). The cell was charged and discharged at a constant current of C/10 (0.2 mA). During the charging process, the cell was charged to 4.95 V or until a 4.0 mAh charge was delivered (100% overcharge). The cell was initially tested at 25°C for 20 cycles and was then heated to 55°C for another 50 cycles to check the stability of redox shuttle under a more aggressive testing condition. After that, the cell was tested with a higher constant current of C/5. The testing condition for each stage has also been labeled in Figure III- 39. During the initial cycling at 25°C, some fluctuation of the discharge capacity was observed. The voltage profiles of the cell were checked, and no evidence of overdischarge was observed. After 50 cycles at 55°C, the overcharge protection of the redox shuttle was maintained and the cell capacity remained very stable, even though the cell was 100% overcharged for each cycle. Afterward, the cell was further tested at 25°C and 55°C respectively with a constant current of C/5 and 100% overcharge. The overcharge protection provided by PFPTFBB finally disappeared after 170 cycles of 100% overcharge. Figure III- 39 also shows that the cell completely lost its capacity after 125 cycles. However, the redox shuttle mechanism remained active for another 50 cycles at 55°C after the cell died. PFPTFBB is believed to be a stable redox shuttle for overcharge protection of 4-V class Li-ion batteries.

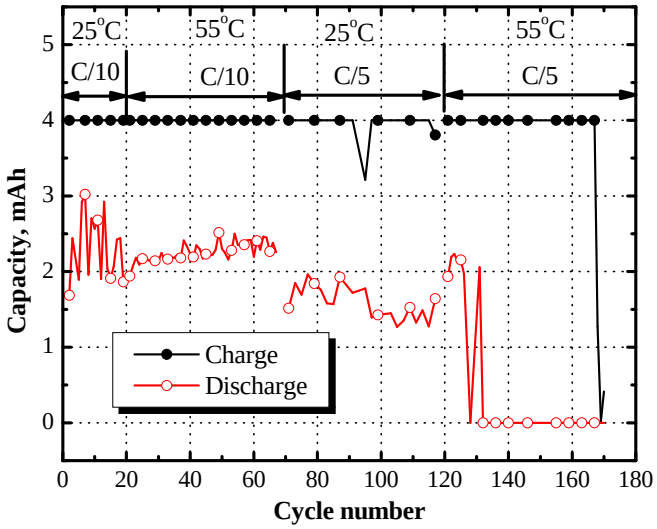

Figure III- 39. Charge and discharge capacity of a graphite/$LiNi_{0.8}Co_{0.15}Al_{0.05}O_2$ Li-ion cell during the whole course of overcharge test. The electrolyte used contained 5 wt% PFPTFBB.

Cell Level Overcharge Protection Studies (Roth) – The goal of this work is to determine the effects of electrochemical overcharge and thermal decomposition leading to cell thermal runaway. Overcharge studies have been performed using custom apparatus designed to allow quantitative measurements of the heat generation of the cells during overcharge and simultaneous real-time gas monitoring of evolved gas species. The team has previously demonstrated that high-rate overcharge can lead to thermal runaway. In addition, overcharge leads to cell venting of gases that can reach explosive levels in the presence of oxygen (in air). Two commercial $LiFePO_4$ cells were compared with a $LiMn_2O_4$ spinel cell during overcharge. The two different $LiFePO_4$ cells showed similar overvoltage profiles at two different currents as shown in Figure III- 40(a). The peak in cell voltage is likely associated with electrolyte breakdown. A $LiMn_2O_4$ spinel cell showed a similar peak voltage but had an extended overcharge range before heat generation resulted in separator shutdown as shown in Figure III- 40(b). Overall, the spinel cathode cell at a 2C charge rate showed greater tolerance to overcharge compared to the two commercial $LiFePO_4$ cells at a 1C rate. This improved $LiMn_2O_4$ response was also seen in comparison with the Gen2 and Gen3 cathodes where the spinel cell at a 2C charge rate showed similar heat output as the Gen2 chemistry at a 1C rate as shown inFigure III- 41. Delayed heating response to overcharge allows time for other controls to prevent a runaway response. Note that the test results of these commercial cells may reflect inherent properties of the cathodes, but may also reflect different carbons in the anodes, different separator, different components or additives in the electrolytes, or other cell differences.

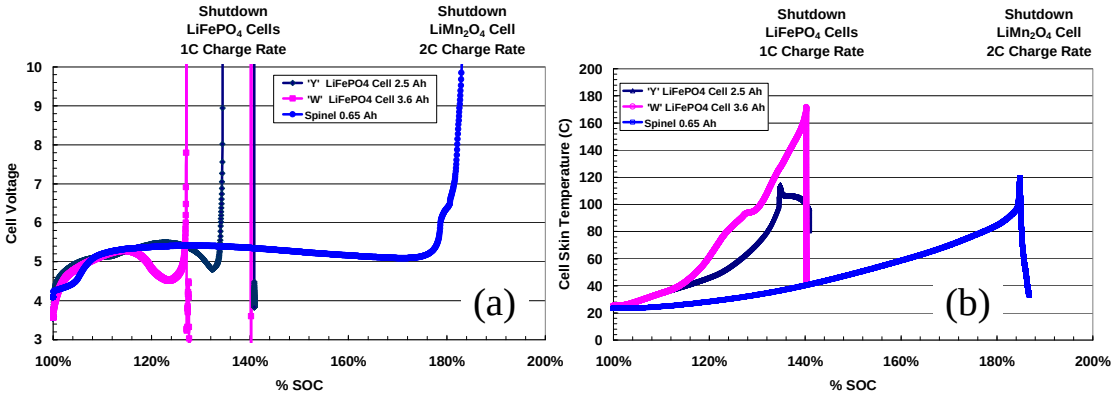

Figure III- 40. (a) Overcharge profile for $LiMn_2O_4$ and two $LiFePO_4$ cells, (b) Overcharge profile of $LiMn_2O_4$ at a 2C charge rate and two commercial $LiFePO_4$ cells at a 1C charge rate showing cell temperature response for different cell capacities.

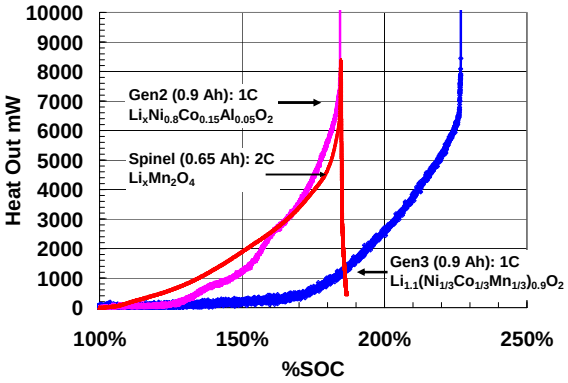

Figure III- 41. Heat output during overcharge for $LiMn_2O_4$ cell at 2C compared with Gen2 and Gen3 cells at 1C.

Thermal Abuse Modeling of an Internal Short (Kim) – The team explored the impact of thermal design of cells and modules and used an electrochemical model for better prediction of thermal runaway initiation. From previous efforts, it was learned that heat transport designs inside a cell and between cells in a multi-cell module/pack has a critical impact on thermal runaway propagation. Therefore, the team continued efforts exploring the impact of thermal design of cells and modules. Recognizing that not only the thermal flow paths but also the electrical configurations inside a cell and between the cells can impact thermal runaway, thermal abuse propagation and electrochemical models were integrated for better prediction of thermal events in Li-ion batteries.

The team used the 3D Li-ion battery thermal abuse "reaction" model to explore the impact of the location of an internal short and the thermal properties of the cell (Figure III- 42). The initial heating pattern under internal short circuit events can be affected by cell characteristics, the nature of the short and electrical configuration. Nevertheless, in this simulation it was assumed that locally concentrated heat was released at the location of shorts. Three dimensional analysis of reaction propagation in a module with 10 cells in series was carried out (Figure III- 43). In the

simulated module, 10 large cylindrical cells are inserted into an insulator block holder and most of the inter-cell heat transfer occurs through electric connectors.

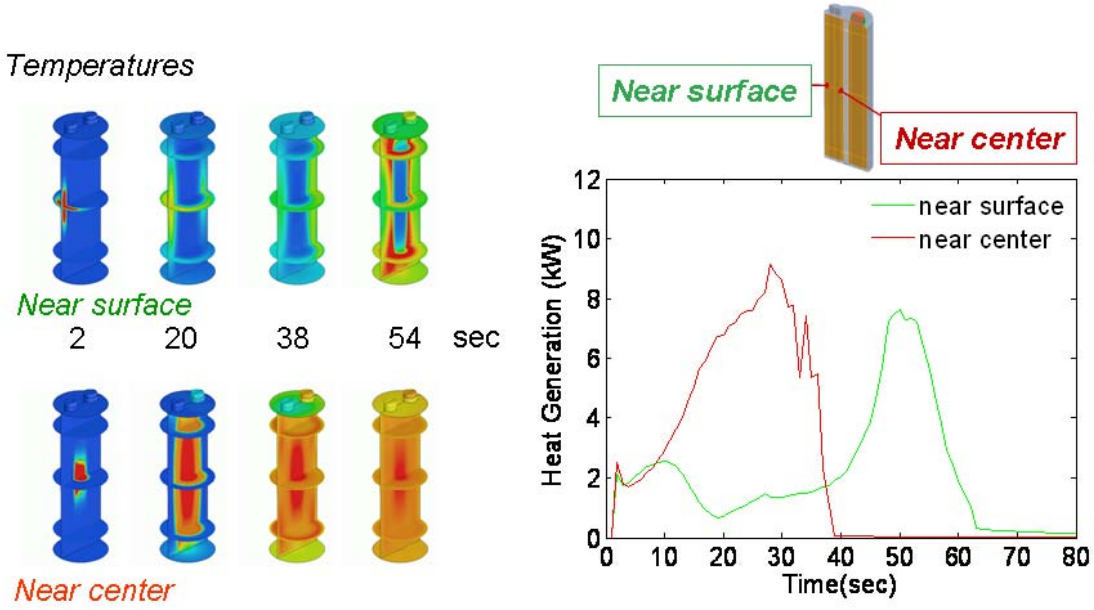

Figure III- 42. Comparison of exothermic reaction propagation for location of internal short

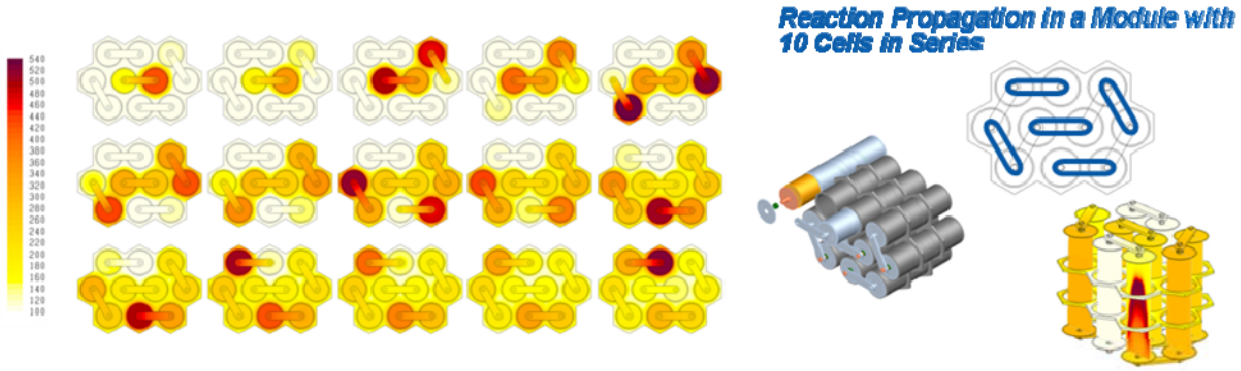

Figure III- 43. 3D model analysis for reaction propagation in a module with 10 cells in series

The team has been developing an understanding of how the amount of heat released at an internal short depends on materials, configuration, and cell size. Both SNL data and the thermal abuse model indicated that some internal shorts may not lead to thermal runaway. This could be likely with high resistance short. The impact of heat release rates for high resistance shorts was examined in 18650 cells using the electrochemical cell model. It is observed from the high resistance short simulation that a relatively low C rate short current is determined by the short resistance rather than by the power rate or by the size of a cell and the external heat transfer becomes critical because of relatively slow heat release rate.

III.E Cell-Level Cost Reduction

Objectives

- Identify and secure advanced low-cost cell materials from material suppliers and evaluate samples for high-power HEV applications and report most promising materials to the USABC-sponsored industrial battery developers.
- Investigate methods to improve the performance and stability of existing anode and cathode materials.
- Develop lower-cost high-power cell materials/chemistries and conduct evaluations to establish their viability.

Approach

- Secure samples of the most advanced materials from material suppliers worldwide.
- Refine rapid screening test protocols. Employ protocols to evaluate material capabilities, provide feedback to the material suppliers.
- Produce cells from the most promising materials and conduct preliminary evaluations on their performance, life, and safety characteristics, using sealed prismatic cells.
- Prepare electrodes with nano-phase coatings and characterize their capacity, power, and stability.

Accomplishments/Findings

- ANL has been developing a high-energy battery system based on a new high capacity fluorinated cathode material. $Li[Li_{0.2}Ni_{0.15+0.5z}Co_{0.10}Mn_{0.55-0.5z}]O_{2-z}F_z$ with 10% fluorine added delivered a reversible capacity of ~250 mAh/g (about 70% higher than conventional Li cobalt oxide), and no capacity fade was observed after 40 cycles at 55°C.
- Several advanced Materials from Asia were studied including $Li_{1+w}[Ni_xCo_yMn_z]_{1-w}O_2$ (NCM) from Toda Kogyo and $LiFePO_4$ from Mitsui Engineering Shipbuilding (MES). Overall, NCM type materials and their modifications from Toda Kogyo demonstrate high-power capability but with appropriate Ni doping can achieve 200mAh/g.

Future Studies

- Please see Section III.F for a description of the planned activities in the ABR program.

III.E.1 Introduction

Since the beginning of this program, researchers have been searching for lower cost cell materials and components that possess enhanced stability. These materials include: electrode active materials, conductive additives for the positive electrode, electrode binders, electrolyte salts, electrolyte solvents, and electrolyte additives. Where it makes sense to do so, a limited amount of internal R&D is performed to develop more stable materials (primarily in terms of electrolyte components and positive electrode materials). Recently, ANL has been investigating a relatively new AlF_3 coating that appears to stabilize the cathode active material leading to enhanced high temperature stability, better power, and enhanced abuse tolerance. ANL has performed all of the work in this area.

III.E.2 High Voltage Cathodes and Advanced Cathode Coatings

Advanced High-Energy Cathode Material (Amine) – The near term target of a 10-mile all-electric range for a mid-size SUV requires 3.4 kWh, which may be achieved using conventional cathodes. To achieve a 40 mile all-electric range PHEV, there is a need for a very high energy density chemistry. ANL has been developing a new high capacity fluorinated cathode material, $Li[Li_{0.2}Ni_{0.15+0.5z}Co_{0.10}Mn_{0.55-0.5z}]O_{2-z}F_z$. The new material provides a very high capacity of 250 mAh/g, ~70% higher than conventional $LiCoO_2$. Figure III- 44 shows the XRD patterns of $Li[Li_{0.2}Ni_{0.15+0.5z}Co_{0.10}Mn_{0.55-0.5z}]O_{2-z}F_z$ with varying concentrations of fluorine. The patterns can be indexed based on the α-$NaFeO_2$–type structure ($R\bar{3}m$) with small extra peaks at 20~23°, which are generally attributed to ordering of Li and Mn in the transition-metal layers. Generally, the structure of the fluorinated materials remained on the α-$NaFeO_2$–type structure ($R\bar{3}m$) with slight increases on the lattice parameters, and the cation mixing between Li and Ni increases with the content of fluorine.

Figure III- 45 shows the capacity retention of $Li(Li_{0.2}Ni_{0.15+0.5z}Co_{0.10}Mn_{0.55-0.5z})O_{2-z}F_z$, materials which have 20% excess Li in the transition metal layer. These cells were cycled between 2.8 V and 4.6 V at room temperature. The material without fluorine had the highest initial discharge capacity, but the capacity retention was poor (~25% loss after 40 cycles at room temperature). When 2% fluorine was added, the material had a slightly lower initial discharge capacity (~225 mAh/g), but no capacity fade over 40 cycles. It is also clear that the initial discharge capacity of the materials greatly suffered when more than 5% fluorine was doped. An activation process was also observed for the materials with high fluorine content, i.e. z=0.10. It is possible that the full discharge capacity of $Li(Li_{0.20}Ni_{0.20}Co_{0.10}Mn_{0.5})O_{1.9}F_{0.1}$ (z=0.10) was not reached after 40 cycles, and the actual capacity retention of this material can only be accessed for longer test period. Alternatively, the evaluation can be carried out at a higher temperature to accelerate the activation process. Figure III- 46 shows the capacity retention of $Li/Li(Li_{0.20}Ni_{0.15+0.5z}Co_{0.10}Mn_{0.55-0.5z})O_{2-z}F_z$ (z=0, 0.02, 0.05, and 0.10 respectively) at 55ºC. The activation process for the high-fluorine-content materials was completed in less than 5 cycles.

The material with high fluorine content (z=0.10) has a lower initial discharge capacity. Figure III-46 shows that the capacity retention increases with fluorine content. When 10 % fluorine was added, the material delivered a reversible capacity of ~250 mAh/g, and no capacity fade was observed after 40 cycles at 55ºC.

Figure III- 47 shows the ASI at 60-80% SOC of graphite/$Li[Li_{0.2}Ni_{0.15+0.5z}Co_{0.10}Mn_{0.55-0.5z}]O_{2-z}F_z$ cells. The ASI for the graphite/$Li[Li_{0.2}Ni_{0.2}Mn_{0.6}]O_2$ cell is also shown. When adding 10% Co to $Li[Li_{0.2}Ni_{0.2}Mn_{0.6}]O_2$, the ASI drops significantly from 290 to 150 Ω-cm^2. This is because cobalt trivalent induces a mixed valence in the system resulting in an increased electrical conductivity. However, when adding less than 5% fluorine to the material, the impedance is reduced to 65Ω-cm^2. This study allows one to optimize the fluorine concentration in the composite electrode material to 5% molar.

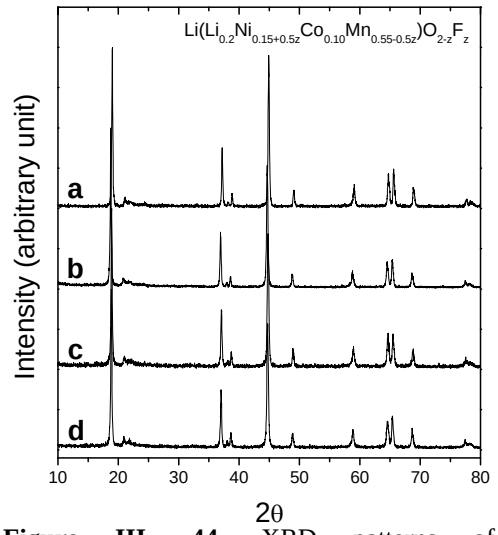

Figure III- 44. XRD patterns of $Li[Li_{0.2}Ni_{0.15+0.5z}Co_{0.10}Mn_{0.55-0.5z}]O_{2-z}F_z$. a, z=0; b, z=0.02; c, z=0.05; d, z=0.10.

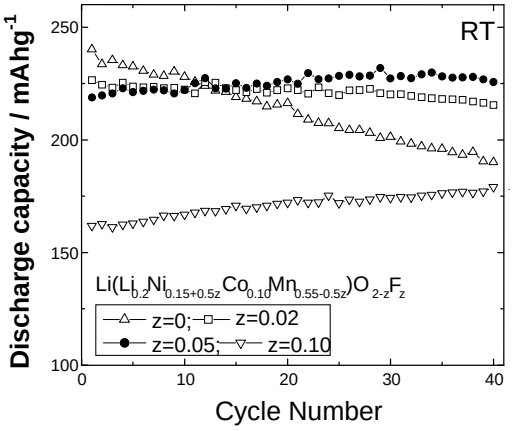

Figure III- 45. Discharge capacity during cycling of $Li/Li[Li_{0.2}Ni_{0.15+0.5z}Co_{0.10}Mn_{0.55-0.5z}]O_{2-z}F_z$ cells cycled between 2.0-4.6V at room temperature.

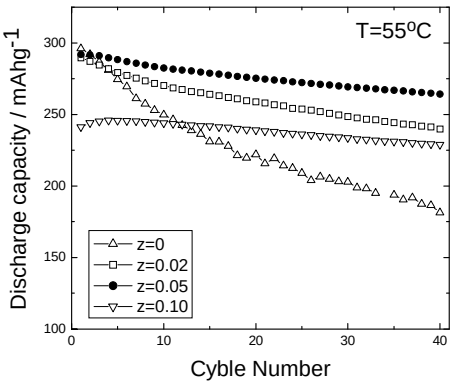

Figure III- 46. Discharge capacity of Li/Li[$Li_{0.2}Ni_{0.15+0.5z}Co_{0.10}Mn_{0.55-0.5z}$]$O_{2-z}F_z$ cells in the voltage range of 2.0-4.6V as a function of cycle number at 55ºC.

It should be noted that some of fluorine may have reacted at the surface with Mn and Ni to form manganese fluoride and nickel fluoride which could play a protective role against surface reactions and thus further improve the cycle life. Figure III- 48 compares the DSC of the $LiNi_{0.8}Co_{0.15}Al_{0.15}O_2$ charged to 4.2V and that of the Li[$Li_{0.2}Ni_{0.175}Co_{0.10}Mn_{0.525}$]$O_{1.95}F_{0.05}$ charged to 4.6V. The amount of heat generated from the fully charged high capacity electrode even when charged to a much higher voltage (4.6V) is much less than $LiNi_{0.8}Co_{0.15}Al_{0.15}O_2$. Also, the onset temperature of the reaction using the high-energy composite cathode is much higher which indicates the improved stability of this material. This is because the material has a low amount of highly reactive tetravalent nickel when charged which is usually unstable and tends to quickly reduce, releaseing oxygen from the cathode as in $LiNi_{0.8}Co_{0.15}Al_{0.15}O_2$. Furthermore, the presence of a large amount of tetravalent manganese in the system further stabilizes the material in the fully charged state. In conclusion, the new high energy density composite electrode could be a promising cathode material for 40 mile PHEVs and EVs.

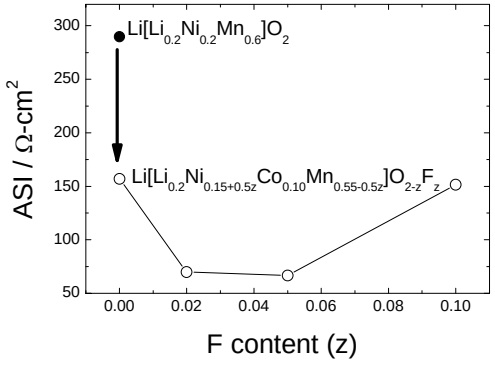

Figure III- 47. Average ASI at 60-80% SOC measured with graphite/ Li[$Li_{0.2}Ni_{0.15+0.5z}Co_{0.10}Mn_{0.55-0.5z}$]$O_{2-z}F_z$ cells as a function of fluorine content. The solid circle is the ASI measured with graphite/Li[$Li_{0.2}Ni_{0.2}Mn_{0.6}$]O_2 cell.

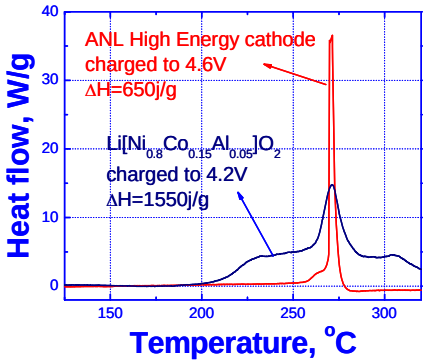

Figure III- 48. DSC curves of $Li[Li_{0.2}Ni_{0.175}Co_{0.10}Mn_{0.525}]O_{1.95}F_{0.05}$ charged to 4.6V and $LiNi_{0.8}Co_{0.015}Al_{0.05}O_2$ charged to 4.2V

One of the current drawbacks of this cathode is the low tap density because the material is made either by the sol-gel or hydroxide process, which results in the formation of a porous material. As a result, the loading of the active material is very low which affects the electrode capacity. The main target in future work is to develop processes that: 1) significantly improve the tap density of the material to at least to 2.2 and 2) tune the process to obtain spherical uniform particles with high homogeneity and similar composition at the particle level. Furthermore, we would also focus on improving the rate capability of this material to meet PHEV requirements.

III.E.3 Advanced Materials from Asia

$Li_{1+w}[Ni_xCo_yMn_z]_{1-w}O_2$ (NCM) from Toda Kogyo (Jansen) – $Li_{1+w}[Ni_xCo_yMn_z]_{1-w}O_2$ (NCM) has been identified as a promising cathode material for HEV/PHEV applications due to its high-power, high-energy, good thermal stability, and long cycle life. This program has been continuing to investigate NCM materials from different vendors for better understanding and to indentify the most promising candidates in this class. A total of five NCM materials from Toda Kogyo were received and tested recently. The material information is shown in Table III- 10. NCM refers to Ni, Co, and Mn and the three digit number refers to three transition metal compositions, respectively. For instance, NCM111 means the ratio of Ni:Co:Mn is 1:1:1. "F" stands for fluorination.

Table III- 10. Toda Kogyo $Li_{1+w}[Ni_xCo_yMn_z]_{1-w}O_2$ Material Summary

Sample		BET	D50	Tap density	Capacity mAh/g		Coulombic efficiency	HPPC ASI
producer	ID	m^2/g	μm	g/cm^3	charg-1	disch-1	%	ohm-cm^2
Japan	NCM111	0.39	6	2.43	169.72	148.65	87.59	43.8
	NCM523	0.23	10.2	2.37	191.26	162.53	84.98	28.5
	NCM622	0.22	10.8	2.61	201.18	166.76	82.89	28.5
Germany	NCM111	0.59	8	2.4	170.00	147.33	86.66	33.9
	NCM111/F	0.36	8.2	2.3	181.70	159.88	87.99	36.1

The specific capacity was tested using Li/NCM half cells, cycled between 3.0 V and 4.3 V at C/10. From Table III- 10, it can be seen that high specific capacity can be obtained with NCM622 due to its high Ni content. According to MAG10/NCM full cell results, the NCM523 and NCM622 also show comparable power capability (see 10 sec ASI results at 50% DOD from 2032 coin cell in

Table III- 10) to Gen2 and Gen3 cathode materials. These two materials also show very good cycleability as shown in Figure III- 49.

On the other hand, Toda Germany NCM materials show improved cycle life of the fluorinated NCM material (Figure III- 50). There is no significant increase in the ASI for the fluorinated NCM111. Toda Kogyo is also working on high density cathode materials, which may further improve the energy density.

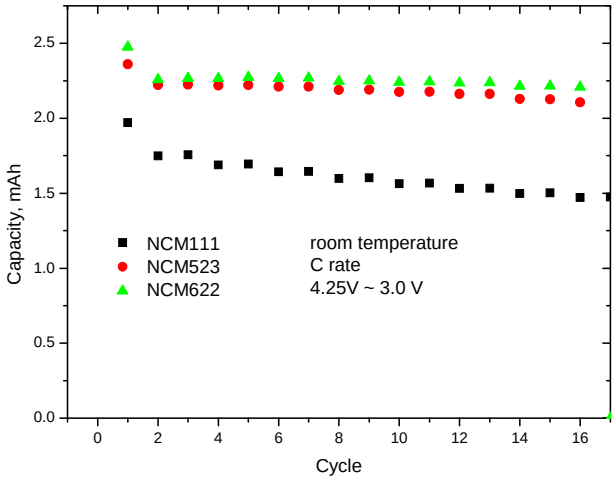

Figure III- 49. Cycling data of NCM from Toda Japan (2032 coin cell)

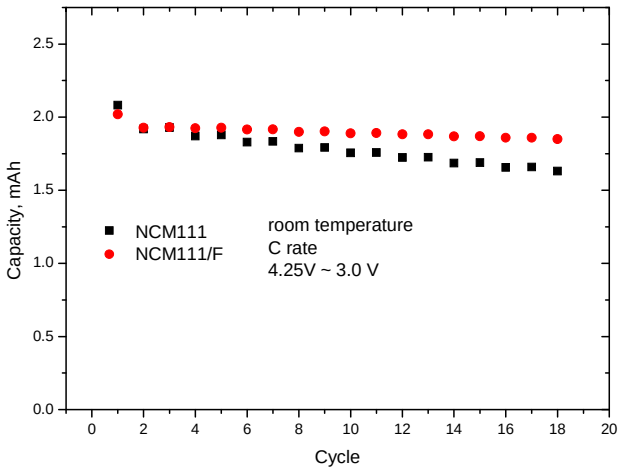

Figure III- 50. Cycling data of NCM from Toda Germany (2032 coin cell)

According to these screening results and previous work, the energy density can be improved if the Co amount is reduced, which would also.reduce its cost. It is also found that fluorination can improve cycle life without a detrimental effect on the power. Therefore, the fluorinated Ni rich NCM material should have a better chance to meet the requirements for HEV/PHEV application and will be evaluated in the future.

$LiFePO_4$ from Mitsui Engineering Shipbuilding (MES) (Jansen) -Another activity in this area is to screen $LiFePO_4$ for HEV application, because it is one of the most thermally stable cathode materials. Unfortunately, $LiFePO_4$ has a relatively low power capability due to its lower electronic conductivity and sluggish Li-ion diffusion. The electronic conductivity of the composite electrode has been addressed successfully by carbon coating. Improvements in the Li-ion diffusion have been attempted by doping or particle size reduction.

Submicron carbon-coated $LiFePO_4$ was received from Mitsui Engineering Shipbuilding (MES) Co. Ltd. The primary particle size (D50) of this material is ~0.1μm and the secondary particle size is ~1.2 μm. The carbon coating is ~5.6 wt. % with roughly 2~3nm thickness. The specific capacity, from a Li/$LiFePO_4$ half cell at C/10, was determined to be 160mAh/g with less than 5% ICL between 3.0 and 3.8V. The 10 C HPPC was carried out on a MAG10/$LiFePO_4$ 2032 coin cell. The 10 second ASI result, shown in Figure III- 51, indicates that carbon coated submicron $LiFePO_4$ has excellent power capability. Currently, MES is working on reduction of the carbon coating to increase the energy density. MES also is investigating a new synthetic process and alternative precursor to reduce the cost. ANL will continue monitoring their development process and test this potential candidate for HEV/PHEV application.

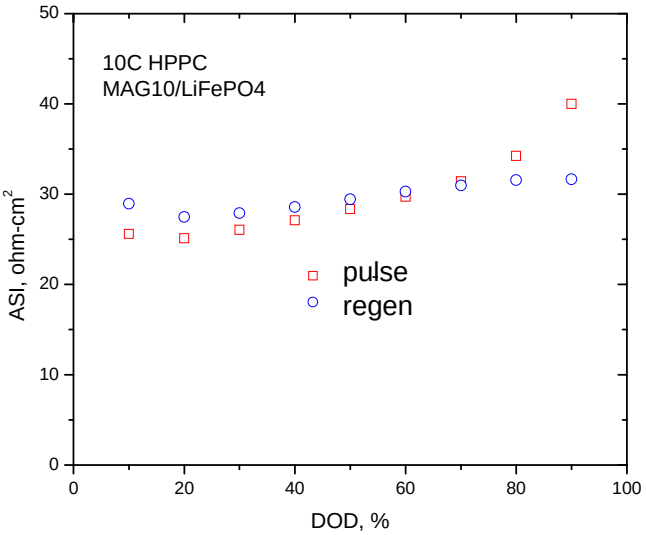

Figure III- 51. ASI plot of submicron carbon coated $LiFePO_4$ in 2032 coin cell

III.F Applied Battery Research for Transportation Program – A Look Ahead at High-energy Battery R&D

Through FY 2008, DOE's applied R&D program, entitled Applied Technology Development (ATD), has been focused on assisting battery developers overcome the key barriers for the Li-ion battery technology in high-power HEV applications. Li-ion battery technologies have matured to the level where they are expected soon to be introduced into the commercial HEV market. Therefore, DOE's applied battery R&D program is being shifted to focus on Li-ion battery technologies for PHEV applications. This new program, denoted the Applied Battery Research (ABR) for Transportation Program, was initiated on October 1, 2008. The goal of this program is to assist the industrial developers of Li-ion batteries to overcome the key barriers for this technology in the high-energy PHEV application. Although DOE's PHEV battery R&D program is relatively new, there is general agreement on the major barriers for Li-ion batteries in this application. These new barriers are:

- Adequate energy density and specific energy to meet the "charge-depleting" energy requirement, within the weight and volume constraints, for the 40-mile all-electric-range for a mid-size passenger PHEV
- Sufficient cycle life stability to achieve the 5,000 "charge-depleting" deep discharge cycles

Also, this new deep-discharge mode of operation and the need for much greater on-board energy could make it more challenging for Li-ion batteries to meet the extended calendar life and the adequate abuse tolerance requirements. Additionally, meeting the cost target ($300/kWh) is another major challenge for this technology. The new program organization is illustrated in Figure III- 52.

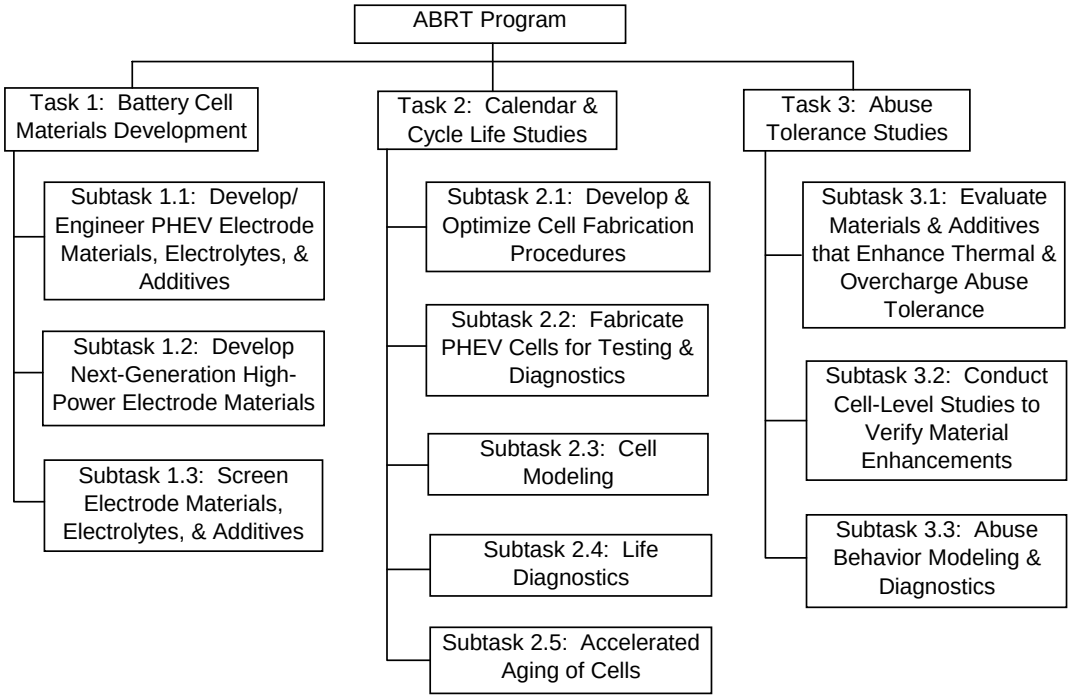

Figure III- 52. Organization of DOE's new ABR Program.

Task 1- The Battery Cell Materials Development task becomes the cornerstone of this program because it addresses the need for new higher energy and more stable materials. Materials R&D under Subtask 1.1 will focus on high-energy anode and cathode materials, as well as electrolyte systems that are stable to higher voltages. Also, this subtask will include R&D on electrolyte additives that stabilize Li-ion cell chemistries at higher voltages. Subtask 1.2 is included in the new program to retain the ability to study new and novel high-power materials that could improve the performance or reduce the cost of Li-ion batteries in HEV applications in a revoluationary way. Subtask 1.3 provides the vehicle for evaluating new materials that are developed outside and inside this program, as well as the mechanism for evaluating all of these new advanced materials on a common basis. The advanced high-energy materials being developed under this new program are ones that offer a reasonable probability of being developed within a 5-year timeframe. Results obtained under Subtask 1.3 will serve as the basis for selecting the new advanced materials and cell chemistries that will be studied more thoroughly under Task 2.

Task 2- The Calendar and Cycle Life Studies task serves as the program element for conducting accelerated aging, detailed diagnostics, and transport modeling of the most promising new materials and cell chemistries. Effective collaborations between the diagnostics and modeling subtasks will facilitate the understanding and mitigation of life-limiting mechanisms for the different cell chemistries studied. Additionally, an in-house capability is being developed to produce sealed cells of adequate quality to facilitate these accelerated aging studies.

Task 3- The Abuse Tolerance Studies task serves as the program element for conducting studies on new cell materials that can help stabilize Li-ion cell chemistries to thermal abuse and overcharge conditions. Further, it provides validation of abuse tolerance enhancements at the cell level, as well as modeling of the abuse behavior of cells and batteries that employ various materials and cell chemistries. Effective collaborations among all three subtasks will facilitate the development of credible abuse models for different cell chemistries.

ANL is the lead laboratory for this new program and will participate in most of the subtasks. BNL will provide diagnostic studies related to structural changes that occur in bulk and near the surface of electrodes that are aged under these PHEV deep cycling conditions. INL will provide testing support for the accelerated aging of cells and electrolyte modeling support to the cell transport modeling. LBNL will provide diagnostic support to help quantify changes that occur in the electrodes and the electrode passivation films during aging, to assist in the determination of aging mechanisms. NREL will develop the abuse behavior models, with input from Argonne and Sandia. SNL will fabricate cells for abuse testing and conduct the cell-level abuse studies to validate the improvements in inherent abuse tolerance established by Argonne at the materials level. Also, the Army Research Laboratory (ARL) will support this program in the area of developing electrolyte systems that are stable at higher voltages.

The annual report for the next fiscal year will summarize the work accomplished on this new Applied Battery Research for Transportation Program during its initial year of existence.

Applied Battery Research Publications

1. A. Jansen, D. Dees, D. Abraham, K. Amine, and G. Henriksen, "Low-Temperature Study of Li-ion Cells using a LiSn Micro-Reference Electrode," JPS[10] 174 (2007) 373.
2. B. Xie, H. Lee, H. Li, X. Yang, J. McBreen, and L. Chen, "New electrolytes using Li_2O or Li_2O_2 oxides and tris(pentafluorophenyl) borane as boron based anion receptor for lithium batteries," Electrochemistry Communications 10 (8) (2008) 1195-1197.
3. B. Park, H. Kim, S. Myung, K. Amine, I. Belharouak, S. Lee, and Y. Sun, "Improvement of structural and electrochemical properties of AlF_3-coated $Li[Ni_{1/3}Co_{1/3}Mn_{1/3}]O_2$ cathode materials at high voltage region," JPS, in press (2008).
4. D. Dees, E. Gunen, D. Abraham, A. Jansen, and J. Prakash, "Electrochemical Modeling of Li-ion Positive Electrodes during Hybrid Pulse Power Characterization tests," JECS[11] 155 (2008) A603.
5. D. Abraham, J. Heaton, S. Kang, D. Dees, and A. Jansen, "Investigating the Low-Temperature Impedance Increase of Li-ion Cells," JECS 155 (2008) A41.
6. D. Abraham, M.M. Furczon, S. Kang, D. Dees, and A. Jansen, "Effect of electrolyte composition on initial cycling and impedance characteristics of Li-ion cells," JPS 180 (2008) 612.
7. D. Abraham, S. Kawauchi, and D. Dees, "Modeling the Impedance versus Voltage Characteristics of $LiNi_{0.8}Co_{0.15}Al_{0.05}O_2$," Electrochimica Acta 53 (2008) 2121.
8. D. Dees, A. Jansen, and D. Abraham, "Theoretical Examination of Reference Electrodes for Li-ion Cells," JPS 174, (2007) 1001.
9. E. Roth, D. Doughty, and D. Pile, "Effects of separator breakdown on abuse response of 18650 Li-ion cells," JPS 174(2), 579-583 (2007)
10. H. Kim, B. Park, S. Myung, K. Amine, and Y. Sun, "Improvement of Electrochemical Performance of AlF_3-coated $Li[Ni_{0.8}Co_{0.15}Al_{0.05}]O_2$ Cathode Materials," JPS, in press (2008).
11. I. Belharouak, W. Lu, D. Vissers, and K. Amine, "Safety Characteristics of the $Li_4Ti_5O_{12}/LiMn_2O_4$ Li-ion Battery," Mater. Res. Soc. Proc. 972 (2007) 339-344.
12. J. Liu, Z. Chen, S. Busking, and K. Amine, "Lithium Difluoro(oxalato)borate as a Functional Additive for Li-ion Batteries," Electrochem. Commun. 9(3) (2007) 475-479.
13. J. Liu, Z. Chen, S. Busking, I. Belharouak, and K. Amine, "Improved Graphite/$Li_{1.1}[Ni_{1/3}Co_{1/3}Mn_{1/3}]_{0.9}O_2$ Li-ion cells Containing Additives," JPS, in press, (2007).
14. K. Amine, Z. Chen, and S. Kang, "Impacts of Fluorine on the Electrochemical Properties of $Li[Ni_{0.5}Mn_{0.5}]O_2$ and $Li[Li_{0.2}Ni_{0.15}Co_{0.1}Mn_{0.55}]O_2$," J. Fluor. Chem. 128(4) (2007) 263-268.
15. K. Lee, H. Bang, S. Myung, J. Prakash, and K. Amine, "Synthesis and Electrochemical properties of spherical spinel $Li_{1.05}M_{0.05}Mn_{1.9}O_4$ (M = Mg and Al) as a cathode material for Li-ion batteries by co-precipitation method," JPS, in press (2008).
16. K. Lee, S. Myung, K. Amine, and Y. Sun, "Structural and Electrochemical Properties of Layered $Li[Ni_{1-2x}Co_xMn_x]O_2$ (x=0.1–0.3) Positive Electrode Materials for Li-ion Batteries," JECS 154 (2007) A971.
17. K. Nam, K. Kim, E. Lee, W. Yoon, X. Yang, and K. Kim, "Pseudocapacitive properties of electrochemically prepared nickel oxides on 3-dimensional carbon nanotube film substrates," JPS 182 (2008) 642.
18. K. Chung, W. Yoon, J. McBreen, X. Yang, S. Oh, H. Shin, W. Cho, and B. Cho, "*In situ* X-Ray Diffraction Studies on the Mechanism of Capacity Retention Improvement by Coating at the Surface of $LiCoO_2$," JPS 174(2) (2007) 619.
19. L. Li, H. Lee, H. Li, X. Yang, K. Nam, W. Yoon, J. McBreen, and X. Huang, "New electrolytes for lithium ion batteries using LiF salt and boron based anion receptors," JPS, 184(2) (2008) 517-521. (DOI information: 10.1016/j.jpowsour.2008.03.016.)
20. S. Ma, K. Nam, W. Yoon, X. Yang, and K. Kim, "A Novel Concept of Hybrid Capacitor Based on Manganese Oxide Materials," Electrochemistry Communications 9 (12) (2007) 2807-2811.
21. S. Kang, and D. Abraham, "Preparation and Examination of Binder- and Carbon-Free Electrodes used in Li-ion Cells," JPS 174 (2007) 1229.
22. S. Kang, D. Abraham, W. Yoon, K. Nam, and X. Yang, "First-cycle irreversibility of layered Li–Ni–Co–Mn oxide cathode in Li-ion batteries," Electrochimicl Acta, (in print).
23. S. Kang, W. Yoon, K. Nam, X. Yang, and D. Abraham, "Investigating the first-cycle irreversibility of lithium metal oxide cathodes for Li batteries," J. Mater Sci 43 (2008) 4701–4706. (DOI 10.1007/s10853-007-2355-6.)

[10] JPS = Journal of Power Sources
[11] JECS = Journal of the Electrochemical Society

24. S. Park, S. Oh, S. Kang, I. Belharouak, and Y. K. Sun, "Comparative study of different crystallographic structure of $LiNi_{0.5}Mn_{1.5}O_4-\delta$ cathodes with wide operation voltage (2.0–5.0 V)," Electrochimica Acta 52 (2007) 7226.
25. S. Kang, D. Abraham, A. Xiao, and B. Lucht, "Investigating the solid electrolyte interphase using binder-free graphite electrodes," JPS 175 (2008) 526.
26. S. Woo, C. Yoon, K. Amine, I. Belharouak, and Y.K. Sun, "Significant Improvement of Electrochemical Performance of AlF_3-coated $Li[Ni_{0.8}Co_{0.1}Mn_{0.1}]O_2$ Cathode Materials," JECS. 154(11) (2007) A1005-A1009.
27. V. Thomas, I. Bloom, J. Christophersen, and V. Battaglia, "Statistical methodology for predicting the life of Li-ion cells via accelerated degradation testing," JPS 184 (2008) 312-317.
28. W. Lu, I. Belharouak, J. Liu, and K. Amine, "Electrochemical and Thermal Investigation of $Li_{4/3}Ti_{5/3}O_4$ Spinel," JECS 154(2) (2007) A114.
29. W. Lu, I. Belharouak, S. Park, Y. Sun, and K. Amine, "Isothermal Calorimetry Investigation of $Li_{1+x}Mn_{2-y}Al_zO_4$ Spinel," Electrochimica Acta 52 (2007) 5837–5842.
30. W. Lu, Z. Chen, H. Joachin, J. Prakash, J. Liu, and K. Amine, "Electrochemical Characterization of MCMB/$LiNi_{1/3}Mn_{1/3}Co_{1/3}O_2$ Using LiBOB as an Electrolyte Additive," JPS 163 (2007) 1074.
31. W. Yoon, K. Chung, J. McBreen, D. Fischer, and X. Yang, "Electronic Structural Changes of the Electrochemically Li-ion Deintercalated $LiNi_{0.8}Co_{0.15}Al_{0.05}O_2$ Cathode Material Investigated by X-ray Absorption Spectroscopy," JPS 174(2) (2007) 1015-1020.
32. W. Yoon, K. Chung, J. McBreen, D. Wang, X. Huang, L. Chen, and X. Yang, "Electronic Structural Changes of the Electrochemically Delithiated $LiFe_{0.5}Co_{0.5}PO_4$ Cathode Material studied by X-ray Absorption Spectroscopy," JPS 183(1) (2008) 427-430.
33. Y. Sun, S. Cho, S. Myung, K. Amine, I. Belharouak, and J. Prakash, "Effect of AlF_3 Coating Amount on High Voltage Cycling Performances of $LiCoO_2$," Electrochimica Acta, in press (2008).
34. Y. Sun, S. Cho, S. Lee, C. Yoon, and K. Amine, "Improvement of High Voltage Cycling Performance of AlF_3-coated $Li[Ni_{1/3}Co_{1/3}Mn_{1/3}]O_2$ Cathode Materials for Lithium Secondary Batteries," JECS 154(3) (2007) A168-A172.
35. Z. Chen, and K. Amine, "Bifunctional Electrolyte Additive for Li-ion Batteries," Electrochem. Commun. 9(4) (2007) 703.
36. Z. Chen, J. Liu, and K. Amine, "Lithium Difluoro(oxalato)borate as New Salt for Li-ion Batteries," Electrochem. Solid-State Lett. 10(3) (2007) A45-A47.

Presentations

1. E. Roth, "Abuse Response of 18650 Li-ion Cells with Different Cathodes Using EC:EMC/$LiPF_6$ and EC:PC:DMC/$LiPF_6$ Electrolytes," Transactions of 212th ECS Meeting, Oct. 7-12, 2007.
2. E. Roth, "Effect of Cathode Composition on Abuse Response of 18650 Li-ion Cells," Proceedings of the 43rd Power Sources Conference, July 7-10, 2008.
3. E. Roth, "Thermal Response and Flammability of Li-ion Cells for HEV and PHEV Applications," Proceedings of the SAE 2008 World Congress, Apr. 14-15, 2008.
4. G. Kim, A. Pesaran, and K. Smith, "Thermal Abuse Modeling of Li-Ion Cells and Propagation in Modules," 4th International Symposium on Large Lithium Ion Battery Technology and Application in conjunction with the 8th AABC, Tampa, FL, May 2008.
5. G. Kim, K. Smith, A. Pesaran and R. Spotnitz, "Analysis of Thermal Behavior of Li-Ion Batteries using Thermal Abuse Reaction Model," 212th Electrochemical Society Meeting, Washington DC, October 2007.
6. G. Kim, K. Smith, and A. Pesaran, "Li-Ion Thermal Abuse Model," The 77th Li- Battery Technical/Safety Group Meeting, San Diego, Feb 2008.
7. X. Yang, H. Lee, W. Yoon, K. Nam, J. McBreen, L. Li, B. Xie, Z. Liu, H. Li, X. Huang, and L. Chen, "New High Voltage Electrolyte Systems For Li-ion Batteries Using LiF or Li_2O with Boron-Based Lewis Acids as Additives," Invited, 1st International Conference on Advanced Lithium Batteries for Automobile Applications, Argonne National Laboratory, Argonne, Illinois, USA 60439, September 15-17, 2008.
8. X. Yang, H. Lee, H. Li, W. Yoon, K. Nam, J. McBreen, X. Huang, and L. Chen, "Boron-Based Lewis Acids as Additives in LiF and $LiBO_4$ Based Electrolytes and their potential to be Used in High Voltage Li-ion Batteries," Invited, 2007 meeting of International Battery Materials Association (IBA2007), November 20, 2007, Shenzhen, China.
9. X. Yang, H. Lee, L. Li, Bin Xie, H. Li, W. Yoon, K. Nam, J. McBreen, X. Huang, and L. Chen, "New LiF or Li_2O based Electrolytes Using Boron-Based Lewis Acids as Additives," Invited, 14th International Meeting of Lithium Batteries" (IMLB 2008), June 20-27, 2008, Tianjin, China.

10. X. Yang, H. Lee, W. Yoon, K. Nam, J. McBreen, L. Li, B. Xie, H. Li, X. Huang, and L. Chen, "Boron-Based Lewis Acids as Additives in LiF Based Electrolytes and Their potential to be Used in High Voltage Li-ion Batteries," Invited, presented at the Advanced Automotive Battery and Ultracapacitor Conference and Symposia, May 12-16, 2008 – Tampa Convention Center, Tampa, Florida.
11. X. Yang, H. Lee, W-S. Yoon, K. Nam, J. McBreen, L. Li, B. Xie, H. Li, X. Huang, and L. Chen, "The Interfacial Studies of Lithium Battery Materials at Nano-scale," Invited, presented at The 2008 International Workshop on Nano Materials, Devices and Physics properties, Institute of Physics, Chinese Academy of Sciences, Beijing, China, July 1 to July 3, 2008, Beijing, China.
12. X. Yang, W. Yoon, K. Nam, H. Lee, J. McBreen, H. Li, X. Huang, L. Chen, J-M. Chen, K. Chung and B. Cho, "Structural Stability and Safety Related Issues of Electrode Materials for Lithium Batteries Studied by Synchrotron Based X-ray," Invited, The 48th Battery Symposium in Japan, November 13-15, 2007, Fukuoka, Japan.

Milestone Report:

1. G. Kim, K. Smith, and A. Pesaran, "Model Analysis for Lithium-Ion Battery Safety," NREL Deliverable Report in fulfillment of DOE Milestone, July 2008.

Patent:

1 patent issued and 2 patents applied for.

IV. FOCUSED FUNDAMENTAL RESEARCH

The focused fundamental research program, also called the Batteries for Advanced Transportation Technologies (BATT) program, is supported by the DOE's Vehicle Technologies program (DOE-VT) to research and analyze new materials for high-performance, next generation, rechargeable batteries for use in HEVs, PHEVs, and EVs. The effort in 2008 continued the increased emphasis on high energy materials for PHEV and EV applications.

Background and Program Context

The BATT Program addresses the fundamental problems of chemical and mechanical instabilities that have impeded the development of automotive batteries with acceptable cost, performance, lifetime, and safety. The aim is to identify and better understand cell and material performance and lifetime limitations before initiating battery scale-up and development. Emphasis is placed on the synthesis of components into cells with determination of failure modes, while continuing with materials synthesis and evaluation, advanced diagnostics, and improved model development. Battery chemistries are monitored continuously with timely substitution of more promising components. This is done with advice from within the BATT Program and from outside experts, including consultation with automotive companies and DOE. Also factored into the BATT Program direction is the monitoring of world-wide battery R&D activities. The Program not only supports research that leads to incremental improvements to existing materials, but also into high-risk "leap-frog" technologies that might have a tremendous impact in the marketplace.

The work is administered by the Lawrence Berkeley National Laboratory (LBNL), with principal researchers from LBNL, four additional laboratories, eleven universities, and one commercial company (see Appendix A). The program is organized into the following areas:

IV.A New Cathode Systems, Performance and Limitations
- *IV.A.1 Phosphate Systems*
- *IV.A.2 Layered Systems*
- *IV.A.3 Mn Spinel and Spinel Composite Systems*

IV.B New Anode Materials

IV.C Novel Electrolytes and their Characterization,

IV.D Li-Ion Modeling, Diagnostics, and Cell Analysis

This section summarizes the research activities of this program in FY 2008. The website for the BATT Program is found at http://berc.lbl.gov/BATT/BATT.html. Brief descriptions of each research area are as follows.

- The ***Phosphate Systems*** area concentrates on iron phosphate, a moderate energy, low (material) cost, and abuse tolerant material; and higher energy Mn phosphate materials. This task includes studies of capacity and power, lower cost synthesis methods, and the impact of processing steps on performance. Finally, researchers are theoretically and experimentally investigating on the impact of carbon coatings on performance.
- The ***Layered Systems*** work includes the $LiNi_{1/3}Mn_{1/3}Co_{1/3}O_2$ (called NMC) cathode material that, with a carbon-coated graphite anode, is a high-energy cell that can be engineered to provide good power. This task aims to understand the failure and

degradation modes in the NMC and other such systems using cell builds, cell cycling, advanced diagnostics, and modeling.

- The ***Mn Spinel Systems*** provides good high-rate capability and improved abuse tolerance over nickelates. This task aims to understand the failure and degradation modes using various material doping, cell cycling, and advanced diagnostics. This work also includes the composite, high voltage, high-energy cathode materials that promise a significant increase in both capacity and voltage over current materials.
- The ***New Anode Materials*** task aims to find improved anode materials that offer at least twice the volumetric and specific energy of graphite. Researchers are investigating composite negative electrodes containing one (or more) metal components within a graphite matrix, for example C/Sn, C/Si, and C/Sb systems, and nano-composite alloys.
- The ***Novel Electrolyte Materials*** task involves investigating the limitations of polymers, ionic liquids, and single-ion conducting gels which promise low cost and abuse tolerant batteries. Post-test analyses and spectroscopic and microscopic techniques are used to investigate morphology, structure, and compositional changes of electrode materials.
- The ***Modeling, Diagnostics, and Cell Analysis*** tasks involve the use of advanced diagnostics techniques, such as FTIR, X-ray absorption fine structure (XAFS), XRD, nuclear magnetic resonance (NMR) and other techniques, to investigate interfacial and other properties in Li-ion batteries. Several modeling approaches are used to understand cell and fundamental material properties, including *ab-initio* calculations, macroscopic cell calculations, and finite element simulations. Finally, standard cell making and testing techniques are developed and applied to provide a common evaluation process for new materials.

IV.A New Cathode Systems, Performance and Limitations

IV.A.1 $LiFePO_4$ and other Phosphate Systems: Performance and Limitations

OBJECTIVES

The overall objectives in these tasks are to understand the effect of structure on the stability and performance of the phosphates, to explore rate limitations and their relation to structure and particle size/morphology, to use this information to improve the performance of promising phosphate materials, and to develop more cost effective synthesis routes.

APPROACH

Employ XRD, *in situ* microscopy, vibrational spectroscopies, and electroanalytical techniques to determine the applicability and reason for the specific performance of the materials. Use NMR and diffraction to characterize material structures as a function of particle size, sample preparation method, SOC, and number of charge cycles. Use calculations and NMR spectroscopy to identify low activation energy pathways for cation migration and to investigate electronic conductivity.

For the PPy and PANI conductive additive work, select a conductive polymer that is electrochemically active in the voltage range of the cathode redox center, develop a convenient synthetic route to achieve and maintain electrical contact of polymer with all individual nanoparticles and with the current collector and compare electrochemical versus chemical synthetic routes and test performance.

ACCOMPLISHMENTS

Simulations of $LiMnPO_4$ Material Properties (Ceder, Grey) – As part of an investigation into nano-scale effects on the electrochemical behavior of phosphates, this team investigated surface energies, equilibrium particle morphology, and surface redox potentials for $LiMnPO_4$. Surfaces of different orientations of the olivine structure were studied with first-principles calculations. The calculated surface energies and resulting equilibrium Wulff shape[12] of the particle of $LiMnPO_4$ are quite similar to $LiFePO_4$. Only six of the fifteen surfaces considered appear in the Wulff shape, Figure IV- 1(a). These low energy surfaces are in the (1 0 0), (0 1 0), (0 1 1), (1 0 1), (2 0 1), and (2 1 0) orientations. Three low energy surfaces, (0 1 0), (0 1 1) and (2 0 1), dominate and contribute about 87% of the total surface area. As in $LiFePO_4$ the (010) surface, important for Li insertion, takes up large fraction of the surface area.

Calculated surface redox potentials for the extraction/insertion of Li from various surfaces range from 3.20 to 4.18V, compared to a calculated Li redox potential of 4.0 V in the bulk. Most of the surfaces have a Li redox potential lower than the bulk value, except for (1 0 0) and (0 1 1). The (0 1 0) surface has the lowest surface redox potential of 3.20 V; therefore, Li is expected to be extracted first from this surface. However, the large difference between the Li redox potential in the (0 1 0) surface layers and the bulk creates a high energy barrier of about 0.8 eV for bulk Li to diffuse out of the $LiMnPO_4$ particle. Figure IV- 1(b) schematically shows the energy landscape for the Li migration along the [0 1 0] channel. Moreover, this energy barrier in $LiMnPO_4$ is 0.2 eV higher than in $LiFePO_4$, which may contribute to the relatively poor kinetics of $LiMnPO_4$.

Phosphate Cathode Performance (Richardson) – The team has earlier shown how specific axes of the metal phosphates are critical to the material's performance. In particular, in $LiFePO_4$, diffusion across the b-axis dominates the material's performance; once the ac surface is converted to $FePO_4$, the underlying $LiFePO_4$ is inaccessible. It is now addressing the challenge of improving the rate, utilization, and stability of $LiMnPO_4$ by studying the inherent properties of the phases involved. Working with hydrothermally prepared crystals, it was found that un-substituted $LiMnPO_4$ crystals undergo severe decrepitation (Figure IV- 2) and a decrease in crystallographic domain size, although the only new phase was $MnPO_4$. This suggests that the high degree of lattice strain and Jahn-Teller effects around Mn^{3+} result in fragmentation of the newly formed $MnPO_4$ and consequent "chemical grinding". This may explain the difficulty of obtaining theoretical capacities in electrodes containing micron-sized particles.

[12] A Wulff shape is an equilibrium minimal surface for a crystal or material particle which has the least anisotropic surface free energy for a given volume.

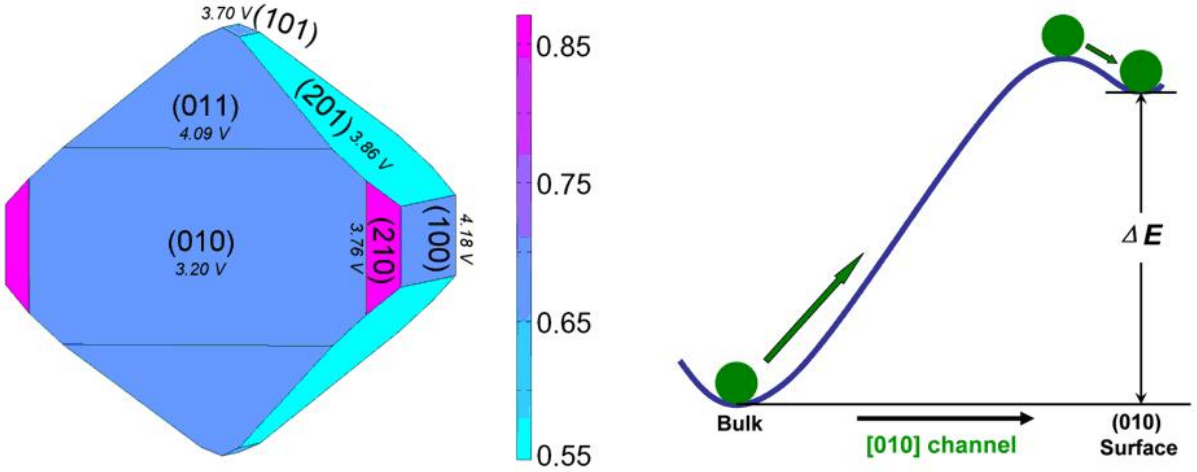

Figure IV- 1. (Left) Wulff shape of $LiMnPO_4$ using calculated surface energies in fifteen directions. The color bar on the right gives the energy scale of the surface in unit of J/m^2. The numbers below the Miller indexes provide the redox potential to extract Li at that surface. (Right) Energy landscape for Li migration along the [010] diffusion channel.

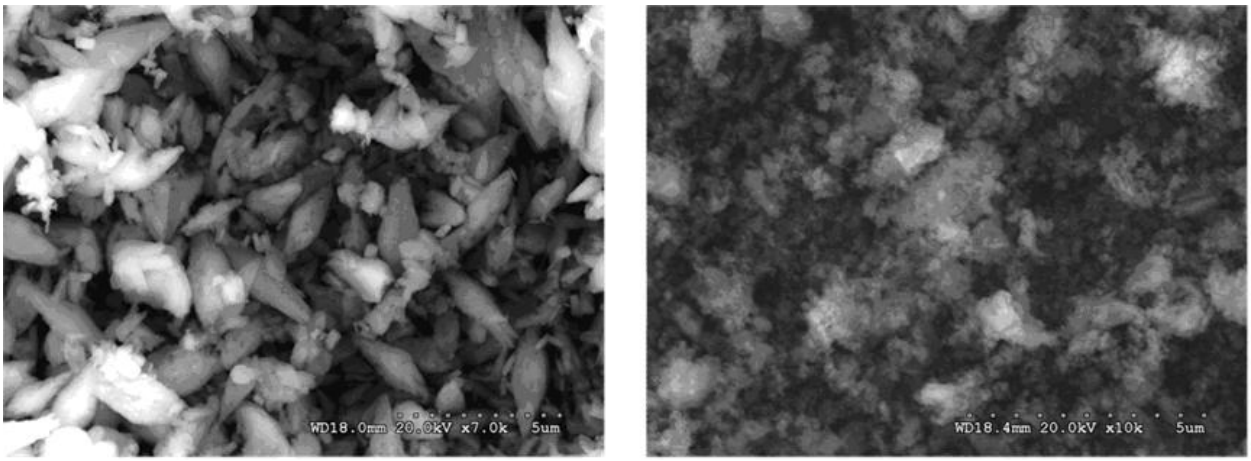

Figure IV- 2. SEM images of $LiMnPO_4$ crystals a) before and b) after chemical delithiation

$LiMg_xMn_{1-x}PO_4$ crystals with x=0.1, 0.2, 0.4 and 0.5 were prepared by the hydrothermal method. The size and shape of the crystals varied with Mg content as shown at left in Figure IV- 3. The use of $Mg(NO_3)_2$ as a precursor instead of sulfate resulted in slight changes in pH of the synthesis solutions, which decreased from 10.0 for x=0.1 to 9.0 for x=0.5. When the Mn source was $Mn(NO_3)_2$, the unsubstituted $LiMnPO_4$ was obtained as smaller, discrete crystals rather than the large aggregates prepared using $MnSO_4$. This sample also showed better reactivity during chemical oxidation and reduction. When $LiMg_xMn_{1-x}PO_4$ samples were chemically oxidized, the percentage and crystalline domain size of the delithiated phases were found to increase with the amount of oxidant present. All of the substituted samples showed improved performance and reduced decrepitation compared to $LiMnPO_4$. The best performance was for x=0.2, with 30% conversion and 18 nm domain size of the delithiated phase when treated with 50 mol% of NO_2BF_4. There appears to be some relation between stability of the delithiated crystals and their dimensions in the *a* crystallographic direction, which may affect the strain between the oxidized and reduced phases within them (we have shown that the phase boundaries lie in the *bc* plane).

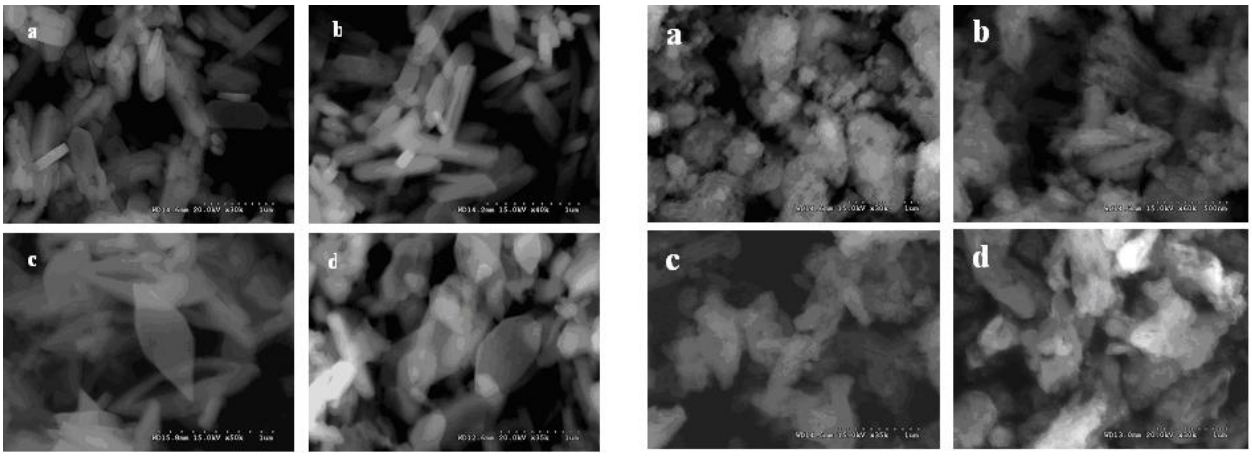

Figure IV- 3. SEM images of fresh (left) and oxidized (right) $LiMg_xMn_{1-x}PO_4$: a) x=0.1, b) x=0.2, c) x=0.4 and d) x=0.5.

To compare these results with electrochemical charging, electrodes were fabricated by ball milling $LiMg_{0.1}Mn_{0.9}PO_4$ and $LiMnPO_4$ crystals with 20 wt% carbon black, then mixing with 10 wt% Poly(vinylidene fluoride) (PVdF), 5 wt% SFG-6 graphite, and an additional 5 wt% acetylene black. The slurries were spread onto carbon-coated Al current collectors and dried at 120°C *in vacuo* for 10 h. Swagelok cells with Li foil anodes and reference electrodes were charged potentiostatically at 4.5 V. The specific current profiles for the two cells are shown in Figure IV- 4 (left). The substituted electrode exhibited higher currents throughout the 20 h of charging, delivering nearly 120mAh/g of active material despite its lower theoretical capacity, 157mAh/g as seen in Figure IV- 4(right). The unsubstituted electrode delivered only about 75mAh/g (theoretical capacity 171mAh/g).

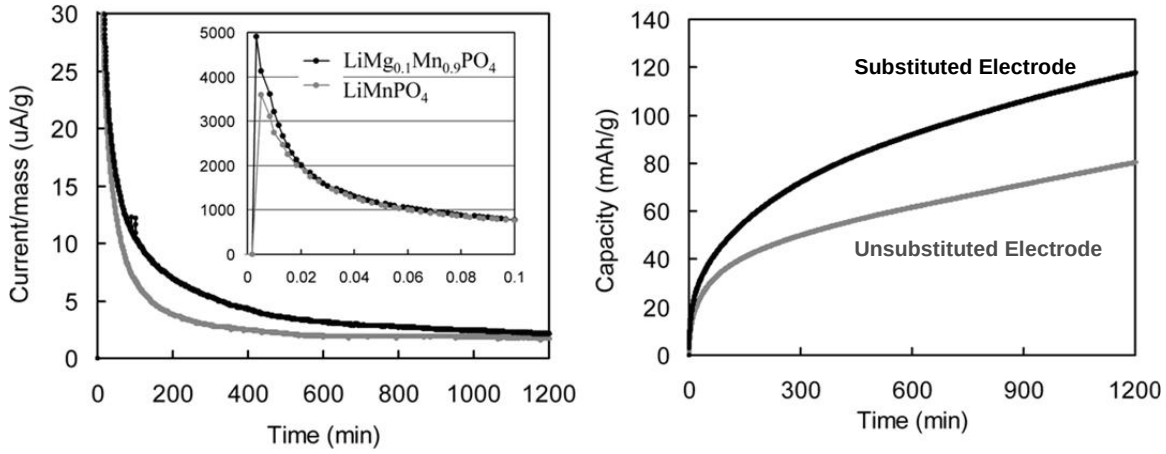

Figure IV- 4. Electrochemical behavior of $MnPO_4$ and Mg-doped $MnPO_4$. (Left) Charging current at 4.5 V, (Right) capacity vs. time at 4.5V.

Synthesize Nano-$LiMnPO_4$ and/or $Li(Mn,Fe)PO_4$ (Doeff) – A combustion method for synthesizing nanoparticulate $LiMnPO_4$ and $LiMg_yMn_{1-y}PO_4$/C composites was developed. In this technique, nitrate and phosphate precursors are dissolved in water and citric acid is added. The solution is heated until combustion occurs. The resulting powders are either partially or fully

amorphous, but undergo crystallization to the desired phase after a short calcination period at 600°C. The fuel:nitrate ratio determines the combustion temperature (which in turn affects the carbon structure and conductivity) and the carbon content. Figure IV- 5 shows a transmission electron microscopy (TEM) image of a $LiMg_{0.1}Mn_{0.9}PO_4$ particle with a carbon coating, produced by the combustion method.

Electrochemical characterization of these materials is carried out in Li half-cells. Best results have been obtained for $LiMg_{0.2}Mn_{0.8}PO_4$ although utilization is still much less than theoretical. Most cells improve upon cycling (sometimes by as much as 50%), probably due to the increased wetting of the carbon coatings by the electrolyte. There is no obvious relationship between the amount of carbon in the composite and electrochemical performance. Interestingly, some of the materials deliver the same discharge capacity regardless of the current density used (from C/25 to C/2 rates). These observations suggest that the poor utilization is due to agglomeration of the nanoparticles and problems with sample homogeneity, rendering a significant portion of the material electrochemically inaccessible. However, a fraction of the material is unagglomerated and shows good electrochemical behavior.

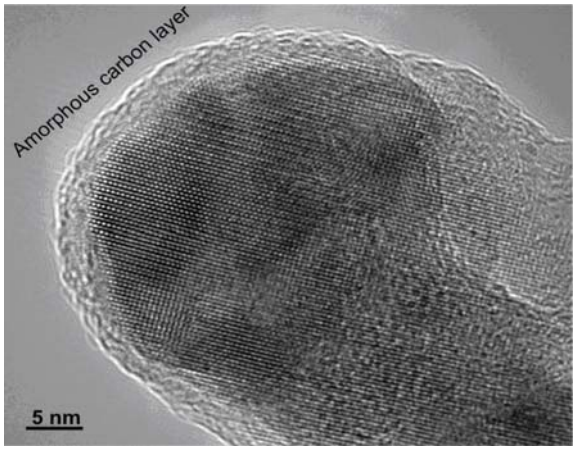

Figure IV- 5. TEM image of a $LiMg_{0.1}Mn_{0.9}PO_4$/C composite, showing carbon coating.

Conductive Polymers (Goodenough) – This team previously clarified the synthetic techniques and obtained the performance of the C-$LiFePO_4$ (LFP) composite cathodes with polypyrrole (PPy) and polyaniline (PANI) prepared *via* two different routes: electrodeposition and simultaneous chemical polymerization. Recent work focused on the fast charging performance of the C-LFP/polymer composite cathodes, an electrodeposition technique for the C-LFP/PANI composite, and a synthetic technique for NMC/ polymer composite cathodes.

All the composite cathodes show an enhanced charging rate capability especially at high rates compared with C-LFP/C/PTFE. The electrodeposited C-LFP/PPy composite exhibits the best fast-charging performance, reaching 94% of full capacity after charging at 10C. Furthermore, this composite shows a good electrochemical reversibility while it is charged and at the same time discharged at a high rate.

Nano-Phosphate Processing (Manthiram) – This team has developed a novel microwave-solvothermal (MW-ST) approach that offers highly crystalline $LiFePO_4$ nanorods

within 5 minutes at temperatures as low as 300°C without requiring any inert atmosphere or post annealing. The width and length of the nanorods can be controlled by altering the reaction conditions (*e.g.*, reactant concentration). Subsequent encapsulation of these nanorods within a mixed electronically and ionically conducting *p*-toluene sulfonic acid (*p*-TSA) doped poly(3,4-ethylenedioxythiophene) (PEDOT) at ambient temperatures offers a discharge capacity of 166mAh/g, close to the theoretical value (170mAh/g), with excellent rate capability and capacity retention, Figure IV- 6(left). Subsequent networking of the nanorods with multi-walled carbon nanotubes (MWCNT) offers similar capacity with excellent cyclability and rate capability, Figure IV- 6(right). Also, the rate capability is found to increase with decreasing dimension of the nanorods, illustrating the influence of Li diffusion length on rate capability. The team has also developed an analogous microwave-hydrothermal method (MW-HT) employing water as a solvent to obtain $LiFePO_4$ nanorods within 15 minutes at 230°C. An *ex situ* carbon coating applied by heating sucrose and $LiFePO_4$ at 700°C and an *in situ* carbon coating obtained by the MW-HT process in the presence of glucose followed by heating at 700°C also give excellent cyclability and rate capability.

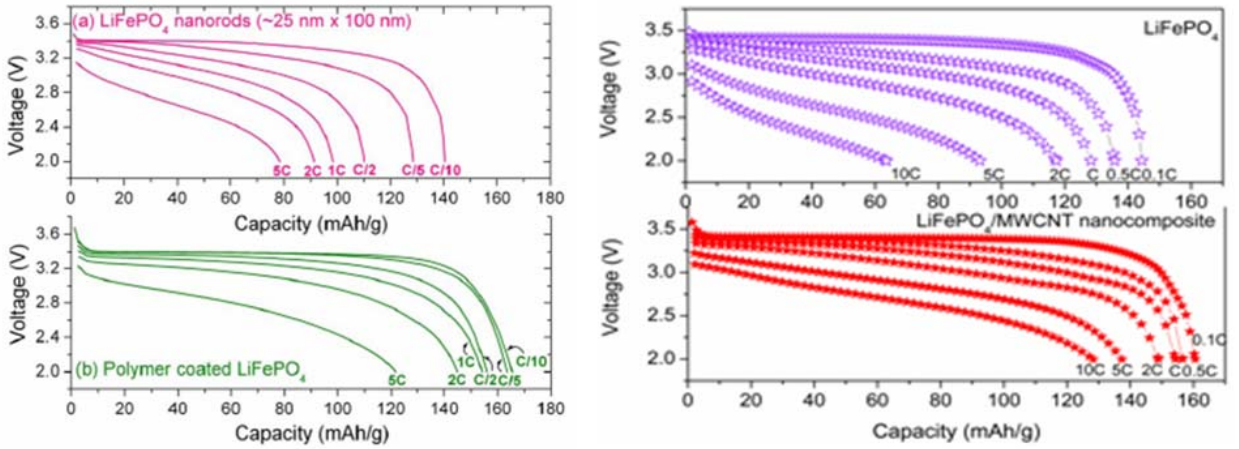

Figure IV- 6. (Left) Comparison of the rate capability of $LiFePO_4$ nanorods before and after coating with a mixed ionically and electronically conducting polymer. (Right) Comparison of the rate capability of $LiFePO_4$ nanorods before and after networking with multi-walled carbon nanotubes (MWCNT).

Low Cost Synthesis of Lithium Iron Phosphate (Whittingham) – Since 2000, this group has explored low cost routes to the formation of the $LiFePO_4$, specifically using hydrothermal techniques, which do not involve heating the reactants above 200°C. It is the group's understanding that Hydro-Québec is now commercializing this hydrothermal method for the olivine.

Substituted Metal Phosphates (Whittingham) – This work continues the exploration of other phosphate structures that might have a higher capacity than $LiFePO_4$. Two structures being considered are those formed by substitution of all or part of the iron by Mn or V. Earlier this group showed that the vanadium phosphate, H_2VOPO_4, had a higher potential than the olivine structure and was capable of intercalating two Li-ions per redox ion leading to a capacity approaching 250mAh/g.

One structure being considered is $LiVPO_4OH$, which might be isostructural with $LiFePO_4OH$ and be more easily synthesized than $LiVO_4F$. While attempting to synthesize pure specimens

of this composition, nanoforms of vanadium pentoxide have also been evaluated. Nanofibers of the delta form of $H_xV_4O_{10}$•nH_2O were synthesized using the electrospinning used for the nano manganese oxide anode. These nanofibers were then hydrothermally treated to remove the polymer precursors, and heated at 450°C to convert to the water-free, single-sheet V_2O_5 lattice. The first discharge (not shown) shows typical multi-step behavior whereas subsequent discharges show the single-phase behavior expected for V_2O_5. The capacity on cycling is shown in Figure IV- 7, falling from 300 to 250mAh/g after 25 cycles. The challenge is to reduce the fading, which appears to be typical of vanadium oxides.

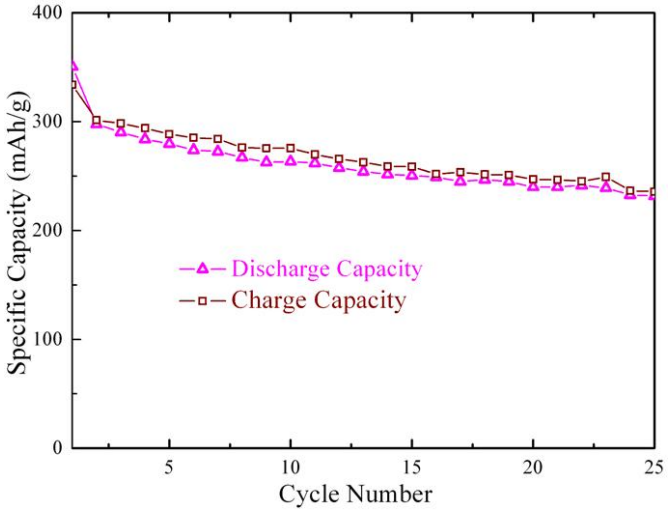

Figure IV- 7. Capacity of nano-sized fibers of vanadium pentoxide. Overcharge is observed on each cycle.

Iron Phosphate Performance and Water Contamination Effects (Zaghib) **–** The resistance of cathodes made with different thicknesses of $LiFePO_4$ and PVdF ranging from 12µm to 100µm has been measured. A four-point probe apparatus was used after calendaring the electrode at 2 g/cc. The results show a linear increase in the electrode resistance with increasing electrode thickness (Figure IV- 8). The electrode resistance shows a maximum at 77 µm.

The impact of water contamination on $FePO_4$ cathodes was also investigated. Materials were dried in vacuum at 120°C, after which they were exposed to 50% relative humidity at 25°C for extended periods of time. The water content was then monitored as a function of time. It was found that $LiFePO_4$ absorbs significant amounts of water in just a few seconds: the material made through the hydrothermal process absorbs more water than that made from the solid-state process; both uncoated and carbon-coated iron phosphate absorbs water, and the water content depends on % carbon in powder. The electrodes could be effectively dried after absorbing water, but the capacity fade was significant and not reversible, increasing with temperature and storage time in the humid environment.

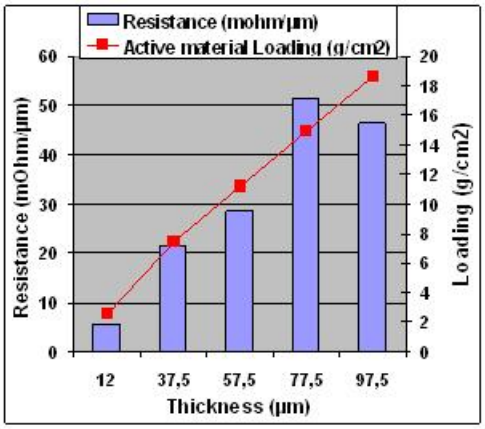

Figure IV- 8. $LiFePO_4$-PVDF electrode resistance as a function of thickness.

IV.A.2 Layered Systems: Performance and Limitations

OBJECTIVES

Find (a) lower-cost and higher-capacity cathodes, exceeding 200mAh/g, and (b) high-rate HEV compatible cathodes, based on environmentally benign materials.

APPROACH

One approach places emphasis on manganese dioxides, both pure and modified with other transition metals, using predominantly low-temperature synthesis approaches. These materials are synthesized and then characterized both structurally and for thermal and chemical stability, and then electrochemically evaluated in a variety of cell configurations.

The surface chemistry and microstructure of oxide-electrolyte interfaces, with and without surface modification and their change as a function of potential and cycle number, are examined by scanning transmission electron microscope (STEM), TEM and XPS. Surface features are correlated to EIS of interfacial processes, cycling data and analysis of intrinsic thermal stability of oxides. This information will be used to design stable interfaces between Li storage particles and electrolyte.

Cathode materials are synthesized and characterized electrochemically, with emphasis on reducing cost and improving electrochemical properties. Relevant physical properties are measured in conjunction with the diagnostics teams. Some work is directed towards surveying new materials with potential for increased energy density.

ACCOMPLISHMENTS

Enhanced Stability during High V Cycling of Li_xCoO_2 with "$AlPO_4$" Coating (Shao-Horn) –
These efforts have been focused on probing the origin of surface instability of Li_xCoO_2 and the enhanced stability associated with $AlPO_4$ coating during high voltages cycling. To understand the physical origin of the enhanced stability of $AlPO_4$-nanoparticle coated $LiCoO_2$ (Figure IV- 9). SEM, XRD and XPS were applied to study the changes in surface chemistry, crystal structure and microstructure upon cycling to 4.7 V and holding at 4.7 V for 4 hours for bare $LiCoO_2$ and "$AlPO_4$"-coated $LiCoO_2$.

Figure IV- 10(a) and (b) show "$AlPO_4$"-coated $LiCoO_2$ particles before and after 20 cycles. Before cycling, coating features are visible on the particle surface. After 20 cycles, in addition to the original coating features, there are many new particles on the surface of coated $LiCoO_2$ while for bare $LiCoO_2$, Figure IV- 10(c) and (d), the surfaces before and after cycling are similar. XPS data reveal the changes in the surface chemistry upon cycling. Figure IV- 10(e), shows new peak formation at a higher binding energy in XPS Co2p region for "$AlPO_4$"-coated $LiCoO_2$ from 1 cycle to 20, which was attributed to CoF_x. In contrast no significant changes were found in Co2p region for the uncoated electrode between cycle 1 and 20, Figure IV- 10(f). This suggests that the environment of Co is steady during cycling, which indicates that bare $LiCoO_2$ directly exposed to the electrolyte during cycling experiences cobalt dissolution, which is responsible for growth of highly resistive surface layers and capacity fading. While for "$AlPO_4$"-coated $LiCoO_2$, the formation of CoF_x species on the surface could trap the Co and effectively decrease its dissolution, which could reduce the growth of highly resistive layers and reduce capacity fading upon cycling.

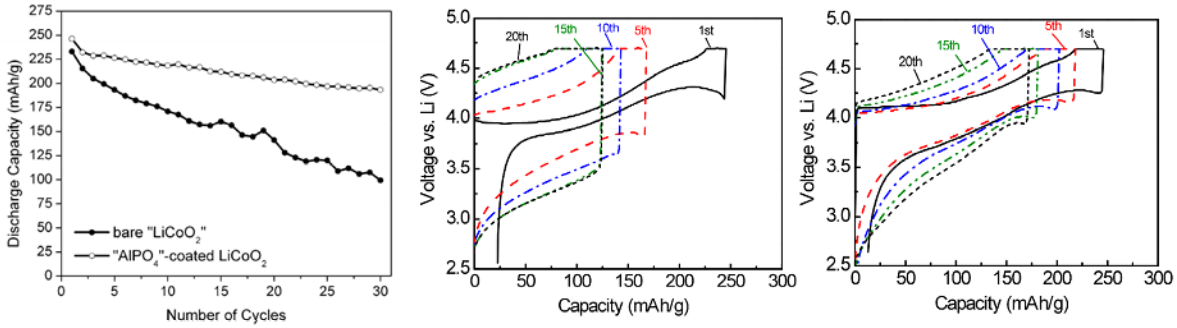

Figure IV- 9. (Left) $AlPO_4$ coated $LiCoO_2$ cathodes exhibit improved cycle life, Appapillai and Shao-Horn et al., Chem Mater, 2007. (center and right) Holding at 4.7 V for 4 hours led to accelerated growth of resistive surface layers, which were examined by SEM, XRD and XPS.

XPS spectra of the O 1s photoemission data (not shown here) reveal, for the bare sample, the appearance of the new peaks after the cycle test. It is hypothesized that the formation and presence of the surface film incorporating -CO and / or -CO_2 groups may result from oxidation of the electrolyte solution with oxygen loss from "bare" Li_xCoO_2 during high-voltage exposure. This surface film could be highly resistive and could impede the Li-ion transfer from the electrolyte solution into the $LiCoO_2$ particles. In contrast, for the coated sample, no significant change of the O 1s photoemission line has been observed.

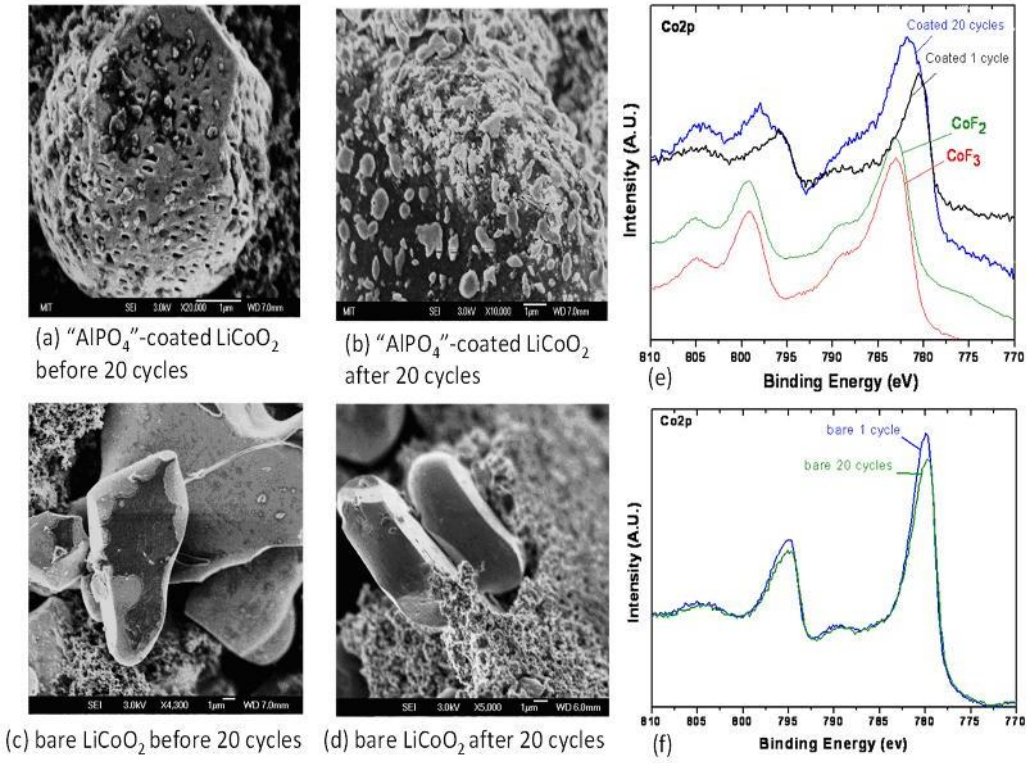

Figure IV- 10. (a)-(d). SEM images of $AlPO_4$-coated and bare $LiCoO_2$ before and after 20 cycles. (e) XPS Co2p region for $AlPO_4$-coated $LiCoO_2$ for 1 cycle (black) and 20 cycles (blue) and the reference spectra collected from CoF_2 and CoF_3. (f) XPS Co2p for bare $LiCoO_2$ for 1 (blue) and 20 (green) cycles.

Stability of $Li_xNi_{0.5}Mn_{0.5}O_2$ at High V (Shao-Horn) – $Li_xNi_{0.5}Mn_{0.5}O_2$ has superior thermal stability to other Li_xNiO_2-related materials based on XRD and TGA data[13]. The taem found 1) a higher onset temperature of oxygen release (~275°C for $Li_{0.2}Ni_{0.5}Mn_{0.5}O_2$, ~100°C higher than $Li_{0.3}NiO_2$ and ~40°C higher than $Li_{0.3}Ni_{0.7}Co_{0.15}Al_{0.15}O_2$) as a result of increased stability of the disordered rhombohedral structure; and 2) reduced oxygen loss as a result of the increased stability of the spinel-type phase to form the rocksalt-type phase upon heating to 600°C. The information not only allows the comparison of intrinsic thermal stability of different electrode materials but also provides new insights into the origin of the electrochemical behavior of $Li_xNi_{0.5}Mn_{0.5}O_2$, and design of new electrode materials with increased thermal stability. For example, the intrinsic stability of $Li_xNi_{0.5}Mn_{0.5}O_2$ structure at low Li contents against oxygen loss is believed key to the good high voltage (~5V) cyclability, Figure IV- 11.

[13] Yabuuchi and Shao-Horn et al. Chemistry of Materials 2008.

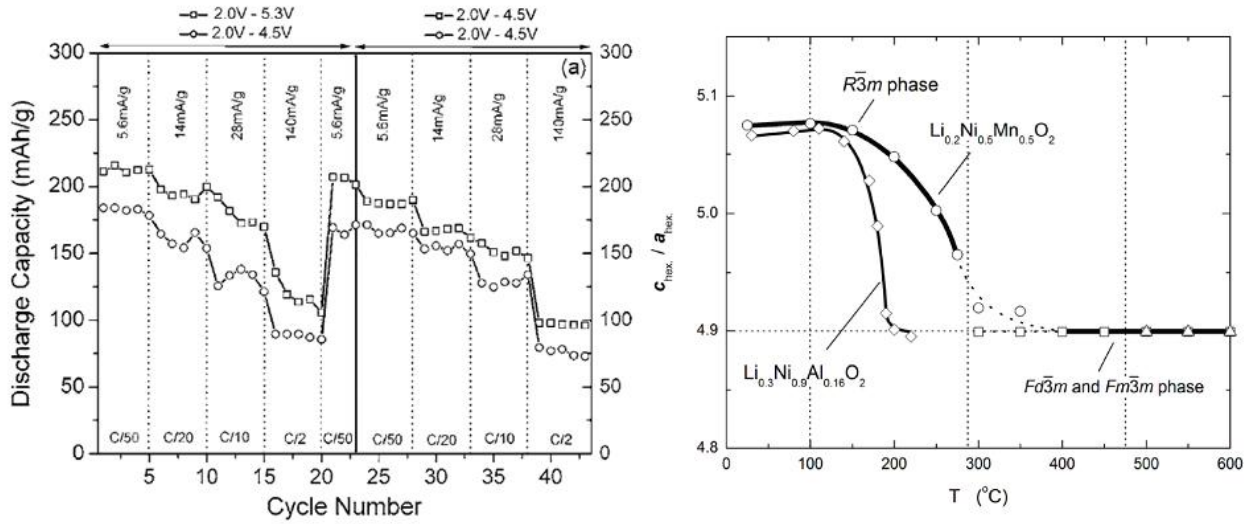

Figure IV- 11. (Left) $Li_xNi_{0.5}Mn_{0.5}O_2$ cycling stability to 4.5V and 5.3V vs. Li and (right) the $c_{hex}./a_{hex}$.ratio of the $Li_xNi_{0.5}Mn_{0.5}O_2$ layered structure vs. heating temperature.

Characterize Substituted Transition Metal Oxides (Doeff) – Partial substitution of Al for Co was previously shown to enhance the rate capabilities of $LiNi_{0.4}Co_{0.2-y}Al_yMn_{0.4}O_2$ substantially, even though Al decreases the electronic conductivity. GITT experiments have been carried out on $Li/LiNi_{0.4}Co_{0.2-y}Al_yMn_{0.4}O_2$ cells and relative diffusion coefficients as a function of SOC have been extracted. For all materials, diffusion coefficients decrease at high SOC. Al-containing materials are generally not delithiated as much as the parent compound on initial charge during normal galvanostatic experiments, thus avoiding the kinetically slow composition regions with low Li content upon subsequent discharges.

Rietveld refinements of XRD patterns and neutron diffraction patterns (Figure IV- 12) indicate that the slab spacing between transition metal oxide layers is increased when Al is substituted for Co. This is thought to lead to enhanced diffusion.

Layered Mixed Metal Oxides (Whittingham) – This work continues the exploration of $Li[NiMnCo]O_2$ compounds with Mn content above that of Ni while maintaining a 10% Co level, specifically compositions between $LiNi_{0.4}Mn_{0.5}Co_{0.1}O_2$ and Li_2MnO_3. A series of compounds with the composition of $Li_{(4-x)/3}Mn_{(2-0.5x)/3}(Ni_{0.4}Co_{0.1})_xO_2$, $0 \leq x \leq 1$ have been prepared and their structural changes, magnetic properties, and heat capacities determined. This structural characterization will allow a better understanding of the interactions between the metal ions and identify the optimum composition for high energy Li-ion cells.

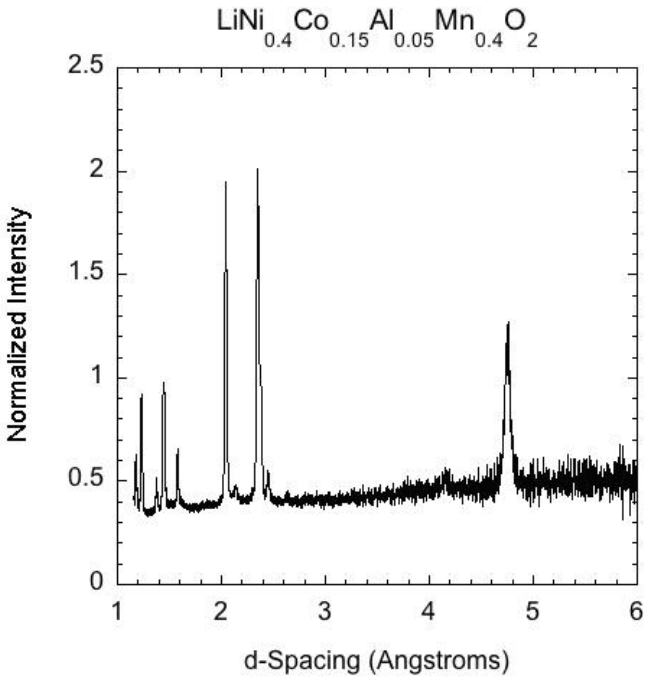

Figure IV- 12. Neutron diffraction pattern of $Li[Ni_{0.4}Co_{0.15}Al_{0.05}Mn_{0.4}]O_2$.

The XRD patterns indicate that the layered structure is maintained over the entire series. The intensities of the satellite peaks become stronger and sharper between 20°-25° with increased amounts of Li and Mn due to the enhanced honey-comb ordering of Li and Mn within the transition metal ™ layers. Rietveld refinement reveals that pure $LiNi_{0.4}Mn_{0.5}Co_{0.1}O_2$ has the largest extent of cation disorder between Li^+ and Ni^{2+} ions, ~6%, suggesting that the excessive amount of Li and Mn helps to suppress the cation exchange. The evolution of the TM ordering in the series using magnetic properties and heat capacities has been investigated.

The temperature dependences of the magnetic susceptibility, Figure IV- 13(a), show that the magnetic moment increases with Mn content as a result of the high effective moment of Mn^{4+} (S=3/2). Field-cooled and zero-field cooled susceptibilities show cluster-glass behavior at the $LiNi_{0.4}Mn_{0.5}Co_{0.1}O_2$ end of series, similar to that observed in compounds with imperfect flower TM order. Spin-glass or paramagnetic state is found in the middle of the series suggesting random TM distribution. An antiferromagnetic transition is found at the Li_2MnO_3 end, which is consistent with honeycomb ordering. The heat capacity data, Figure IV- 13(b), indicate a gradual destruction of the honeycomb ordering with increasing Co and Ni content.

Structural Changes in $Li_{1+x}M_{1-x}O_2$ During Cycling (Yoon, Yang) – To investigate structural changes in $Li_{1+x}(Mn_{0.5}Ni_{0.5})_{1-x}O_2$ during cycling, this group has conducted *in situ* XRD with Dr. Kang at ANL. Figure IV- 14 shows the lattice spacing variations during first charge of $Li_{1.2}(Mn_{0.5}Ni_{0.5})_{0.8}O_2$ as determined from *in situ* XRD. This layered phase shows a contracting "a" axis and an expanding "c" axis in the early stage of charge. The "a" axis continues to decrease until the plateau at ~ 4.6 V is reached, consistent with the change of the TM oxidation state in the *in situ* XAS study on the same electrode. After the 4.6 V plateau is reached, the changes in "a" axis are small until the end of first charge. The "c" axis does not change significantly until the end of

the plateau. At the end of charge, the "c" axis starts to decrease slightly. This structural behavior is somewhat different from that of $xLi_2MnO_3 \bullet (1-x)LiMn_{0.5}Ni_{0.5}O_2$ systems, with a different Mn/Ni ratio.

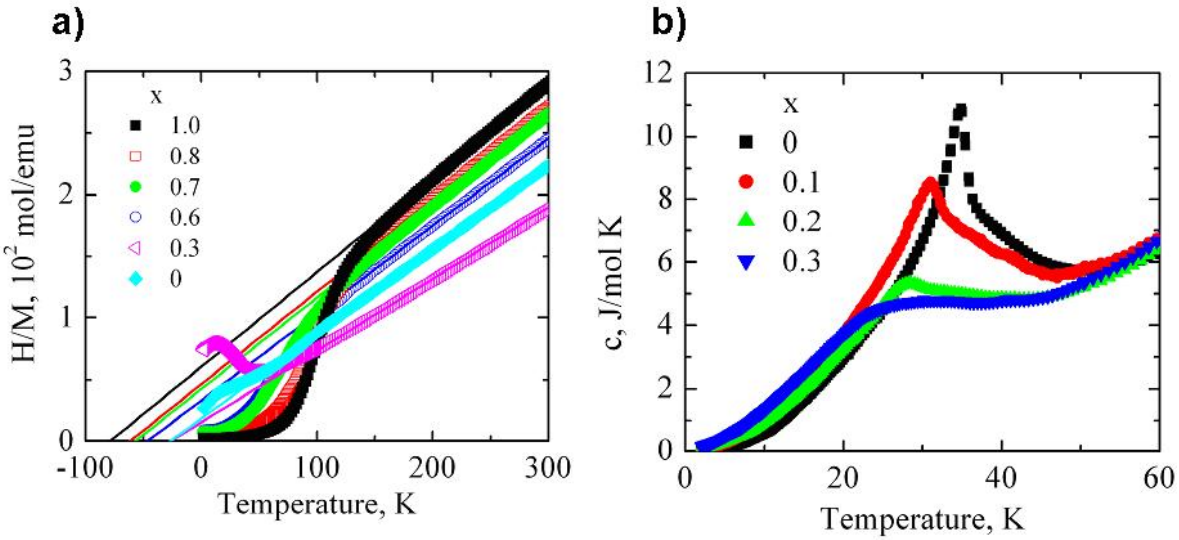

Figure IV- 13. (a) Reciprocal magnetic susceptibilities and their fit to the Curie-Weiss law, and (b) heat capacities of $Li_{(4-x)/3}Mn_{(2-0.5x)/3}(Ni_{0.4}Co_{0.1})_xO_2$.

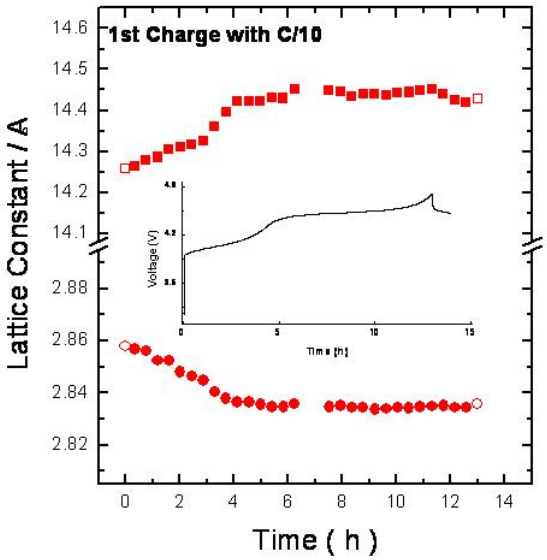

Figure IV- 14. Variations of lattice parameters of $Li_{1.2}(Mn_{0.5}Ni_{0.5})_{0.8}O_2$ during first charging process.

Stabilizing $Li_{(1+x)}(Mn_{0.5}Ni_{0.5})_{1-x}O_2$ (Yoon, Yang) – Excess Li in $Li_{(1+x)}(Mn_{0.5}Ni_{0.5})_{1-x}O_2$ has been found to improve its capacity and cycling stability, as seen in Figure IV- 15. To understand this behavior, *in situ* Mn and Ni K-edge XAS has been carried out during multiple charges/discharges. Figure IV- 16(a) shows the *in situ* Ni K-edge X-Ray absorption near edge structure (XANES) spectra of $Li_{1.0}(Mn_{0.5}Ni_{0.5})_{1.0}O_2$ and $Li_{1.2}(Mn_{0.5}Ni_{0.5})_{0.8}O_2$ electrodes during first charge/discharge.

In situ Ni K-edge XANES spectra of the $Li_{1.0}(Mn_{0.5}Ni_{0.5})_{1.0}O_2$ electrode shows reversible changes in the oxidation state from Ni^{2+} to Ni^{4+} and back to Ni^{2+} during first charge/discharge. However, the average oxidation state of Ni in $Li_{1.2}(Mn_{0.5}Ni_{0.5})_{0.8}O_2$ changes from ~ Ni^{3+} to Ni^{4+} upon first charge, but reduces below Ni^{3+} after first discharge. Thus, the charge compensation range at the Ni ions in the $Li_{1.2}(Mn_{0.5}Ni_{0.5})_{0.8}O_2$ system might progressively expand from Ni^{3+}/Ni^{4+} to the final Ni^{2+}/Ni^{4+} during the extended charge/discharge cycles.

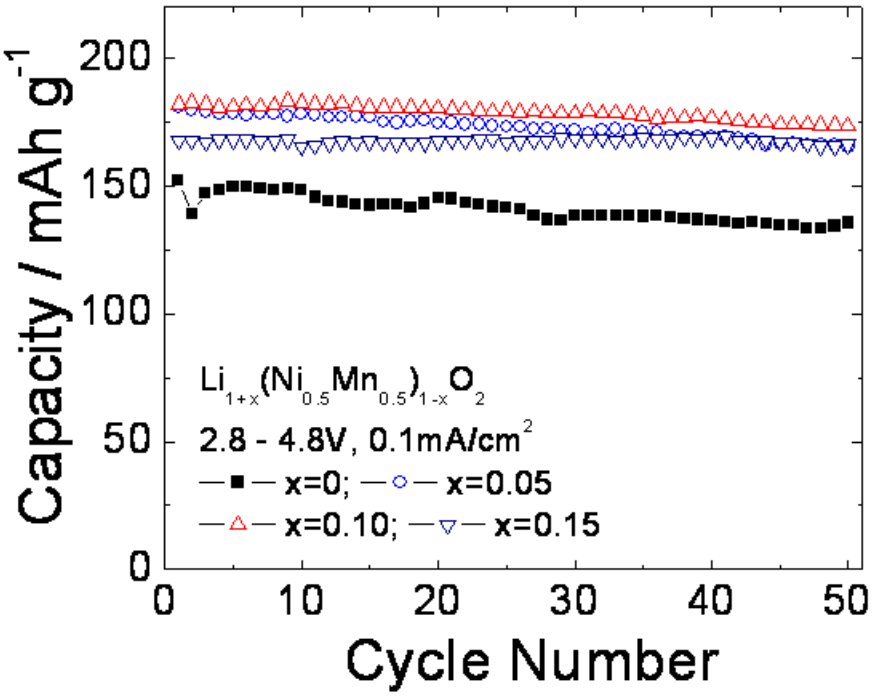

Figure IV- 15. Cycle behavior of $Li_{(1+x)}(Mn_{0.5}Ni_{0.5})_{1-x}O_2$

The active role of Li_2MnO_3 or Li_2MnO_3-like phases in $Li_{1.2}(Mn_{0.5}Ni_{0.5})_{0.8}O_2$ electrode during first charge were also investigated using *in situ* Mn K-edge extended x-ray absorption fine structure (EXAFS) (Figure IV- 16(b) and (c)). Very little change is seen in the local structure around Mn ions for $Li_{1.0}(Mn_{0.5}Ni_{0.5})_{1.0}O_2$. A clearly increased structural disorder around Mn ions, particularly in Mn-O bond, upon first charge is observed in $Li_{1.2}(Mn_{0.5}Ni_{0.5})_{0.8}O_2$. Therefore, the abnormal capacity above 4.5V during first charge could be attributed to the structural rearrangement of Li_2MnO_3 or Li_2MnO_3-like phases, due to e.g., the removal of Li_2O from the system.

Additional analysis of the first charge behavior of $Li_{(1+x)}(Mn_{0.5}Ni_{0.5})_{1-x}O_2$ charged to 4.8 V showed that the electrodes with excess Li have an additional dQ/dVpeak at ~4.5 V, whose intensity increases with Li content. This additional peak is attributed to the activation of Li_2MnO_3 component in the composite structure ($Li_2MnO_3 \rightarrow 2Li+2e+MnO_2+1/2O_2$) as has been commonly observed from $zLi_2MnO_3 \bullet (1-z)Li(Ni_{0.5}Mn_{0.5})O_2$, which is believed to be responsible for the capacity close to or higher than theoretical values.

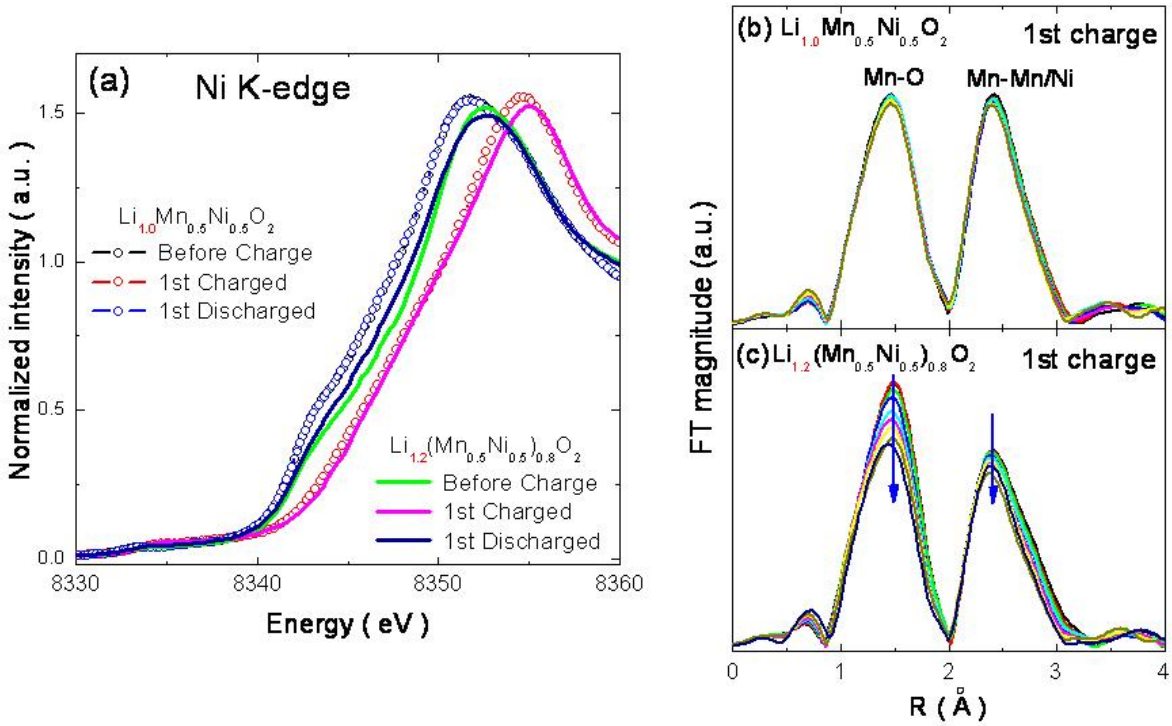

Figure IV- 16. (a) *In situ* Ni K-edge XANES spectra of $Li_{1.0}(Mn_{0.5}Ni_{0.5})_{1.0}O_2$ and $Li_{1.2}(Mn_{0.5}Ni_{0.5})_{0.8}O_2$ during first charge/discharge process; *In situ* Mn K-edge EXAFS spectra of (b) $Li_{1.0}(Mn_{0.5}Ni_{0.5})_{1.0}O_2$ and (c) $Li_{1.2}(Mn_{0.5}Ni_{0.5})_{0.8}O_2$ during first charge.

Effect of Synthesis Conditions on the Performance of $Li_xNi_{0.5}Mn_{0.5}O_2$ (Shao-Horn) – Annealing $LiNi_{0.5}Mn_{0.5}O_2$ can provide high reversible capacity (~230mAh/g) upon cycling to 4.5 V and high rate capability at elevated temperatures. $LiNi_{0.5}Mn_{0.5}O_2$ samples were prepared by heat-treating a mixture of $NiMnO_3$ and Li_2CO_3 from 900°C to 1,050°C for a period of 30 minutes to 18 hours. Samples that were heat-treated at 1,000°C for 30 minutes then quenched to room temperature were found to provide the best reversible capacity (~200mAh/g) upon cycling to 4.6 V at 30°C. The reversible capacity could be further increased by an annealing step at 700°C for 12 hours (Figure IV- 17(a). The origin in this enhancement is under investigation.

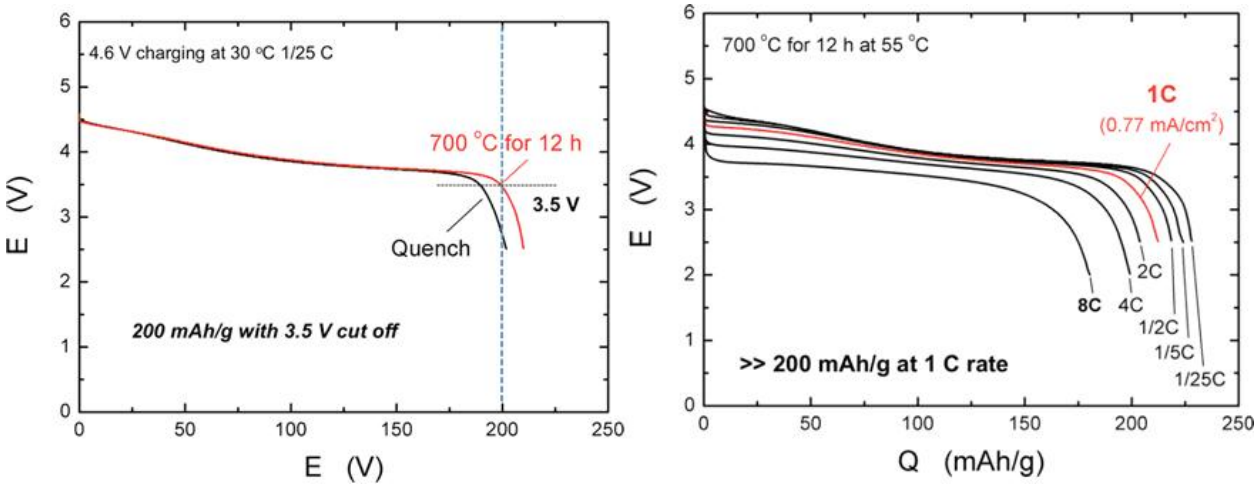

Figure IV- 17. (a) Reversible capacity of $LiNi_{0.5}Mn_{0.5}O_2$. (b) Rate capability at 55°C.

XRD data show that the annealing step reduced the intermixing from 11% to 9%. XPS data are being collected in order to examine the influence of surface chemistry changes associated with the annealing on the reversible capacity. Increasing testing temperature from 30°C to 55°C led to a reversible capacity of 230mAh/g. Moreover, the samples after the annealing step at 700°C exhibit very good rate capability at 55°C (~210mAh/g at 1C and ~185mAh/g at 8C, Figure IV- 17(b)). The reversible capacity at 8C was found to be sensitive to temperature, where ~120mAh/g was found at 30°C, in contrast to ~180mAh/g at 45°C and 55°C.

Conductive Polymers (Goodenough) – This work focused on the fast charging performance of NMC/polymer composite cathodes prepared with conducting polymers using a synthetic technique. NMC prepared *via* oxalic-acid co-precipitation shows good rate capability, shown in Figure IV- 18. With electrodeposition, NMC particles can be well-incorporated into PPy matrices to form a homogenous film. A composite capacity of more than 100mAh/g was obtained; however, the deposited NMC/PPy cathode film exhibits a low electronic conductivity. The capacity was improved with addition of a small amount of carbon in the precursor solution for electrodeposition.

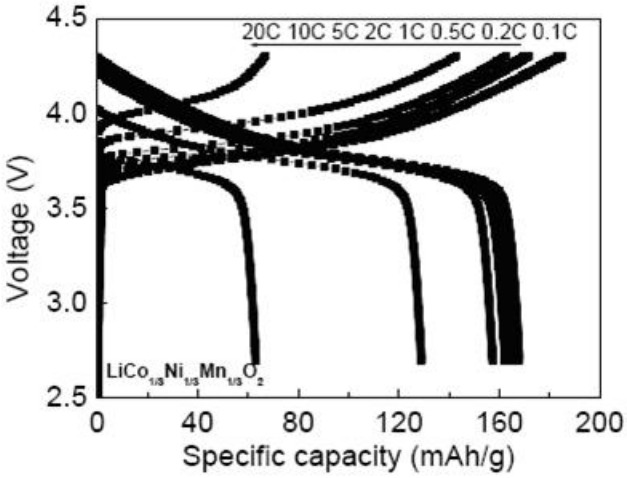

Figure IV- 18. Rate capability of NMC charged at 0.1C– 20C and discharged at 0.1C.

IV.A.3 Spinel and Composite Systems: Performance and Limitations

OBJECTIVES

To develop low-cost spinel manganese oxides that offer excellent capacity retention, high rate, low ICL, and good storage characteristics at elevated temperatures.

APPROACH

Develop an understanding of the factors that influence the performance of spinel oxide cathodes and use that to develop higher performing materials. Cationic and anionic substitutions and surface modifications of 4 V and 5 V spinel oxide cathodes as well as composites consisting of high-power spinel oxides and high-energy layered oxides are being pursued. Conventional ceramic and solution-based synthesis, chemical and structural characterization, electrochemical evaluation of coin cells with Li and carbon anodes, and a fundamental understanding of their structure-property-performance relationships are being pursued.

Continue to search for, characterize, and develop low-cost Mn oxide cathodes, specifically composite structures such as 'layered-layered' $xLi_2M'O_3\bullet(1\text{-}x)LiMO_2$ and 'layered-spinel' $xLi_2M'O_3\bullet(1\text{-}x)LiM_2O_4$ in which M′ is predominantly Mn and M is predominantly from Mn, Ni and Co. Fabricate electrodes that remain stable at high potentials (>4.4 V) in the hope of suppressing oxygen evolution thus mitigating the safety hazards of Li-depleted metal oxide cathodes at high SOC.

ACCOMPLISHMENTS

Composite Layered/Spinel Cathodes (Manthiram) – Previous work showed that the incorporation of layered oxides like $LiCoO_2$ or NMC into a stabilized spinel oxide like $LiMn_{1.8}Li_{0.1}Ni_{0.1}O_{3.8}F_{0.2}$, followed by charging to 4.7 V in the first cycle, traps protons from the electrolyte in the layered lattice, suppresses Mn dissolution and improves capacity retention. Similar experiments have been carried out with various spinel oxyfluoride to layered oxide ratios and it is found that mixtures consisting of ~30 wt% layered oxide offer the best performances at elevated temperatures. Similar experiments with mixtures consisting of the stabilized spinel oxide $LiMn_{1.85}Li_{0.075}Co_{0.075}O_4$ and the layered NMC also indicate that mixtures with ~30 wt% layered oxide show the best combination of cyclability and discharge capacity (Figure IV- 19).

Surface Coatings (Manthiram) – Previous work showed that the cyclability of the cation-substituted 5 V spinel cathodes ($LiMn_{1.5}Ni_{0.42}Zn_{0.08}O_4$ and $LiMn_{1.42}Ni_{0.42}Co_{0.16}O_4$) can be improved by surface modification with oxides like Al_2O_3. The enhanced capacity retention is due to the improved stability of the cathode surface. One of the attractive features of the spinel cathodes is their high rate performance. Although the bare 5 V cathodes $LiMn_{1.5}Ni_{0.42}Zn_{0.08}O_4$ and $LiMn_{1.42}Ni_{0.42}Co_{0.16}O_4$ were found to retain 66 and 71% of their capacity on going from C/6 to 10C at the 3rd cycle, the rate capability was found to decrease rapidly as the cycle number increased from 3 to 50.

The rate retention can be improved by surface modification with other oxides, as seen in Figure IV- 20. The rate capability retention was obtained by first calculating the percentage capacity retained on going from C/6 to 10C at the 3rd and 50th cycles separately and then dividing the latter by the former. For example, modification of $LiMn_{1.42}Ni_{0.42}Co_{0.16}O_4$ with Al_2O_3 leads to a rate

capability retention of ~ 97 % on going from C/6 to 10C rate while the bare $LiMn_{1.42}Ni_{0.42}Co_{0.16}O_4$ has a rate capability retention of only ~55% under the same conditions. By examining the discharge curves at various C rates, it is found that the poor rate capability retention of the bare 5 V cathodes is due to the increase in polarization resistance R_P on cycling. Surface modification suppresses the increase in R_P and improves the rate capability retention.

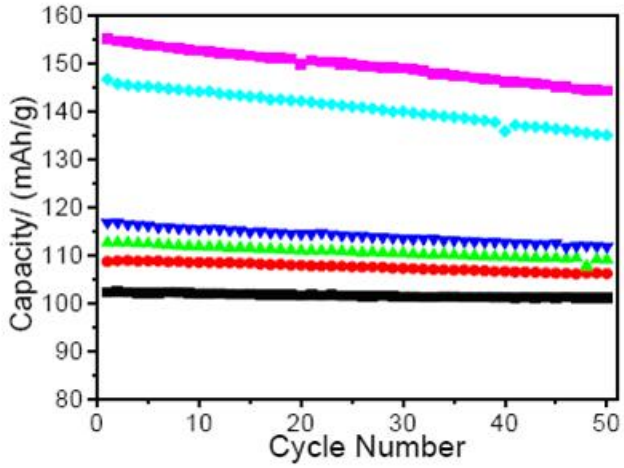

Figure IV- 19. Cyclability of the stabilized spinel + layered oxide composite cathodes at C/5 rate: (■)100 wt% $LiMn_{1.85}Li_{0.075}Co_{0.075}O_4$, (●) 80 wt% $LiMn_{1.85}Li_{0.075}Co_{0.075}O_4$ + 20 wt% NMC, (▲) 70 wt% $LiMn_{1.85}Li_{0.075}Co_{0.075}O_4$ + 30 wt% NMC, (▼) 60 wt. % $LiMn_{1.85}Li_{0.075}Co_{0.075}O_4$ + 40 wt% NMC, (◆) 10 wt. % $LiMn_{1.85}Li_{0.075}Co_{0.075}O_4$ + 90 wt% NMC, (■) 100 wt. % NMC

EIS analysis indicates that the fast increase in R_P in the case of the bare 5 V spinel cathodes during cycling is due to a large increase in both the SEI resistance and the electron transfer resistance, Figure IV- 21. Surface modification slows the increase in both the SEI and electron transfer resistance. XPS data reveal that the various coatings differ in their surface chemical stability during cycling, which leads to differences in electrochemical performances.

High Voltage Composite Cathodes (Thackeray) – Following ANL's success in synthesizing composite 'layered-layered' $xLi_2M'O_3\bullet(1\text{-}x)LiMO_2$ and 'layered-spinel' $xLi_2M'O_3\bullet(1\text{-}x)LiM_2O_4$ electrodes, the possibility of synthesizing close-packed 'olivine-spinel' and 'olivine-layered' composite structures to stabilize metal oxide electrodes was explored. For proof of concept, attempts were made to synthesize an olivine-spinel intergrowth, $LiNiPO_4$ (olivine) and $LiNiVO_4$ (spinel) because in this model system, the Li^+ and Ni^{2+} ions are located in octahedral sites and the pentavalent P and V ions in tetrahedral sites of both structure types.

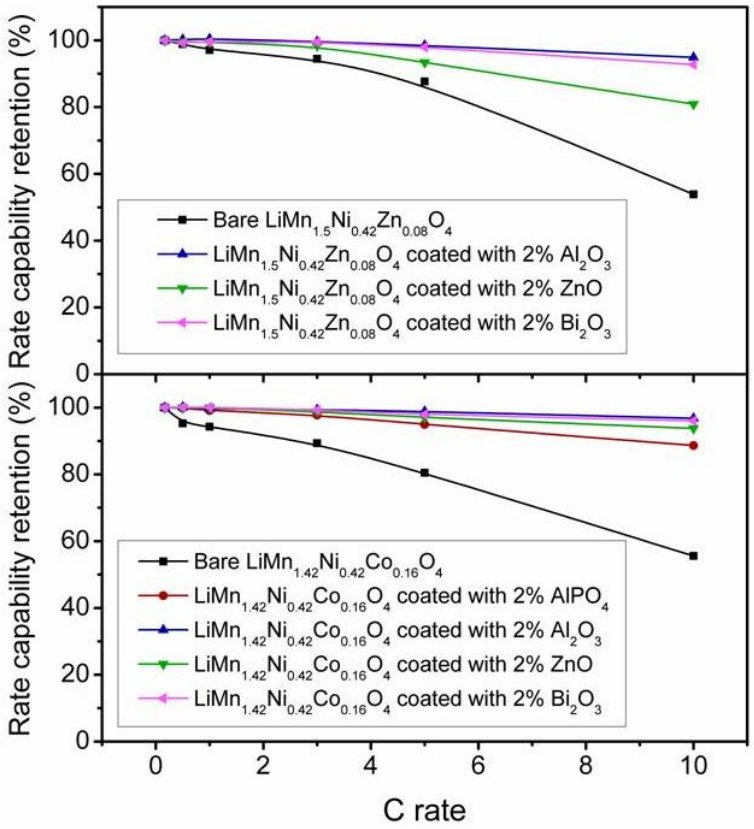

Figure IV- 20. Rate capability of the bare and surface modified $LiMn_{1.5}Ni_{0.42}Zn_{0.08}O_4$ and $LiMn_{1.42}Ni_{0.42}Co_{0.16}O_4$ cathodes after 50 cycles.

$LiNiVO_4$ and $LiNiPO_4$ were first synthesized individually by conventional solid state reactions prior to annealing at 600 and 800°C in air. XRD showed that the annealed mixture consisted essentially of both olivine and spinel. However, high resolution transmission electron microscopy (HRTEM) [Convergent beam electron diffraction (CBED)] data did not show conclusive evidence of a fully integrated structure unlike the 'layered-layered' and 'layered-spinel' Li-metal-oxide structures. Although energy dispersive spectroscopy (EDS) compositional analyses suggested that discrete spinel $LiNiVO_4$ and olivine $LiNiPO_4$ regions dominate a 50:50 $LiNiVO_4$-$LiNiPO_4$ sample, regions in which strong P, V, and Ni signals were observed suggested an olivine-spinel intergrowth might exist at least at phase boundaries. This study is being continued with the hope of being able to grow epitaxial Li^+-ion conducting olivine (SEI) layers (notably $LiNiPO_4$ or $LiCoPO_4$) on either ccp spinel or layered Li-metal-oxide electrode structures to protect them from surface degradation at high potentials (>4.6 V).

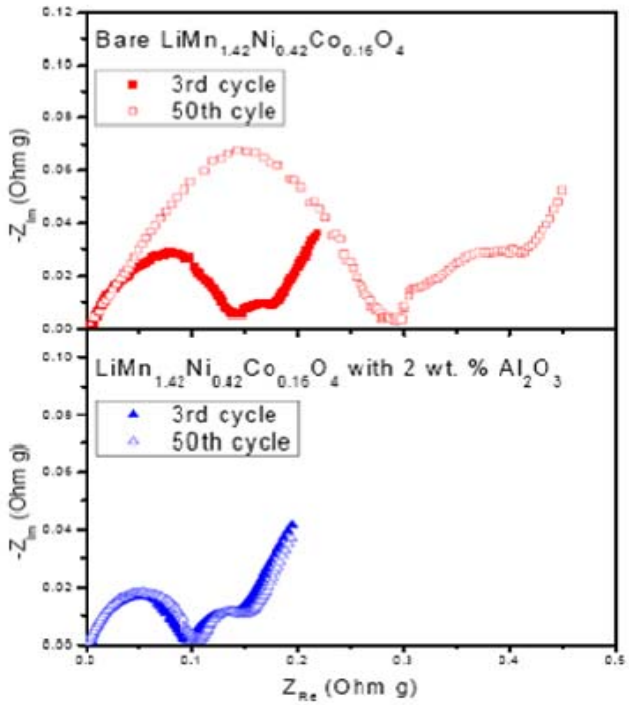

Figure IV- 21. Comparison of EIS data of the bare and Al_2O_2 modified $LiMn_{1.42}Ni_{0.42}Co_{0.16}O_4$ at 50% SOC after 3 or 50 cycles.

The team is continuing to use integrated structures containing a Li_2MnO_3 component to stabilize layered $LiMO_2$ (M=Mn, Ni, Co) and spinel $Li[Mn_{2-x}M_x]O_4$ (M=Li, Ni) electrodes. Integrated $xLi_2MnO_3•(1-x)LiMO_2$ ('layered-layered') and $xLi_2MnO_3•(1-x)LiMn_{2-x}Li_xO_4$ ('layered-spinel') electrodes can provide anomalously high capacities (240-250mAh/g) when cycled between 5 and 2 V, albeit at relatively low rates. Instead of using Li_2MnO_3 alone to stabilize $Li[Mn_{2-x}M_x]O_4$ spinel electrodes, three-component systems are being investigated, whereby a stabilized layered $xLi_2MnO_3•(1-x)LiMn_{0.5}Ni_{0.5}O_2$ component that delivers most of its capacity between 4.5 and 3 V is integrated with a $Li[Mn_{1.5}Ni_{0.5}]O_4$ spinel component that delivers its capacity over two voltage plateaus, one at 4.7 V and the other just below 3 V. For the initial studies, the system $xLi[Mn_{1.5}Ni_{0.5}]O_4•(1-x)(Li_2MnO_3•Li[Mn_{0.5}Ni_{0.5}]O_2)$ ($0 \le x \le 1$), in which the Mn:Ni ratio of 3:1 remains invariant for all values of x, was selected.

Representative charge/discharge profiles of three Li half cells for x=0, 0.5 and 1.0 in $Li/xLi[Mn_{1.5}Ni_{0.5}]O_4•(1-x)(Li_2MnO_3•Li[Mn_{0.5}Ni_{0.5}]O_2)$, between 4.95 and 2.0 V, are shown in Figure IV- 22(a-c), respectively. The end members provide the expected response of the layered and spinel electrodes. On the other hand, for x=0.5, the profile appears to indicate an electrode structure that has significantly more layered character than expected for a 50:50 ratio, providing evidence that the integrated structure has highly complex atomic arrangements.

Cycling data of these cells show that several break-in cycles are required to obtain a maximum capacity of ~250mAh/g, Figure IV- 22(b); the reason why the capacity increases with cycling is not yet understood. These high capacities are, however, obtained at a relatively low rate (0.1 mA/cm^2). Attempts are being made with Primet Precision to overcome the rate limitations by reducing the particle size.

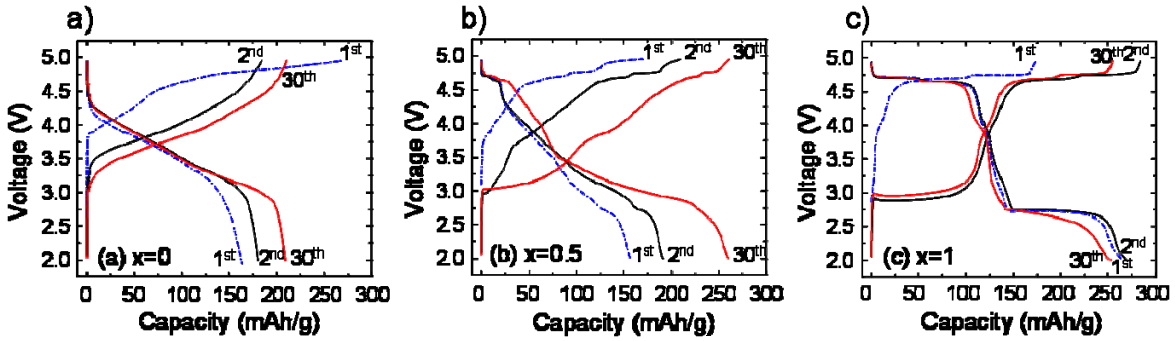

Figure IV- 22. Electrochemical profiles of Li/x$Li[Mn_{1.5}Ni_{0.5}]O_4$•(1-x)($Li_2Mn_{0.3}Li[Mn_{0.5}Ni_{0.5}]O_2$) cells for a) x=0 (layered) b) x=0.5 (layered-spinel), and c) x=1 (spinel).

The team is also continuing to investigate the impact of fluorination of electrodes and the ability to improve the materials' cyclability. Charging xLi_2MnO_3•(1-x)$LiMO_2$ electrodes to high potentials (>4.4 V) damages the electrode surface. However, fluorination of spinel $LiMn_2O_4$ and layered xLi_2MnO_3•(1-x)$LiMO_2$ electrodes improves both capacity and cycling stability. In this work, mildly acidic fluorinated solutions are used to wet and passivate xLi_2MnO_3•(1-x)$LiMO_2$ particles without damaging or corroding the surface. Figure IV- 23 shows significantly improved cycling behavior obtained from mildly fluorinated electrodes. Fluorinated surfaces were found to provide lower impedance and a higher rate capability.

Sample Future Plans in Cathodes

The future plans in the cathodes area all aim to either improve the performance of existing and emerging materials, or to fabricate new, inexpensive, very high energy materials, and include:

- Investigate the electrochemical properties of composite cathodes consisting of stabilized, surface-modified 5V cathodes and a high energy layered oxide solid solution between $Li[Li_{1/3}Mn_{2/3}]O_2$ and $Li[Ni_{1-y-z}Mn_yCo_z]O_2$ (which exhibits capacities over 250mAh/g).
- Address the rate limitations of 'layered-layered' $xLi_2M'O_3$•(1-x)$LiMO_2$ and 'layered-spinel' $xLi_2M'O_3$•(1-x)LiM_2O_4 electrodes.
- Design and characterize 3D electrode/electrolyte architectures with epitaxially grown, ionically and electronically conducting layers at the interface to protect the cathode. The goal is to allow free access of Li to the bulk of the electrode, enhancing Li-ion conductivity and rate capability. Physical blends of spinel $LiMn_2O_4$ and $xLi_2M'O_3$•(1-x)$LiMO_2$ powders will be investigated. Theoretical studies of dissolution vs. H^+-ion exchange reactions in layered- and spinel Li-metal-oxide electrodes will continue. Molecular dynamics (MD) simulations of the aqueous-spinel interface to investigate surface structure and dissolution will be initiated.
- To better understand the reaction mechanism of olivine materials so that higher rates can be obtained, iron substitution is being considered to create some disorder to better allow the nucleation of the $LiFePO_4/FePO_4$ interface.
- The mechanism for the two-phase reaction in $LiMnPO_4$ (perhaps similar to that of $LiFePO_4$) will be identified. With this knowledge, particle morphologies can be selected that maximize energy and power density. The chemical and electrochemical properties of these crystals will be correlated with their composition, dimensions, and morphologies.
- Expand the investigation of the structural changes of $LiFe_{1-x}M_xPO_4$ (M=Mn, Co, and Ni) materials, especially when cycled to high voltages (>4.8V).

- Further probe the formation mechanism of metal fluorides on Li storage oxide surfaces during cycling and test the hypothesis that the presence of surface metal fluorides protects the surface and suppress the growth of resistive, high-impedance layers during cycling.
- Investigate possible mechanisms for the enhanced rate capability associated with the annealing process of $LiNi_{0.5}Mn_{0.5}O_2$.
- Develop a new class of functionalized carbon nanotube based positive electrodes for high-rate applications.

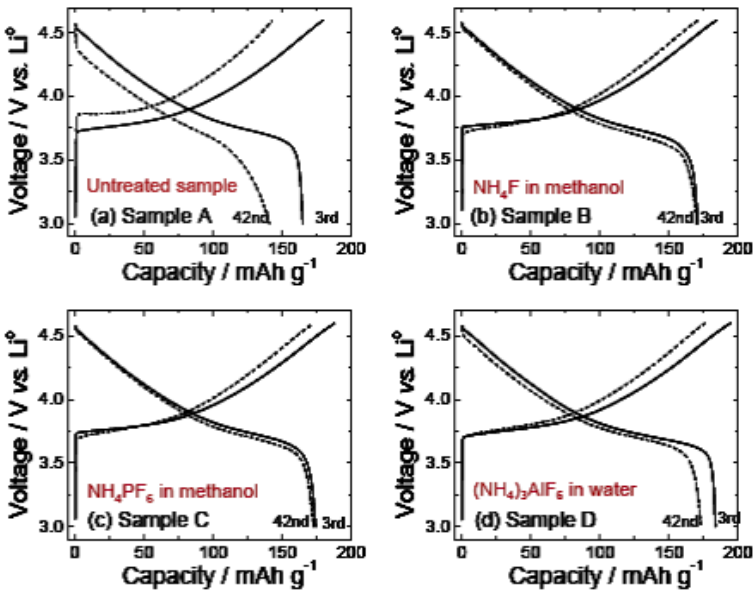

Figure IV- 23. Electrochemical Behavior of surface-treated $xLi_2MnO_3 \cdot (1-x)LiMO_2$ electrodes (half cells)

IV.B New Anode Materials

OBJECTIVES

The primary objective of these tasks is to replace carbon anodes with inexpensive, high energy, anodes made from environmentally benign materials. The anode should also have slightly more positive insertion voltage with respect to Li/Li^+ in order to minimize risks of Li plating while charging at high rates and at low temperatures. The objective of the intermetallic electrodes work is to search for inexpensive materials (powder laminates rather than thin films) that have a potential a few hundred mV above that of metallic Li, and a capacity of at least 400mAh/g (>1500 mAh/ml).

Another objective is to understand the influence of electrolyte composition, deposition rate, and applied potential on interfacial stability of Li metal electrodes, to investigate the root causes of dendrite formation, and to use these studies to identify new strategies to stabilize the Li interface.

APPROACH

The focus of the research into intermetallic electrodes is mainly on Sn- and Si-based systems. Promising anodes are evaluated in full cells against high capacity metal oxides, and for thermal, kinetic and structural stability.

One approach into alloy anodes is to design and manufacture nano-composite C/Sn thin-film electrodes, and to establish direct correlations between electrode surface chemistry, morphology, and power, life, and capacity fade. Specifically, microwave plasma chemical vapor deposition is used to synthesize nano-composite C/Sn-Me and C/Si thin-film anodes, and diagnostics techniques are applied to detect and characterize surface processes in graphite and Sn anodes.

Another approach into alloy anodes is to focus on exploring novel low-cost approaches to generate nano-scale heterostructures comprising Si and a variety of carbon forms derived from graphitic carbon as well as polymer derived carbons. The purpose is to exploit the nano-scale electrochemical phenomena of the active materials, and also the active-inactive interface.

Thin films of MoO_3 nanoparticles have a reversible capacity of 630mAh/g (~5.170mAh/l of active material, 2,230mAh/l of electrode material, over three times that of graphite) with high rate capability. A particular focus of recent research has been to optimize the nanoparticles for a thicker electrode in a coin cell configuration.

Another approach is to identify and develop sulfochlorides that are thermodynamically stable *vs.* the electrolyte so as to eliminate the SEI layer, but have a smaller voltage *vs.* Li/Li^+ than $Li_4Ti_5O_{12}$.

One group working to understand dendrite formation and growth on Li metal surfaces is monitoring surfaces by electrochemical and optical methods as a function of electrolyte composition and current density. Another group is investigating how SEI formation and Li current distribution depends on surface composition and microstructure of the Li metal surface.

ACCOMPLISHMENTS

Synthesis and Characterization of Si/C Composite Anodes (Kumta) – Intra-type Si/C nano-composites, with ~700mAh/g, have been synthesized by high energy mechanical milling (HEMM) using graphite, Si and polyacrylonitrile (PAN) polymer following heat-treatment at ~1073K-1173K. PAN acts as a diffusion barrier to the interfacial reaction between graphite and Si preventing the formation of electrochemically inactive SiC, while also reducing the amorphization kinetics of graphite. Both issues are known to cause significant deterioration in the electrochemical properties of the composites.

The XRD patterns, Figure IV- 24 (left), of the 12h milled and heat treated Si/C nano-composite powder indicate the presence of graphite and Si with no detectable SiC. Elemental X-ray maps of C and Si combined with the secondary electron SEM image of the Si/C nano-composite also show the homogeneous distribution of the electrochemically active Si on the graphite matrix. TEM bright field image along with selected area diffraction pattern (SAD), Figure IV- 24 (right), confirms that the embedded Si is nano-crystalline (~15nm) and is homogenously distributed on the mechanically compliant graphite matrix resulting in an intra-type nano-composite.

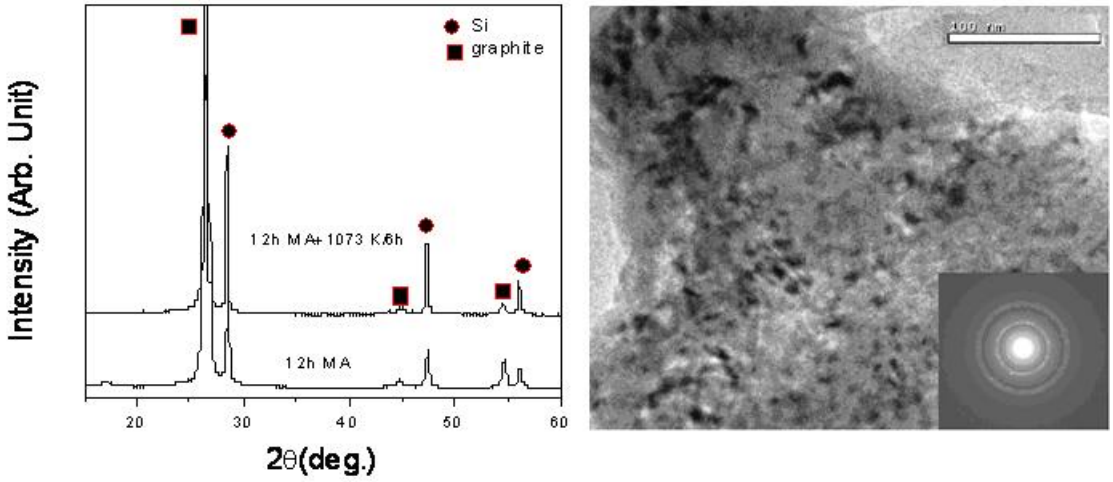

Figure IV- 24. (Left) XRD patterns of 42% C-28wt.% Si-30wt.% PAN generated after 12h of mechanical milling and after thermal treatment at 1073K for 6h. (Right) - TEM bright field image and SAD pattern (inset) of Si/C nano-composite before cycling shows the Si nanoparticle (~15nm) embedded and distributed on the graphite matrix.

Figure IV- 25 (left) shows the cycling data of the resultant Si/C nano-composite of different nominal compositions cycled at ~160mA/g in the ~0.02V-1.2V potential window. As expected, increase in Si content leads to a capacity increase and an increase in the capacity loss per cycle. The Si/C nano-composite shows a 1st discharge and charge capacity of ~1215mAh/g and ~1019mAh/g, respectively, an ICL of ~16%. This composite also exhibits ~0.34% capacity loss per cycle up to 30 cycles, unlike pure microcrystalline Si which collapses within a few cycles. The result suggests that the HEMM derived Si/C composite vastly improves the cyclability and the structural stability of Si/C composite.

Microstructural investigation of the Si/C nano-composite electrode after 40 cycles (Figure IV- 25 (right)) shows excellent integrity and stability after cycling. This improvement is attributed to the

likely improved mechanical properties of the composite arising from the dual influence of achieving a homogeneous dispersion of nano-scale Si within the graphite matrix and the amorphous surface coating of PAN derived carbon at the Si-graphite interface. However, the formation of a thick SEI layer on the electrode surface after cycling appears in Figure IV- 25 (right), which may be one of the causes of the capacity fade. FTIR analysis confirms the formation of Li_2CO_3 and alkyl lithium carbonates on the cycled electrode surface due to the reductive decomposition of the electrolyte on the Si/C particle surface in the initial state of charging. However, the Si/C nano-composite shows a lower ICL (~15-25%) in contrast to pure Si or pure graphite (~35%) due to the amorphous carbon coating on the surface which is expected to reduce the particle reactivity. Future work will be directed towards reducing the irreversible capacity even further by exploiting the electrochemical properties of the amorphous carbon (*a*-C)-Si interface.

Role of Amorphous Silicon (Kumta) – The differential capacity plot (dQ/dV *vs.* V in Figure IV-26 (left)) of the Si/C nano-composite shows the alloying/dealloying processes occurring during the charge/discharge cycle. The formation of the high Li content alloy, $Li_{3.5}Si$, at ~0.10V with a peak potential ~0.06V has been identified during the 1st discharge. The appearance of peaks at ~0.24V, ~0.3V and ~0.09V in the 2nd discharge cycle suggests the transformation of crystalline/nano-crystalline Si (*c/nc*-Si) to amorphous Si (*a*-Si).

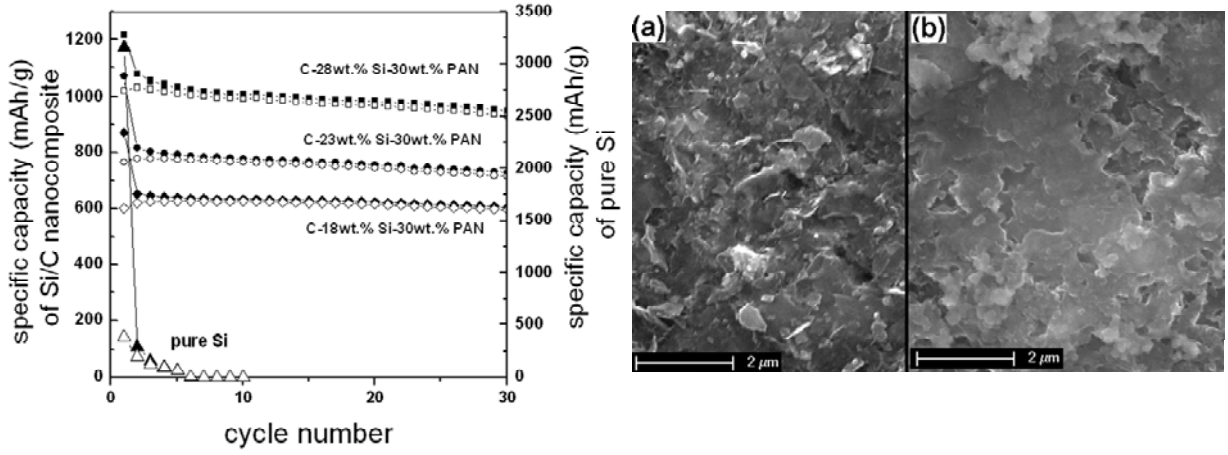

Figure IV- 25. (Left) Specific capacity vs. cycle number of Si/C nano-composite of different nominal composition cycled at a constant current of ~160mA/g. (Right) SEM micrograph of Si/C nano-composites of nominal composition 42wt.% C-28wt.% Si-30wt.% PAN (a) before and (b) after cycling.

To study the effect of the formation of $Li_{3.5}Si$ on the stability of the Si/C composite, the as-prepared composite was cycled for the 1st four cycles between 0.02-1.2V to activate the electrode and ensure completion of the *c/nc*-Si to *a*-Si phase transition. The electrode was then cycled between 0.07-1.2 V in order to bypass the formation of $Li_{3.5}Si$. Figure IV- 26 (right) shows the Si/C performance when cycled between 0.07-1.2V at a rate of ~160mA/g. It shows a reversible capacity of ~700mAh/g which is ~27% lower than the 1st charge capacity (~963mAh/g) obtained for pure Si/C of composition 42wt.% C-28wt.% Si-30wt.% PAN cycled between 0.02-1.2V (Figure IV- 25 (left)). However, the capacity fade of the Si/C cycled between 0.07-1.2V has been reduced to ~0.14% per cycle vs. ~0.34% per cycle for the Si/C cycled between ~0.02-1.2V. Microstructural assessment of the activated Si/C composite electrode, cycled between 0.07-1.2V

for 30 cycles shows better structural integrity than the electrode cycled between 0.02-1.2V. This result clearly suggests that the formation of high Li content $Li_{3.5}Si$ (near ~0.10V) is the main cause of structural failure of the Si/C nano-composite during long term cycling. Future work will be directed to generating nano-composites preventing the formation of this phase.

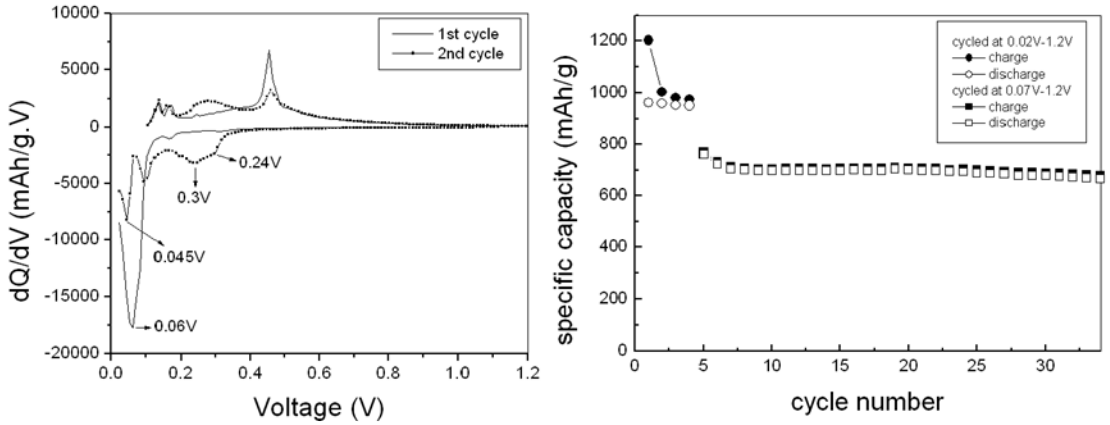

Figure IV- 26. (Left) Differential capacity vs cell potential curve of Si/C composite after 1st and 2nd cycle cycled at a constant current of 160mA/g. (Right) Specific capacity *vs.* cycle number of activated Si/C composite cycled in the potential window 0.07V-1.2V.

The differential capacity plot (dQ/dV *vs.* V) as well as the expected phase fields at different potentials in the de-alloying process during the 2nd charge cycle of the Si/C composite of nominal composition 42wt.% C-28wt.% Si-30wt.% PAN is shown in Figure IV- 27 (right). In order to synthesize *in situ a*-(Li-Si/C) composite phases of different compositions and investigate their electrochemical properties, the Si/C composite was discharged/charged for the first four cycles in the potential window ~0.02V-1.2V with respect to pure Li to ensure formation of *a*-Si. Subsequently, charging was terminated at the 5th cycle at different potentials of ~0.6V and ~0.5V, respectively to stabilize the *a*-(Li-Si/C) phase. Figure IV- 27 (left) shows the performance of the *a*-(Li-Si/C) composite, synthesized *in situ* at ~0.6V and ~0.5V, cycled between ~0.02V-0.6V and ~0.02V-0.5V, respectively, at a rate of ~160mAh/g. The *a*-(Li-Si/C) composites shows a 1st charge capacity of ~819mAh/g (.6V) and ~700mAh/g (.5V). Despite the reduced capacity, the capacity retention of the *a*-(Li-Si/C) composites have been improved to ~0.21% and ~0.13% loss per cycle, respectively, in comparison to ~0.34% loss per cycle of Si/C composite cycled between ~0.02V-1.2V. Furthermore, the data suggests that the average voltage expected for a full cell using the *a*-(Li-Si/C) anode cycled in the reduced potential window could be higher and as a result, enhancement in energy density could be expected in contrast to pure silicon used as an anode when cycled in the potential window 0.02V-1.2V at the same rate. The composition of the alloy formed *in situ* in the *a*-(Li-Si/C) composite obtained at ~0.6V and ~0.5V is determined to be Li-55at%Si and Li-42at%Si, respectively, based on the capacity of the *a*-(Li-Si/C) composite. These results suggest that the formation of nano-crystalline or amorphous Si *a-priori* would likely lead to much improved capacity and cycling stability.

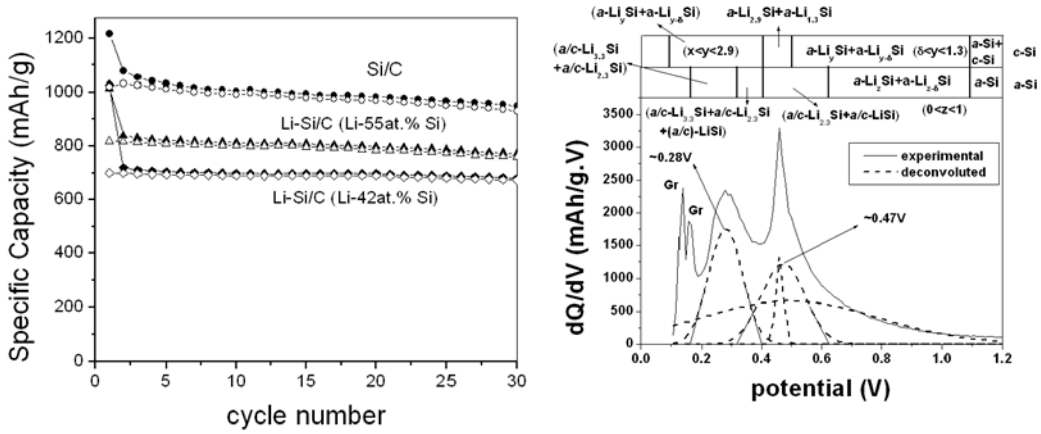

Figure IV- 27. (Left) Specific capacity vs cycle number of Si/C and Li-Si/C composite cycled at a constant current of ~160mA/g. (Right) Differential capacity vs. cell potential curves of Si/C composite electrode at 2nd charge and the expected phase/phases at different potential.

Sn and Si-based Alloys (Kostecki) – Previously, this team developed a microwave-based technique to produce thin film Sn/C composite anodes with a reversible capacity of ~440mAh/g, originating exclusively from Sn, and good cycleability. The high ICL of ~400mAh/g is mainly associated with SEI formation.

In 2008, this group developed an *in situ* atomic force microscopy (AFM) procedure to detect and characterize early stages of SEI formation and Li alloying on Sn. A Sn foil (d = 1.2 cm) was mechanically and electrochemically polished to surface roughness of <5 nm. The Sn electrode was investigated in an *in situ* AFM electrochemical cell equipped with two Li wire counter and reference electrodes with 1 M $LiPF_6$, EC:DEC 1:2 w/w electrolyte. The surface morphology of the tin electrode was monitored continuously during the potential scan. Figure IV- 28 shows the current response during a potential scan (0.5 mV/s) from the open circuit potential (2.8V *vs.* Li/Li^+) to 0.3 V, which corresponds to the early stage of Sn alloying with Li. The charge consumed in the process of SEI layer formation at E > 0.6V was determined to be ~0.12 C/cm^2.

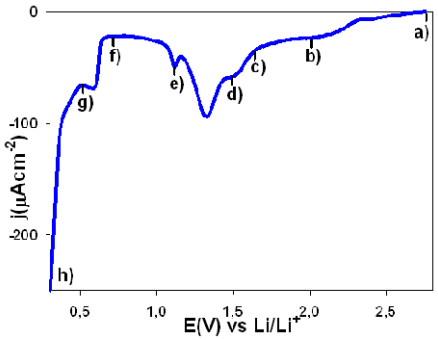

Figure IV- 28. 1st voltammetric scan (0.5mVs-1) of a tin foil anode from open circuit potential (OCP) to 0.3 V vs. Li/Li+ (*in situ* AFM cell under Ar atmosphere)

A sequence of corresponding *in situ* AFM images of the Sn electrode recorded at different potentials shows significant changes in the surface morphology, which are associated entirely with surface film formation, Figure IV- 29. The SEI growth was highly non-uniform and produced a rough, multilayer deposit of small <50 nm particles fused into large (μm) sized platelets. The average roughness of the film is ~200 nm at 0.33 V. *Ex situ* current-sensing AFM images revealed no electronic conductivity across the SEI film. The formation of such a thick and insulating SEI layer is consistent with earlier FTIR microscopy results and literature data.

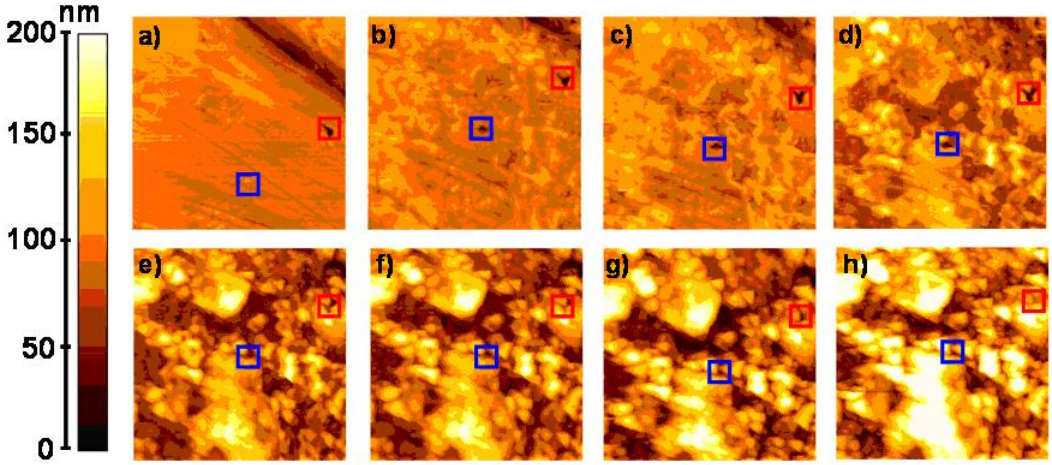

Figure IV- 29. *In situ* 10x10μm AFM pictures of Sn foil anode in 1M $LiPF_6$, EC:DEC 1:2 w/w recorded at (a) 2.74, (b) 2.00, (c) 1.65, (d) 1.44, (e) 1.11, (f) 0.72, (g) 0.51, (h) 0.33 V vs. Li/Li+.

The surface film is highly non-uniform and rough. The charge consumed during the film formation between 2.5 and 2 V is relatively low ~6-7 $mCcm^{-2}$ and corresponds to a hypothetical 100nm thick layer formed in a $2e^-$ reduction of EC. Interestingly, a Sn-foil electrode that was artificially coated with tin oxide showed no sign of SEI formation at potentials above 1V. However, rapid growth of the SEI was observed at potentials below ~1V, mainly due to the reduction of tin oxide to Sn. Surprisingly, the surface morphology of the SEI layer on Sn remains almost unchanged till 0.7 V despite an intense irreversible reduction current peak at 1.2V, Figure IV- 30(a). Moreover, no significant morphology changes or film dissolution is observed during cycling between 0.8 and 2.7 V, even though the intensity of the reduction peak at 1.2V increases substantially. It is postulated that the growth of the passive layer occurs at the interface between the existing layer and the Sn surface or else some soluble reduction products are formed that diffuse into the electrolyte. If the scan was extended into the Li-alloying region, Figure IV- 30(b), a similar reduction peak is observed at ~1.2V during the reverse scan. The peak's huge intensity, (note the scale) is associated with the reduction of electrolyte that occurs on a freshly exposed tin surface due to particle decrepitation during Li-alloying/dealloying.

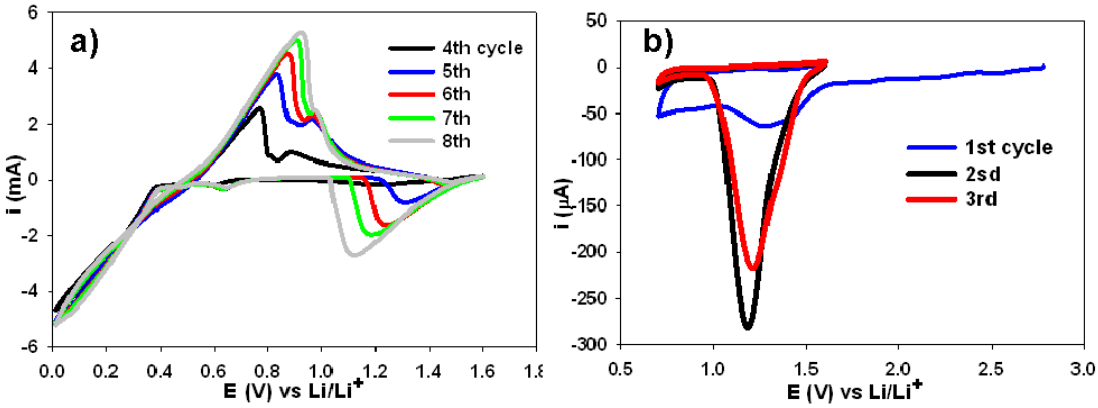

Figure IV- 30. Tin foil cycled in EC: DEC 1:2 / LiPF6 (1mV/s) between 2.7 and 0.7 V (a), and 1.6 and 0.01 V (b).

MoO_3 Nanoparticles (Dillon) – MoO_3 nanoparticles undergo significant volume change during cycling and lose structural order. The volume changes are tolerated at the nanoscale but for larger particles lead to fracturing, loss of electrical conductivity, and thus capacity fade. To further investigate the cycling of the nanoparticles, fully-atomistic first-principles MD calculations were performed. The individual chemical potentials of each Li atom in a theoretical nanoparticle were derived. It was found that the Li energy distribution is consistent with the experimental voltage-composition trace. The study also showed that Li is inserted irreversibly when a strong interaction with oxygen atoms occurs.

Next, MoO_3 nanoparticles, 30 m^2/g surface area, sufficient for coin cell testing were obtained with a single filament, 0.5mm diameter, ~20cm in length. (The procedure is scalable by running more filaments in series and expanding the dimensions of the reactor.) First, an electrode (~100 µm thick) was fabricated from 70:15:15 active material: acetylene black: PVdF. The electrode was heated to 150˚C for 12 hours in a glove box prior to cell fabrication.

Cycling data against Li metal is shown in Figure IV- 31, which shows a high ICL. The majority of the inserted Li is not removed in the first two cycles with the reversible capacity diminished to ~200mAh/g. Subsequently a similar electrode was heated to 250˚C for 12 hours, and significantly improved performance was achieved, Figure IV- 31(b). A reversible capacity of ~ 900mAh/g is obtained at C/12, and a capacity similar to the thin film of ~ 600mAh/g at C/3.

To investigate the surprising effect of the aggressive heat treatment, the nanoparticles were probed with temperature programmed desorption (TPD). Water was desorbed from the MoO_3 nanoparticles up to 250˚C suggesting stable hydroxyl groups on the oxide particle surfaces. These surface hydroxyl groups could be reacting with and/or irreversibly binding to Li atoms forming a layer that may inhibit reversible insertion. This is supported by time-of-flight secondary-ion mass spectrometry (TOF-SIMS) which shows that, following one Li insertion/extraction process, without heat treatment, MoO_3 nanoparticles have Li on the surface. Furthermore, the Li layer is several monolayers thick as it is not possible to detect surface Mo atoms. Future work will include extensive surface analysis to probe the SEI.

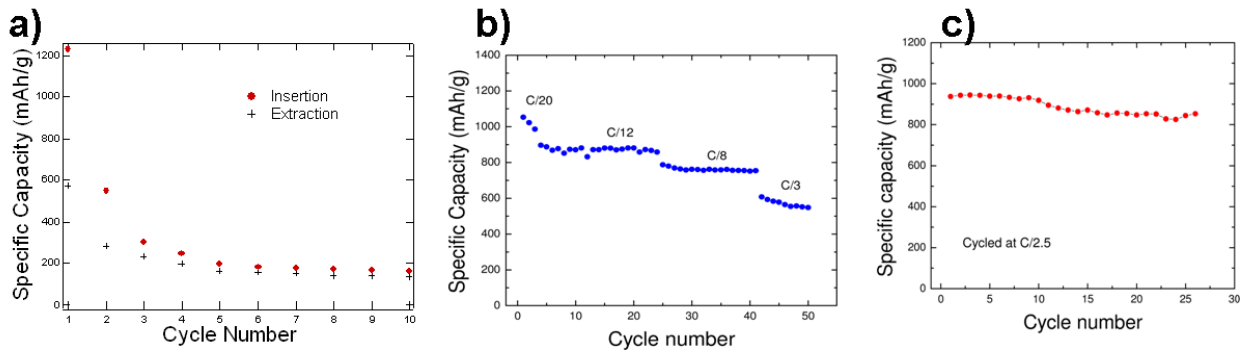

Figure IV- 31. Coin cell cycling data for MoO_3 nanoparticles with the electrode (a) heated to 150˚C in the glove box, (b) heated to 250˚C in the glove box, and (c) heated to 250˚C in the glove box with an increase in conductive additive.

The cycling data for a cell comprised of 70:20:10 active material:acetylene black:PVdF (250˚C for 12 hours) is displayed in Figure IV- 31(c) and shows that by increasing the conductive additive, a reversible capacity of ~ 900mAh/g is achieved. For this coin cell, as well as for other configurations, significant capacity fade began to occur between 35-40 cycles. Upon disassembling the cells it was found that dendritic growth was occurring on the Li-anode.

The MoO_3 anode has been coupled with a $Li_{1.05}(Ni_{1/3}Co_{1/3}Mn_{1/3})_{0.95}O_2$ cathode from ANL. The use of MoO_3 as opposed to graphite increases the cell specific capacity to 140mAh/g from 105mAh/g. Four cycles have been completed at C/7, and relatively stable cycling has been achieved. More cycling data will be obtained and presented in the near future.

Although a Li extraction potential higher than Li/Li^+ is desired, the potential for the MoO_3 coin cell at 50% capacity is ~1.5 V. Ideally this voltage should be slightly lower. Calculations predict that crystalline MoO_2 would have an average potential of ~ 1.0 V. By decreasing the oxygen content in the hot-wire chemical vapor deposition (HWCVD) reactor, MoO_x nanoparticles were made with some Mo metal according to XRD data. Upon cycling this film, however, the voltage profile was not significantly different from that of MoO_3. The discrepancy with theory may be attributed to the nanoparticles becoming highly disordered upon cycling. *In situ* Raman shows that the nanoparticles become disordered in the initial cycle.

Intermetallic Anodes (Thackeray) – Intermetallic anodes offer much higher gravimetric and volumetric capacity than graphite, various reaction potentials (*vs.* Li metal) and, depending on their constituents, improved safety. Problems to be overcome include combating the first-cycle, ICL by developing an understanding of capacity fade mechanisms, and controlling the large volume changes that occur during cycling, which leads to short cycle life.

Recent work has focused on $LaSn_3$. The hope was that the $LaSn_3$ structure, in which the Sn atoms are bonding agents for Li, might act as a Li storage material similar to the hydrogen storage compound $LaNi_5$ in which the Ni atoms bond to the H atoms. Attempts to prepare $LaSn_3$ by high-energy ball-milling lead, in general, to a two-phase product containing $LaSn_3$ and a minor amount of Sn, Figure IV- 32(a). The product has a peculiar morphology, as found by SEM, in which the $LaSn_3$ particles are surrounded by strands of Sn that form during annealing as a result of Sn's low melting point (232°C). In an attempt to increase the utilization and capacity of the electrodes (200-250mAh/g), samples were sent to Primet Precision Materials Inc. to reduce the

size of the primary particles to 100-200 nm. The XRD pattern of this product is shown in Figure IV- 32(b). Despite the reduction in particle size and excellent homogenization of the sample by Primet's process, the XRD pattern shows that the $LaSn_3$ product had decomposed into unidentified phases, which is tentatively attributed to the meta-stability of this highly Sn-rich compound. Investigations of Primet's process (and variations thereof) to reduce the particle size of $LaSn_3$ and other intermetallic materials are continuing.

Studies of Cu_6Sn_5 electrodes, synthesized by electrochemical deposition on high surface area copper foams, were initiated. This synthesis technique, which allows the creation of nanostructured intermetallic materials on a highly porous, electronically-conducting substrate, is being adopted to make use of the pores to accommodate the volume expansion and to use the interpenetrating copper network to ensure good electrical contact during cycling. Cyclic voltammograms are being used to determine deposition parameters for controlling the composition of electrochemically-deposited Cu-Sn compounds. For example, Figure IV- 33 shows that copper and tin reduction from chloride solutions occurs at ~ -300 mV and -650 mV, respectively, *vs.* a reference saturated calomel electrode (SCE).

Studies to determine the reactions conditions necessary for producing desired Cu_6Sn_5 electrode compositions and to optimize electrochemical performance are in progress.

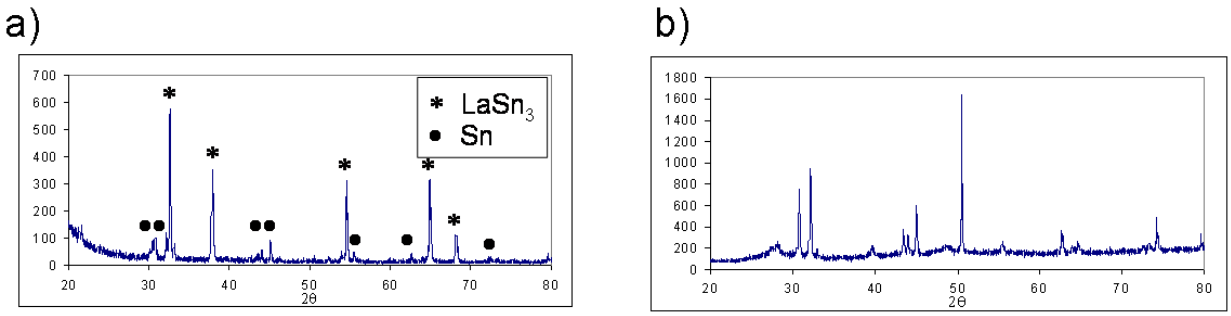

Figure IV- 32. XRD pattern of (a) ball-milled $LaSn_3$, and (b) 100 to 200 nm particles after the Primet process.

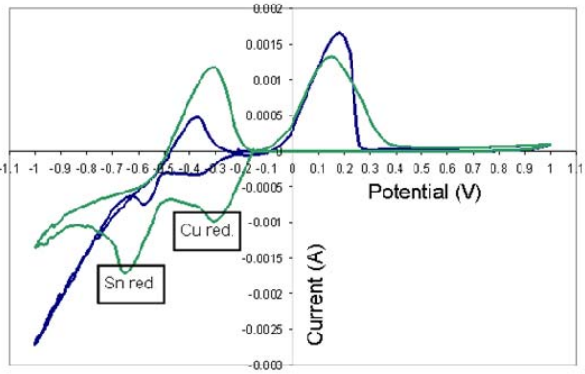

Figure IV- 33. Cyclic voltammogram of cupric- and stannous-chloride solution (SCE reference electrode).

Alloy and LTO Anodes (Whittingham) – Earlier this group reported on their study of two nanosized anode materials: the Sony Sn-Co-Ti-C anode and nano manganese oxides. The work on MnO anodes showed that LiBoB additives removed the large ICL.

A challenge with all nano-sized materials is their low tap density, which results in a poor volumetric energy density. This group decided to produce μm-sized $Li_4Ti_5O_{12}$ (LTO) that would be effective electrochemically and have a high tap density. Unlike the manganese oxides, this material reacts by an intercalation reaction with little structural change. As a result the charge/discharge curve is almost flat with a redox couple ~1.5V. This makes it more feasible to use in Li cells, even though it will come with a substantial energy loss. An ideal case would be similar behavior but with a potential ~0.5 – 0.8 volts.

This LTO made by this group has a conductivity six orders of magnitude higher than the nano-sized material. It shows ~100% capacity and 100% efficiency over extended cycling, as shown in Figure IV- 34(a). It also shows reasonable power capability as shown in Figure IV- 34(b). No increase of the impedance over 22 cycles was found, even when using a Li anode. Better performance should be possible with a more optimized synthesis method, and the effective tap density will be determined.

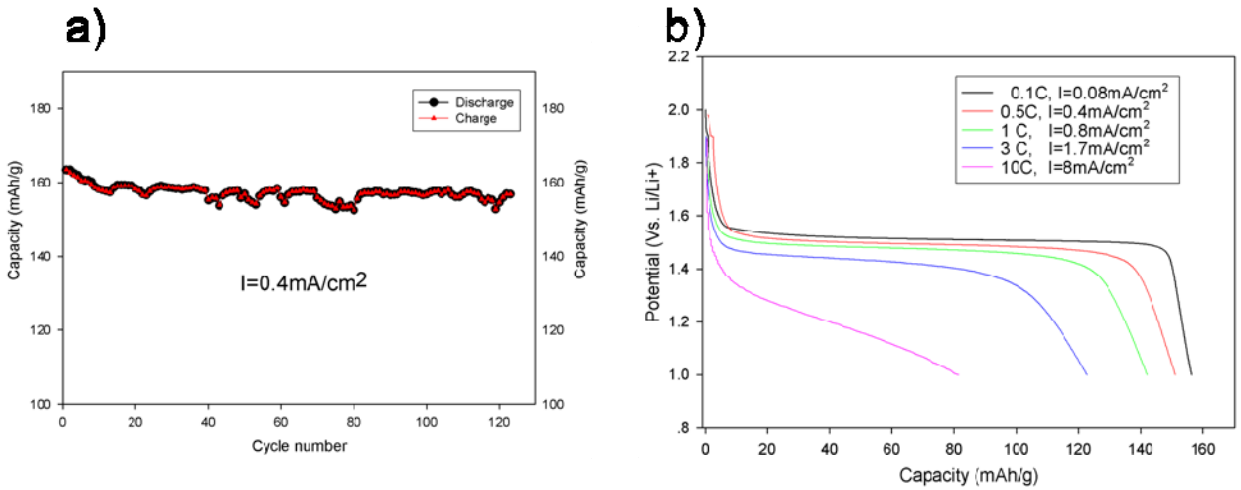

Figure IV- 34. (a) Retention of capacity of $Li_4Ti_5O_{12}$, as a function of cycling at a C/2 rate, and (b) the rate capability of a Li/$Li_4Ti_5O_{12}$ cell.

This group has continued to explore the possibility of a Si-based equivalent of the Sony Sn-Co-C system. A low Co content Si-Co-C sample has been prepared by mechanically grinding the components with a carbon precursor. The data are shown in Figure IV- 35. Higher capacities can be obtained, with either Co or Fe admixed with the Si, but the capacity falls off continuously from over 1000mAh/g to ~400mAh/g over the first 40 cycles. Structural changes that occur in these composites will be studied with BNL.

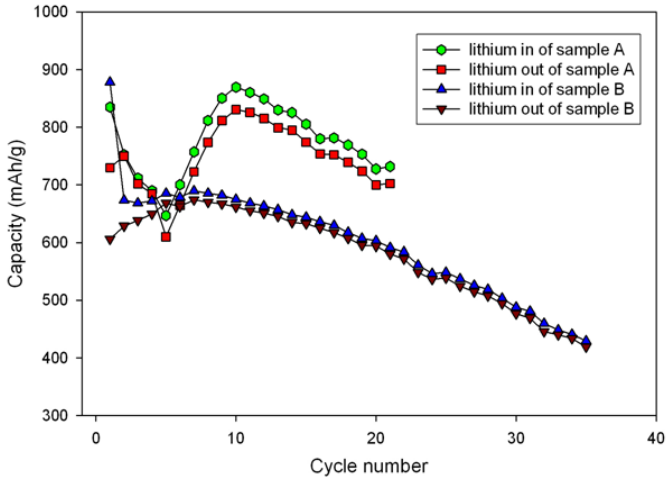

Figure IV- 35. Electrochemical performance of two silicon-cobalt-graphite nano-composite anodes (A – annealed for five hours, and B – annealed for two hours).

Cermets (Richardson) – A series of Li-Mg alloy cermets ranging from 10% to 50% Mg have been prepared by solid-state metathesis from Li nitride and magnesium powders. Diffusion coefficients and other properties of the alloys are being measured by electrochemical titration and impedance methods. A spectroscopic study of the SEI formed on the alloys is also in progress. A detailed investigation of the solid-state reaction between Li_3N and Si has shown that the expected product, Si_3N_4 is not formed. Instead, elemental nitrogen is formed along with $Li_{12}Si_7$ and other Li-Si intermetallics. This increases the utility of the reaction in pre-lithiating Si anodes as it avoids a reduction in capacity due to the weight of an inert byproduct. Reactions with other metals are being studied. This approach has the potential to reduce or eliminate the irreversible early cycle losses of active Li, which is an obstacle to their use in cathode-limited cells.

Effects of 2D Geometry on Lithium Deposition (Newman) – Empirical observations show that by extending the negative electrodes of Li-ion batteries beyond the positive electrodes on all sides by ≈ 1 mm, Li deposition during charging can be reduced. To explain this behavior, a two-dimensional model of potential and current distributions during cell charging has been built using COMSOL Multiphysics. Simulations have been run in which the length of the negative electrode relative to the positive varied from 0 to 2 mm. Results show qualitative agreement with observations. When electrodes are evenly matched, Li concentration increases at the edge of the anode faster than it does in the bulk. This drives down the exchange current density and causes a higher overpotential at the edge of the electrode, leading to a potential drop which permits Li deposition. An electrolyte-phase potential difference of 0.3 mV between the edge and center causes the potential drop at the edge of the electrode to reach 0 V. This favors Li plating at the edge, despite unused capacity in the center of the electrode. Extending the negative electrode beyond the edge of the positive provides excess capacity where it is needed and prevents deposition from occurring before the cutoff potential is reached. For electrodes where the negative is initially in excess by 10%, an extension of 0.5 mm is sufficient to postpone the onset of Li deposition until after the cutoff potential is reached (Figure IV- 36).

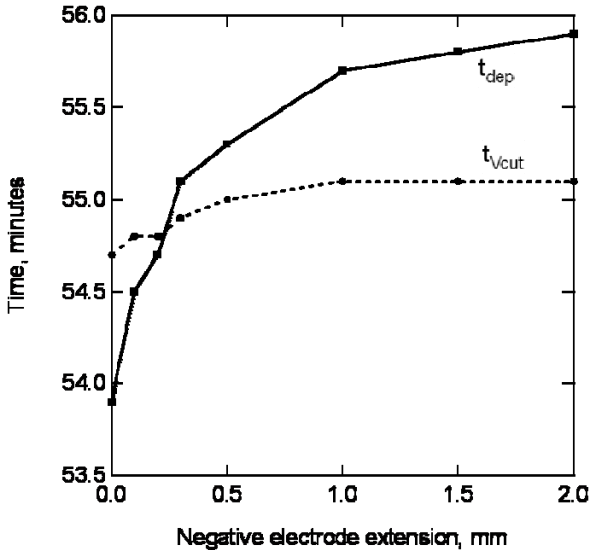

Figure IV- 36. Time to reach conditions for lithium deposition (t_{dep}) and cell cutoff potential (t_{Vcut}) as excess capacity is added by extending the negative electrode beyond the positive. When $t_{dep} > t_{Vcut}$, cell charging would stop before deposition occurs.

Lithium Anode Investigation (Dudney) – Vacuum evaporated Li metal which is dense, smooth, and relatively pristine is being used with $LiPF_6$ in EC+DMC or EC+EMC electrolyte. When the Li is soaked for ~24 hours, the resulting SEI is highly resistive, ~25 kΩ. The SEI layer does not appear to passivate, but becomes increasingly resistive as it ages and thickens over several days. This differs from reports of lithium anodes formed of commercial ribbon or by electrodeposition. The effect of an addition of VC to the electrolyte is being evaluated.

Breakdown of the resistive SEI layer, as studied by chronopotentiometry, occurs within 1-2 ms of the start of current and results in a 100-fold reduction in the interface impedance. Most interesting is the rapid recovery of the resistive SEI when the current is stopped; within just a few minutes the impedance is >10 kΩ. Ongoing experiments will help identify the fundamental mechanisms for the breakdown/recovery processes, whether formation/healing of an electrical path or a physical hole through the SEI film. Plans are underway to investigate the SEI formed at both graphite and Li electrodes using *in situ* cells for electron microscopy in collaboration with researchers at the Oak Ridge National Laboratory (ORNL) High Temperature Materials Laboratory.

Li Metal Dendrite Research (West) – This team has been examining the effects of two common additives, VC and vinylene triacetoxyvinylsilane (VS), on dendrite initiation and propagation. The base electrolyte for these experiments is 1.2 M $LiPF_6$ in EC:EMC (3:7 by weight). Figure IV-37(left) shows the effect of current density, *i*, on the time of first observed dendrite, t_{FOD}, for different electrolytes. The onset of dendritic growth is delayed when VS is used at both 2 and 5% concentrations. Dendrites are not significantly inhibited using VC for *i* of 4 and 10 mA cm^{-2}. However, VC does inhibit dendrites at 1 and 2mA/cm^2. Videos (located at http://lithiumdendrite.blogspot.com/) show that dendrites propagate slower when VC is used.

Figure IV- 37(right) shows the dendrites' area as a function of time (after first observed dendrite). This area was obtained using ImageJ software. All data was repeated three times and the error bars are the standard deviation. The dendrite area increases nearly linearly during Li deposition. Once a dendrite forms it grows at a slower rate in VC.

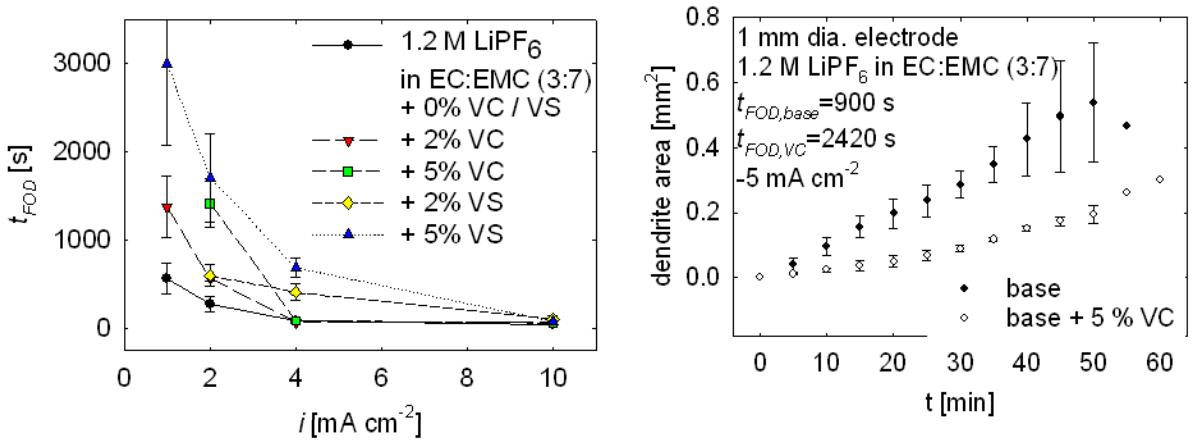

Figure IV- 37. (Left) Effect of i on t_{FOD} for various additives, and (Right) dendrite area growth with and without VC.

Figure IV- 38(left) shows the effect of the ratio of PC and DMC on $t_{FOD,}$ for two current densities. The limiting current, i_{lim}, of these electrolytes is between 150mA/cm^2 for PC and 50mA/cm^2 for DMC. t_{FOD} decreases linearly with increasing PC content, and t_{FOD} increases by a factor of 3–4 when the current density doubles, except for pure DMC. If mass transfer plays a dominant role, it may be expected that t_{FOD} would decrease with increasing amounts of DMC because i_{lim} increases. However, t_{FOD} increases with DMC. This suggests that the mass transfer of Li to the electrode might not be the cause of Li dendrite initiation. Furthermore, the microfluidic device quickly sets up a steady diffusion layer calculated to be ~10µm depending on the electrolyte and electrolyte flow rate. The flow system demonstrates that dendrites would form under conditions where mass transfer is not an issue.

Figure IV- 38 (right) shows current density at the dendrite tip, i_{tip}, for deposition from the base electrolyte for 300 s after t_{FOD}. This calculated current density is even less than the actual current density due to branching. The calculated current density is similar for the averaged current densities of 2 and 4 mA/cm^2. That the current density at the dendrite tip only varies slightly when the average current density doubles suggests that the deposition may be mass transfer controlled. The dendrite tip radius is 29 and 20 µm during the 2 and 4 mA/cm^2 depositions. The dendrite with the smaller radius has the higher maximum i_{tip}. The limiting current density for a hemisphere is calculated as 164mA/cm^2 for 29µm and 241mA/cm^2 for 20µm. In the figure, the maximum i_{tip} is greater than i_{lim} for both of these cases. These observations lead us to believe that although dendrite initiation may not be correlated with the fraction of the limiting current density averaged over the entire surface, growth is mass transport controlled.

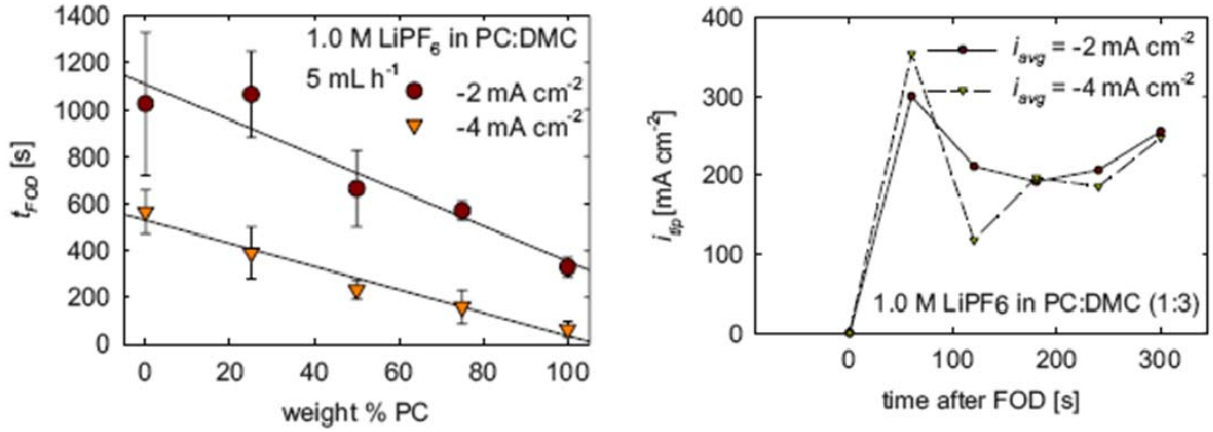

Figure IV- 38. Left-Effect of solvents and *i* on t_{FOD}. Right–Time dependence of I_{tip} at different average current densities.

Figure IV- 39 (left) shows that dendrite initiation is delayed when a resistance given by the Tafel slope, R_{Tafel}, is increased (the line is fit to the 1.0 M $LiPF_6$ in PC:DMC data). The 1.2 M $LiPF_6$ in EC: EMC (3:7 by wt) and 1.0 M lithium bis(trifluoromethane-sulfonyl)imide (LiTFSI) in PC:DMC (1:3 by wt) data are, however, included and fit well to the trend. This shows that the type of solvent or salt does not affect the relationship between t_{FOD} and R_{Tafel}. These results are published in *J Electrochem Soc*, 155 A806, (2008).

Figure IV- 39(right) shows the impact on t_{FOD} of an anodic pulse. The pulse amplitude is the ratio of the current density while the anodic pulse is on to that while the pulse is off. The amplitude of 0 is galvanostatic Li deposition at -4 mA cm^{-2}. The pulses are 100 ms every 9.9 s. Using the pulse amplitude of 10 can delay the formation of dendrites by an average of 2.5 times.

In summary, mass transport does not seem to play a role in dendrite initiation. However, deposition quickly becomes mass transfer controlled after dendrite formation. High interfacial resistance inhibits dendrite formation; however, it also hurts battery performance due to slowed Li transport. Dendrite initiation can also be delayed using additives and pulse plating.

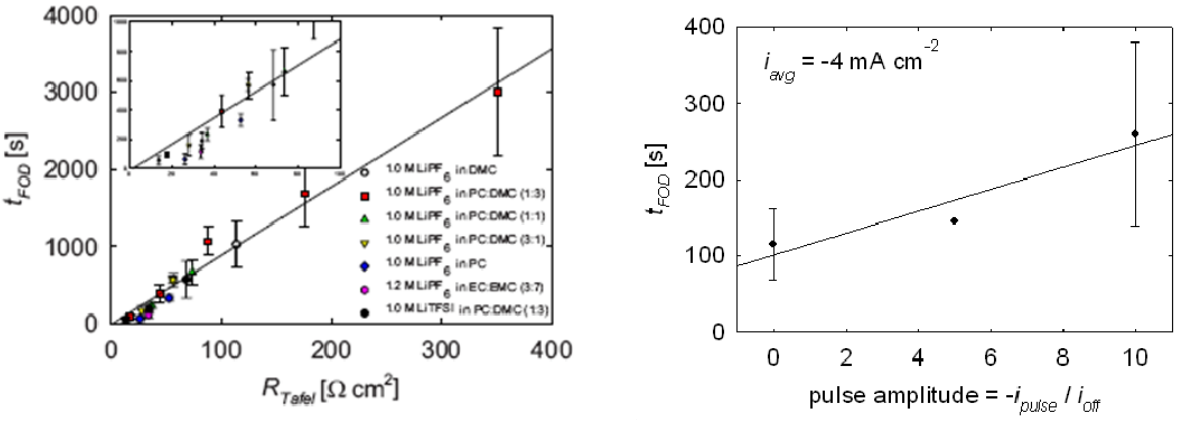

Figure IV- 39. Left - Effect of R_{Tafel} on t_{FOD}. Right - Effect of anodic pulse plating on t_{FOD}

Sulfide and Sulfochloride Anode Materials (Goodenough) – As a first step, this team studied the displacement reaction $2Li + MS = Li_2S + M$ to determine the energies of the bottom of the 4s band relative to the Fermi energy, E_F, of Li in the monosulfides with the $B8_1$ structure: yielding two important facts: (1) The bottom of the 4s band falls progressively to lower energies with increasing atomic number of the 3d-block M^{2+} ions in MS; in $Ti_{1-x}S$, it is at or just above the Fermi energy of Li and by NiS it has dropped by about 1.5 V to 1.47 V *vs.* Li. The only viable 4s-band edge is associated with the Ti^{3+}/Ti^{2+} and V^{3+}/V^{2+} couples, both of these edges are above ~0.85 V *vs.* Li in the $M_{1-x}S$ compounds. (2) Reversibility of the Li-insertion reaction only occurs for FeS, $Co_{1-x}S$, and NiS where the product of the insertion reaction is an amorphous phase rather than the predicted $Li_2S + M$. Capacity fades with the production of Li_2S at the surface of the particles, Figure IV- 40. Formation of the amorphous phase increases as the bottom of the 4s band is lowered relative to E_F, which suggests that the amorphous phase is made more competitive with formation of Li_2S by hybridization of the Li-2s and M-4s states.

In the exploration of insertion compounds operating on the Ti^{3+}/Ti^{2+} and V^{3+}/V^{2+} couples, this team has found that where E_F of the anode is less than 0.8 eV below that of Li, a Lowest Unoccupied Molecular Orbital (LUMO) in the electrolyte lying at 0.8 eV relative to Li is reduced with the formation of an SEI layer. The SEI layer on the surface of carbon is permeable to Li^+ ions. However, with the oxides, the SEI layer does not appear to be permeable to Li^+ ions, so diffusion of Li is blocked. In the case of the layered sulfides $Li_{1+x}TiS_2$ and $Li_{1+x}VS_2$, an SEI forms on the surface of $LiTiS_2$ at 0.8 V *vs.* Li, Figure IV- 41(a), is followed by a reversible plateau at 0.5 V, which appears to corresponds to the Ti^{3+}/Ti^{2+} couple. This result is interpreted to mean that the SEI layer formed on the sulfide is permeable to Li^+ ions. In the case of $Li_{1+x}VS_2$, the V^{3+}/V^{2+} couple is seen to be at 1.0 V *vs.* Li in Figure IV- 41(b), which means that its E_F lies below the LUMO of the electrolyte. In this case, no SEI layer is formed, and this anode material can be cycled. However, there is some capacity fade. Nanoparticles will be prepared to minimize any problem of volume changes.

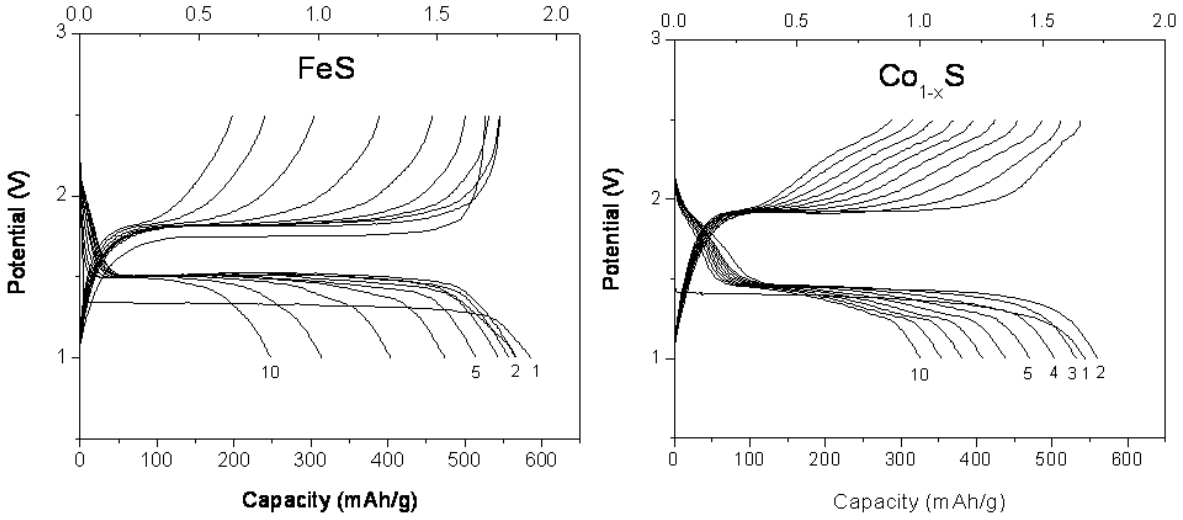

Figure IV- 40. Discharge and charge curves for the FeS and CoS for the first ten cycles between 1.0 - 2.5 V at rate of 0.1 mA/cm^2.

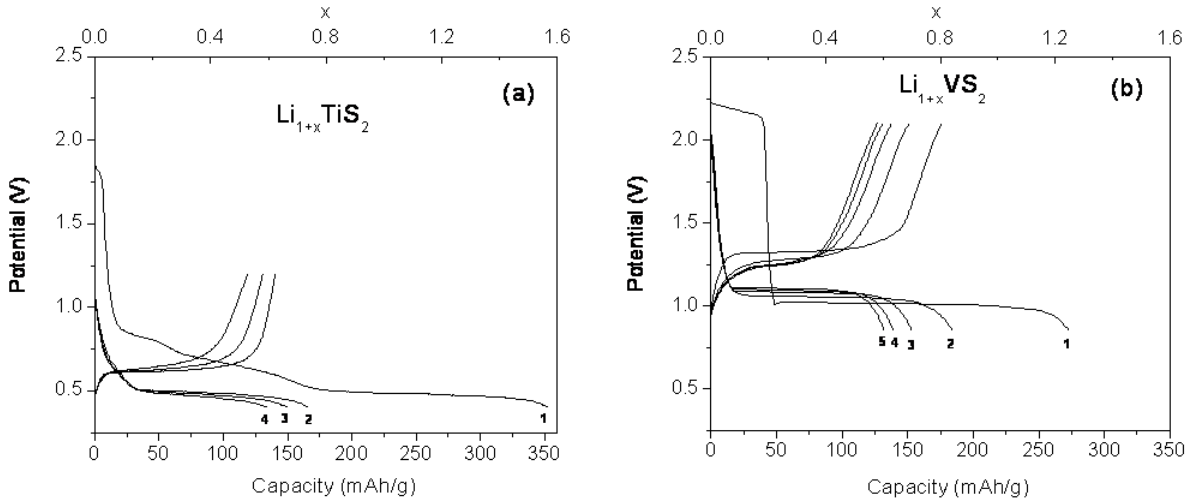

Figure IV- 41. Discharge and charge curves for the (a) LiTiS2 and (b) $LiVS_2$ for the first five cycles at rate of 0.1 mA/cm^2.

Sample Future Plans in Anode R&D

- Continue to study the MoO_3 SEI and attempt to eliminate its formation by changing voltage cut-offs or applying a protective coating to achieve the theoretical capacity and better cycling stability.
- Perform calculations to understand the hysteresis in the charge/discharge profiles of MoO_3 nanoparticles.
- Solutions for better anode materials appear to require either the development of an electrolyte with a higher LUMO energy or coating the particles with an amorphous carbon that provides a kinetic barrier to the formation of an SEI layer on the active particles. Both alternatives will be explored in the future.
- Continue searching for Si- and Sn-based intermetallics, notably those with a structural relationship between the parent and lithiated products. Exploit multi-component systems to improve cycle life by minimizing Li diffusion distances. The approach is influenced by the fully reversible sodium insertion-nickel displacement reaction that occurs in high-T (300°C) $Na/NiCl_2$ cells. The volume expansion of the close-packed Cl^- array during the $NiCl_2$ to NaCl transformation is ~47% and the total cathode expansion is ~64% if the extruded Ni is also taken into account. The excellent coulombic efficiency and cycle life is attributed the constrained grain growth of the extruded Ni particles during discharge and keeping the Ni particles in contact with the NaCl particles and in contact with a porous 'inactive' Ni current collector. It should be possible, in principle, to design a similar intermetallic electrode for Li-ion cells that can operate with similar efficiency but at room temperature.
- Investigate interfacial properties of intermetallic anodes. Focus on Sn-, Si-based materials. Investigate diffusion through thin-layer (<20 nm) metallic anodes and surface phenomena at the metal/electrolyte interface. Use thin <40 μm HOPG membranes as a template, with one side coated with a metallic layer. Develop a time-dependent mass transport model to validate the experimental behavior and determine Li^+ transport parameters in metal coated graphite anodes.

The very large ICL associated with intermetallic anodes can be reduced or eliminated by preparing composite materials in a pre-lithiated state. The lithium nitride metathesis route, for example: $4Li_3N + 7Si = Li_{12}Si_7 + 2N_2$, can be used to prepare fully or partially lithiated Si. The level of pre-lithiation can be limited to only that required to reduce native oxides, leaving the powder in a less reactive state amenable to electrode fabrication. It may be possible to carry out the reaction in the presence of carbon black so that subsequent mixing is unnecessary.

- Explore Sn and Si compounds as well as simple oxides; the role of cobalt will be understood to allow cobalt-free materials to be used. Investigate the impact of depth of cycling for Sn.
- Synthesize different structural morphologies of nano-scale Si (*e.g.*, amorphous, nano-rods or nano-wires) and *in situ* generated Si/C based nano-composites to bypass the formation of $Li_{3.5}Si$. This strategy is expected to yield stable electrodes exhibiting excellent performance including a higher specific capacity as well as improved capacity retention and rate capability. Explore economical methods to synthesize *a*-Si and *a*-Si/C based anodes for obtaining capacities >700mAh/g cycled in the potential window 0.02V-1.2V. Explore chemical vapor deposition (CVD) derived MWCNTs, Figure IV- 42, along with graphite and Si for obtaining stable capacities greater than 1000mAh/g.
- Use *in situ* spectroscopic ellipsometry to investigate the early stages of surface film formation on Sn and Si during formation. SEI thickness and composition will be monitored. Determine the nature and kinetics of surface phenomena and their impact on performance of the intermetallic anodes. Use *in situ* and *ex situ* AFM, Raman and FTIR spectroscopy to provide parameters of the surface film and support the numerical analysis of the ellipsometric data.

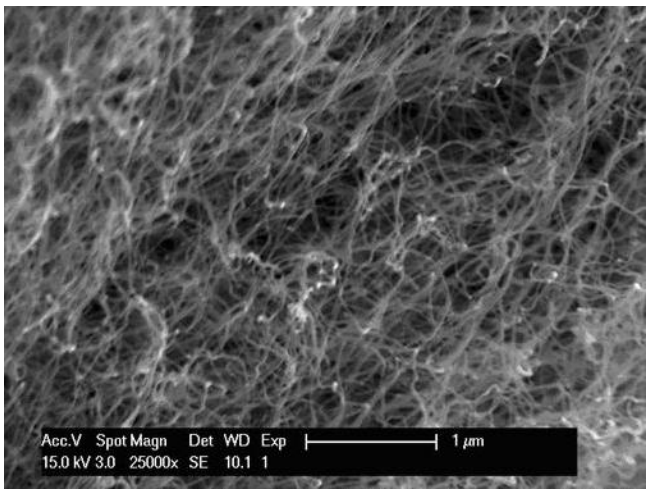

Figure IV- 42. Carbon nanotube generated by CVD method.

- Study the growth of single Li dendrites. We have designed a system to grow single Li dendrites using common microfabrication techniques. Thermal evaporation is used to obtain a smooth layer of Cu to use as the working electrode. Wells, 30 to 100 µm in diameter and ~100 µm deep, are patterned onto the Cu in an insulating photoresist. A drop of electrolyte is placed in the well as well as a thin Cu wire counter electrode outside the

well. Li will be deposited using galvanostatic and potentostatic techniques. A single dendrite should form that will be unable to spread due to the confines of the well. The electrochemical response hopefully will give more insight to the mechanism of dendrite formation.

IV.C Novel Electrolytes and Their Characterization

OBJECTIVES

Study the stability of Polystyrene (PS)- Poly(ethylene oxide) (PEO)/LiTFSI electrolytes against Li electrodes, test their properties against Li-metal anodes and $LiFePO_4$ cathodes, and investigate the use of block copolymers as separators with liquid electrolytes.

Investigate the impact of water on electrolyte stability and electrode performance. Determine whether the interfacial impedance of single ion conductors (SIC) can be reduced to practical values (< 20 Ωcm^2).

Synthesize fluorosulfonimide ionomers of variable structure in lithiated form (LiFSI) as dispersions in solvent; fabricate high-voltage cathodes using the resulting LiFSI ionomers as binders and/or as integral electrolytes; characterize the resulting cathodes with respect to initial capacity, high-rate charging/discharging capability, and capacity fade.

Gain molecular level understanding of Li^+ transport mechanisms in ionic liquids, SEI layers and the process of Li intercalation/deintercalation from/into graphite, and from cathodes into/from liquid electrolytes. Provide guidance for design of novel electrolytes with improved Li^+ transport, reduced interfacial resistance, and/or improved electrochemical stability allowing higher voltage operation. Explore ability of reactive force fields to predict SEI layer composition and structure on graphite in contact with ethylene carbonate solvent.

APPROACH

Salt/polymer mixtures are characterized by AC-impedance spectroscopy and DC measurements on Li cells. Interfacial impedance is often very high with solid electrolytes, thus efficient contact between the electrolyte and electrodes are sought, and the stability of the electrolyte against Li metal and $LiFePO_4$ electrodes is being evaluated. Finally, polymer separators are prepared using a block copolymer with a degradable block. The pores left behind by the degradable block are filled with conventional electrolytes and used in Li cells.

Ionomer synthesis focuses on copolymerization of functionalized trifluorovinyl ether monomers with tetrafluoroethylene, and also homopolymerization of trifluorovinyl ether monomers. Characterization utilizes NMR, IR, calorimetry, titration, and other approaches. Electrode fabrication uses mixtures of active materials NMC, conductive additives, and binders (PVdF and LiFSI ionomers). Electrode characterization is accomplished using galvanostatic polarization at variable current density using flooded three-electrode cells.

Extend a set of many-body polarizable force fields to predict ion transport, structural and thermodynamic properties of ILs, liquid electrolytes, and representative SEI components using molecular dynamics (MD) simulations. Calculate resistance and a free energy barrier associated with Li^+ intercalation from electrolyte into the representative cathode materials and graphite.

ACCOMPLISHMENTS

Composite Polymer Electrolytes (Balsara) – Several polymers have been synthesized and characterized, including three with low molecular weights (MW) (below 10 kg/mol) and three

with very high MWs (over 300 kg/mol). These polymers, when doped with LiTFSI, form solid polymer electrolytes (SPE). A summary of materials is given in Table IV- 1.

Recently, this group has completed conductivity measurements on cylindrical (70% styrene) and lamellar (50% styrene) samples. Ideally, conductivity in PS-PEO ($\sigma_{PS\text{-}PEO}$) can be predicted by assuming that the conductivity of PEO in these samples is the same as the bulk (σ_{PEO}), and that deviations from the bulk conductivity will depend proportionally on the volume fraction of PEO (φ_{PEO}). If one assumes no added transport resistance across grains, a constant morphology factor (MF) can be applied to account for 1- or 2-dimensional conductivity in cylindrical (MF = 3) or lamellar (MF = 3/2) samples (see Sax and Ottino[14]), resulting in a normalized conductivity parameter of $\sigma_{Normalized} = \frac{\sigma_{PS-PEO}}{\sigma_{PEO}\phi_{PEO}} xMF$.

Table IV- 1. Current polymer inventory. All polydispersities are less than 1.20, most are less than 1.10.

Code	Mn PS (kg/mol)	Mn PEO (kg/mol)	Vol. Fr. PEO	PEO Structure	Code	Mn PS (kg/mol)	Mn PEO (kg/mol)	Vol. Fr. PEO	PEO Structure
SEO-1	36.3	24.6	0.38	Lamellar	SEO-10	313.5	38.6	0.101	Spherical
SEO-2	39.7	31.3	0.42	Lamellar	SEO-11	6.3	7.2	0.519	Lamellar
SEO-3	18.8	29.1	0.58	Lamellar	SEO-12	1.4	2.5	0.62	Lamellar
SEO-4	39.6	53.6	0.55	Lamellar	SEO-13	2.3	4.6	0.65	Lamellar
SEO-5	74	98	0.55	Lamellar	SEO-14	3.1	5.1	0.60	Lamellar
SEO-6	16.2	16.3	0.48	Lamellar	SEO-15	216	102	0.3	Cylindrical
SEO-7	52.9	67.6	0.54	Lamellar	SEO-16	360	165	0.295	Cylindrical
SEO-8	37	25.4	0.385	Lamellar	SEO-17	170	187	0.505	Lamellar
SEO-9	53.5	22.9	0.281	Cylindrical					

If all assumptions hold about transport in PEO microdomains, $\sigma_{Normalized}$ will be 1. Results for a variety of cylinder- and lamellae-forming polymers at fixed salt concentration and temperature show that this varies widely with MW and morphology (Figure IV- 43). Lamellar samples approach expected behavior as the MW of the PEO block increases. Departures from ideality at low MWs and in cylindrical samples are under investigation. Understanding and correcting these deviations would lead to significant improvements to electrolyte performance.

Structural studies using small-angle X-ray scattering are underway and have provided insight on what structures are forming, how they are affected by the addition of salt, and how that impacts electrochemical performance. For instance, it has been found that structures exhibiting excellent long-range order with well-defined channels show no clear advantages in terms of conductivity.

Measurements of diffusion coefficients as a function of salt concentration, temperature, morphology, and MW have begun. Transference number measurements are also underway using the current interrupt method and the concentration cell method developed by Newman et al.[15] The

[14] Sax, Ottino, *Polym. Eng. and Sci.*, **1983**, *23*, 3.

[15] S. Stewart and J. Newman, JECS 155, A458, (2008)

salt diffusion coefficient varies from 2 to 5 x10^{-12} m^2/s and the Li^+ transference number varies between 0.15-0.35.

Cycle experiments on a Li/SPE/$FePO_4$ cell have been performed at 80°C with no capacity loss, see Figure IV- 44. We are working on methods to improve contact between hard SPEs and $FePO_4$ particles. Extended cycling experiments are underway, with plans to run experiments with increased area of the polymer film, higher current densities and thinner polymer films. The effect of temperature on cell cycling will also be examined.

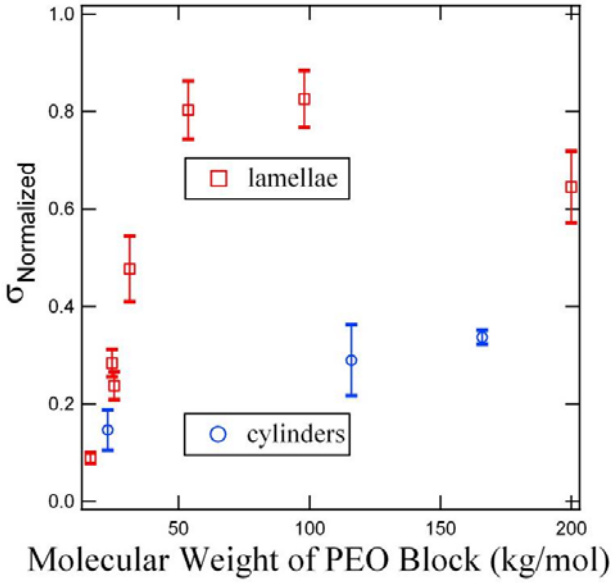

Figure IV- 43. Normalized conductivities for lamellar and cylindrical samples show significant deviations from ideality at low MW and in cylindrical samples. Salt concentration fixed at [Li]/[EO] = 0.085, T = 100°C.

Modification of Electrode/Electrolyte Interfaces to Optimize Interfacial Impedance and Minimize Side Reactions (Kerr) – The battery community appears to agree that water contamination can severely impact cell performance, but little quantitative analysis has been published. This group is evaluating electrolytes by aging samples at various temperatures and following the evolution of the viscosity and chemical composition, and by subjected the electrolytes to defined water contamination (8 ppm, 15ppm and 150ppm). Both $LiPF_6$ and LiTFSI electrolyte solutions have been prepared and subjected to heating at 40°C under sealed conditions in glove boxes. Samples have been taken to follow the evolution of the water content, electrolyte viscosity, and reaction of the electrolyte components. Electrolyte samples have been analyzed by GC/MS and gel permeation chromatography (GPC) after 7 days at 40°C and the GPC clearly shows the evolution of a small amount of product in the $LiPF_6$ electrolyte with an elevated molecular weight ~5-10k. No such peak is observed with the bis(trifluoromethanesulfonyl)imide (TFSI) control.

Measurement of the solution viscosities were carried out before and after heating. The viscometer is in a glove box with a heating and cooling system built in. Thus samples can be prepared, titrated

by Karl–Fischer for water, measured for viscosity and incorporated into cells or other measuring devices without any exposure to atmosphere. The effect of heat on the viscosity of the 8-15ppm water content electrolytes is shown in Figure IV- 45. Effects are negligible for the conditions used; higher temperatures and higher water contents are under test.

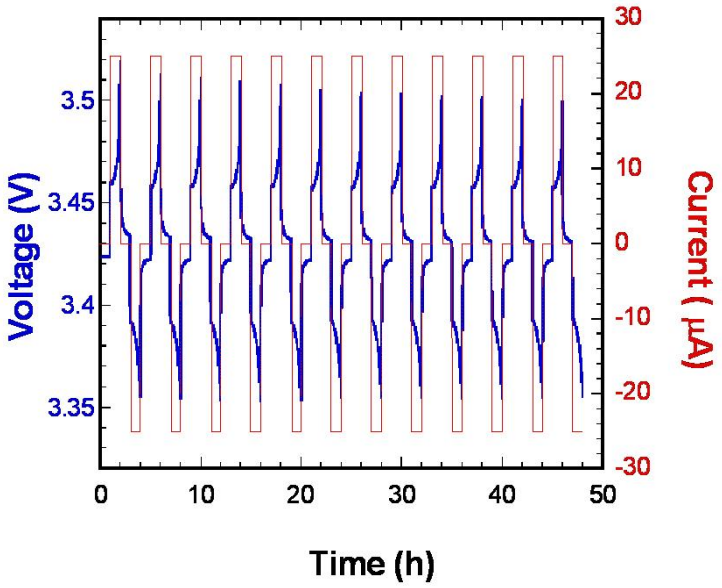

Figure IV- 44. Cycling of Li/SPE/$FePO_4$ cell with r = Li/EO= 0.067, i = 200 uA/cm^2

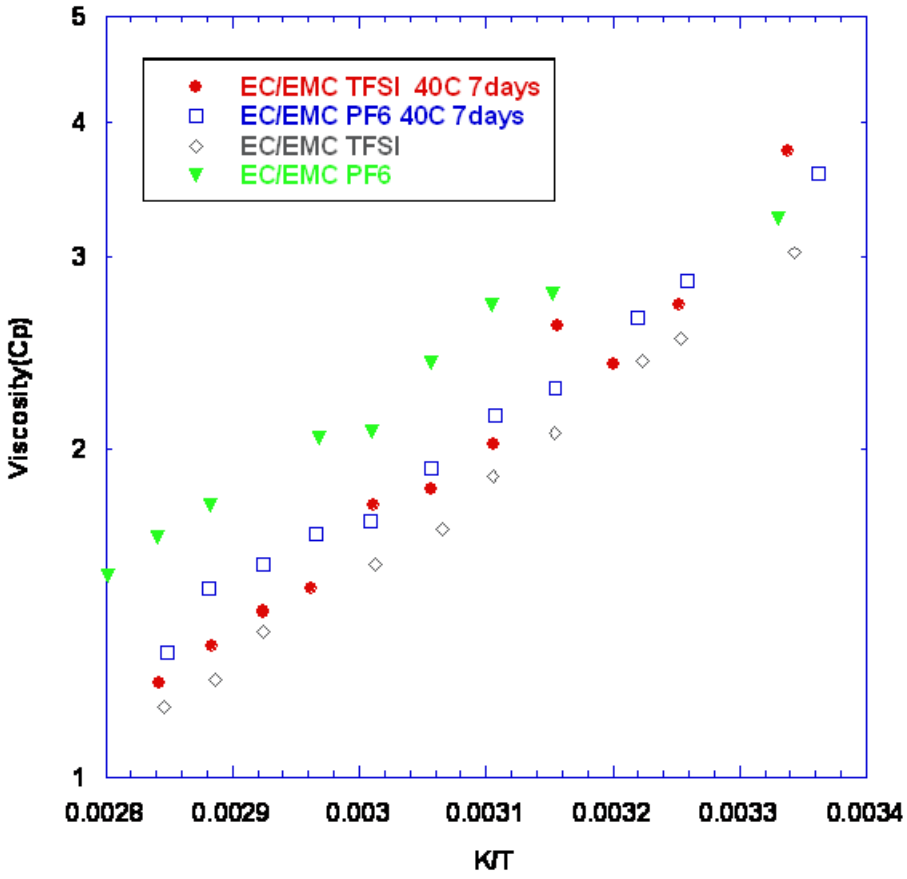

Figure IV- 45. Viscosity of dry electrolytes (1M Li salt) as a function of salt and temperature.

GPC analysis of $LiPF_6$ electrolyte, further heated at 50°C for several days, shows that the molecular weight of the polymeric products decrease and capillary electrophoresis (CE) analysis shows the formation of phosphate anions. Li phosphate is essentially insoluble in the electrolyte, so in a real cell it will precipitate on the surface of the electrodes. Thus, the use of $LiPF_6$ electrolytes has the advantage of generating compounds that are presently under study as protective layers for cathodes. The reactions that lead to this chemistry appear to be promoted by water and the effect of the water on the interfacial impedance has been monitored. Figure IV- 46 shows the impedance behavior of a "wet "electrolyte at a Gen 3 graphite anode. The right hand plot shows the Nyquist plots at different SOCs. It should be noted that prior to intercalation of Li into the electrode the interfacial impedance is 10 times greater. It is clear that some chemistry occurs on charging that alters the electrode surface which probably results in better wetting of the electrode which is likely due to the formation of surfactant-type products such as phosphates. The left hand plot shows the exchange current densities for cells with aged "wet" electrolytes, which are obtained from impedance measurements as a function of temperature. The most interesting result is that the activation energy for the fresh "wet" electrolyte is clearly different. The aged electrolytes show steeper temperature dependence and the water content measurement shows the disappearance of water with aging that correlates with interfacial impedance changes. These measurements are made with a two-electrode cell with a lithium counter electrode. More accurate

three electrode measurements with a reference electrode, currently underway, will provide more useful information. In the coming year, more revealing GPC/MS and CE/MS measurements in combination with FTIR and Raman spectroscopy will allow identification of the species on the electrode surfaces that are responsible for the observed behavior.

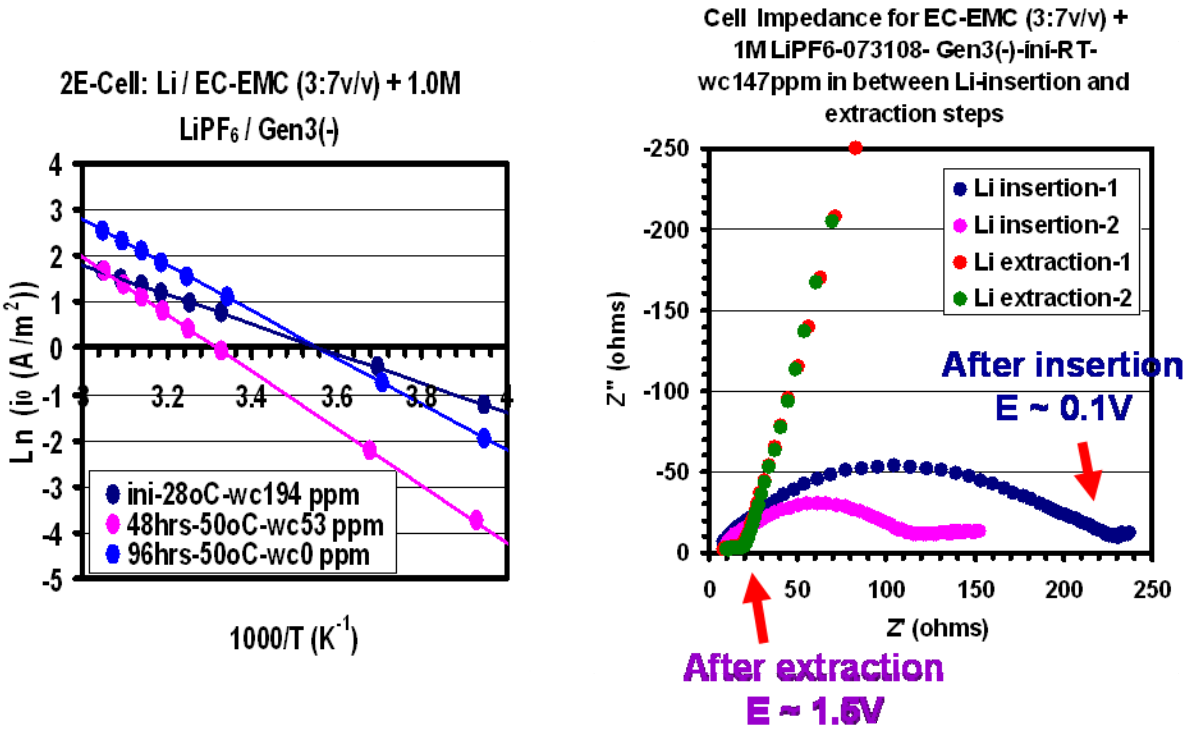

Figure IV- 46. (Left) Exchange current densities obtained from impedance measurement after aging the electrolyte separately from the electrodes, (Right) Interfacial impedance of $LiPF_6$-EC/EMC electrolyte at Gen 3 graphite anodes as a function of SOC (Note the decrease in water content with time).

Single-ion Conducting (SIC) Polymer Electrolytes (Kerr) – Preparation of SIC materials is proceeding following the methods previously published[16]. Materials such as that shown in Figure IV- 47 should be stable in excess of 4V. In the structure shown, solvents such as EC and EMC will be necessary to achieve conduction. However, since these materials are likely to show some phase separation with the solvents, there is scope to investigate how preparation as a block co-polymer can affect the morphology. It is of interest to determine whether some of the Y groups could be replaced with cyclic carbonate groups to provide a solid polymer electrolyte capable of 4V operation.

A major issue previously observed with the use of SICs has been the large interfacial impedance at both lithium metal and intercalation electrodes. The source of this impedance is not understood and it is hoped that studies of the interfacial behavior similar to those described above will lead to insights into the nature of the interfacial barriers and how the electrode interface can be tailored to minimize the impedance and hence increase the energy and power density of Li-ion batteries.

[16] Sun XG, Hou J, Kerr JB. *Electrochimica Acta* 2005; 50:1139; Sun XG, Reeder CL, Kerr JB. *Macromolecules* 2004;37:2219; Sun XG, Liu G, Xie JB, Han YB, Kerr JB. *Solid State Ionics* 2004;175:713; Sun XG, Reeder CL, Kerr JB, DesMarteau DD. Abstracts of Papers of the American Chemical Society 2004;228:U352-U352.

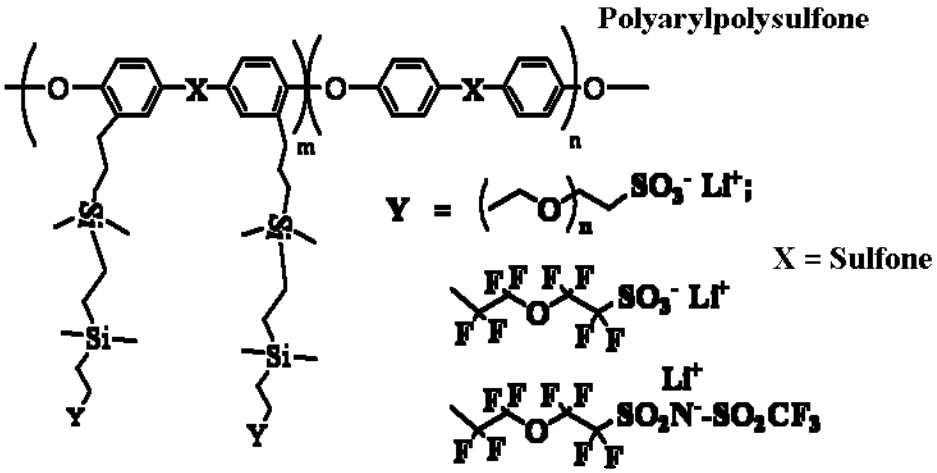

Figure IV- 47. Sample single ion conductor (SIC) structure

Molecular Dynamics (MD) Simulations of Bulk Electrolytes (Smith) – MD simulations of liquid electrolytes doped with LiTFSI salts have been extended to include $LiBF_4$ and $LiPF_6$ salts. A new generation of force fields has been developed for a number of electrolytes based on EC, PC, DMC, EMC, γBL doped with $LiPF_6$ and $LiBF_4$. MD simulations accurately predicted electrolyte density, viscosity, conductivity and ion self-diffusion coefficients. Figure IV- 48 shows electrolyte conductivity vs. salt concentration for PC doped with $LiBF_4$ and $LiPF_6$ salts from MD simulations and experiments. Similar quality agreement has been obtained for other electrolytes, validating the ability of MD simulations to predict ion transport. In accord with experimental evidence, a much higher degree of ion aggregation has been found for $LiBF_4$ compared to $LiPF_6$ and LiTFSI salts in EC, PC and γBL solvents. Li^+ was found to be coordinated on average by four solvent and anion molecules.

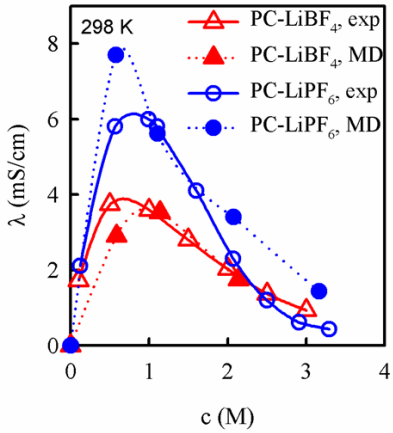

Figure IV- 48. Electrolyte conductivity predicted from MD simulations and from experiments (J. Phys. Chem. B 2003, 107, 10962).

Particular attention has been paid to understanding the lithium cation coordination in mixed solvent electrolytes composed of linear and cyclic carbonates. Mixtures of highly-polar EC with

lower melting point low viscosity DMC are utilized extensively in Li-ion batteries. While EC is very effective in dissolving lithium salts, the much less polar DMC is not. There is great interest in understanding the roles of EC and DMC in solvating and transporting Li^+ in mixed EC/DMC systems where DMC is often the majority component. Previous Raman and NMR measurements yielded a conflicting picture of Li^+ solvation. Quantum chemistry studies revealed that while binding is much stronger (by 6.5 kcal/mol) for EC/Li^+ than for DMC/Li^+ with DMC in its lowest energy, nonpolar gas phase conformer (cis-cis), the polar conformer of DMC (cis-trans) binds Li^+ only 2.5 kcal/mol weaker than EC binds to a Li^+. Those studies also revealed that when complexation of Li-PF_6 ion pairs is considered, the DMC(cis-cis)/$LiPF_6$ complex is about one kcal/mol more stable than the EC/$LiPF_6$ complex. The EC_3DMC(cis-cis)/Li^+ complex was found to be the most energetically stable among EC_nDMC_m/Li^+, n+m=4 investigated complexes followed by EC_4/Li^+ indicating that for gas-phase Li-solvent clusters DMC presence in the first Li solvation shell is expected.

MD simulations using quantum chemistry based potential accurately reproduce ionic conductivity in EC/DMC + $LiPF_6$ electrolytes as a function of composition and temperature. From these simulations, it was demonstrated that conductivity has a maximum due to offsetting effects of faster dynamics and greater ion pairing with increasing DMC content. Both EC and DMC were found to participate in Li^+ solvation in mixed EC:DMC electrolytes despite a large difference between their dielectric constants (90 for EC vs. 3 for DMC liquids). In contrast to previous NMR studies, where dominance of EC in cation solvation was reported, a slight preference was found for DMC in the cation solvation shell for EC:DMC(1 wt : 1 wt) electrolytes and show that re-analyzing previous Raman spectroscopy experiments (Morita, M. et al. *J. Chem. Soc.-Faraday Transactions* 1998, *94*, 3451) leads to good agreement with results of MD simulations if the changes in Raman peak intensities upon binding to a lithium cation and the existence of the cis-trans conformer of DMC in electrolyte are taken into account. Analysis of solvent residence times reveals that cation transport is dominated by motion of the cation with the solvent with respect to solvating DMC and approximately equal contributions from vehicular motion with the first solvation shell and solvent exchange with respect to solvating EC.

Ionic Liquid (IL) Electrolytes for High V Cathodes (DesMarteau) – Progress has focused on synthesis of fluoroionomer electrolytes in Li form, electrode fabrication and cell testing of composite cathodes prepared using fluorinated ionomers in Li form, and new IL solvents. Reported here are details of the synthesis of the homopolymer ionomer from monomer B in Figure IV- 49, not previously published. The synthesis proceeds as follows: 30% (w/w) of $[CF_2=CFOCF_2CF_2SO_2]_2NNa$ solution in water was treated with $K_2S_2O_8$ at 65-70°C for 24 hours to induce polymerization. After the water was removed, the homopolymer was washed with hot water several times and then treated with concentrated HNO_3 at room temperature overnight. After HNO_3 was removed, the gel polymer was again washed with hot water until the washings had a pH of ~7. Then the sample was neutralized with LiOH and dried under vacuum.

Composite cathode electrodes were fabricated using two fluorinated ionomers for which monomer structures are shown in Figure IV- 50. Monomer A was copolymerized with tetrafluoroethylene and monomer B was homopolymerized. In each case the cathode composition was 86% $LiCoO_2$, 5% carbon black, 5% ionomer (dissolved in N-Methylpyrrolidone), and 4% LHB-108P binder. Electrodes were deposited on 0.25 inch diameter stainless-steel rod current collectors and dried at 150°C under vacuum. Cell testing was attempted with LTO anodes using 1 M $LiPF_6$ / EC:DEC

(1:1) electrolyte, however, the results were compromised by unexpected humidity leaks in the glove box. This problem is being rectified.

Many ILs suffer from low conductivity due to high viscosity, thus this group has been attempting to decrease it. Two new ILs are being studied. The first consists of a partially fluorinated imidazolium cation of structure $(CF_3CH_2\text{-}C_3H_3N_2\text{-}CH_3)^+$, coupled with a TFSI anion. This IL is liquid at ambient temperature and appears to have a much lower viscosity than the corresponding non-fluorinated 1-ethyl-3-methylimidazolium - Bis(fluorosulfonyl)imide (EMI-TFSI) IL. Ionic conductivity exceeds 1mS/cm at room temperature. The second IL consists of a symmetric imidazolium, $(CH_3\text{-}C_3H_3N_2\text{-}CH_3)^+$, coupled with an asymmetric sulfonimide anion of structure $(CF_3\text{-}SO_2NSO_2\text{-}C_4F_9)^-$. This salt is liquid at ambient temperature whereas the corresponding material with TFSI anion is solid. The IL dissolves 20-30 wt% of the Li salt of the same anion. Conductivity studies are in progress.

Figure IV- 51 shows ionic conductivity data for a polymer electrolyte prepared by homopolymerization of monomer B shown in Figure IV- 49, and wetted by a 1:1 EC:DEC mixture. The polymer has a complex structure that is still being evaluated; however, even without definitive structural data it is clear from the conductivity data that the material is promising. Conductivities are above 0.3 mS/cm at all temperatures tested, which is much higher than for similarly swelled Nafion in lithiated form. The high conductivity is thought to reflect a combination of the relatively high ion-exchange capacity of this polymer electrolyte and its capacity to absorb large amounts of solvent (*i.e.*, it is a gel). Currently ongoing work will seek to prove that this material is in fact a single-ion conductor, and to test it as a battery separator.

Battery cathodes were prepared using $LiCoO_2$ as active material with acetylene black additive, with and without ionomer present in the binder. Battery testing was performed on cells prepared using an LTO anode and lithium salts (LiTFSI and $LiPF_6$) in EC:DEC (1:1) solvent. Preliminary cycle testing shows that when salt concentration is low (*e.g.*, 0.1 M) the cells with the ionomer from Figure IV- 49 in the cathode were much more easily charged than cells without ionomer in cathode. Ongoing work will explore more thoroughly the microstructure of cathodes containing ionomer, the effect of ionomer in the cathode on high-rate charging and discharging, and the capacity retention with $LiCoO_2$ and other cathodes.

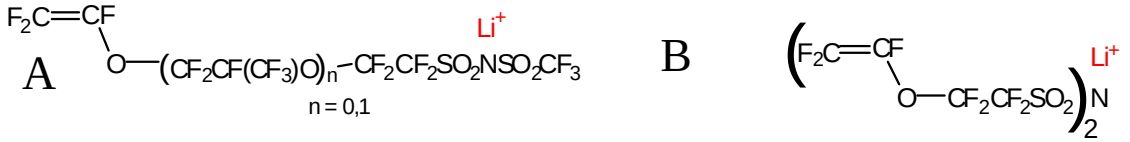

Figure IV- 49. Structures of trifluorovinyl ether lithium fluorosulfonimide monomers that will be used to make LiFSI ionomers for study in high-voltage NMC cathodes

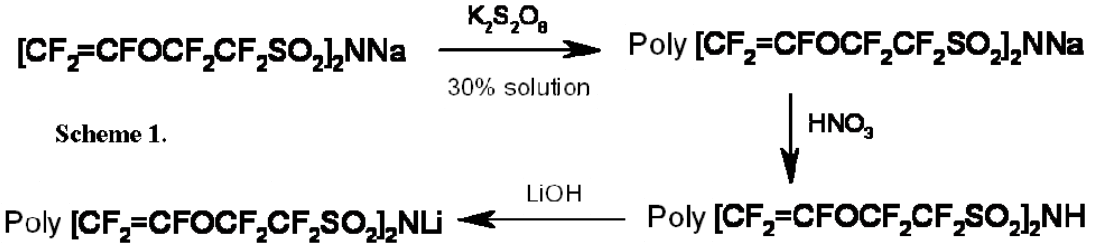

Scheme 1.

Figure IV- 50. Preparation Scheme 1

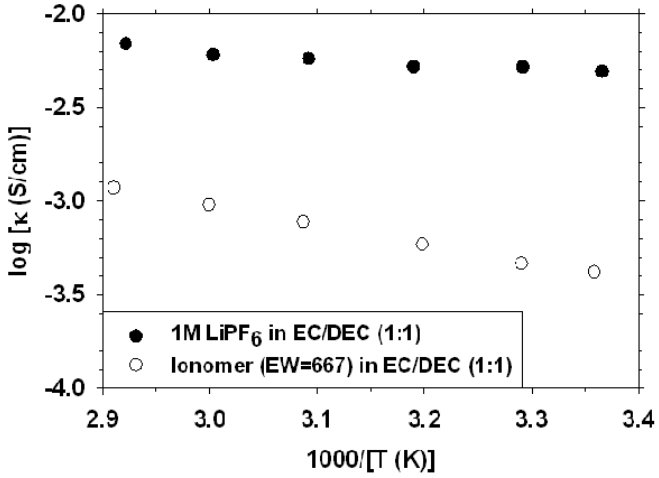

Figure IV- 51. Ionic conductivity of lithiated ionomer from monomer in Figure IV- 49, wetted with a 1:1 EC:DEC mixture.

Electrolytes using Li_2O or Li_2O_2 and Tris(pentafluorophenyl) Borane as Boron-based Anion Receptor (Yoon, Yang) – This new electrolyte family is based on the interactions between Li_2O or Li_2O_2 and tris(pentafluorophenyl) borane (TPFPB) in carbonate based solvents. This opens up a new approach in developing non-aqueous electrolytes. In general, the solubility of Li_2O or Li_2O_2 is very low in organic solvents and the ionic conductivities of these solutions are almost undetectable. As shown in Table IV- 2, by adding TPFPB, the conductivity of Li_2O or Li_2O_2 in carbonate based solvents is significantly enhanced. In addition, the Li^+ transference numbers of these new electrolytes are as high as 0.7, more than 100% higher than that for conventional electrolytes. These new electrolytes are compatible with $LiMn_2O_4$ cathodes for Li-ion batteries. The new electrolytes are also very valuable in the high energy density lithium-air battery systems.

Table IV- 2. Conductivity comparison of different Li_2O_2 and Li_2O based electrolytes at several temperatures.

No.	Electrolyte	Conductivity (mS/cm)				
		-40 °C	-20 °C	0 °C	20 °C	60 °C
a	0.4 M TPFPB-0.2 M Li_2O-PC:DMC (1:1)	0.105	0.434	0.901	1.43	2.82
b	0.2 M Li_2O-PC:DMC (1:1)	$7.55e^{-4}$	0.00246	0.00424	0.00620	0.0105
c	0.4M TPFPB-PC:DMC (1:1)	-	0.00225	-	-	0.0207
d	0.2 M Li_2O_2-PC:DMC (1:1)	0.00246	0.0119	0.0214	0.0329	0.0594
e	0.4M TPFPB-0.2 M Li_2O_2-PC:DMC (1:1)	0.186	0.673	1.16	1.76	3.18
f	0.4 M TPFPB-0.2 M Li_2O-EC:DMC (1:1)	2.26E-5	0.00952	0.624	1.72	3.10

Sample electrolyte future plans

- Continue synthesis and characterization of block copolymer electrolytes.
- Measure Li transference number and diffusion coefficient in block copolymer electrolytes.
- Complete electrolyte degradation analysis (with defined water contamination) under rigorously controlled conditions.
- Continue to explore how electrolyte degradation affects impedance growth at both electrodes.
- Conduct detailed analysis of cathode side reaction products and effects on interfacial behavior.
- Continue to study the effects of impurities (water, acids, additives) on interfacial behavior.
- Investigate dependence of the R_{ct} for electrolyte/graphite interface on the composition of electrolyte and choice of anion. Compare BF_4^- and PF_6^- and (fluorosulfonyl)-imide (FSI) - anions.
- Predict structure and transport in selected SEI components. Investigate interfacial resistance at the interface between a carbonate electrolyte and SEI components.
- Investigate the effect of different electrolytes and coatings on the high voltage processes, focusing on rate performance.
- Use simulations (using ReaxFF) on Li-metal to investigate reduction mechanisms and SEI formation, and on graphite to provide interfaces with lower interfacial lithium concentration. Formation of SEI at these interfaces will be investigated as a function of thermodynamic conditions and electrolyte composition.

IV.D Li-Ion Modeling, Diagnostics, and Cell Analysis

OBJECTIVES

Electrode fabrication is an area that many believe lies at the heart of poor cell performance, yet a fundamental understanding of how to fabricate an effective electrode does not exist. The objectives of the Cell Fabrication and Materials Characterization task are:

Provide a comprehensive and independent assessment of promising materials developed in the BATT program and to bring fundamental understanding to the area of electrode fabrication.

Improve battery power and life through novel electrode structures. Increase understanding of how electrode morphology influences performance. Develop modeling tools to analyze and predict high-rate performance.

Develop experimental methods for measuring transport and thermodynamic properties. Determine the effect of structure on the stability of electrode materials, and explore rate limitations and their relation to structure and particle size/morphology.

Reduce the inactive mass fraction in cathodes using advanced simulation and experimentation. Determine optimal particle blends for high power and long lifetime for both energy- and power-dense systems. Predict failure mechanisms in cells, considering coupled electrochemical and mechanical effects.

Use mathematical models combined with experiments to quantify the usefulness of alloy anodes, specifically silicon, for use in PHEVs. Develop experimental methods to extract the relevant controlling parameters from model thin film materials. Use models to extrapolate thin film behavior to behavior of porous electrodes.

APPROACH

Apply diagnostic techniques including Brunauer, Emmett, and Teller (BET), scanning electron microscopy (SEM), particle size analysis (PSA), inductively-coupled plasma (ICP), TEM and others, to obtain physical, chemical, thermal, and electrochemical characterization of materials as they relate to battery performance. Insight into electrode fabrication is accomplished through engineering design analysis of each of the steps of the electrode fabrication process.

Use NMR and diffraction to characterize material structures as a function of particle size, sample preparation method, SOC, and number of charge cycles. Develop *in situ* and *ex situ* NMR methods to identify structural changes and SEI formation. Use calculations and NMR spectroscopy to identify low activation energy pathways for cation migration and to investigate electronic conductivity.

Use finite element simulations, with continuum modeling of V. Srinivasan, to eliminate inactive mass from cathodes, improving gravimetric properties. Coupled mechanical and electrochemical effects will be considered to develop optimal combinations of materials for high power and long life. These will inform electrode design. New atomistic simulation results will be used to provide

first-principles-estimates of conductivity. Shapes and type of materials will be considered with other BATT workers (M. Doeff, LBNL; K. Zaghib, Hydro-Québec).

Develop models for candidate Li-ion chemistries. Design experiments to test theoretical predictions and estimate properties needed for the models. Use models to connect fundamental material properties to performance and provide guidance to material-synthesis and cell-development PIs and quantify the ability of candidate chemistries to meet performance goals.

Use simulations such as 1 – A simplified, 0-dimensional model, for basic insights, and 2 - A detailed battery and vehicle model for examination of the complexities of the battery's usage. Develop improved experimental methods for measuring transport and thermodynamic properties, including restricted diffusion to measure diffusion coefficients, AC impedance for conductivity, and melting point depression for activity coefficients.

ACCOMPLISHMENTS

In situ NMR Diagnostics (Ceder, Grey) – A new *in situ* NMR has been constructed to permit studies of operating batteries. The design is based on that of Letellier and co-workers[17] and uses small plastic batteries (with electrodes of area ~0.35 x 0.9 cm^2) that can fit inside a 5 mm NMR coil in a static NMR probe. The set up has been tested with (bulk and nano-) $LiCoO_2$/Li and Si/Li cells. In the case of the Si system, the approach has been used to directly observe the self-charge of the Si cells vs. Li (i.e., self-discharge, in a cell where Si acts as the negative electrode), which is extremely rapid at deep discharge.

Figure IV- 52 shows the *in situ* NMR spectra of the Si/Li cell, and the corresponding electrochemical data. The NMR spectra were compared with *ex situ* spectra of samples taken from batteries cycled to different SOC, and from model compounds in the Li-Si phase diagram. Surprisingly, a new local environment was identified in the *in situ* NMR experiments at deep discharge (close to 0 V, *vs.* Li), which is associated with a negative chemical shift (~10 ppm). This local environment was not observed in the *ex situ* NMR experiments. This new NMR signal is ascribed to Li insertion into the crystalline phase, $Li_{15}Si_4$. The results suggesting that this phase, which has previously been shown to form at ~50 meV at the end of the discharge process,[18] is not a line-phase, but it can accommodate additional Li. Furthermore, the phase with additional Li is extremely reactive. The self-charge of the battery at deep discharge can be directly monitored in the *in situ* NMR set-up, the intensity of peak at –10 ppm, decreasing to zero over a period of 10 hours. This is ascribed to the oxidation of $Li_{15+\delta}Si_4$, and the accompanying reduction of the electrolyte. The effect of the different binders on the rate of this reaction is being explored.

[17] Letellier, M.; Chevallier, F.; Clinard, C.; Frackowiak, E.; Rouzaud, J. N.; Beguin, F.; Morcrette, M.; Tarascon, J. M.. *J. Chem. Phys.* 2003, 118, 6038-6045.
[18] Obrovac, M. N.; Christensen, L., *Electrochem. Solid St. Lett.* 2004**,** 7, (5), A93-A96.

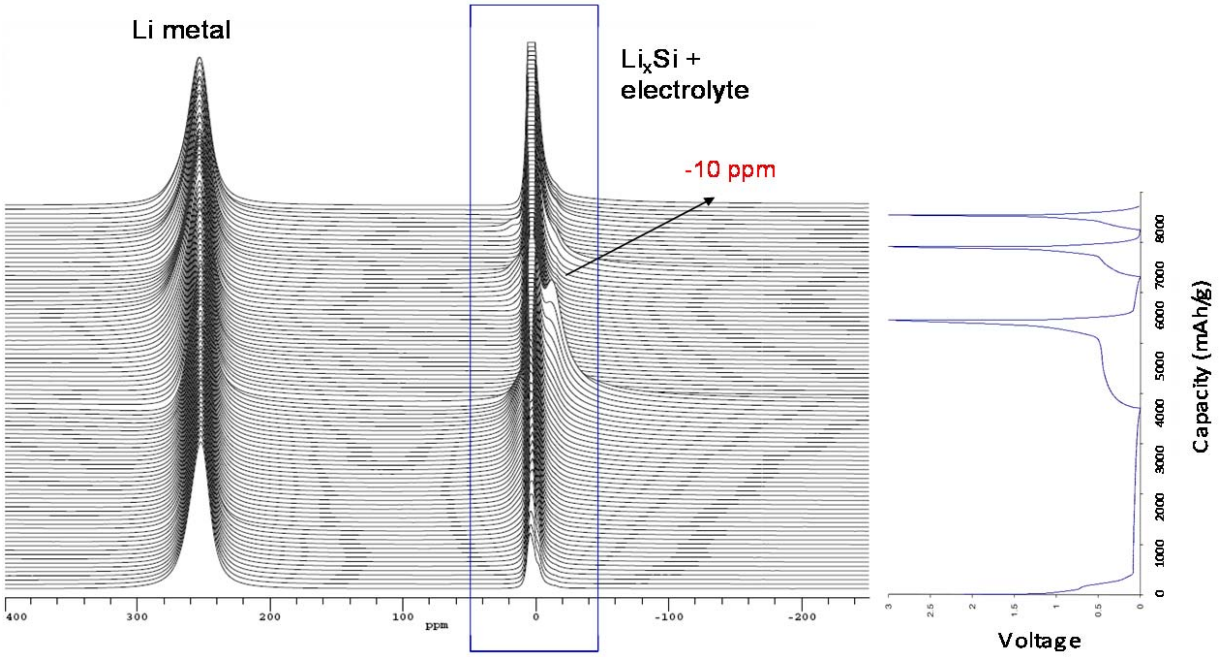

Figure IV- 52. ^{7}Li NMR (left) and electrochemistry (C/75) of a Li/Si cell. The Si electrode comprises Si:C (1:1 by weight) + PVdF binder.

Models of Si Anodes (Srinivasan) – The motivation of this study was to understand lithiation and delithiation kinetics in silicon and evaluate the usefulness of Si anodes for PHEV applications. Specifically, the impact of the offset in potential between charge and discharge is studied to understand its impact during operation. This goal was accomplished by studying the electrochemical behavior on both crystalline and amorphous thin-film Si anodes and estimating the parameters that control the offset. The films were obtained through pulse laser deposition (PLD) and magnetron sputtering techniques, respectively. The films were cycled galvanostatically between 0 and 1.2 V vs. Li/Li^+, Figure IV- 53(a). The difference between lithiation and delithiation capacities between the cutoff potentials, which results in the cycle to cycle marching seen in the figure (as well as the cycling efficiency of 98% in these films) was attributed to solvent reduction and SEI formation, and is a persistent problem with all Si electrodes. In addition to this, the large voltage offset seen in Figure IV- 53(a) between lithiation and delithiation curves lowers the energy efficiency.

The presence of the side reaction complicates the estimation of the lithiation/delithiation parameters, necessitating the correction of the data for the side reaction. This was accomplished by using a kinetic model to eliminate the cycle-to-cycle marching, Figure IV- 53(b). An equilibrium potential of 0.8 V vs. Li/Li^+ and a transfer coefficient of 0.5 for the side-reaction was assumed. Only reduction reaction (*i.e.*, tafel kinetics) was taken into account. By performing this elimination starting from initial cycles (e.g., cycles 2-4) to steady state cycles (e.g., cycles 20-23), one can track the decrease in the side reaction rate and thus understand increasing columbic efficiency with cycling.

Subsequently, open circuit voltage (OCV) relaxation data were obtained on these films as a function of SOC and used to estimate the kinetic parameters that control the lithiation/delithiation

reaction. The characteristic shape of the relaxation curve when plotted as voltage *vs.* log time suggested that the system is limited by Tafel kinetics.

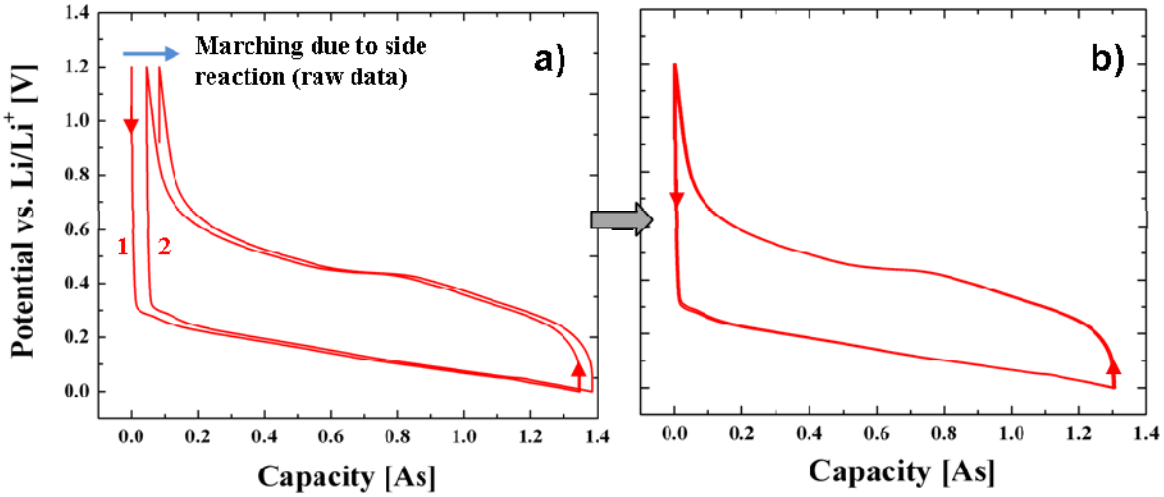

Figure IV- 53. (a) Voltage curves of PLD Si film cycled at C/7 rate between 0 and 1.2 V vs. Li/Li+ (b) data after correcting for side reaction.

Accordingly, the OCV relaxation data obtained as a function of SOC was fit to a model based on Tafel kinetics and double layer capacitance. The open-circuit relaxation behavior at 83% SOC was then simulated using both the main reaction and the side reaction and compared to data obtained at the same SOC. The model with side reaction predicts the open-circuit relaxation better at longer time-scales than one without the side reaction (Figure IV- 54). However, note that the side reaction correction does not impact the prediction at shorter times; the region that was used to estimate the kinetics of the main reaction. Data similar to that shown in Figure IV- 54 was obtained across the SOC range and used to estimate the kinetics of the main reaction.

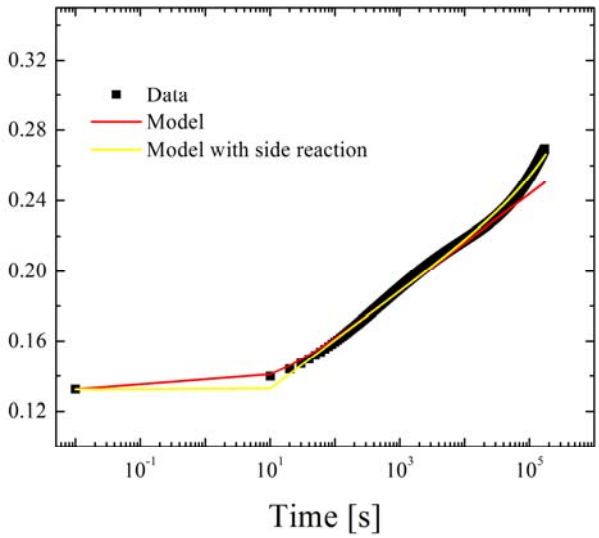

Figure IV- 54. OCV relaxation data obtained at 83% SOC shown with fits corresponding to main reaction with and without side reaction

The estimated kinetic parameters (exchange current density and apparent transfer coefficient as a function of SOC) were then used to predict the galvanostatic charge/discharge behavior of the system. The model predicts the C/7 lithiation and delithiation behavior of Si well, Figure IV- 55(a). This suggests that a large kinetic resistance causes the potential offset between charge and discharge, inherent to Si. The model also predicts the charge/discharge behavior under different rates, the result of which is shown as voltage offset at 50% SOC in Figure IV- 55(b). The dimensionless parameter $I/(a_f L i_0)$ relates the lithiation/delithiation current density (I) to its exchange current density (i_0), the surface area per volume (a) and the thickness (L). As expected by a kinetically-limited system, currents ranging from C/30 to C/2 result in a similar voltage offset; therefore, the ASI of the cell would decrease significantly with increasing current (until other effects, such as diffusion and ohmic drops start to dominate). Removing the offset necessitates parameter changes by many orders of magnitude; suggesting that the offset in potential is unavoidable. The impact of this result is that decreasing the surface area of silicon would not impact its rate capability.

The energy efficiency was calculated by assuming a cathode voltage of 3.8 V *vs.* Li, resulting in an energy efficiency of 90% under operating conditions approaching C/2. Experiments conducted under limited SOC range cycling (3%) show that energy efficiencies greater than 98% are achievable in this system, providing hope for use in PHEVs.

To summarize, the kinetic parameters of the side reaction, as well as the the main reaction, were estimated for both crystalline as well as amorphous thin film silicon electrodes. The parameters estimated for the main reaction were then used in a model that showed good predictive capability. This suggests that the reaction of the lithium with the silicon is the rate-determining step that controls the offset in voltage. Ongoing efforts include quantifying the side-reaction kinetics for various electrolytes including estimation of corresponding activation energies as well as understanding mass transport effects at higher lithiation/delithiation rates.

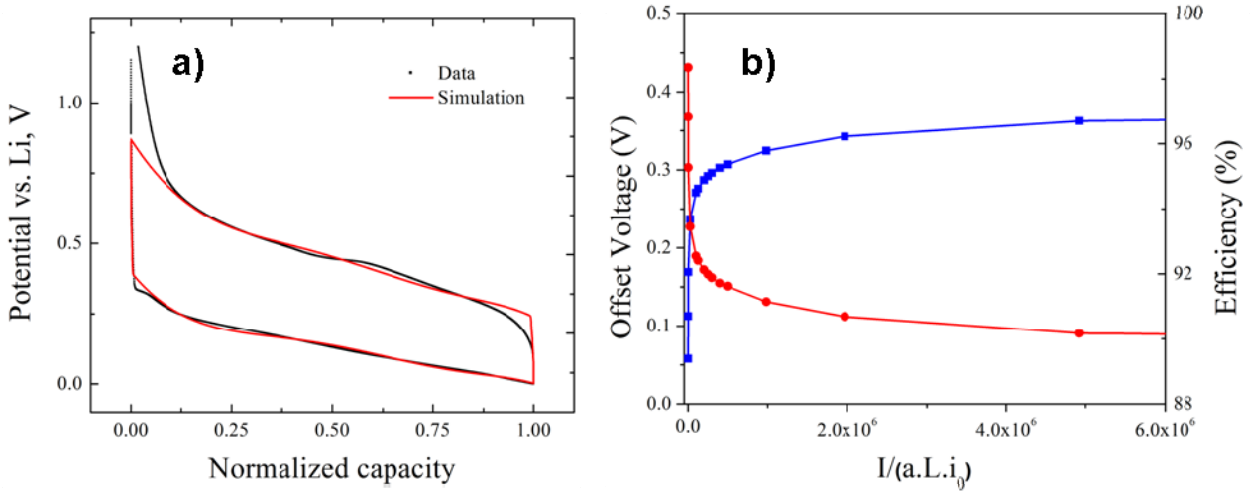

Figure IV- 55. (a) Simulation and data corresponding to galvanostatic (C/7) lithiation and delithiation. (b) Voltage offset and % efficiency for different C rates as predicted by the model

Behavior of Graphite/Electrolyte Interfaces (Smith) – The experimentally measured charge transfer resistance (R_{ct}) commonly included the terms associated with Li desolvation from electrolyte and its intercalation into outer part of SEI or cathode in addition to the electron transfer. R_{ct} is known to dominate cell resistance under low temperature operation. Previous investigation by Richard Jow's group at ARL found that R_{ct} is an order of magnitude larger for EC/1M $LiPF_6$ compared to EC:DMC(3:7)/1M $LiPF_6$, while the activation energy for R_{ct} was similar (68 kJ/mol vs. 71 kJ/mol)[19]. The reason behind the dramatic difference between R_{ct} for EC/$LiPF_6$ vs. EC:DMC(3:7)/$LiPF_6$ electrolytes is not understood. It is clear that the higher (by a factor of two) diffusion coefficient in EC:DMC(3:7)/$LiPF_6$ compared EC/$LiPF_6$ cannot explain an order of magnitude difference in R_{ct} measured at ARL.

The goal is to utilize MD simulations of EC/$LiPF_6$ and EC:DMC(3:7)/$LiPF_6$ electrolytes next to the material blocking for anion and solvent but non-blocking to Li cation and measure the interfacial resistance and free energy due to Li desolvation from electrolyte. At the initial stage, graphite has been chosen as the electrode material but does not include an SEI. MD simulations have been performed at 298 K. The free energy profiles for the lithium disolvation from these two electrolytes are shown in Figure IV- 56. A similar barrier for $\Delta G(z)$ is observed for both electrolytes, in accord with experiments, indicating similarity of the activation energy for R_{ct} for these electrolytes. The magnitude of the $\Delta G(z)$ barrier is also consistent with the experimentally observed activation energy for R_{ct}. The team is currently performing analysis of the local diffusion coefficients needed for calculation of absolute values of the interfacial resistance.

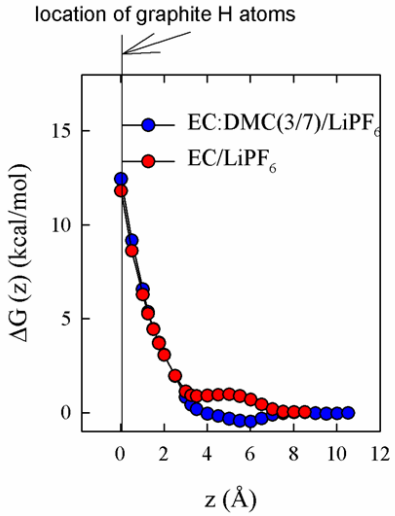

Figure IV- 56. The free energy of Li desolvation (ΔG) from electrolytes from MD simulations at 298 K.

Behavior of $LiFePO_4$/Electrolyte Interfaces (Smith) – The team carried out MD simulations of the interface between a $LiFePO_4$ cathode and two electrolytes: a liquid electrolyte comprised of EC/DMC + 1 M $LiPF_6$ and an IL electrolyte comprised of 1-ethyl-3-methyl imidizolium (EMIM)/(fluorosulfonyl)-imide (FSI) + 1 M LiFSI. A detailed analysis of the liquid electrolyte/electrode interface reveals a highly structured interface, a high potential barrier for Li^+ transport to the surface, and a large negative potential at the electrode surface (Figure IV- 57).

[19] Electro Chemical Society (ECS) Transactions, 3, 51-58 (2007).

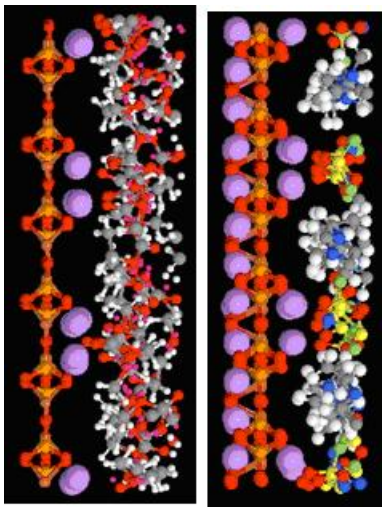

Figure IV- 57. The EC/DMC + 1 M $LiPF_6$ (left) and [EMIM][FSI] + 1 M LiFSI (right) interface with $LiFePO_4$.

An analysis of the IL/electrode interface reveals even more structure at the interface, a larger potential barrier for Li^+ transport to the surface, and a less negative potential at the electrode surface due to adsorption of EMIM cations. Potential-of-mean-force calculations reveal that the barrier for Li^+ adsorption is significantly less than that indicated by the Poisson potential likely as the result of coordinated motion of anions with Li^+ and restructuring of the electrolyte as Li^+ moves toward the surface. The barrier for Li^+ adsorption is significantly higher in the IL than observed in the liquid electrolyte**.**

EC and VC Decomposition Products (Smith) – This work has involved a quantum chemistry investigation of reaction paths for gas phase EC decomposition in the presence of lithium. Specifically, ring opening at different locations for the Li-EC and Li_2-EC complexes was investigated, as well as relative energies of possible combinations of reduction compounds. In collaboration with Adri van Duin (Penn State), this information has been used in the parameterization of the atomistic reactive force field (ReaxFF). Utilizing ReaxFF, EC reduction mechanisms in condensed phases have been investigated. Specifically, MD simulations of liquid EC containing various amounts of Li (neutral) have been initiated. In these simulations, when Li binds to a neutral EC molecule electron transfer occurs resulting in a Li^+-EC^- pair. Simulations show that the ring structure for EC^- becomes unstable and ring opening is observed. Additional simulations have shown that that the barrier for ring opening in the presence of Li is much higher for VC than for EC. The current version of the ReaxFF accurately captures this difference in the energy barriers and relative energy difference of reaction products predicted by quantum chemistry calculations.

Electrode Engineering Studies (Battaglia) – Work on electrode engineering includes evaluating the amount of carbon, binder, porosity, and electrode thickness needed to make an electrode capable of meeting the PHEV-40 energy goal. An analysis of the impact of conductive carbon to binder ratio is shown in Figure IV- 58. The vertical line shows the percolation threshold for spheres. As shown, the ratio of conductive carbon to binder significantly impacts the electrode

conductivity but does not result in a continuously increasing conductivity with increasing conductive carbon content. It was found that for high power, HEV applications, a C/(C+B) of ~4/9 will give the lowest impedance. Where energy density is important, a smaller fraction of C/(C+B) of ~1/3 may be best. Next this ratio's impact on cycle life will be determined.

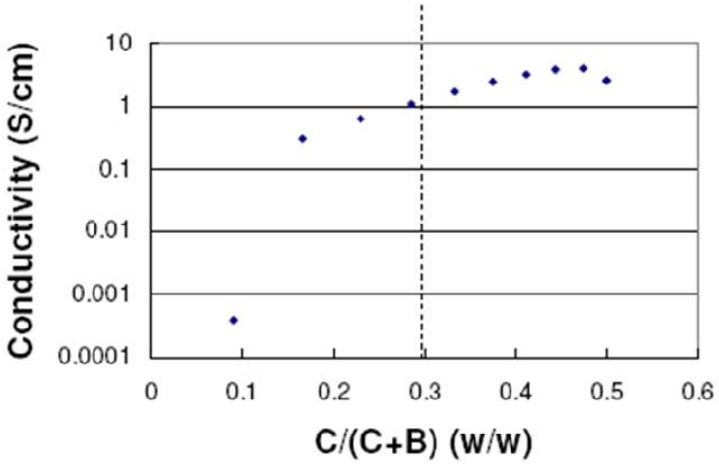

Figure IV- 58. Conductivity vs. ratio of conductive carbon to binder

Two electrode materials have been evaluated: the NMC and $LiNi_{0.8}Co_{0.15}Al_{0.05}O_2$ (NCA) cathodes. One way to achieve high energy density is to use a cathode material with a high capacity and high voltage. NMC is such a material, with a theoretical capacity of 278mAh/g. One step is to determine how much Li could be removed without causing irreversible capacity fade. Thin laminates of NMC were made into button cells with matched, MCMB-1028-based counter electrodes.

Cycling results to different upper voltage cut-off limits at 1.92 mA/cm^2 discharge currents are shown in Figure IV- 59. Previous cut-off voltage experiments against Li as a counter electrode clearly showed a side reaction at the oxide at voltages greater than 4.4 V that was much more detrimental to cycling than a side reaction below 4.4 V. The full cell cycling data with MCMB as the counter electrode show the same results. It is also clear that cycling to 4.3 V *vs.* graphite gave no more capacity fade than cycling to 4.1 V, at least for the first 500 cycles.

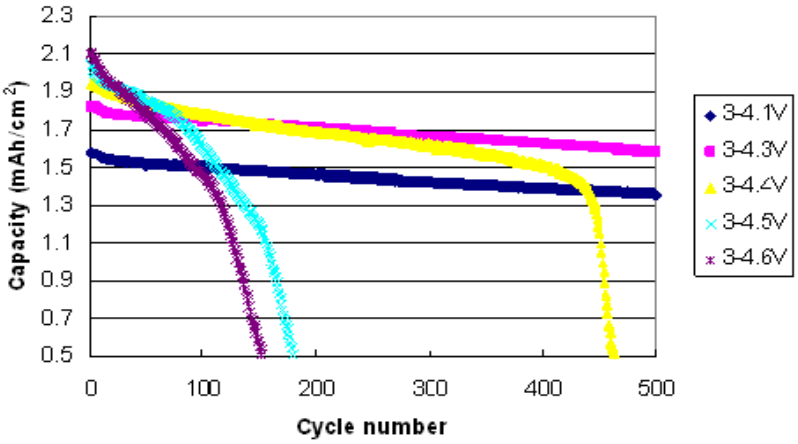

Figure IV- 59. Cycling data for NMC cathodes for differnt upper voltages.

Next, NCA cathodes were evaluated, and it was found that electrodes of ~140μm thickness and 35% porosity with standard ATD electrode formulations should meet the PHEV-40 power/energy requirements. Up to 60% higher energy densities could be achieved by using much less binder and conductive additive. The ultimate evaluation is the cycling capability as a function of carbon and binder content and the electrode porosity. This assessment requires the use of a non-Li metal anode.

Towards that end, three graphites were evaluated to determine which one is the most appropriate for further development as an advanced anode material. Reversible and irreversible capacities, and the rate of side reactions, were measured after formation. Reversible and first cycle irreversible capacities were measured for SNG-12 (Hydro-Québec), OMAC-15 (Osaka Gas), and MCMB-1028, Figure IV- 60. Reversible capacities of 280, 308, and 291mAh/g were measured for SNG, OMAC, and MCMB, respectively. First cycle irreversible capacities of 18.8±0.4, 11±2, and 11±1 % were also measured for SNG, OMAC, and MCMB, respectively. We were also able to measure the irreversible capacity loss per cycle *vs.* a Li counter electrode at a C/10 charge and discharge rate. Values of 0.52±0.08, 0.39±0.17, and 0.21±0.05% per cycle at the 12^{th} cycle for SNG, OMAC, and MCMB, respectively, were measured. MCMB-1028 provides the best combination of reversible and irreversible capacity. As sufficient MCMB is available for analysis, it will be used in initial assessments of the Graphite/NMC system for PHEV-40 applications.

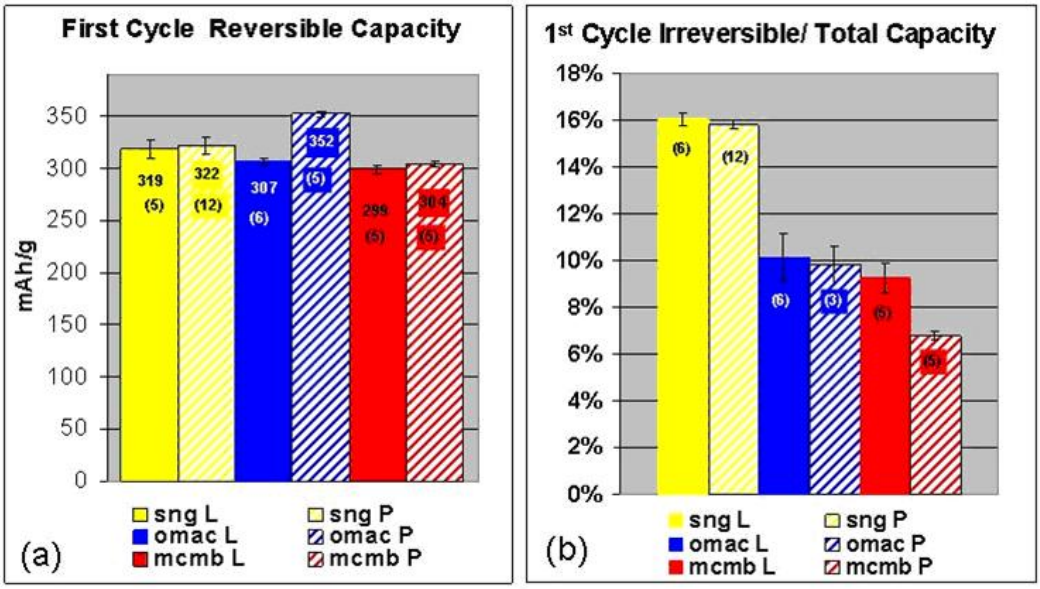

Figure IV- 60. First cycle reversible and irreversible capacities for various carbons. Value in parentheses is the number of cells cycled. L: anode laminates made at Hydro-Québec (HQ); P: anode laminates made at LBNL.

***Performance of Graphite Anodes and Additives (Zaghib)* –** The performance of OMAC graphite from Osaka Gas was evaluated and compared with SNG12 (HQ) and MCMB28-10 in 1M $LiPF_6$–EC/DEC. These two new graphitic anodes have a spherical shape similar to MCMB and it is hoped that they would form an effective SEI and provide reasonable rate capability. The OMAC-15 showed high first cycle coulombic efficiency - 92% compared to 85% with SNG12. Recently Osaka Gas sent their latest product, OMAC12, which is being tested with water-dispersed binder and compared against SNG12 due to their comparable particle size.

Recently, the impact of additives in the electrolyte on electrode performance has been investigated, including the additives' role in SEI layer formation. VC, vinyl ethylene carbonate (VEC), and their mixtures were investigated as additives in 1M-$LiPF_6$-EC/DEC. SNG12 and OMAC-15 graphite electrodes were used. The SNG12 was found to be sensitive to the additives, and the first coulombic efficiency (CE) was affected when small amount of additives are introduced. The first CE improved to 93% with the addition of 2%VEC or the mixture (1%VEC + 1%VC) compared to 85% in the cell without additives. In addition, the reversible capacity is reduced to 345 mAh/g and 336 mAh/g, respectively, compared to 369 mAh/g without additives. No effect was found when 2%VC is added to the SNG12 cell, yielding the optimum reversible capacity.

Figure IV- 61 shows the first cycle at C/24 of the Li/SNG12 cells with different electrolytes. With OMAC graphite, the first CE did not show any improvement compared to the cell without additives (93%). The 1st CE was 92%, 92% and 87%, respectively when 2%VC, 2%VEC and 1%VC+1%VEC is added. However, the reversible capacity was strongly affected compared to cell without additives (Table IV- 3). A lower capacity with VEC as the additive was obtained with OMAC15 compared to SNG12. More work is underway to understand the effect of these additives on the SEI layer and the reversible capacity.

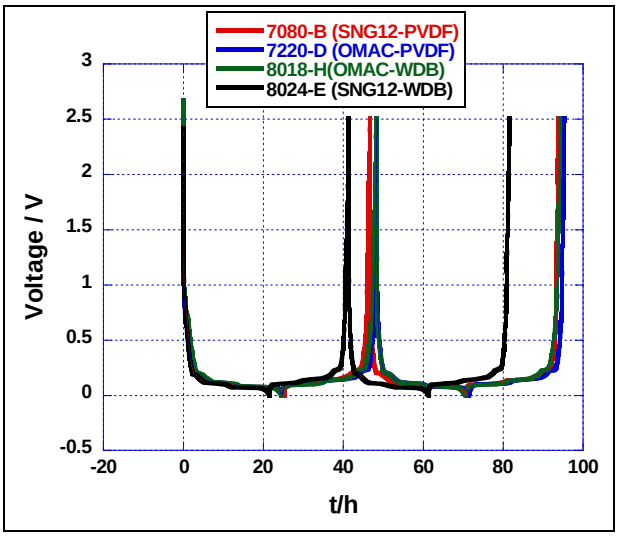

Figure IV- 61. First cycle of Li/Graphite cells in 1M LiPF6 1M-EC/DEC with different binders

Table IV- 3. Impact of electrolyte additives on graphite electrochemical performance.

	SNG12		OMAC15	
Additives	**1st CE (%)**	**Qrev (mAh/g)**	**1st CE (%)**	**Qrev (mAh/g)**
No	**85**	**369**	**93**	**358**
2%VC	**86**	**366**	**92**	**355**
2%VEC	**93**	**345**	**92**	**321**
1%VC + 1%VEC	**93**	**336**	**87**	**352**

When the water soluble binder is used, SNG12 has shown better 1st CE than PVdF with 92% but lower capacity, however the OMAC maintained its 1st CE of 95% and reversible capacity at 365 mAh/g. Next, OMAC-12 was evaluated with water-dispersed binder. The results are comparable to PVdF, with 95% CE in the first cycle, and a 352 mAh/g reversible capacity. However, this performance is higher than SNG12, with 92% 1st CE and a 315 mAh/g reversible capacity. The relative rate capability of these graphites depends upon the binder use, as seen in Figure IV- 62.

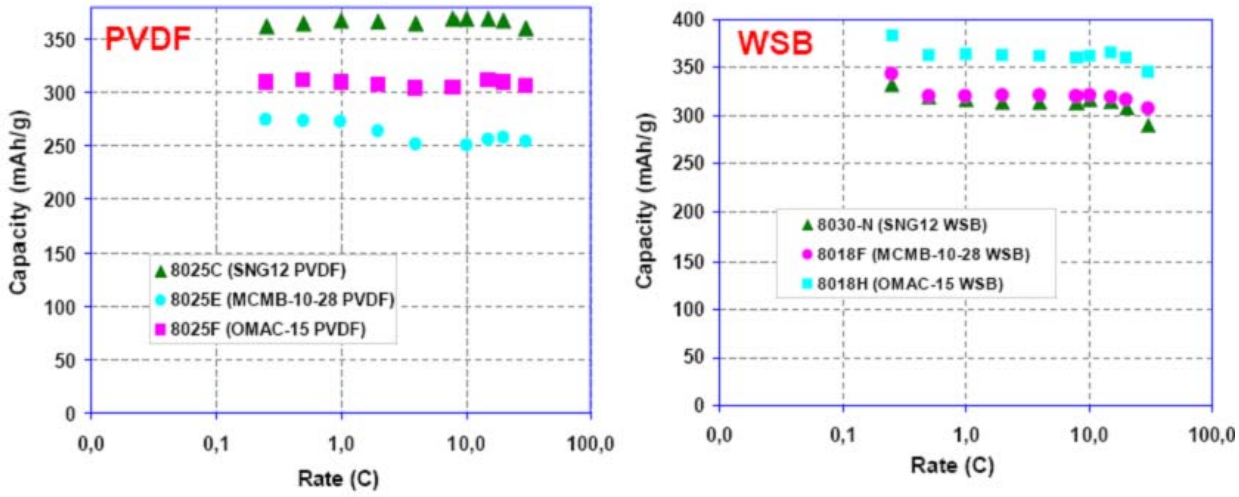

Figure IV- 62. Rate capability of three graphitic anodes with PVdF vs. water soluble binders.

Modeling—Optimization (Sastry) – This group is applying numerical estimations of the electrical conductivity using a 3D mathematical technique[20], allowing prediction of ionic conductivity of the electrolyte phases. Predictions of conductivities were compared with cathodes from Battaglia's group. The cathode had been compressed after casting on the current collector to various porosities from 50% (uncompressed) to 40%, 30%, 20%, 10%, and 0%. With further cathode compression, low ionic conductivity may reduce battery performance.

To evaluate the battery performance in terms of conductivity and to identify optimal blends, the team introduced estimated conductivities to the battery performance model. The battery performance model was modified from a 1D porous electrode model coupled with 2D spherical particle diffusion modeling[21]. A surrogate-based analysis approach was also introduced to perform optimized design for cathode system. Findings from comparisons among simulation and experimental results confirm the advantage of carbon coating, and infusion of conductive additives into polymeric binders. Some questions remain regarding compaction, and these are being studied.

To close the gap between numerical predictions of conductivity and experiment, the team refined the models of microstructure via more intensive SEM. Results showed that distribution of PVdF/C became less uniform with reduced porosity. Also, sedimentation of active material particles was observed, especially for cathodes with low porosity. Non-uniformities in cathode structures were shown to influence four-point-probe results[22]. In parallel, numerical estimations of ionic and electronic conductivities of cathodes were generated via 3D mathematical approach[23], see Figure IV- 63. Conductivities were then used to optimize cathode systems, including 1D porous electrode models coupled with 2D spherical particle diffusion models.

[20] Y. H. Chen, C. W. Wang, G. Liu, X. Y. Song, V. Battaglia, and A. M. Sastry, *JECS* **154**, (10), A978 (2007).
[21] M. Doyle, J. Newman, A. S. Gozdz, C. N. Schmutz, and J. -M. Tarascon,, *JECS*, **143** (6), 1890-1903 (1996).
[22] C. -W. Wang, A. M. Sastry, K. A. Striebel, and K. Zaghib, *J. Electrochem. Soc.* **152** (5), A1001-A1010 (2005).
[23] Y. H. Chen, C. W. Wang, G. Liu, X. Y. Song, V. Battaglia, and A. M. Sastry, *JECS.* **154**, (10), A978 (2007).

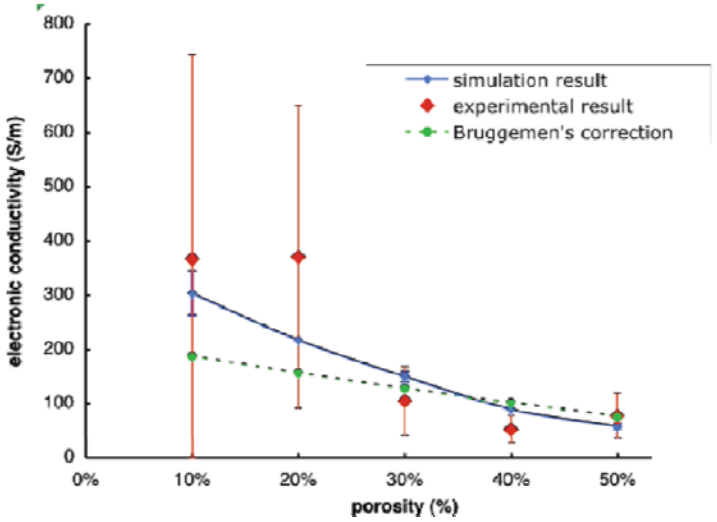

Figure IV- 63. Experimental and theoretical conductivity vs porosity.

With the results of the trade-off between ionic and electronic conductivity as the baseline, optimal schema for high specific energy will now be identified by considering the kinetic performance of the cathode *via* using a battery performance model. Current results allow mapping of specific energy as a function of electronic conductivity and ionic conductivity, respectively, for a specific cathode thickness. The specific energy drops from its maximum value with an increase or decrease in electronic or ionic conductivity around optimal points. The relationships among specific energy, cathode thickness, and volume fraction of active material with conductive additives will be further studied. The results will include identification of optimal cathode compositions with high capacity, along with suggested guidelines for preparation of electrodes, for automotive applications.

Graphite Current Collectors (Dudney) – Highly conductive foams and fiber mats are being evaluated as cathode current collectors. In the absence of an organic binder and stresses from compaction, the high temperature bonding of the C coated $LiFePO_4$ to the graphite skeleton is expected to improve the uniformity of the temperature and current, and hence cycle life of the cathode. This team is examining these particle bonds and projecting the energy and power performance of a complete battery.

The first projection of the energy density of electrodes with carbon current collectors has been completed for $LiFePO_4$ coated graphite foam, Table IV- 4. The top lines show the cathode composition. The $LiFePO_4$/C ratio needs to be at least 3 times higher than the current samples to match the capacity and energy density achieved by K2 Energy. To work towards this goal, the slurry has been reformulated with 7-times higher solids loading, which is still fluid enough to penetrate and coat the porous foam or carbon fiber skeleton.

Table IV- 4. Projection of electrode-and current collector energy density with graphite current collector

For cathode and current collector only	**K2 Energy Solutions**	**Projected AR foam**	**Projected LQI foam**
$LiFePO_4$ wt. (g)	12	12	12
$LiFePO_4$/C wt. ratio		3X current	4X current
Current collector wt. (g)	1.5–2.6** Al foil	4.8 foam	9.4 foam
Binder+additive (g)	(1-3, est.)	0	0
Energy (Wh/kg)	250 – 310	270	210
$LiFePO_4$ coating (μm-thick)		50 (50% dense)	140 (50% dense)
Heat transport (W/°K)	0.035 – 0.062	0.19	0.75
Foam pore diameter (μm)		500	1500
Foam surface area (cm^2/g)		260	50
Thermal cond. (W/m/°K)	235	50	180

The shaded rows contain results for the cathode energy density, coating thickness, and heat transport by Al or graphite through the ends of the cell. The lower lines show properties of the two types of foam. The estimates show that a competitive energy density is obtained with the graphite foam current collector. Also, the remaining volume in the pore is adequate for good electrolyte permeation. However, the most important result is that the heat transport is greatly enhanced by the graphite foam. This should improve the thermal management and lifetime of the battery.

Cathodes of $LiFePO_4$ supported with carbon fibers in the form of carbon-bonded carbon fibers and commercially available carbon fiber papers (Toray) have been evaluated with good results. The energy and power are higher for these fiber-scaffolds than for the graphite foams reported above, likely due to the more open structure. In addition, the fiber cathodes are more robust and easily assembled into a battery. Although these fiber structures have a lower thermal conductivity than the graphite foams, with proper choice of materials this property can likely be improved. Even so, projections of $LiFePO_4$-filled Toray paper indicate that the carbon fiber will support comparable loading and provide heat transport equal to that of Al foil. Figure IV- 64 shows specific energy and power, based on the total weight of the active cathode + graphite.

This team has also addressed concern about the lower-than-expected $LiFePO_4$ utilization, which has been ~80%. Investigations reveal that the carbon loading is likely 3-5% higher than the originally estimated 2 wt% from the slurry composition. Continuing efforts will reduce the residual carbon content to a more acceptable level. Investigation of the particle and fiber bonds formed at 700°C will continue and $LiFePO_4$-coated Toray samples will be fabricated for testing.

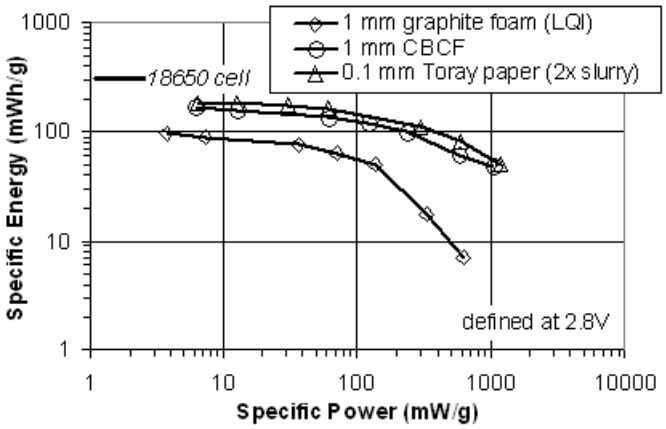

Figure IV- 64. Specific energy and power with various carbon current collectors

Transport-Property Measurement and Performance of Hybrid Capacitors (Newman) – A dissertation was filed in December 2007 detailing methods of transport-property measurement in Li-ion electrolytes. A technique for measuring diffusion coefficients in electrolytes for Li-ion batteries was developed that allows for temperature control in $LiPF_6$ in acetonitrile as well as the Gen2 electrolyte, 1.2 M $LiPF_6$ in EC:EMC (3:7). Results indicate that the diffusion coefficient for $LiPF_6$ is a factor of five higher in acetonitrile than in baseline electrolytes. The activity coefficient in $LiPF_6$ electrolytes was also measured using melting-point depression and a concentration-cell experiment, and a phase diagram was experimentally determined for $LiPF_6$ in EC.

These transport properties were used in a system model to optimize the design of batteries with one intercalative electrode replaced with a capacitive electrode, where charge is stored in the double layer. The effect of various parameters (including electrode thickness and porosity) on high-rate performance of an asymmetric hybrid supercapacitor system was investigated. This technology involves the use of a lithium titanate spinel anode and activated carbon cathode. It was found that such as system could meet the 25kW HEV goals.

Quantifying Capacity Usage and Battery Size in HEVs and PHEVs (Newman) – Modeling work on battery size and capacity use in cells for HEVs and PHEVs has been completed. The combined model indicates that solid-phase concentration gradients across an electrode are unable to relax when the open-circuit potential of an electrode is uniform. Figure IV- 65 shows the asymmetric ten-second pulse-power capability of a Li_xC_6 / $Li_yMn_2O_4$ cell obtained using the HPPC test. The reason for the asymmetric shape is that the HPPC protocol uses consecutive discharge pulses (a 1C discharge, followed by a rest, followed by a high-rate discharge pulse). The solid-phase concentration gradient across the electrode built up during the first discharge will persist, resulting in increased overpotential relative to a sloped-potential system during the subsequent discharge.

The persistence of concentration gradients can be clearly seen in Figure IV- 66, taken after a 1 h relaxation at SOC ≈ 0.2. This plot gives the surface stoichiometric coefficient (x in Li_xC_6 or y in $Li_yMn_2O_4$) of the negative and positive electrodes through the depth of the cell sandwich. For the normal (sloped) potential system, the concentration gradients relax while, for the flat potential system, they do not.

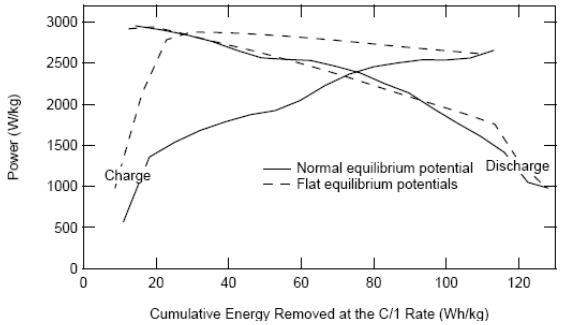

Figure IV- 65. Pulse power capability

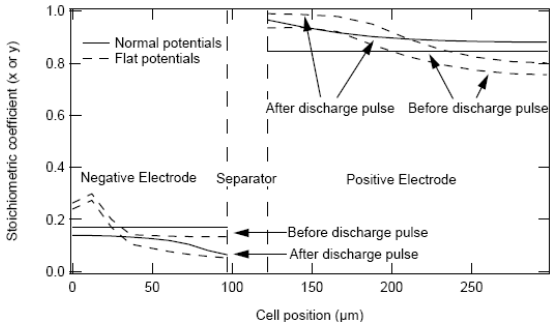

Figure IV- 66. Concentration gradients

This group is now experimentally investigating whether a flat-potential system subjected to consecutive pulses will suffer a reduction in performance due to solid-phase concentration gradients through the depth of a porous electrode. Tests have been completed on a number of coin cells, but there have been some unusual features in the $FePO_4$ data. Tests are ongoing on pouch cells with $FePO_4$ vs. Li metal, and 18650 cells with $FePO_4$ *vs.* graphite. Preliminary results do show a history dependence of a constant-current discharge from 50% SOC when the cell is brought to that point at different rates from full charge.

Improved Understanding of the Effect of Transport Restrictions in Separators (Wheeler) – Figure IV- 67 shows a simple cell discharge experiment in which the number of separator layers is varied from one to three. First a cell is built and tested with three separators. Then the same cell is retested after removing two separators from the cell. The difference in the performance is significant. There is considerable under-utilization of the electrode when three separators are used. While it is understood that each separator layer has a discrete value of ohmic impedance associated with it, the additional concentration polarization evident at higher rates was somewhat surprising. This suggests that the liquid-phase diffusional resistance in the separator is not negligible. The group then devised a series of measurements and a computer model to directly determine the tortuosity in the separator, which affects both ohmic and diffusional resistances. The results surprisingly showed that prior literature values of the tortuosity of the separator erroneously included impedances associated with the electrode surfaces used in the experiments. Researchers now have a more accurate value that can be used to analyze the effect of separator transport limitations on cell performance.

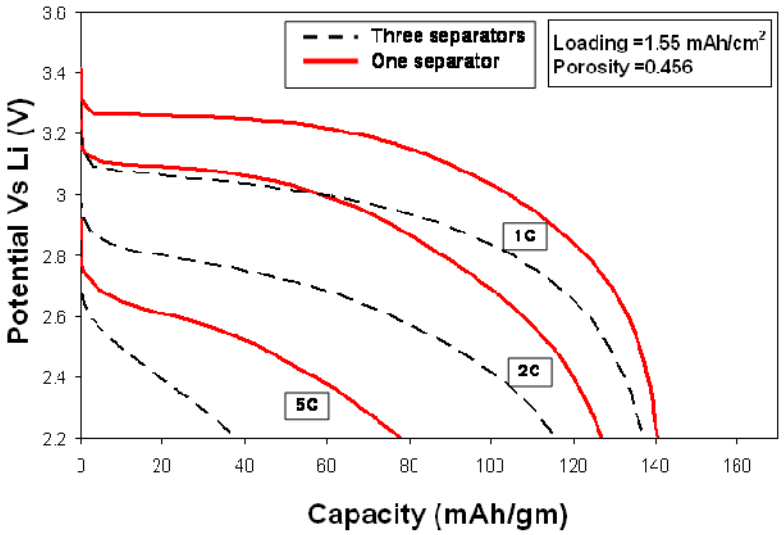

Figure IV- 67. Discharge curves for a single $LiFePO_4$ cell with different number of separators and a Li-foil anode.

Improved Understanding of Transport Limitations in Porous Cathodes (Wheeler) – In conjunction with the work on separators, the group also used a computer model combined with experiments to evaluate the transport properties in porous cathodes. Excellent agreement between model and experiment is obtained. Figure IV- 68 shows results from a series of experiments on cathodes of differing porosity and composition. This work suggests that the liquid-phase resistance in the cathode is larger (by a factor of ~2) than predicted by the Bruggeman relation. This is in agreement with the expectation that for the particle distributions typical of Li electrodes, the liquid resistance will be larger than that predicted by Bruggeman relation. This information is needed to accurately model and optimize cells for PHEV use.

Work is continuing to correlate the effective liquid-phase transport resistance with cathode morphology, such as porosity and carbon fraction. For this, several experiments are underway.

Evaluation of the effect of fibers (Wheeler) – Finally, during this FY, the team concluded their investigation into the use of carbon fibers to enhance electrode performance. They found that for uncalendered electrodes, fibers can provide a significant increase in performance, however under typical conditions (in which the electrode is calendered for example), the enhancement is much less and is in some cases barely noticeable.

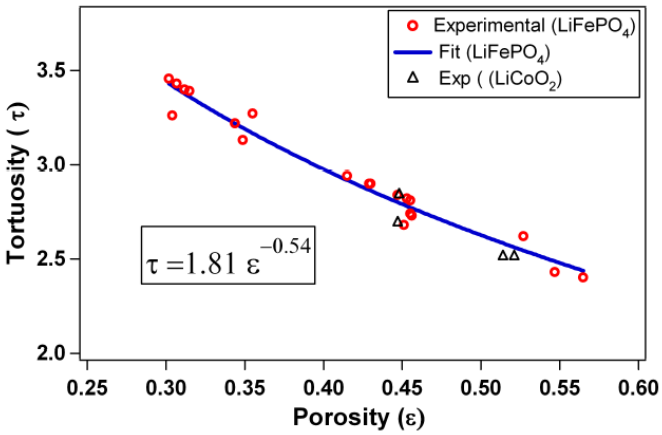

Figure IV- 68. The effect of porosity on the tortuosity of cathode films. The tortuosity dependence is well-approximated by the oft-used Bruggeman exponent, however the tortuosity is nearly two times higher than that predicted by the Bruggeman relation. $LiCoO_2$ cathodes appear to follow the same trend as $LiFePO_4$ cathodes

Sample Future Plans in Modeling, Diagnostics, and Cell Analysis

- Quantify carbon/binder and binder/active material interactions from DSC experiments.
- Complete HEV testing with various Mn-spinel cathodes.
- Evaluate NMC cycle performance using an optimized graphite electrode.
- Evaluate NMC dissolution properties.
- Evaluate graphite cycle performance using an optimized cathode electrode.
- Establish a high-throughput computing environment in which a large number of potential electrode materials can be evaluated computationally.
- Influence of the electrolyte chemistry on R_{ct} will be further examined in simulations of IL/electrode interfaces. R_{ct} was experimentally found to be even larger for the safer IL electrolytes compared to carbonate electrolytes. Influence of the plasticizer on the charge resistance of ionic liquids will be investigated.
- Simulations using a new electro-active interface code will allow investigation of the structure of electrode/electrolyte interfaces and the charge-state of model electrodes as a function of voltage, which can be controlled in the EIS.
- Investigate SEI and redox shuttles. Experiment with shuttle species in cells with negative electrodes made of graphite, which is known to have a stable SEI, and $Li_xTi_5O_{12}$, the potential of which is high enough to prevent SEI formation. Couple the experimental work on this system with simulations that adequately model system performance as well as overcharge protection.

Focused Fundamental R&D Publications

1. A. Appapillai, A. Mansour, J. Cho, and Y. Shao-Horn, "Microstructure of "$LiCoO_2$" with and without "$AlPO_4$" nanoparticle coating: Combined STEM and XPS Studies," Chemistry of Materials 19 (2007) 5748-5757.
2. A. Dillon, A. Mahan, R. Deshpande, P. Parilla, K. Jones, and S. Lee "Metal Oxide Nanoparticles for Improved Electrochromic and Lithium-Ion Battery Technologies," Thin Solid Films 516 (2008) 794-797.
3. A. Manthiram, A. Murugan, A. Sarkar, and T. Muraliganth, "Nanostructured Materials for Electrochemical Energy Storage and Conversion," Energy and Environmental Science (in press).
4. A. Murugan, T. Muraliganth, and A. Manthiram, "Comparison of Microwave Assisted Solvothermal and Hydrothermal Syntheses of $LiFePO_4$/C Nanocomposite Cathodes for Li-ion Batteries," Journal of Physical Chemistry C 112 (2008) 14665-14671.
5. A. Murugan, T. Muraliganth, and A. Manthiram, "One-Pot Microwave-Hydrothermal Synthesis and Characterization of Carbon-Coated $LiMPO_4$ (M = Mn, Fe, and Co) Cathodes," JECS[24] (in press).
6. A. Murugan, T. Muraliganth, and A. Manthiram, "Rapid, Size-controlled, Microwave-Solvothermal Synthesis of Phospho-olivine Nanorods and Their Coating with a Mixed Conducting Polymer for Li-ion Batteries," Electrochemistry Communications 10 (2008) 903-906.
7. C. Delacourt, P. Ridgway, J. Kerr, and J. Newman, "Design of an Electrochemical Cell Making Syngas ($CO + H_2$) from CO_2 and H_2O Reduction at Room Temperature," JECS 155 (2008) B42-B49.
8. C. Johnson, N. Li, C. Lefief, J. Vaughey and M. Thackeray, "Synthesis, Characterization and Electrochemistry of Lithium Battery Electrodes: $xLi_2MnO_3 \bullet (1-x)LiMn_{0.333}Ni_{0.333}Co_{0.333}O_2$ ($0 \leq x \leq 0.7$)," Chem. Mater. 20 (2008) 6095.
9. D. Zeng, J. Cabana, J. Breger, W. Yoon, and C. Grey, "Cation ordering in $Li[Ni_xMn_xCo_{(1-2x)}]O_2$-Layered Cathode Materials: A Nuclear Magnetic Resonance (NMR), Pair Distribution Function, X-ray Absorption Spectroscopy, and Electrochemical Study," Chem. Mater. 19 (2007), 6277–6289.
10. G. Chen, and T. Richardson, "Improving the Performance of Lithium Manganese Phosphate Through Divalent Cation Substitution," ESSL[25] 11 (2008) A190.
11. G. Chen, and T. Richardson, "Solid Solution Lithium Alloy Cermet Anodes," JPS[26], 174 (2007) 810.
12. H. Chen, and C. Grey, "Molten Salt Synthesis and High Rate Performance of the "Desert-Rose" form of $LiCoO_2$," Adv. Mater. 20 (2008) 2206-2210.
13. H. Li, N. Yabuuchi, Y. Meng, S. Kumar, J. Breger, C. Grey, and Y. Shao-Horn, "Changes in the Cation Ordering of Layered O3 $Li_xNi_{0.5}Mn_{0.5}O_2$ During Electrochemical Cycling to High Voltages: An Electron Diffraction Study," Chem. Mater. 19 (2007) 2551- 2565.
14. J. Bréger, K. Kang, J. Cabana, G. Ceder, and C. Grey, "NMR, PDF and RMC Study of the Positive Electrode Material $Li(NiMn)_{0.5}O_2$ Synthesized by Ion-Exchange Methods," J. Mater. Chem. 17 (2007) 3167-3174.
15. J. Chen, M. Vacchio, S. Wang, N. Chernova, P. Zavalij, and M. S. Whittingham, "The hydrothermal synthesis and characterization of olivines and related compounds for electrochemical applications," Solid State Ionics 178 (2008) 1676-1693.
16. J. Nanda, M. Datta, J. Remillard, A. Neil, and P. Kumta, "In-situ Raman Microscopy during discharge of a high capacity Silicon-Carbon composite Li-ion battery negative electrode," Electro. Commun. (2008), in Press.
17. J. Saint, et al., "Compatibility of $Li_xTi_yMn_{1-y}O_2$ (y=0, 0.11) electrode materials with pyrrolidinium-based ionic liquid electrolyte systems," JECS 155 (2008) A172-A180.
18. J. Vaughey, J. Owejan, and M. Thackeray, "Substituted $M_xCu_{6-x}Sn_5$ Compounds (M=Fe, Co, Ni, Zn) for Lithium Batteries," ESSL 10 (2007) A220-A224.
19. J. Xiao, N. Chernova, and M. S. Whittingham, "Layered Mixed Transition Metal Oxide Cathodes with Reduced Cobalt Content for Li-ion Batteries," Chemistry of Materials, accepted for publication.
20. L. Hardwick, J. Saint, I. Lucas, M. Doeff, and R. Kostecki, "FTIR and Raman Study of the $Li_xTi_yMn_{1-y}O_2$ (y = 0, 0.11) Cathodes in Pyrrolidinium-based Ionic Liquid Electrolyte Systems," JECS, submitted.
21. L. Hardwick, M. Marcinek, L. Beer, J. Kerr, and R. Kostecki, "An Investigation of the Effect of Graphite Degradation on the Irreversible Capacity in Li-ion Cells," JECS 155 (2008) A442.
22. L. Trahey, J. Vaughey, D. Dees, H. Kung, and M. Thackeray, "High Capacity, Microporous Cu_6Sn_5-Sn Anodes for Li-Ion Batteries," Electrochem. Comm. (2008). Submitted.

[24] JECS: Journal of the Electrochemical Society
[25] ESSL: Electrochemical and Solid State Letters
[26] JPS: Journal of Power Sources

23. M. Datta, and P. Kumta, "Alloy design for long term cyclability of Si based anode materials for Li-ion batteries," Society of Automotive Engineers, Special Publication (SP) (2008), SP-2177 (Nanotechnology for Automotive Applications—Nano-materials for Energy Devices), 1-6.
24. M. Doeff, J. Wilcox, R. Yu, A. Aumentado, M. Marcinek, and R. Kostecki, "Impact of Carbon Structure and Morphology on the Electrochemical Performance of $LiFePO_4$/C Composites," J. Solid State Electrochem., 12 (2008) 995.
25. M. Marcinek, J. Wilcox, M. Doeff, and R. Kostecki "Microwave Plasma Chemical Vapor Deposition of Carbon Coatings on $LiNi_{1/3}Co_{1/3}Mn_{1/3}O_2$ for Li-ion Battery Composite Cathodes,"JECS, accepted.
26. M. S. Whittingham, "Inorganic nanomaterials for batteries," Dalton Transactions 2008 (DOI: 10.1039/b806372a.)
27. M. S. Whittingham, "Materials Challenges Facing Electrical Energy Storage," Mater. Res. Soc. Bulletin 33 (2008) 411.
28. M. Thackeray, "The Structural Design of Electrode Materials for High Energy Lithium Batteries," J. Chem. Eng. of Japan 40 (2007) 1150.
29. N. Chernova, M. Ma, J. Xiao, M. S. Whittingham, J. Breger, and C. Grey, "Layered $Li_xNi_yMn_yCo_{1-2y}O_2$ Cathodes for Li-ion Batteries: Understanding Local Structure via Magnetic Properties," Chem. Mater. 19 (2007) 4682.
30. N. Yabuuchi, S. Kumar, H. Li, Y. Kim, and Y. Horn, "Changes in the Structural and Transport Properties of Layered O3 $Li_xNi_{0.5}Mn_{0.5}O_2$ during Electrochemical Cycling to High Voltages," JECS 154 (2007) A566-A578.
31. N. Yabuuchi, Y. Kim, H. Li, and Y. Horn, "Structural Instability of $Li_xNi_{0.5}Mn_{0.5}O_2$ upon Heating: An In-Situ Synchrotron X-ray Diffraction Study," Chemistry of Materials 20 (2008) 4936-3951.
32. O. Borodin; G. Smith, "Molecular Dynamics and Quantum Chemistry Study of Li^+ Solvation in Dimethyl Carbonate/Ethylene Carbonate Doped $LiPF_6$ Electrolytes," J. Phys. Chem. B, in press.
33. P. Albertus, and J. Newman, "I. A Simplified Model for Determining Capacity Usage and Battery Size for Hybrid and Plug-in Hybrid Vehicles," JPS 183 (2008) 376-380.
34. P. Albertus, J. Christensen, and J. Newman, "Modeling Side Reactions and Nonisothermal Effects in Nickel Metal-Hydride Batteries," JECS 155 (2008) A48-A60.
35. P. Albertus, J. Couts, V. Srinivasan, and J. Newman, "II. A Combined Model for Determining Capacity Usage and Battery Size for Hybrid and Plug-in Hybrid Vehicles," JPS 183 (2008) 771-782.
36. Q. Fan, P. Chupas, and M. S. Whittingham, "Characterization of Amorphous and Crystalline Tin–Cobalt Anodes," ESSL 10 (2007) A274-A278.
37. R. Benedek, M. Thackeray, and A. van de Walle, "Free Energy for Protonation Reaction in Li-ion Battery Cathode Materials," Chem. Mater. 20 (2008) 5485.
38. S. Davis, E. Takeuchi, W. Tiedemann, and J. Newman, "Simulation of Pulse Discharge of the Li-CF_x System," JECS 155 (2008) A24-A28.
39. S. Kang, and M. Thackeray, "Stabilization of $xLi_2MnO_3 \bullet (1-x)LiMO_2$ Electrode Surfaces (M=Mn, Ni, Co) with Mildly Acidic, Fluorinated Solutions," JECS 155 (2008) A269.
40. S. Lee, Y. Kim, R. Deshpande, P. Parilla, E. Whitney, D. Gillaspie, K. Jones, A. Mahan and S. Zhang, "Reversible Li-Ion Insertion in Molybdenum Oxide Nanoparticles," Advanced Materials, 2008.
41. S. Stewart, and J. Newman, "Measuring the Salt Activity Coefficient in Lithium-Battery Electrolytes," JECS 155 (2008) A458-A463.
42. S. Stewart, and J. Newman, "The Use of UV/vis Absorption to Measure Diffusion Coefficients in $LiPF_6$ Electrolytic Solutions," JECS 155 **(**2008) F13-F16.
43. S. Stewart, P. Albertus, V. Srinivasan, I. Plitz, N. Pereira, G. Amatucci, and J. Newman, "Optimizing the Performance of Lithium Titanate Spinel Paired with Activated Carbon or Iron Phosphate," JECS 155 (2008) A253.
44. T. Muraliganth, A. Murugan, and A. Manthiram, "Nanoscale Networking of $LiFePO_4$ Nanorods Prepared by a Microwave-solvothermal Route with Carbon Nanotubes for Li-ion Batteries," Journal of Materials Chemistry (in press).
45. W. Choi, and A. Manthiram, "Influence of Fluorine Substitution on the Electrochemical Performance of 3 V Spinel $Li_4Mn_5O_{12-\eta}F_\eta$ Cathodes," Solid State Ionics 178 (2007) 1541-1545.
46. Y. Lu, A. Mansour, N. Yabuuchi, and Y. Shao-Horn, "The Origin of Enhanced Stability of "$AlPO_4$" nanoparticle coated $LiCoO_2$ during Cycling**,"** submitted to Chemistry of Materials (2008).
47. Y. Nabuuchi, Y.C. Lu, and Y. Shao-Horn, "The Effect of Synthesis Conditions on Reversible Capacity and Rate Capability of $LiNi_{0.5}Mn_{0.5}O_2$," to be submitted (2008).

Patents (FY2008)

1. A. Gadgil, S. Amrose, and R. Kostecki, "Electrochemical Removal of Arsenic," US Patent Application No. 61/093,245 (Aug. 2008).
2. C. Johnson, M. Thackeray, J. Vaughey, A. Kahaian, and J. Kim, "Layered Electrodes for Lithium Cells and Batteries," US Patent 7,358,009 (15 April 2008).
3. M. Doeff, J. Wilcox, R. Kostecki, and G. Lau, "Optimization of Carbon Coatings," US Patent Application No. 110,489 (Aug. 2008).
4. M. Thackeray, C. Johnson, and N. Li, "Manganese Oxide Composite Electrodes for Lithium Batteries," US Patent 7,303,840 (4 December 2007).
5. M. Thackeray, J. Kim, and C. Johnson, "Lithium Metal Oxide Electrodes for Lithium Batteries," US Patent 7,314,682 (1 January 2008).
6. M. Marcinek, and R. Kostecki, "Microwave Plasma CVD of Nano-Structured Tin/Carbon Composites," U.S. Patent Application No. 61/093,976 (Sept. 2008).
7. P. Kumta, "In situ synthesis of novel nano-scale silicon based composite anodes for lithium ion batteries," Provisional patent application filed September 25, 2008.
8. Regents of the University of California on behalf of T. Richardson, "Metal and alloy cermets and method for making same," PCT/US 08/65966 (5 June 2008).

Milestone Report

1. A. Dillon, et al., "High Energy Anodes," NREL Deliverable report fulfillment of end-of-year DOE milestone, Golden, CO, September 2008.

Sample Presentations

1. A. Kercher, N. Dudney, J. Kiggans, and J. Klett, "Coated porous carbon cathodes for Li-ion batteries," ECS Transactions (2008).
2. J. Vaughey, and M. Thackeray, "Intermetallic Negative Electrode Materials," 14th International Meeting on Lithium Batteries (IMLB), Tianjin, China, June 22-28 (2008).
3. J. Xiao, J. Chen, N. Chernova and M. S. Whittingham, "The Electric Economy and Energy Storage: The Impact of Order and Disorder in Cathodes for Lithium Batteries," Wuhan University, China, July 5th, 2008. (Invited)
4. J. Xiao, N. Chernova, and M. S. Whittingham, "Influence of Manganese Content on Performance of Layered $LiNi_{0.9-y}Mn_yCo_{0.1}O_2$ in Li-ion Batteries," MRS Spring Meeting, San Francisco, CA, March 24th, 2008.
5. J. Xiao, N. Chernova, and M. S. Whittingham, "Influence of Manganese Content on Structure and Electrochemical Behavior of $Li_{(4-X)/3}Mn_{(2-0.5x)/3}(Ni_{0.4}Co_{0.1})_XO_2$ in Li Batteries," IMLB Tianjin, China, June 30th, 2008.
6. L. Hardwick, M. Marcinek, and R. Kostecki, "Rechargeable Lithium and Li-ion Batteries," ECS Transactions - Washington, DC, Volume 11, February 2008.
7. M. Thackeray, "Anodes and Cathodes for Lithium Batteries - the Importance of Using Safe Materials," The 3rd Southern China Li-ion Battery Top Forum (CLTF2008), Shenzhen, China, March 3-5, 2008 (Invited).
8. M. Thackeray, "Chemical Storage - Battery Anodes and Cathodes," Materials Research Society (MRS) Spring Meeting, San Francisco, March 24-28, 2008 (Invited).
9. M. Thackeray, "Key Problems in Advanced Automobile Batteries," ACG Advanced Battery Technology Investment Summit, Chicago, June 17, 2008 (Invited).
10. M. Thackeray, "The Need for New Li-ion Battery Electrode Materials," The 25th International Battery Seminar, Fort Lauderdale, Florida, March 17-20, 2008 (Invited).
11. M. Thackeray, "The Structural Design of Electrode Materials for High Energy Lithium Batteries," International Symposium on Innovative Materials for Processes in Energy Systems (IMPRES), Kyoto, Japan, October 28-31, 2007 (Invited).
12. M. Thackeray, C. Johnson, S. Kang, and J. Vaughey, "High Capacity Manganese-Based Electrodes for Li-ion Batteries," 14th International Meeting on Lithium Batteries (IMLB), Tianjin, China, June 22-28 (2008) (Invited).
13. M. Thackeray, R. Benedek, C. Johnson, S. Kang, V. Pol, L. Trahey, and J. Vaughey, "Designing Structurally-Integrated Electrodes for Li-Ion Batteries," International Conference on Advanced Lithium Batteries for Automobile Applications, Argonne National Laboratory, September 15-17, 2008 (Invited).
14. M. S. Whittingham, "Homogeneous Intercalation Reactions: Bulk and Nano Materials," Int. Workshop on Fundamentals of Lithium-based Batteries, Schloss Ringberg, Tegernsee, Germany, November 23rd 2008. (Invited)

15. M. S. Whittingham, "The Frontiers of Advanced Battery Research," General Electric Battery Technology Symposium, Niskayuna, NY, Ocober 23rd 2008. (Invited)
16. M. S. Whittingham, "The Holy Grail of Energy Storage," EPRI-Great Lakes Workshop, Case-Western Reserve University, Cleveland, Ohio, October 21st 2008. (Invited)
17. M. S. Whittingham, "The Impact of Order and Disorder in Cathodes for Lithium Batteries," IMLB Tianjin, China, June 30th, 2008. (Invited)
18. N. Chernova, J. Miller, S. Upreti, M. S. Whittingham and O. Yakubovich, "The Role of Defects in Mixed Transition Metal Phosphates with Olivine Structure," MRS Spring Meeting, San Francisco, CA, March 25th, 2008.
19. N. Chernova, J. Xiao, M. S. Whittingham, J. Cabana, D. Zeng, and C. Grey, "Transition Metal Ordering in Layered Cathode Materials for Li-ion Batteries: Insight From the Magnetic Studies," MRS Spring Meeting, San Francisco, CA, March 24th, 2008.
20. Q. Fan, R. Zhang, C. Ban, and M. S. Whittingham, "Electrospun Manganese Oxide Nanofibers as Anode for Li-ion Batteries," MRS Fall Meeting, Boston, November 2007.

Appendix A – Contributors

Technology Development	
J. Barnes	Naval Surface Warfare Center West Bethesda, MD 20817-5700
J. Deppe[27]	Deppe Consulting Services, LLC PO Box 366 Davidsonville MD 21035 jbdeppe@lbl.gov
M. Keyser, G. Kim, T. Markel, A. Pesaran, J. Powell, K. Smith	National Renewable Energy Laboratory 1617 Cole Boulevard Golden, CO 80401-3393

Applied Battery Research	
DOE Program Manager	**David Howell** U.S. Department of Energy Office of Vehicle Technologies 1000 Independence Avenue, SW Washington, DC 20585
National Laboratory Program Manager	**Gary Henriksen** Argonne National Laboratory Chemical Engineering Division, Bldg 205 9700 South Cass Avenue Argonne, IL 60439
Understand Life-Limiting Mechanisms and Enhance Life	
Focus area point of contact	**Gary Henriksen** Chemical Engineering Division Argonne National Laboratory, Building 205 9700 South Cass Avenue Argonne, IL 60439 Phone: 630.252.4591, E-mail: henriksen@cmt.anl.gov
D. Abraham, I. Bloom, D. Dees, A. Jansen	Argonne National Laboratory Argonne, IL 60439
H.S. Lee, K.Y. Nam, X. Yang, W. Yoon	Brookhaven National Laboratory P.O. Box 5000, MSD Bldg. 555, Upton, NY 11973-5000

[27] Preparer of this report.

Applied Battery Research	
J. Christophersen, K. Gering	Idaho National Laboratory Idaho Falls, ID 83415-3830
V. Battaglia, F. McLarnon	Lawrence Berkeley National Laboratory Berkeley CA 94720-8168
Understand and Enhance Low-Temperature Performance	
Focus area Point of Contact	**Dennis Dees** Chemical Engineering Division Argonne National Laboratory, Building 205 9700 South Cass Avenue Argonne, IL 60439 Phone: 630.252.7349, E-mail: dees@cmt.anl.gov
A. Jansen	Argonne National Laboratory Argonne, IL 60439
K. Gering	Idaho National Laboratory Idaho Falls, ID 83415-3830
Understand and Enhance Abuse Tolerance	
Focus area point of contact	**E. Pete Roth** Advanced Power Sources R&D Sandia National Laboratories, MS: 0613 P.O. Box 5800 Albuquerque, NM 87185 Phone: 505.844.3949, E-mail: eproth@sandia.gov
K. Amine	Argonne National Laboratory Argonne, IL 60439
G. Kim	National Renewable Energy Laboratory 1617 Cole Boulevard Golden, CO 80401-3393
Cell-Level Cost Reduction	
Focus area point of contact	**Khalil Amine** Chemical Engineering Division Argonne National Laboratory, Building 205 9700 South Cass Avenue Argonne, IL 60439 Phone: 630.252.3838, E-mail: amine@cmt.anl.gov
A. Jansen	Argonne National Laboratory Argonne, IL 60439

Focused Fundamental Research	
DOE Program Manager	**David Howell** U.S. Department of Energy Office of Vehicle Technologies 1000 Independence Avenue, SW Washington, DC 20585 **Tien Duong**[28] U.S. Department of Energy Office of Solar Energy Technologies 1000 Independence Avenue, SW Washington, DC 20585
National Laboratory Program Manager	**Venkat Srinivasan** Lawrence Berkeley National Laboratory One Cyclotron Road, MS 70R-0108B Berkeley, CA 94720
New Cathode Systems, Performance and Limitations	
$LiFePO_4$ and other Phosphate Systems	
G. Ceder	Massachusetts Institute of Technology Cambridge, MA 02139-4307
C. Grey	State University of New York at Stony Brook, Department of Chemistry Stony Brook, NY
M. Doeff, T. Richardson	Lawrence Berkeley National Laboratory Berkeley CA 94720-8168
J. Goodenough	University of Texas at Austin 1 University Station C2200 Mechanical Engineering Dept. Austin, TX 78712-0292
A. Manthiram	Univ of Texas Texas Materials Institute , ETC 9-104 Austin TX 78712-0292
S. Whittingham	State University of New York at Binghamton Chemistry and Materials Research Center Binghamton, NY 13902-6000
K. Zaghib	Hydro-Québec Varennes, J3X 1S1 Québec Canada

[28] Project manager until July 2008 in the DOE Office of Vehicle Technologies – currently located in the DOE Office of Solar Technologies.

Focused Fundamental Research	
Layered Systems	
Y.S. Horn	Massachusetts Institute of Technology Mechanical Engineering, 3-158 77 Massachusetts Avenue Cambridge, MA 02139
M. Doeff	Lawrence Berkeley National Laboratory Berkeley CA 94720-8168
S. Whittingham	State University of New York at Binghamton Chemistry and Materials Research Center Binghamton, NY 13902-6000
X. Yang, W. Yoon	Brookhaven National Laboratory P.O. Box 5000, MSD Bldg. 555, Upton, NY 11973-5000
Spinel and Composite Systems	
A. Manthiram	Univ of Texas Texas Materials Institute , ETC 9-104 Austin TX 78712-0292
M. Thackeray	Argonne National Laboratory Chemical Technology Division Argonne IL 60439
New Anode Materials	
P. Kumta	Dept of Mechanical Engineering and Materials Science Swanson School of Engineering University of Pittsburgh Pittsburgh, PA 15260
R. Kostecki, J. Newman, T. Richardson	Lawrence Berkeley National Laboratory Berkeley CA 94720-8168
A. Dillon	National Renewable Energy Laboratory 1617 Cole Boulevard Golden, CO 80401-3393
M. Thackeray	Argonne National Laboratory Chemical Technology Division Argonne IL 60439
S. Whittingham	State University of New York at Binghamton Chemistry and Materials Research Center Binghamton, NY 13902-6000

Focused Fundamental Research	
N. Dudney	Oak Ridge National Laboratory P.O. Box 2008, MS 6030 Oak Ridge, TN. 37830-6030
A. West	Columbia University Chemical Engineering 812 Mudd Bldg New York, NY 10027-0000
J. Goodenough	University of Texas at Austin 1 University Station C2200 Mechanical Engineering Dept. Austin, TX 78712-0292
Novel Electrolytes and their Characterization	
N. Balsara, J. Kerr	Lawrence Berkeley National Laboratory Berkeley CA 94720-8168
G. D. Smith	University of Utah Department of Materials Science and Engineering Salt Lake City, UT
D. DesMarteau	Clemson University Department of Chemistry Clemson, SC 29634-0973.
W.-S. Yoon, X. Yang	Brookhaven National Laboratory Upton, NY 11973
Li-ion Modeling, Diagnostics, and Cell Analysis	
V. Battaglia, J. Newman, V. Srinivasan	Lawrence Berkeley National Laboratory Berkeley CA 94720-8168
A. M. Sastry	University of Michigan Dept of Mechanical Engineering and Applied Mechanics Ann Arbor, MI 48109-2125
G. Ceder	Massachusetts Institute of Technology Cambridge, MA 02139-4307
C. Grey	State University of New York at Stony Brook, Department of Chemistry Stony Brook, NY
N. Dudney	Oak Ridge National Laboratory P.O. Box 2008, MS 6030 Oak Ridge, TN. 37830-6030

Focused Fundamental Research	
G. D. Smith	University of Utah Department of Materials Science and Engineering Salt Lake City, UT
K. Zaghib	Hydro-Québec Varennes, J3X 1S1 Québec Canada
D. Wheeler	Brigham Young University Chemical Engineering Department, 350 CB Provo, UT 84602

Appendix B – 2008 Energy Storage R&D Highlights

Block Copolymer Electrolytes for Lithium Batteries

Researchers in the Batteries for Advanced Transportation Technologies Program, managed by the Lawrence Berkeley National Laboratory, are investigating the possibility of using dry polymers as the solvent for lithium salts in formulating electrolytes for Li-ion batteries. The block polymers being investigated include polystyrene-block-polyethylene oxide in which both the polystyrene (PS) and polyethylene oxide (PEO) phases are bi-continuous. The soft PEO phase conducts the lithium ions, whereas the PS imparts rigidity to the electrolyte. The resulting electrolyte has a conductivity of 0.001 S/cm and a shear modulus of 0.1 GPa at 90ºC. This combination of electrolyte properties provides both acceptable performance and good mechanical stability. Efforts to commercialize this patented technology are being pursued by a start-up company, Seeo, Inc., located in Berkeley, CA.

LBNL Researcher Receives R&D-100 Award

Professor Nitash Balsara, of the University of California - Berkeley, received an R&D 100 Award for his work on novel polymer electrolytes for rechargeable lithium batteries. Dr. Balsara's research, sponsored by the Office of Vehicle Technologies, uses composite polymer electrolytes comprised of an extremely hard, but non-conducting polystyrene-based portion to block dendrite formation, interwoven with a conducing PEO based portion to permit Li diffusion. The objective is to develop an electrolyte for rechargeable lithium batteries that will permit the use of metallic lithium electrodes to increase the energy storage capability of batteries for hybrid and plug-in hybrid electric vehicles. The R&D-100 Award is generally considered one of the most prestigious technology-oriented awards and provides a mark of excellence known to industry, government, and academia.

Studies of Structural Changes in Cathodes Useful in Improving Energy Density of Lithium-Ion Batteries

Scientists at BNL, working in collaboration with scientists at LG Chemical Corp. in Korea, have used *in situ* synchrotron-based XRD techniques to study the structural changes of mixed cathode materials ($LiCo_{1/3}Ni_{1/3}Mn_{1/3}O_2$ and $LiMn_2O_4$) during charge and discharge. The structural changes during charge/discharge at various rates have provided a clearer understanding of the Li insertion/desertion behavior of the mixed cathode materials, information that will be valuable for further improving this new type of mixed cathode. Such mixed cathodes, made by mixing layered oxides with $LiMn_2O_4$ spinel, have been suggested as a means of reducing self-discharge, capacity fading, and cost in high-power lithium-ion batteries for hybrid electric vehicles and plug-in hybrid electric vehicles. These studies are part of BNL's search for cathode materials that yield high energy and power density at low cost.

Argonne Licenses Advanced Cathode Materials for Li-Ion Batteries

ANL has licensed cathode materials and associated processing technology, developed under DOE's exploratory and applied battery R&D programs, to the Toda Kogyo Corporation. These advanced materials, a family of lithiated mixed metal oxide layered composite cathode materials, possess enhanced stability compared to conventional $LiCoO_2$ cathode material. These new materials incorporate electrochemically inactive components that are structurally integrated with

electrochemically active components to form cathode materials with enhanced structural stability. Members of this family possess sufficient stability to allow charging to higher voltages, which in turn results in higher specific capacities (~250 mAh/g). This family of materials also includes lithium-rich NMC type cathode materials. The Toda Kogyo Corporation plans to manufacture these materials in a plant located in Sarnia, Ontario, Canada.

Examining Life Limiting Mechanisms in Lithium-ion Cells

Scientists at ANL are developing and using new diagnostic tools to investigate phenomena limiting the life and performance of lithium-ion cells developed for use in HEVs. They recently achieved significant progress in understanding factors responsible for the gradual performance loss observed during long-term aging of high-power cells that employ nickel-manganese-cobalt mixed metal oxide (NMC) cathodes. Data from test cells containing reference electrodes show that a significant portion of the cell impedance rise on aging occurs at the graphite anode. Examination of aged graphite anodes, using dynamic secondary ion mass spectrometry, indicates that transition metal elements accumulate at the graphite anode and may be partially responsible for anode impedance rise during cell aging. Use of Argonne-developed electrolyte additives, which provide better electrode surface protection, has significantly extended the longevity of lithium-ion cells that use NMC type cathodes.

Researchers Receive Award for Battery Cathodes with Enhanced Rate Capability

Researchers supported by the Vehicle Technologies' exploratory battery research activity received a third place award at the April 2008 CleanTech Innovation contest sponsored by the Center for Entrepreneurship and Technology of the University of California at Berkeley. The award was for work that led to the discovery that partial replacement of cobalt (Co) with aluminum (Al) greatly improves the rate capabilities of layered-mixed-transition-metal-oxide electrodes in lithium battery configurations. The amount of cobalt is reduced by more than half, which should result in considerable cost savings in vehicular applications.

Advanced Battery Developed with Vehicle Technologies Support Wins R&D- 100 Award

ANL, teamed with EnerDel, Inc, was granted an R&D 100 award for the joint development of an advanced, high-power Lithium-Ion battery system. This new battery, recognized by R&D Magazine as one of the year's most significant technological innovations, is based on the use of the lithium titanium oxide/manganese-spinel cell chemistry. This chemistry is very stable under abusive conditions such as short circuits and accidental overcharging, and may enable the development of a battery system that is inherently safe compared to other Lithium-Ion battery technologies. The new batteries can achieve the power levels required by hybrid vehicles and show promise of meeting cold temperature (0°C to -30°C) operating requirements. EnerDel is currently evaluating this new Li-Ion battery technology in a modified Prius HEV.

Research Leads to Lower Cost Cathodes for Li-ion Batteries

Researchers in the BATT Program have been investigating ways to increase the content of the low-cost manganese and minimizing the content of the high-cost and rare cobalt in cathodes for

advanced lithium ion batteries. The studies allowed an upper limit of 50% manganese to be achieved along with a minimum of 10% cobalt, while still maintaining high capacity and rate. Higher manganese contents can be achieved when extra lithium is incorporated into the structure giving the so-called lithium-rich cathode but at the expense of power capability. The energy storage capacity at higher rates was found to be optimized when there was a slight deficiency of lithium in the initial cathode material.

Battery Usage and Size in HEVs and PHEVs

Researchers in the BATT program, managed by Lawrence Berkeley National Laboratory, have modeled Li-ion battery behavior under conditions that simulate the power and energy requirements of HEVs and PHEVs. The study found that PHEVs are limited by the energy required and HEVs by the power. This means that increasing the battery size does not improve the performance of a HEV in the same way that it does for a PHEV. The model also found that using electrode materials with flat discharge potentials, such as lithium iron phosphate, would improve the performance only if the battery is energy-limited as in a PHEV. The results of this study will help battery manufacturers select the most efficient battery size and materials.

Appendix C – List of Acronyms

ABR	Applied Battery Research
ACN	Acetonitrile
AEM	Advanced electrolyte model
AFM	Atomic force microscopy
ANL	Argonne National Laboratory
ARC	Accelerated rate calorimetry
ARL	Army Research Laboratory
ASI	Area specific impedance
ATD	Advanced Technology Development
ATR	Attenuated total reflection
BATT	Batteries for Advanced Transportation Technologies
BCF	Binder and carbon free
BET	Brunauer, Emmett, and Teller surface area
BF	Binder free
BNL	Brookhaven National Laboratory
CBED	Convergent beam electron diffraction
C_{ch}	Charge cycling rate
CD	Charge depleting
C_{dis}	Charge cycling rate
CE	Counter electrode
CPI	Compact Power Inc.
CRADA	Cooperative research and development agreement
CS	Charge-sustaining
CVD	Chemical vapor deposition
DEC	Diethyl carbonate
DMC	Dimethyl carbonate
DOD	Depth-of-discharge
DOE	Department of Energy
DOEx	Design of experiment
DSC	Differential scanning calorimetry
EC	Ethylene carbonate
ECS	The Electrochemical Society
EDS	Energy dispersive spectroscopy
EIS	Electrochemical impedance spectroscopy
EMC	Ethyl methyl carbonate
EMIM	1-ethyl-3-methyl imidizolium
EMI-TFSI	1-ethyl-3-methylimidazolium - Bis(fluorosulfonyl)imide

EPD	Electrophoretic deposition
EV	Electric vehicle
EXAFS	Extended x-ray absorption fine structure
FSI	(fluorosulfonyl)-imide
FTIR	Fourier transform infrared
FVM	Finite volume method
γBL	γ-butyrolactone
GC	Gas chromatography
GITT	Galvanostatic intermittent titration technique
GPC	Gel-permeation chromatography
HEMM	High energy mechanical milling
HEV	Hybrid electric vehicle
HOPG	Highly oriented pyrolytic graphite
HPPC	Hybrid pulse power characterization
HQ	Hydro-Québec
HRTEM	High resolution transmission electron microscopy
HWCVD	Hot-wire chemical vapor deposition
IBA2007	International Battery Materials Association
ICL	Irreversible capacity loss
ICP	Inductively coupled plasma
IL	Ionic liquids
IMLB	International Meeting on Lithium Batteries
IMPRES	Innovative Materials for Processes in Energy Systems
INL	Idaho National Laboratory
IR	Infra-red
JCI	Johnson Controls, Incorporated
JCS	Johnson Controls – Saft
JECS	Journal of the Electrochemical Society
JPS	Journal of Power Sources
JR	Jelly Roll
kHz	kilo-Hertz
kW	kilo-Watt
kWh	kilo-Watt Hour
LBNL	Lawrence Berkeley National Laboratory
LFP	Li iron phosphate
LiBOB	Lithium bis(oxolato)borate

LiTFSI	Lithium bis(trifluoromethane-sulfonyl)imide
LTO	Lithium titanate, $Li_4Ti_5O_{12}$
LUMO	Lowest unoccupied molecular orbital
MAG	Massive activated graphite
MCMB	Mesocarbon micro beads
MD	Molecular dynamics
MEK	Methyl ethyl ketone
MES	Mitsui Engineering Shipbuilding
MF	Morphology factor
MHz	Megahertz
MPPC	Minimum pulse power characterization
MRS	Materials Research Society
MS	Mass spectroscopy
MSMD	Multi-scale, multi-dimensional
MW	Molecular weight
MWCNT	Multi-walled carbon nanotubes
MW-HT	Microwave-hydrothermal method
MW-ST	Microwave-solvothermal
NASA	National Aeronautics and Space Administration
NCA	$LiNi_{0.8}Co_{0.15}Al_{0.05}O_2$
NCM	$Li_{1+w}[Ni_xCo_yMn_z]_{1-w}O_2$
n_{cyc}	Net number of complete formation cycles per cell
NMC	$LiNi_{1/3}Co_{1/3}Mn_{1/3}O_2$
NMR	Nuclear magnetic resonance
NREL	National Renewable Energy Laboratory
OCP	Open circuit potential
OCV	Open circuit voltage
ORNL	Oak Ridge National Laboratory
PAn	Polyaniline
PC	Propylene carbonate
PEDOT	p-toluene sulfonic acid (p-TSA) doped poly(3,4-ethylenedioxythiophene)
PEO	Poly(ethylene oxide)
PEY	Partial electron yield
PFPTFBB	pentafluorophenyl)-tetrafluoro-1,3,2-benzodioxaborole
PHEV	Plug-in hybrid electric vehicle
PLD	Pulse laser deposition
PS	Polystyrene
PVdF	Poly(vinylidene fluoride)
R&D	Research and development

RE	Reference electrode
RMS	Root mean square
RVE	Response variable expressions
SAD	Selected area diffraction
SBIR	Small Business Innovative Research
SCE	Saturated calomel electrode
SEI	Solid electrolyte interphase
SEM	Scanning electron microscopy
SIC	Single ion conducting
SIMS	Secondary ion mass spectrometry
SNL	Sandia National Laboratories
SOC	State of charge
SPE	Solid polymer electrolytes
STEM	Scanning transmission electron microscope
STTR	Small Business Technology Transfer Program
SUNY	State University of New York
T	Temperature
TEM	Transmission electron microscopy
TFSI	bis(trifluoromethanesulfonyl)imide
TGA	Thermal gravimetric analysis
TLVT	Technology life verification test
TM	Transition metal
t_{ocv}	Open circuit rest period
TOF-SIMS	Time of flight secondary ion mass spectrometry
TPD	Temperature programmed desorption
TPFPB	tris(pentafluorophenyl) borane
UCV	Upper cutoff voltage
USABC	United States Advanced Battery Consortium
USCAR	United States Council for Automotive Research
VC	Vinylene carbonate
VEC	Vinyl ethylene carbonate
VS	Vinylene triacetoxyvinylsilane
VT	Vehicle Technology
XAFS	X-Ray absorption fine structure
XANES	X-Ray absorption near edge structure
XAS	X-Ray absorption spectroscopy
XPS	X-ray photoelectron spectroscopy
XRD	X-ray diffraction

DOE/CM-3014

A Strong Energy Portfolio for a Strong America

Energy efficiency and clean, renewable energy will mean a stronger economy, a cleaner environment, and greater energy independence for America. Working with a wide array of state, community, industry, and university partners, the U.S. Department of Energy's Office of Energy Efficiency and Renewable Energy invests in a diverse portfolio of energy technologies.

For more information contact:
EERE Information Center
1-877-EERE-INF (1-877-337-3463)
www.eere.energy.gov